Studies of Zγ Production and Constraints on Anomalous Triple Gauge Couplings in pp Collisions at $\sqrt{s} = 7$ TeV

Thesis by

Jan Veverka

In Partial Fulfillment of the Requirements

for the Degree of

Doctor of Philosophy

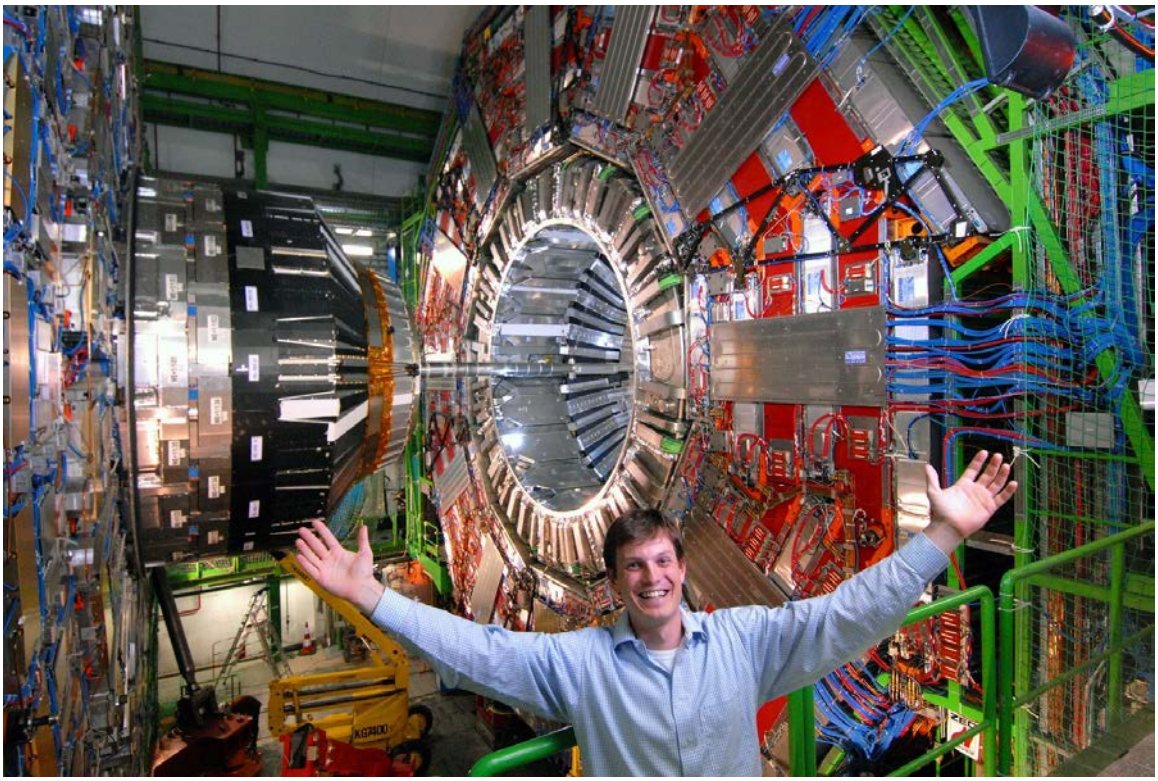

California Institute of Technology

Pasadena, California

2013

(Defended May 15, 2013)

To my family

Abstract

We test the electroweak sector of the Standard Model of particle physics through the measurements of the cross section of the simultaneous production of the neutral weak boson Z and photon γ, and the limits on the anomalous $Z\gamma\gamma$ and $ZZ\gamma$ triple gauge couplings h_3 and h_4 with the Z decaying to leptons (electrons and muons) $Z \to \ell^+\ell^-$, with ℓ = e, μ. We analyze events collected in proton-proton collisions at center of mass energy of $\sqrt{s} = 7\,\text{TeV}$ corresponding to an integrated luminosity of $5.0\,\text{fb}^{-1}$. The analyzed events were recorded by the Compact Muon Solenoid detector at the Large Hadron Collider in 2011.

The production cross section has been measured for hard photons with transverse momentum $E_\text{T}^\gamma > 15\,\text{GeV}$ that are separated from the the final state leptons in the η-ϕ plane by $\Delta R > 0.7$, whose sum of the transverse energy of hadrons over the transverse energy of the photon in a cone around the photon with $\Delta R < 0.3$ is $\epsilon^h < 0.5$, and with the invariant mass of the dilepton system $M_{\ell\ell} > 50\,\text{GeV}$. The measured cross section value is $\sigma(\text{pp} \to \text{Z}\gamma \to \ell\ell\gamma) = 5.33 \pm 0.08\,(\text{stat.}) \pm 0.25\,(\text{syst.}) \pm 0.12\,(\text{lumi.})\,\text{pb}$. This is compatible with the Standard Model prediction that includes next-to-leading-order $O(\alpha\alpha_\text{S})$ contributions: $\sigma_\text{NLO}(\text{pp} \to \text{Z}\gamma \to \ell\ell\gamma) = 5.45 \pm 0.27\,\text{pb}$.

The measured 95 % confidence-level limits on the anomalous $Z\gamma\gamma$ and $ZZ\gamma$ couplings h_3 and h_4 are $|h_3^\gamma| < 0.01$ and $|h_4^\gamma| < 8.8 \times 10^{-5}$ for the $Z\gamma\gamma$ couplings and $|h_3^\text{Z}| < 8.6 \times 10^{-3}$ and $|h_4^\text{Z}| < 8.0 \times 10^{-5}$ for the $ZZ\gamma$ couplings. These values are also compatible with the Standard Model where they vanish in the tree-level approximation. They extend the sensitivity of the 2012 results from the ATLAS collaboration based on $1.02\,\text{fb}^{-1}$ of data by a factor of 2.4 to 3.1.

Contents

List of Figures

List of Tables

Chapter 1

Introduction

Particle physics emerged through the realization that both matter and radiation are made of enormous numbers of seemingly indivisible constituents, elementary particles. It aims at understanding these building blocks of nature on the most fundamental level: How many different kinds of particles are there? Are they composite objects made of yet smaller elementary ones? How do they interact with each other?

Based on the foundations of quantum mechanics, special relativity and quantum electrodynamics, the Standard Model (SM) of particle physics has proven very successful in describing practically all experimental particle physics data over the several last decades [1]. Despite its successes, it does not give the complete picture:

- it does not explain dark matter and dark energy,
- it does not support mass of neutrinos,
- it does not include gravitation.

This thesis aspires to shed light on some of these open questions by looking for signs of new physics in events with the weak neutral bosons Z and photons γ.[1] The multiboson self-interactions represent the least well-measured sector of the SM. Precise measurements of such interactions may therefore reveal potential deviations from the theoretical predictions of the SM. Such deviations may hint at some new, not yet accounted for, phenomena. Moreover, the Zγ interactions are special among the various possible multiboson interactions. They are strongly suppressed as Z and γ

[1] Photons are also bosons, same as Z bosons.

do not couple directly in the SM. These features make the studies of $Z\gamma$ production particularly attractive.

Chapter 2 gives a comprehensive introduction of the SM including a complete list of known elementary particles and their interactions. It formally introduces the concepts of fields and Lagrangian density and shows explicitly the lack of direct $Z\gamma$ interactions. It discusses the SM paramaters that have to be estimated experimentally. Finally, it focuses on the subject of this work in the last two sections. Section describest the $Z\gamma$ production in the SM. Section introduces the anomalous triple gauge couplings (ATGCs) as components of a formalism that extends the SM by the inclusion of direct $Z\gamma$ interactions. This formalism gives a way to quantitatively interpret the $Z\gamma$ interaction measurements.

Chapter 3 describes the Large Hadron Collider (LHC) and the Compact Muon Solenoid (CMS) experiment. We explain important LHC features, properties of the beam, and its parameters during the running in 2010-2012. We then introduce the various systems of CMS and discuss their main roles and properties relevant to this work.

Chapter 4 explains how the detector signals are combined to reconstruct and identify particles originating from proton-proton collisions at the center of CMS. We focus on particles employed in this analysis—photons, electrons, and muons—and the related algorithms.

Chapter 5 presents the analysis methodology. We discuss the measurement of the $Z\gamma$ production cross section and setting limits on the $Z\gamma\gamma$ and $ZZ\gamma$ ATGCs. We provide details about the auxiliary measurements and estimates of the systematic uncertainties.

Chapter 6 then provides the resulting measured $Z\gamma$ production cross sections and limits on the $Z\gamma\gamma$ and $ZZ\gamma$ ATGCs. We also compare our results with previous measurements and discuss future analyses.

Chapter 2

Theory

The Standard Model (SM) is our current best theoretical description of elementary particle physics. It describes the properties of all known elementary particles and their interactions (except for gravity). It enables a number of quantitative predictions that have been experimentally confirmed with unprecedented precision.

2.1 Gauge Theory

Mathematically, the SM is a special case of a *gauge field theory*. It is defined in terms of a Lagrangian $\mathcal{L}$. This is a polynomial expression involving fields[1] $\phi(x)$, $\psi(x)$, $A^\mu(x)$, ..., and their derivatives $\partial_\nu\phi(x)$, $\partial_\nu\psi(x)$, $\partial_\nu A^\mu$, ... where $x = (x^\mu)_{\mu=0}^3 = (t, x, y, z)$ is the 4-vector of the space-time coordinates and $\partial_\mu = 1/\partial x^\mu$ the derivatives with respect to them.

The fields permeate all of space-time and their values are linear operators. Generally, they do not commute. They act on states in the *Fock space* — a field-theoretical equivalent of the quantum-mechanical wave function fully describing a state of a physical system.

The SM Lagrangian is constructed as the most general renormalizable expression fulfilling a set of given symmetries. The *gauge symmetry* plays a pivotal role in the process. It is a local internal symmetry related to a *gauge group* G — a *Lie group*

[1]Spin-0, -1/2 and -1 fields are usually denoted $\phi(x), \psi(x)$ and $A^\mu(x)$, respectively. A spin-1/2 field has 4-components whose indices are usually suppressed. A spin-1 field has four components labeled by the Lorentz index μ.

of transformations whose action on the fields ϕ_a leaves the Lagrangian $L = L[\phi_a]$ invariant:

$$\phi_a(x) \to \phi'_a(x) = U(x)\phi(x), \tag{2.1}$$

$$\mathcal{L} \to \mathcal{L}' = \mathcal{L}[\phi'_a] = \mathcal{L}[\phi_a] \tag{2.2}$$

where $U(x)$ is an element of some representation of G that varies arbitrarily with x. The Yang-Mills Lagrangian of a generic non-Abelian theory for a fermionic field multiplet ψ of mass m corresponding to an irreducible representation r of a gauge group G is [2]:

$$\mathcal{L} = \overline{\psi}(i\not{D} - m)\psi - \frac{1}{4}\left(F^a_{\mu\nu}\right)^2, \tag{2.3}$$

where we sum the index a over the generators T^a of G, the indices μ and ν label the space-time components and $\overline{\psi} := \psi^\dagger\gamma^0$ is the *conjugate field*. $F^a_{\mu\nu}$ is the *field strength tensor*:

$$F^a_{\mu\nu} = \partial_\mu A^a_\nu - \partial_\nu A^a_\mu + g f^{abc} A^b_\mu A^c_\nu, \tag{2.4}$$

where A^a_μ are the *gauge fields*, g is the *coupling constant*, and f^{abc} are the *structure constants* of G satisfying:

$$[T^a, T^b] = i f^{abc} T^c. \tag{2.5}$$

$\not{D}$ is Feynman's shorthand *slash notation* for the sum $\not{D} = \gamma^\mu D_\mu$; defined generally for an arbitrary vector A_μ as $\not{A} := \gamma^\mu A_\mu$. D_μ is the *covariant derivative*:

$$D_\mu = \partial_\mu - i g t^a_r A^a_\mu, \tag{2.6}$$

where t^a_r are the r representation matrices of G. The gauge fields correspond to vector bosons that mediate the interactions between the fermions.

The gauge group of the Standard Model is $SU(3)_\mathrm{C} \times SU(2)_\mathrm{L} \times U(1)_\mathrm{Y}$. The subscripts C, L and Y stand for color, left and hypercharge, respectively. The $SU(3)_C$ factor describes the strong interaction and the $SU(2)_L \times U(1)_Y$ factor the unified elec-

	Generation	Symbol	Flavor	Charge (e)	Mass (MeV)	Anti-partner
Leptons	1	e^-	electron	-1	0.511	e^+
		ν_e	electron neutrino	0	$< 3 \times 10^{-6}$	$\overline{\nu}_e$
	2	μ^-	muon	-1	105.7	μ^+
		ν_μ	muon neutrino	0	< 0.19	$\overline{\nu}_\mu$
	3	τ^-	tau	-1	1777	τ^+
		ν_τ	tau neutrino	0	< 18.2	$\overline{\nu}_\tau$
Quarks	1	u	up	$+2/3$	~ 3	$\overline{\text{u}}$
		d	down	$-1/3$	~ 5	$\overline{\text{d}}$
	2	c	charm	$+2/3$	$\sim 1.2 \times 10^3$	$\overline{\text{c}}$
		s	strange	$-1/3$	~ 100	$\overline{\text{s}}$
	3	t	top	$+2/3$	$\sim 178 \times 10^3$	$\overline{\text{t}}$
		b	bottom	$-1/3$	$\sim 4.5 \times 10^3$	$\overline{\text{b}}$

Table 2.1: Fermions in the Standard Model. Antiparticles are identical except for opposite charge [3]

troweak interactions. The $SU(2)_L \times U(1)_Y$ also contains $U(1)_{\text{em}}$ subgroup describing the electromagnetic interactions.

The fermion representations of the SM gauge group factors are related to various kinds of *charge* carried by the fermions. The $SU(3)_{\text{C}}$ acts on fermions that bear the *color charge*, the $SU(2)_{\text{L}}$ on fermions that bear the *weak isospin*, the $U(1)_{\text{Y}}$ on fermions that bear the *weak hypercharge*, and $U(1)_{\text{em}}$ on fermions that bear the *electric charge*.

2.2 Fermions

There are seventeen fields in the SM. They correspond to the different elementary particles which are their quanta. The particles that are quanta of twelve of the SM fields represent matter. They have a spin 1/2, obey Fermi statistics, and are called *fermions*, cf. Table 2.1. They follow the *Pauli exclusion principle* and their volume density is limited.

All fermions carry weak hypercharge and interact weakly. They are further subdivided into leptons which have no color charge and do not interact strongly, and

quarks which do have color charge and do interact strongly.

All quarks are electrically charged and participate in the electromagnetic interactions. Leptons are further split into charged leptons which carry electric charge and interact electromagnetically, and neutrinos which are electrically neutral and do not interact electromagnetically.

Fermions are organized into three generations based on their masses. The different generations are identical in terms of the properties of their members except for their masses. The higher generation members are heavier than the corresponding lower generation members.

All fermions have anti-partners representing anti-matter. These antiparticles are also quanta of the same twelve fermionic fields. For each fermionic field, its particle and antiparticle are identical to each other in terms of their mass and quantum properties except for the opposite values of their charges, including the color charge, the electric charge, the weak isospin components, and the weak hypercharge.

Mathematically, a fermionic field forms a quadruplet. We denote it ψ with the component indices suppressed treating it as a 4×1 column matrix. It can be decomposed into two independent components based on its *chirality*. Chirality is defined as the projection of the spin on the direction of the momentum. The chiral eigenstates of a field ψ are referred as *left-handed* ψ^{L} and *right-handed* ψ^{R}. Formally, we write:

$$\psi^{\mathrm{L}} = \frac{1}{2}(1 - \gamma^5)\psi,$$
$$\psi^{\mathrm{R}} = \frac{1}{2}(1 + \gamma^5)\psi,$$

where 1 in $1-\gamma^5$ is a 4×4 unit matrix, and $\gamma^5 := i\gamma^0\gamma^1\gamma^2\gamma^3$ is the *fifth gamma matrix*. γ^μ, $\mu = 0, \ldots, 3$ are the *Dirac gamma matrices*. The left and right projections play an important role in the theory of electroweak interactions which acts differently on the left- and right-handed components.

Force	Boson	Coupling Strength	Charge (e)	Spin	Mass (GeV)	Range (m)
Electromagnetic	γ (photon)	α	0	1	0	∞
Weak	$W^{\pm}$	G_F	± 1	1	80.4	10^{-18}
	Z^0		0	1	91.2	
Strong	g (gluon)	α_S	0	1	0	10^{-15}

Table 2.2: Forces and gauge bosons in the SM [3].

2.3 Bosons

Of the seventeen SM fields, there are remaining five whose quanta mediate interactions and represent radiation. They attain integer spin values, obey Bose-Einstein statistics, and are called *bosons*. They do not follow the Pauli exclusion principle and their volume density is not limited.

Four of the five bosonic fields are the *gauge fields* of the theory, mediate interactions, and correspond to carriers of forces. They have spin 1 and hence are referred to as *vector bosons*, cf. Table 2.2. Their quanta are:

- the *photon* γ, the carrier of the electromagnetic force.
- the *weak bosons* $W^{\pm}$ and Z^0, the carriers of the weak force, and
- the *gluon* g, the carrier of the strong force.

The photon is neutral and massless. It is its own antiparticle. The weak bosons are all massive and they self-interact. The Z boson is electrically neutral and it is its own antiparticle. The $W^{\pm}$ bosons are electrically charged and interact electromagnetically. The W^+ is the anti-partner of the W^-. The gluon is massless. It carries the color charge, interacts with itself, and is its own anti-particle.

Of the five bosonic SM fields, the last one is associated with the *Higgs boson* H. It differs from the gauge bosons by the fact that it does not mediate interactions, it is not a gauge boson and it is not a vector boson with spin 1. It is a *scalar boson* and has spin 0. It is massive and is responsible for the *Higgs mechanism* describing the

spontaneous breaking of the electroweak symmetry — a process through which the elementary particles acquire mass.

2.4 Perturbation Theory

A Lagrangian specifies the time evolution of the fields. An exact solution is known for the case of vanishing coupling constant $g = 0$. In this case, the Yang-Mills Lagrangian (2.3) leads to a free fermion field and a gauge boson field that do not interact.

The perturbation theory provides a prescription for calculations of the mutual interactions of the fields. This enables one to make predictions about the observable behavior of the associated particles that can be studied with particle accelerators like the Large Hadron Collider.

The perturbative calculations are approximations to the free field solutions in the form of a Taylor expansion in the coupling constant g. The individual terms in the series are given as sums of Feynman diagrams corresponding to gauge bosons mediating interactions among fermions and themselves. These follow from the terms in the Lagrangian that involve products of the fields and their derivatives.

The particle content and dynamics of a specific gauge field theory are fully defined by the choice of the gauge group G and its representation r of the fermionic fields. It contains a number of fermions equal to the dimension $d(r)$ of the representation r, and a number of bosons $d(G)$ equal to the number of generators of G. The value of the fermion mass m and the strength of the coupling constant g are free parameters of the theory that have to be estimated experimentally.

2.5 Quantum Chromodynamics

Quantum chromodynamics (QCD) is the theory of the strong interaction among particles carrying *color charge*: quarks and gluons. It is described by the $SU(3)$ sector of the SM Lagrangian coupled to fermions in the fundamental representation. The

QCD Lagrangian is [3]:

$$\mathcal{L}_{\mathrm{QCD}} = \sum_{q,a,b} \overline{q}_a \left(i\gamma^\mu D_{\mu,ab} - m_q \delta_{ab} \right) q_b - \frac{1}{4} \left(G^A_{\mu\nu} \right)^2 , \tag{2.7}$$

where we sum:

- the fermionic field q over the quark flavors $q =$ u, d, c, s, t, and b,
- the indices a and b over the colors $a, b = 1$ to $N_c = 3$ (red, green, blue) — elements of the fermionic representation of the gauge group — and finally
- the index A over the gluon color states $A = 1, 2, \ldots, N_c^2 - 1 = 8$ — elements of the adjoint representation of the gauge group.

$\psi_{q,a}$ denotes a quark field of flavor q, color a and mass m_q. $D_{\mu,ab}$ is the covariant derivative for the color indices a and b:

$$D_{\mu,ab} = \partial_\mu \delta_{ab} - i g_{\mathrm{s}} t^{\mathcal{C}}_{ab} G^{\mathcal{C}}_\mu, \tag{2.8}$$

where δ_{ab} is the *Kronecker delta* symbol:

$$\delta_{ab} = \begin{cases} 1 & \text{for } a = b, \\ 0 & \text{otherwise,} \end{cases} \tag{2.9}$$

g_{s} is the strong coupling constant, $t^{\mathcal{C}}_{ab}$ are the $SU(3)$ adjoint representation generators, and $G^{\mathcal{C}}_\mu$ is the gluon gauge field in the color-state $\mathcal{C}$. It is convenient to define $t^{\mathcal{A}} =$

$\mathcal{ABC}$	$f^{\mathcal{ABC}}$
123	1
147, 165, 246, 257, 345, 376	$\frac{1}{2}$
458, 678	$\frac{\sqrt{3}}{2}$

Table 2.3: Structure constants $f^{\mathcal{ABC}}$ of the $SU(3)$ gauge group. All other non-zero constants correspond to permutations of the indices $\mathcal{ABC}$ with respect to which $f^{\mathcal{ABC}}$ is totally antisymmetric: $f^{\mathcal{ABC}} = f^{\mathcal{CAB}} = f^{\mathcal{BCA}} = -f^{\mathcal{BAC}} = -f^{\mathcal{CBA}} = -f^{\mathcal{ACB}}$.

$\lambda_{\mathcal{A}}/2$ where $\lambda_{\mathcal{A}}$ are the *Gell-Mann matrices* [4]:

$$\lambda_1 = \begin{pmatrix} 0 & 1 & 0 \\ 1 & 0 & 0 \\ 0 & 0 & 0 \end{pmatrix}, \quad \lambda_2 = \begin{pmatrix} 0 & -i & 0 \\ i & 0 & 0 \\ 0 & 0 & 0 \end{pmatrix}, \quad \lambda_3 = \begin{pmatrix} 1 & 0 & 0 \\ 0 & -1 & 0 \\ 0 & 0 & 0 \end{pmatrix},$$

$$\lambda_4 = \begin{pmatrix} 0 & 0 & 1 \\ 0 & 0 & 0 \\ 1 & 0 & 0 \end{pmatrix}, \quad \lambda_5 = \begin{pmatrix} 0 & 0 & -i \\ 0 & 0 & 0 \\ i & 0 & 0 \end{pmatrix}, \quad \lambda_6 = \begin{pmatrix} 0 & 0 & 0 \\ 0 & 0 & 1 \\ 0 & 1 & 0 \end{pmatrix}, \tag{2.10}$$

$$\lambda_7 = \begin{pmatrix} 0 & 0 & 0 \\ 0 & 0 & -i \\ 0 & i & 0 \end{pmatrix}, \quad \lambda_8 = \frac{1}{\sqrt{3}} \begin{pmatrix} 1 & 0 & 0 \\ 0 & 1 & 0 \\ 0 & 0 & -2 \end{pmatrix}.$$

These matrices generalize the Pauli spin matrices in the sense that they are traceless, Hermitian, and $\mathrm{tr}(\lambda_{\mathcal{A}}\lambda_{\mathcal{B}}) = 2\delta_{\mathcal{AB}}$.

The gluon field strength tensor is:

$$G^{\mathcal{A}}_{\mu\nu} = \partial_\mu G^{\mathcal{A}}_\nu - \partial_\nu G^{\mathcal{A}}_\mu + g_{\mathrm{s}} f^{\mathcal{ABC}} G^{\mathcal{B}}_\mu G^{\mathcal{C}}_\nu \tag{2.11}$$

where the indices $\mathcal{B}$ and $\mathcal{C}$ are summed over the gluon color states and $f^{\mathcal{ABC}}$ are the $SU(3)$ structure constants, cf. Table 2.3.

The last term in eq. (2.11) leads to gluon self-interaction and quark *confinement*. There exist no free colored states. Only color-less bound states of quarks can propagate freely.

2.6 Electroweak Theory

The $SU(2)_{\mathrm{L}} \times U(1)_{\mathrm{Y}}$ gauge group of the SM Lagrangian describes interactions of particles with non-zero values of the third component of the weak isospin T^3 and the weak hypercharge quantum number Y.

The $SU(2)_{\mathrm{L}}$ acts on the gauge fields W^1_μ, W^2_μ, W^3_μ coupled to the helicity eigenstates of the fermionic fields. The gauge group representation associated with the fermions depends on their helicity:

- The right-handed components of the fermionic fields ($\psi_{\mathrm{R}} = \frac{1}{2}(1+\gamma_5)\psi$, chirality $+1$) transform as singlets under $SU(2)_{\mathrm{L}}$. They have the third component of the weak isospin equal to zero $T_3 = 0$ and thus effectively do not participate in interactions mediated by W^a_μ.

- The left-handed components of the fermionic fields ($\psi_{\mathrm{L}} = \frac{1}{2}(1-\gamma_5)\psi$, chirality -1) transform as doublets under $SU(2)_{\mathrm{L}}$. These doublets are defined as:

$$\Psi_{\mathrm{L}} = \begin{pmatrix} \Psi^+ \\ \Psi^- \end{pmatrix}_{\mathrm{L}}, \qquad \Psi \in \left\{ \begin{pmatrix} \nu^i \\ e^i \end{pmatrix}, \begin{pmatrix} u^i \\ d^i \end{pmatrix} \right\}_{i=1}^{3} \tag{2.12}$$

  where the index i runs over the three generations of fermions:

$$\begin{pmatrix} \nu^i \\ e^i \end{pmatrix}_{i=1}^{3} = \begin{pmatrix} \nu^e \\ e \end{pmatrix}, \begin{pmatrix} \nu^\mu \\ \mu \end{pmatrix}, \begin{pmatrix} \nu^\tau \\ \tau \end{pmatrix}$$
$$\begin{pmatrix} u^i \\ d^i \end{pmatrix}_{i=1}^{3} = \begin{pmatrix} u \\ d \end{pmatrix}, \begin{pmatrix} c \\ s \end{pmatrix}, \begin{pmatrix} t \\ b \end{pmatrix}. \tag{2.13}$$

  The third component of the weak isospin is $T^3 = +1/2$ for the top components of these doublets $\Psi^+_{\mathrm{L}} = \nu^i_{\mathrm{L}}$, u^i_{L}, and $T^3 = -1/2$ for the bottom components

$\Psi_{\mathrm{L}}^{-} = e_{\mathrm{L}}^{i},\, d_{\mathrm{L}}^{i}$:

$$T^3\Psi_{\mathrm{L}} = \frac{1}{2}\begin{pmatrix} 1 & 0 \\ 0 & -1 \end{pmatrix}\Psi_{\mathrm{L}}. \tag{2.14}$$

The $U(1)_{\mathrm{Y}}$ acts on the gauge field B_μ and fermionic fields with non-zero value of the weak hypercharge Y. For the right-handed fields, the weak hypercharge is equal to the electric charge $Y = Q$. For the left-handed fields, the weak hypercharge is different for leptons $Y = -1/2$ and quarks $Y = +1/6$, cf. Table 2.4.

With the definitions (2.12) and (2.13), we can describe the fermion representation of the gauge group concisely through the way the $SU(2)_{\mathrm{L}}$ and $U(1)_{\mathrm{Y}}$ generators T^a and Y act on them:

$$T^a\Psi = \frac{1}{2}\tau^a(1-\gamma^5)\Psi,$$

$$Y\begin{pmatrix}\nu^i \\ e^i\end{pmatrix} = -\frac{1}{2}\begin{pmatrix}\nu^i \\ e^i\end{pmatrix}_{\mathrm{L}} + \begin{pmatrix}0 & 0 \\ 0 & -1\end{pmatrix}\begin{pmatrix}\nu^i \\ e^i\end{pmatrix}_{\mathrm{R}}, \quad \text{and} \tag{2.15}$$

$$Y\begin{pmatrix}u^i \\ d^i\end{pmatrix} = +\frac{1}{6}\begin{pmatrix}u^i \\ d^i\end{pmatrix}_{\mathrm{L}} + \begin{pmatrix}\frac{2}{3} & 0 \\ 0 & -\frac{1}{3}\end{pmatrix}\begin{pmatrix}u^i \\ d^i\end{pmatrix}_{\mathrm{R}},$$

where τ^a are $SU(2)$ generators related to the *Pauli matrices* σ^a by:

$$\tau^a = \frac{1}{2}\sigma^a. \tag{2.16}$$

The Pauli matrices are defined as:

$$\sigma_1 = \sigma_x = \begin{pmatrix}0 & 1 \\ 1 & 0\end{pmatrix}, \quad \sigma_2 = \sigma_y = \begin{pmatrix}0 & -i \\ i & 0\end{pmatrix}, \quad \sigma_3 = \sigma_z = \begin{pmatrix}1 & 0 \\ 0 & -1\end{pmatrix}. \tag{2.17}$$

They are Hermitian, traceless, and unitary.

Having specified the gauge group and its fermion representation, we can write the

F	Field	ψ	P	R_C	T	T^3	Y	Q	Physical Quanta
1	electron neutrino	ν_e	L	**1**	1/2	1/2	−1/2	0	$\nu_1\,\overline{\nu}_1\,\nu_2\,\overline{\nu}_2\,\nu_3\,\overline{\nu}_3$
			R	**1**	0	0	0	0	$\nu_1\,\overline{\nu}_1\,\nu_2\,\overline{\nu}_2\,\nu_3\,\overline{\nu}_3$
	electron	e	L	**1**	1/2	−1/2	−1/2	−1	$e^-\ e^+\ \mu^-\ \mu^+\ \tau^-\ \tau^+$
			R	**1**	0	0	−1	−1	$e^-\ e^+\ \mu^-\ \mu^+\ \tau^-\ \tau^+$
	up quark	u	L	**3**	1/2	1/2	+1/6	+2/3	$u\ \overline{u}\ c\ \overline{c}\ t\ \overline{t}$
			R	**3**	0	0	+2/3	+2/3	$u\ \overline{u}\ c\ \overline{c}\ t\ \overline{t}$
	down quark	d	L	**3**	1/2	−1/2	+1/6	−1/3	$d\ \overline{d}\ s\ \overline{s}\ b\ \overline{b}$
			R	**3**	0	0	−1/3	−1/3	$d\ \overline{d}\ s\ \overline{s}\ b\ \overline{b}$
2	muon neutrino	ν_μ	L	**1**	1/2	1/2	−1/2	0	$\nu_1\,\overline{\nu}_1\,\nu_2\,\overline{\nu}_2\,\nu_3\,\overline{\nu}_3$
			R	**1**	0	0	0	0	$\nu_1\,\overline{\nu}_1\,\nu_2\,\overline{\nu}_2\,\nu_3\,\overline{\nu}_3$
	muon	μ	L	**1**	1/2	−1/2	−1/2	−1	$e^-\ e^+\ \mu^-\ \mu^+\ \tau^-\ \tau^+$
			R	**1**	0	0	−1	−1	$e^-\ e^+\ \mu^-\ \mu^+\ \tau^-\ \tau^+$
	charm quark	c	L	**3**	1/2	1/2	+1/6	+2/3	$u\ \overline{u}\ c\ \overline{c}\ t\ \overline{t}$
			R	**3**	0	0	+2/3	+2/3	$u\ \overline{u}\ c\ \overline{c}\ t\ \overline{t}$
	strange quark	s	L	**3**	1/2	−1/2	+1/6	−1/3	$d\ \overline{d}\ s\ \overline{s}\ b\ \overline{b}$
			R	**3**	0	0	−1/3	−1/3	$d\ \overline{d}\ s\ \overline{s}\ b\ \overline{b}$
3	tau neutrino	ν_τ	L	**1**	1/2	1/2	−1/2	0	$\nu_1\,\overline{\nu}_1\,\nu_2\,\overline{\nu}_2\,\nu_3\,\overline{\nu}_3$
			R	**1**	0	0	0	0	$\nu_1\,\overline{\nu}_1\,\nu_2\,\overline{\nu}_2\,\nu_3\,\overline{\nu}_3$
	tau	τ	L	**1**	1/2	−1/2	−1/2	−1	$e^-\ e^+\ \mu^-\ \mu^+\ \tau^-\ \tau^+$
			R	**1**	0	0	−1	−1	$e^-\ e^+\ \mu^-\ \mu^+\ \tau^-\ \tau^+$
	top quark	t	L	**3**	1/2	1/2	+1/6	+2/3	$u\ \overline{u}\ c\ \overline{c}\ t\ \overline{t}$
			R	**3**	0	0	+2/3	+2/3	$u\ \overline{u}\ c\ \overline{c}\ t\ \overline{t}$
	bottom quark	b	L	**3**	1/2	−1/2	+1/6	−1/3	$d\ \overline{d}\ s\ \overline{s}\ b\ \overline{b}$
			R	**3**	0	0	−1/3	−1/3	$d\ \overline{d}\ s\ \overline{s}\ b\ \overline{b}$

Table 2.4: **SM Fermion Field Content**. The fields are in their interaction eigenstates which are superpositions of the mass eigenstates. F is the family, ψ is the interaction eigenstate symbol, P the chirality (L and R denote the left- and right-handed chirality components $\psi_L = \frac{1-\gamma^5}{2}\psi$ and $\psi_R = \frac{1+\gamma^5}{2}\psi$ of $\psi = \psi_L + \psi_R$), R_C is the $SU(3)_{\rm C}$ representation, T the weak isospin magnitude, T_3 the third component of the weak isospin, Y the weak hypercharge, and Q the electric charge. The right-handed neutrinos are hypothetical and are only added for completeness. They are sterile — do not participate in the interactions except for gravity. They are considered an extension of the SM by some authors and are not treated in the text.

Lagrangian of the electroweak sector before symmetry breaking as:

$$\mathcal{L}_{\text{EW}} = \sum_{\Psi} \overline{\Psi} i\gamma^{\mu} D_{\mu} \Psi - \frac{1}{4} \left(W^{a}_{\mu\nu}\right)^2 - \frac{1}{4} \left(B_{\mu\nu}\right)^2, \tag{2.18}$$

where the summation runs over all the fermionic doublets (2.12), $\overline{\Psi}$ is defined as:

$$\overline{\Psi} = \left(\overline{\Psi}^{+},\ \overline{\Psi}^{-}\right), \tag{2.19}$$

and the covariant derivative as:

$$D_{\mu} = \partial_{\mu} - igW^{a}_{\mu} T^{a} - ig' B_{\mu} Y. \tag{2.20}$$

Here, g and g' are the weak isospin and weak hypercharge coupling constants. The field strength tensors in the last two terms of (2.18) follow directly from the Yang-Mills Lagrangian (2.4):

$$\begin{aligned} W^{a}_{\mu\nu} &= \partial_{\mu} W^{a}_{\nu} - \partial_{\nu} W^{a}_{\mu} + g\epsilon^{abc} W^{b}_{\mu} W^{c}_{\nu}, \quad \text{and} \\ B_{\mu\nu} &= \partial_{\mu} B_{\nu} - \partial_{\nu} B_{\mu}, \end{aligned} \tag{2.21}$$

where ϵ^{abc} are the $SU(2)$ structure constants also known as the *Levi-Civita symbol*:

$$\epsilon^{abc} = \begin{cases} +1 & \text{if } (a,\ b,\ c) \text{ is } (1,\ 2,\ 3),\ (3,\ 1,\ 2) \text{ or } (2,\ 3,\ 1), \\ -1 & \text{if } (a,\ b,\ c) \text{ is } (3,\ 2,\ 1),\ (1,\ 3,\ 2) \text{ or } (2,\ 1,\ 3), \\ \ \ 0 & \text{otherwise.} \end{cases} \tag{2.22}$$

2.6.1 Higgs Mechanism

The Higgs mechanism is a process of adding the *Higgs field* and related terms to the electroweak Lagrangian.

The Higgs field is a complex doublet:

$$\phi = \frac{1}{\sqrt{2}} \begin{pmatrix} \phi^{+} \\ \phi^{0} \end{pmatrix}. \tag{2.23}$$

It transforms as a spinor under $SU(2)_{\rm L}$. Its weak hypercharge is 1/2 and the superscripts "+" and "0" denote the electric charge of the components which are 1 and 0:

$$T^a\phi = \tau^a\phi, \qquad Y\phi = \frac{1}{2}\phi, \quad \text{and} \qquad Q\phi = \begin{pmatrix}\phi^+\\ 0\end{pmatrix}, \tag{2.24}$$

so its full gauge transformation is:

$$\phi \to \mathrm{e}^{\mathrm{i}\alpha^a\tau^a}\mathrm{e}^{\mathrm{i}\beta/2}\phi. \tag{2.25}$$

The components of ϕ transform as scalars under the Lorentz transformation.

The corresponding Lagrangian describing the Higgs field and its coupling to the gauge bosons and fermions is:

$$\mathcal{L}_\phi = |D_\mu\phi|^2 + \mathcal{L}_{\phi\Psi} - V(\phi), \tag{2.26}$$

where D_μ is the covariant derivative given by eq. (2.20) with T^a and Y corresponding to the ϕ representation of $SU(2)_{\rm L}\times U(1)_Y$ (2.24).

The Higgs doublet couples to fermions through a *Yukawa coupling* described by the $\mathcal{L}_{\phi\Psi}$ term. It is the most generic Lorentz invariant, renormalizable, and gauge invariant expression involving the products of ϕ and fermion fields:

$$\begin{aligned}\mathcal{L}_{\phi\Psi} = -\sum_{i,j=1}^{3}\Big(&\lambda_e^{ij}\,\overline{L}^i_{\rm L}\cdot\phi\, e^j_{\rm R} + \lambda_\nu^{ij}\epsilon^{ab}\overline{L}^i_{{\rm L}a}\phi^\dagger_b\nu^j_{\rm R}\\ &+ \lambda_d^{ij}\,\overline{Q}^i_{\rm L}\cdot\phi\, d^j_{\rm R} + \lambda_u^{ij}\epsilon^{ab}\overline{Q}^i_{{\rm L}a}\phi^\dagger_b\, u^j_{\rm R} + \text{h.c.}\Big),\end{aligned} \tag{2.27}$$

where we sum the indices i and j over the three fermion generations (2.13), and the indices a and b over the components of the $SU(2)_{\rm L}$ doublets:

$$L = \begin{pmatrix}L_1\\ L_2\end{pmatrix} \in \left\{\begin{pmatrix}\nu^i\\ e^i\end{pmatrix}\right\}_{i=1}^{3}, \qquad Q = \begin{pmatrix}Q_1\\ Q_2\end{pmatrix} \in \left\{\begin{pmatrix}u^i\\ d^i\end{pmatrix}\right\}_{i=1}^{3}, \tag{2.28}$$

and ϕ. The elements of the matrices λ_f^{ij}, $f = e, \nu, u, d$ are complex dimensionless coupling constants whose values are not specified by the theory. In the first and third term on the right-hand side of (2.27), the $SU(2)_{\rm L}$ indices of the fermion doublets $\overline{L}_{\rm L}$ and $\overline{Q}_{\rm L}$ are contracted with the $SU(2)_{\rm L}$ indices of the Higgs doublet ϕ: $\overline{\Psi}_{\rm L} \cdot \phi = \delta^{ab}\overline{\Psi}_{{\rm L}a}\phi_b$ for $\Psi = L, Q$. The letters "h.c." in the end of (2.27) stand for *Hermitian conjugate* terms.

Originally, the SM was formulated without the second term of $\mathcal{L}_{\phi\Psi}$ involving the hypothetical *sterile* right-handed neutrinos. Keeping this term can provide a mechanism for neutrinos to acquire mass which is compatible with the observations of the *neutrino oscillations*.

The potential $V(\phi)$ in (2.26) is defined as:

$$V(\phi) = -\mu^2\phi^\dagger\phi + \frac{\lambda}{2}(\phi^\dagger\phi)^2, \tag{2.29}$$

with λ and $\mu^2 > 0$ being some real constants that have to be specified by experiment.

This potential leads to a degenerate vacuum state of the Higgs field that lies on a hypersphere in the space of the ϕ components satisfying $|\phi^+|^2 + |\phi^0|^2 = \mu^2/\lambda$. The physically observable particles correspond to redefined fields that are small perturbations around the vacuum state. We have to choose a particular point on the hypersphere of the degenerate vacuum states to rewrite the theory in terms of the physical fields.

We can always perform gauge transformations to the so called *unitarity gauge* in which the Higgs field attains the vacuum expectation value:

$$\langle\phi\rangle = \frac{1}{\sqrt{2}}\begin{pmatrix}0\\ v\end{pmatrix}, \tag{2.30}$$

where $v = \mu^2/\lambda$ in the tree-level perturbation expansion. We then define the physical Higgs field h by:

$$\phi(x) = \frac{1}{\sqrt{2}}U(x)\begin{pmatrix}0\\ v + h(x)\end{pmatrix}, \tag{2.31}$$

Where $U(x)$ is a $SU(2)$ gauge transformation defined such that $h(x)$ is real. Fixing the gauge to the unitarity gauge eliminates $U(x)$ from the Lagrangian. This reduces the number of real-valued components of ϕ from four to one.

Such a choice of the vacuum state breaks the original gauge symmetry. The Lagrangian in terms of the physical fields is not symmetric under $SU(2)_{\mathrm{L}} \times U(1)_{\mathrm{Y}}$ anymore. Adding the Higgs field to the theory thus breaks this symmetry. This is what we refer to as the *spontaneous breaking of electroweak symmetry*.

2.6.2 Gauge Boson Masses

Expanding the kinetic term of (2.26) for the physical Higgs field $h(x)$ in the unitarity gauge with explicit substitution of the Pauli matrices (2.17) for the $SU(2)$ generators gives:

$$\begin{aligned}
|D_\mu \phi|^2 &= \frac{1}{2}\left|\left[\partial_\mu + \frac{ig}{2}\left(W_\mu^1\sigma_1 + W_\mu^2\sigma_2 + W_\mu^3\sigma_3\right) + \frac{ig'}{2}B_\mu\right]\frac{1}{\sqrt{2}}\begin{pmatrix}0\\ v+h\end{pmatrix}\right|^2 \\
&= \frac{1}{2}\left|\begin{pmatrix}0\\ \partial_\mu h\end{pmatrix} + \frac{ig}{2}\begin{pmatrix}W_\mu^1 - iW_\mu^2\\ -W_\mu^3 + \frac{g'}{g}B_\mu\end{pmatrix}(v+h)\right|^2 \\
&= \frac{1}{2}(\partial_\mu h)^2 + \frac{1}{2}\left(\frac{vg}{2}\right)^2\left[(W_\mu^1)^2 + (W_\mu^2)^2 + \left(W_\mu^3 - \frac{g'}{g}B_\mu\right)^2\right]\left(1+\frac{h}{v}\right)^2 \\
&= \frac{1}{2}(\partial_\mu h)^2 + \frac{1}{2}\left[m_W^2|W_\mu^+|^2 + m_W^2|W_\mu^-|^2 + m_Z^2(Z_\mu)^2\right]\left(1+\frac{h}{v}\right)^2,
\end{aligned} \tag{2.32}$$

where we transform the gauge fields W^1, W^2, W^3 and B of the $SU(2)_{\mathrm{L}} \times U(1)_{\mathrm{Y}}$ to the fields $W^\pm$, Z and A:

$$\begin{aligned}
W^\pm &= \frac{1}{\sqrt{2}}(W^1 \mp iW^2) \\
\begin{pmatrix}Z\\ A\end{pmatrix} &= \begin{pmatrix}\cos\theta_{\mathrm{W}} & -\sin\theta_{\mathrm{W}}\\ \sin\theta_{\mathrm{W}} & \cos\theta_{\mathrm{W}}\end{pmatrix}\begin{pmatrix}W^3\\ B\end{pmatrix},
\end{aligned} \tag{2.33}$$

or, conversely:

$$\begin{pmatrix} W^1 \\ W^2 \end{pmatrix} = \frac{1}{\sqrt{2}} \begin{pmatrix} 1 & 1 \\ i & -i \end{pmatrix} \begin{pmatrix} W^+ \\ W^- \end{pmatrix}, \qquad \begin{pmatrix} W^3 \\ B \end{pmatrix} = \begin{pmatrix} \cos\theta_{\mathrm{W}} & \sin\theta_{\mathrm{W}} \\ -\sin\theta_{\mathrm{W}} & \cos\theta_{\mathrm{W}} \end{pmatrix} \begin{pmatrix} Z \\ A \end{pmatrix}. \tag{2.34}$$

Here, θ_{W} is the *Weinberg angle* or *weak mixing angle* which is defined in terms of the coupling constants:

$$\begin{aligned} \sin\theta_{\mathrm{W}} &= \frac{g'}{\sqrt{g^2 + g'^2}}, \quad \text{and} \\ \cos\theta_{\mathrm{W}} &= \frac{g}{\sqrt{g^2 + g'^2}}. \end{aligned} \tag{2.35}$$

The parameters m_W and m_Z in the last row of eq. (2.32) are:

$$\begin{aligned} m_W &= g\,\frac{v}{2}, \quad \text{and} \\ m_Z &= \sqrt{g^2 + g'^2}\,\frac{v}{2} = \frac{m_W}{\cos\theta_{\mathrm{W}}}, \end{aligned} \tag{2.36}$$

where v is the vacuum expectation value of ϕ. We observe that the transformation of the fields W^i and B leads to mass terms for the fields $W^\pm$ and Z with masses m_W and m_Z while the field A remains massless:

$$m_A = 0. \tag{2.37}$$

$W^\pm$, Z and A are indeed the physical fields whose quanta are the massive $\mathrm{W}^\pm$ and Z^0 bosons, and the massless photon γ with masses m_W, m_Z, and m_A, respectively. The relations (2.36) and (2.37) represent a prediction of the electroweak symmetry breaking and are the basis of important successful tests of the SM.

2.6.3 Coupling to Fermions

To see how the physical gauge fields couple to fermions, we rewrite the covariant derivative (2.20) in terms of $W^{\pm}$, Z and A using (2.34):

$$\begin{aligned} D_\mu &= \partial_\mu - i\frac{g}{\sqrt{2}}(W_\mu^+ T^+ + W_\mu^- T^-) - i\frac{1}{\sqrt{g^2+g'^2}} Z_\mu (g^2 T^3 - g'^2 Y) \\ &\quad - i\frac{gg'}{\sqrt{g^2+g'^2}} A_\mu (T^3 + Y) \\ &= \partial_\mu - i\frac{g}{\sqrt{2}}(W_\mu^+ T^+ + W_\mu^- T^-) - i\frac{g}{\cos\theta_{\mathrm{W}}} Z_\mu (T^3 - Q\sin^2\theta_{\mathrm{W}}) - ieA_\mu Q, \end{aligned} \tag{2.38}$$

where we define the generators $T^{\pm}$ to simplify the above expression:

$$T^{\pm} = T^1 \pm iT^2, \tag{2.39}$$

$$\tau^{\pm} = \frac{1}{2}(\sigma^1 \pm i\sigma^2) = \sigma^{\pm}, \qquad \sigma^+ = \begin{pmatrix} 0 & 1 \\ 0 & 0 \end{pmatrix}, \qquad \sigma^- = \begin{pmatrix} 0 & 0 \\ 1 & 0 \end{pmatrix}. \tag{2.40}$$

We see that the photon couples to the fermions with the coupling constant

$$e = \frac{gg'}{\sqrt{g^2+g'^2}} = g\sin\theta_{\mathrm{W}}, \tag{2.41}$$

and we identify the related charge operator:

$$Q = T^3 + Y \tag{2.42}$$

with the electric charge. The physical field A_μ plays the role of a gauge field also after the symmetry breaking and we recover the $U(1)_{\mathrm{EM}}$ gauge symmetry of QED.

Plugging the covariant derivative (2.38) in terms of the physical gauge fields in the first term of the electroweak Lagrangian (2.18), we see how the physical gauge fields couple to fermions:

$$\sum_\Psi \overline{\Psi}\left(i\not{D}\right)\Psi = \sum_\psi \overline{\psi}\left(i\not{\partial}\right)\psi + g\left(W_\mu^+ J_W^{\mu+} + W_\mu^- J_W^{\mu-} + Z_\mu J_Z^\mu\right) + eA_\mu J_{\mathrm{EM}}^\mu, \tag{2.43}$$

where:

$$
\begin{aligned}
J_W^{\mu\pm} &= \frac{1}{\sqrt{2}} \sum_{\Psi} \overline{\Psi} \gamma^\mu T^\pm \Psi = \frac{1}{2\sqrt{2}} \sum_{\Psi} \overline{\Psi} \gamma^\mu \tau^\pm \left(1 - \gamma^5\right) \Psi = \frac{1}{\sqrt{2}} \sum_{\Psi} \overline{\Psi}_L^\pm \gamma^\mu \Psi_L^\mp, \\
J_Z^\mu &= \frac{1}{2 \cos\theta_{\mathrm{W}}} \sum_{\psi} \overline{\psi} \gamma^\mu (g_{\mathrm{V}} - g_{\mathrm{A}} \gamma^5) \psi \\
J_{\mathrm{EM}}^\mu &= \sum_{\psi} \overline{\psi} \gamma^\mu Q \psi,
\end{aligned}
\tag{2.44}
$$

Here, we sum Ψ over all $SU(2)_{\mathrm{L}}$ fermion doublets (2.12) and ψ over all fermion fields $\psi = \{\nu^i,\, e^i,\, u^i,\, d^i\}_{i=1}^3$. The *vector* and *axial-vector couplings* g_{V} and g_{A} are:

$$
\begin{aligned}
g_{\mathrm{V}} &= T^3 - 2Q \sin^2 \theta_{\mathrm{W}} \\
g_{\mathrm{A}} &= T^3.
\end{aligned}
\tag{2.45}
$$

The third component of the weak hyperspin T^3 and the electric charge Q are to be evaluated in each term specifically for the given fermion, cf. Table 2.4:

$$
\begin{aligned}
T^3 \Psi_{\mathrm{L}}^\pm &= \pm \frac{1}{2} \Psi_{\mathrm{L}}^\pm, & T^3 \Psi_{\mathrm{R}}^\pm &= 0, \\
Q\nu^i &= 0, & Qu^i &= +\frac{2}{3} u^i, \\
Qe^i &= -e^i, & Qd^i &= -\frac{1}{3} d^i.
\end{aligned}
\tag{2.46}
$$

Writing out the sums over fermions specifically for the interaction eigenstates, the

currents (2.44) read:

$$
\begin{aligned}
J_W^{\mu+} &= \frac{1}{\sqrt{2}} \sum_{i=1}^{3} \left(\overline{\nu}_{\mathrm{L}}^{i} \gamma^{\mu} e_{\mathrm{L}}^{i} + \overline{u}_{\mathrm{L}}^{i} \gamma^{\mu} d_{\mathrm{L}}^{i} \right), \\
J_W^{\mu-} &= \frac{1}{\sqrt{2}} \sum_{i=1}^{3} \left(\overline{e}_{\mathrm{L}}^{i} \gamma^{\mu} \nu_{\mathrm{L}}^{i} + \overline{d}_{\mathrm{L}}^{i} \gamma^{\mu} u_{\mathrm{L}}^{i} \right) = \left(J_W^{\mu+} \right)^{*}, \\
J_Z^{\mu} &= \frac{1}{\cos\theta_{\mathrm{W}}} \sum_{\psi} \left[\overline{\psi}_L \left(T^3 - Q \sin^2\theta_{\mathrm{W}} \right) \psi_L + \overline{\psi}_R \left(-Q \sin^2\theta_{\mathrm{W}} \right) \psi_R \right] \\
&= \frac{1}{\cos\theta_{\mathrm{W}}} \sum_{i=1}^{3} \Bigg[\overline{\nu}_{\mathrm{L}}^{i} \gamma^{\mu} \left(\frac{1}{2} \right) \nu_{\mathrm{L}}^{i} \\
&\qquad \overline{e}_{\mathrm{L}}^{i} \gamma^{\mu} \left(-\frac{1}{2} + \sin^2\theta_{\mathrm{W}} \right) e_{\mathrm{L}}^{i} + \overline{e}_{\mathrm{R}}^{i} \gamma^{\mu} \left(\sin^2\theta_{\mathrm{W}} \right) e_{\mathrm{R}}^{i} + \\
&\qquad \overline{u}_{\mathrm{L}}^{i} \gamma^{\mu} \left(\frac{1}{2} - \frac{2}{3} \sin^2\theta_{\mathrm{W}} \right) u_{\mathrm{L}}^{i} + \overline{u}_{\mathrm{R}}^{i} \gamma^{\mu} \left(-\frac{2}{3} \sin^2\theta_{\mathrm{W}} \right) u_{\mathrm{R}}^{i} + \\
&\qquad \overline{d}_{\mathrm{L}}^{i} \gamma^{\mu} \left(-\frac{1}{2} + \frac{1}{3} \sin^2\theta_{\mathrm{W}} \right) d_{\mathrm{L}}^{i} + \overline{d}_{\mathrm{R}}^{i} \gamma^{\mu} \left(+\frac{1}{3} \sin^2\theta_{\mathrm{W}} \right) d_{\mathrm{R}}^{i} \Bigg], \\
J_{\mathrm{EM}}^{\mu} &= \sum_{i=1}^{3} \left[\overline{e}^{i} \gamma^{\mu} \left(-1 \right) e^{i} + \overline{u}^{i} \gamma^{\mu} \left(+\frac{2}{3} \right) u^{i} + \overline{d}^{i} \gamma^{\mu} \left(-\frac{1}{3} \right) d^{i} \right],
\end{aligned}
\tag{2.47}
$$

2.6.4 Fermion Masses

Similarly to the gauge bosons, the fermions also acquire their mass through the interaction with the Higgs field. The second term of $\mathcal{L}_{\phi}$ (2.26) for the physical Higgs field in the unitarity gauge can be expanded as:

$$
\begin{aligned}
\mathcal{L}_{\phi\Psi} &= -\sum_{i=1}^{3} \left(m_{\nu}^{i} \overline{\nu}_{\mathrm{L}}^{\prime i} \nu_{\mathrm{R}}^{\prime i} + m_{e}^{i} \overline{e}_{\mathrm{L}}^{\prime i} e_{\mathrm{R}}^{\prime i} + m_{d}^{i} \overline{d}_{\mathrm{L}}^{\prime i} d_{\mathrm{R}}^{\prime i} + m_{u}^{i} \overline{u}_{\mathrm{L}}^{\prime i} u_{\mathrm{R}}^{\prime i} \right) \left(1 + \frac{h}{v} \right) + \mathrm{h.c.} \\
&= -\sum_{i=1}^{3} \sum_{f} m_{f}^{i} \overline{f}_{\mathrm{L}}^{\prime i} f_{\mathrm{R}}^{\prime i} \left(1 + \frac{h}{v} \right) + \mathrm{h.c.} \\
&= -\sum_{\psi} m_{\psi} \overline{\psi}^{\prime} \psi^{\prime} \left(1 + \frac{h}{v} \right),
\end{aligned}
\tag{2.48}
$$

where

$$
m_{f}^{i} = \frac{1}{\sqrt{2}} D_{f}^{ii} \, v, \qquad\qquad f \in \{\nu,\, e,\, u,\, d\} \tag{2.49}
$$

are elements of diagonal real-valued matrices D_f. These are related to the coupling matrices λ_f (2.27) through unitary transformations U_f and W_f:

$$\lambda_f \lambda_f^\dagger = U_f D_f^2 U_f^\dagger, \qquad \lambda_f^\dagger \lambda_f = W_f D_f^2 W_f^\dagger, \tag{2.50}$$

where f stands for one of the fermion types as in (2.49). The above relations define uniquely both D_f, U_f, and W_f. They imply that λ_f can itself be diagonalized:

$$D_f = U_f^\dagger \lambda_f W_f, \qquad \lambda_f = U_f D_f W_f^\dagger. \tag{2.51}$$

The unitary transformations U_f and W_f rotate the triplets of fermion families between their interaction eigenstates ψ and their mass eigenstates ψ':

$$f_{\mathrm{L}}^i = U_\psi^{ij} f_{\mathrm{L}}'^i, \qquad f_{\mathrm{R}}^i = W_\psi^{ij} f_{\mathrm{R}}'^i. \tag{2.52}$$

We see that the last line of (2.48) gives mass terms for the fermions. The fermion masses m_ψ are defined by the couplings to the Higgs field λ_f^{ij} through the relations (2.49), (2.50), and (2.51).

The currents describing the coupling of the gauge bosons to fermions (2.47) are expressed in terms of the fermion interaction eigenstates. The mixing of the fermion mass and interaction eigenstates (2.52) raises the question: "How do the gauge bosons couple to the fermion *mass* eigenstates?" To answer this question we plug the transformations (2.52) in the currents (2.47).

The transformation matrices (2.52) commute with the gauge group operators T^3 and Q because the fermion gauge group representations and charges are identical for the different families. For the *neutral currents* J_Z and J_{EM}, it suffices to investigate

the term:

$$\begin{aligned}
\sum_{i=1}^{3} \overline{f}^i \gamma^\mu f^i &= \sum_{i=1}^{3} \left(\overline{f}^i_{\mathrm{L}} \gamma^\mu f^i_{\mathrm{L}} + \overline{f}^i_{\mathrm{R}} \gamma^\mu f^i_{\mathrm{R}} \right) \\
&= \sum_{i,j,k=1}^{3} \left(\overline{f}'^j_{\mathrm{L}} U_f^{\dagger ji} \gamma^\mu U_f^{ik} f'^k_{\mathrm{L}} + \overline{f}'^i_{\mathrm{R}} W_f^{\dagger ji} \gamma^\mu W_f^{ik} f'^i_{\mathrm{R}} \right) \\
&= \sum_{i,j,k=1}^{3} \left(\overline{f}'^j_{\mathrm{L}} \gamma^\mu \underbrace{(U_f^\dagger U_f)^{jk}}_{\delta^{jk}} f'^k_{\mathrm{L}} + \overline{f}'^i_{\mathrm{R}} \gamma^\mu \underbrace{(W_f^\dagger W_f)^{jk}}_{\delta^{jk}} f'^i_{\mathrm{R}} \right) \\
&= \sum_{i=1}^{3} \overline{f}'^i \gamma^\mu f'^i.
\end{aligned} \tag{2.53}$$

We see that U_f and W_f cancel out and the expressions (2.44) and (2.47) hold for both the fermion interaction and mass eigenstates $\psi = f^i$ and $\psi' = f'^i$.

The situation is different for the *charged currents* $J^{\pm}_W$:

$$\begin{aligned}
J^{\mu+}_W &= \frac{1}{\sqrt{2}} \sum_{i,j,k=1}^{3} \left[\overline{\nu}'^j_{\mathrm{L}} U_\nu^{\dagger ji} \gamma^\mu U_e^{ik} e'^k_{\mathrm{L}} + \overline{u}'^j_{\mathrm{L}} U_u^{\dagger ji} \gamma^\mu U_d^{ik} d'^k_{\mathrm{L}} \right] \\
&= \frac{1}{\sqrt{2}} \sum_{j,k=1}^{3} \left[\overline{\nu}'^j_{\mathrm{L}} \gamma^\mu V^{jk}_{\mathrm{PMNS}} e'^k_{\mathrm{L}} + \overline{u}'^j_{\mathrm{L}} \gamma^\mu V^{jk}_{\mathrm{CKM}} d'^k_{\mathrm{L}} \right].
\end{aligned} \tag{2.54}$$

V_{PNMS} is the *Pontecorvo-Maki-Nakagawa-Sakata matrix* (*PMNS matrix* also known as the *Maki-Nakagawa-Sakata matrix*, *MNS matrix*, *lepton mixing matrix*, or *neutrino mixing matrix*) [5–7]. V_{CKM} is the *Cabibbo-Kobayashi-Maskawa matrix* (*CKM matrix*, *quark mixing matrix*) [8, 9]. They are defined as:

$$V_{\mathrm{PMNS}} = U_\nu^\dagger U_e, \qquad\qquad V_{\mathrm{CKM}} = U_u^\dagger U_d. \tag{2.55}$$

They are unitary 3×3 matrices that can be parametrized in terms of three *Euler angles* θ_{12}, θ_{13}, θ_{23} (*CKM mixing angles* in case of V_{CKM}) and a complex phase δ_{13}

(*CKM CP violating phase* in case of V_{CKM}):

$$V = \begin{pmatrix} 1 & 0 & 0 \\ 0 & c_{23} & s_{23} \\ 0 & -s_{23} & c_{23} \end{pmatrix} \begin{pmatrix} c_{13} & 0 & s_{13}\mathrm{e}^{\mathrm{i}\delta_{13}} \\ 0 & 1 & 0 \\ -s_{13}\mathrm{e}^{\mathrm{i}\delta_{13}} & 0 & c_{13} \end{pmatrix} \begin{pmatrix} c_{12} & s_{12} & 0 \\ -s_{12} & c_{12} & 0 \\ 0 & 0 & 1 \end{pmatrix}, \tag{2.56}$$

where $s_{ij} = \sin\theta_{ij}$, $c_{ij} = \cos\theta_{ij}$ for i, $j = 1, 2, 3$, cf. Table 2.5.

The magnitudes of the CKM matrix elements have been constrained experimentally [3] to the following values:

$$V_{\mathrm{CKM}}^{|\cdot|} = \begin{pmatrix} 0.97427 \pm 0.00015 & 0.22534 \pm 0.00065 & 0.00351^{+0.00015}_{-0.00014} \\ 0.22520 \pm 0.00065 & 0.97344 \pm 0.00016 & 0.0412^{+0.0011}_{-0.0005} \\ 0.00867^{+0.00029}_{-0.00031} & 0.0404^{+0.0011}_{-0.0005} & 0.999146^{+0.000021}_{-0.000046} \end{pmatrix}, \tag{2.57}$$

where the superscript "$|\cdot|$" stands for the absolute values of the matrix elements $(V^{|\cdot|})_{ij} = |V_{ij}|$.

The mismatch between the quark interaction and mass eigenstates leads to *quark flavor changing* — a property unique for the weak interactions mediated by the $\mathrm{W}^{\pm}$ bosons that lead to mixing of the quark families.

An analogous mechanism leads to the description of *neutrino oscillations* among their different flavors as they propagate freely in their mass eigenstates that are mixtures of the weak interaction eigenstates.

2.6.5 The Higgs Boson

Now we turn our attention to the potential term of $\mathcal{L}_\phi$ (2.26). We expand it in the unitarity gauge around the vacuum expectation value $v = \mu/\sqrt{\lambda}$ adding a constant

term $\frac{\lambda v^2}{4}$ to simplify the result:

$$\begin{aligned} V(\phi) + \frac{\lambda v^2}{4} &= \lambda \left[\left(\phi^\dagger \phi\right)^2 - \frac{v^2}{2} \right]^2 \\ &= \lambda \left(\frac{1}{2}(v+h)^2 - \frac{v^2}{2} \right)^2 \\ &= \frac{1}{2} m_h^2 h^2 \left(1 + \frac{h}{2v} \right)^2, \end{aligned} \tag{2.58}$$

where we define m_h as:

$$m_{\mathrm{H}} = \sqrt{2\lambda}\, v. \tag{2.59}$$

In addition to the self-interaction of h, the expression (2.58) yields a mass term for the physical Higgs field. Its quanta have the mass m_{H} and correspond to the Higgs bosons H.

2.6.6 Gauge Boson Self-Interactions

The gauge boson self-interactions are a direct consequence of the non-Abelian structure of the electroweak sector of the SM. Elements of a non-Abelian group do not commute. This causes the structure constants f^{abc} in eq. (2.5) to acquire non-zero values. The last term in eq. (2.6) then leads to non-vanishing terms involving products of the gauge fields and their derivatives in the Lagrangian.

This is generally true for both the strong and the electroweak interactions. We focus on the electroweak gauge boson self-interactions in the following since these can be studied experimentally with contemporary colliders.

To describe the self-interaction of the physical fields, we plug the mass-to-interaction eigenstate transformations of the gauge fields (2.34) in the second and third terms of

the electroweak Lagrangian (2.18):

$$\begin{aligned}
&-\frac{1}{4}(W^a_{\mu\nu})^2-\frac{1}{4}(B_{\mu\nu})^2\\
&\quad=-W^{a[\mu,\nu]}W^a_{[\mu,\nu]}-B^{[\mu,\nu]}B_{[\mu,\nu]}+g\epsilon^{abc}W^{b\mu}W^{c\nu}\left(W^a_{[\mu,\nu]}+g\epsilon^{adf}W^d_\mu W^f_\nu\right)\\
&\quad=-\frac{1}{4}\left(|W^+_{\mu\nu}|^2+|W^-_{\mu\nu}|^2+|Z_{\mu\nu}|^2+|A_{\mu\nu}|^2\right)\\
&\qquad+\left[\mathrm{i}W^+_{\mu\nu}W^{-\mu}(g\cos\theta_\mathrm{W}Z+eA)^\nu-\mathrm{i}W^+_\mu W^-_\nu(g\cos\theta_\mathrm{W}Z+eA)^{\mu,\nu}+\mathrm{h.c.}\right]\\
&\qquad+g^2\cos^2\theta_\mathrm{W}\left(|W^+_\mu Z^\mu|^2-|W^+_\mu|^2|Z_\nu|^2\right)+e^2\left(|W^+_\mu A^\mu|^2-|W^+_\mu|^2|A_\nu|^2\right)\\
&\qquad+2ge\cos\theta_\mathrm{W}\left(W^+_\mu W^-_\nu Z^{(\mu}A^{\nu)}-|W^+_\mu|^2\,Z_\nu A^\nu\right)+g^2W^+_{[\mu}W^-_{\nu]}W^{+\mu}W^{-\nu},
\end{aligned}\tag{2.60}$$

where we sum the indices a, b, c, d, e, and f over the three components of the $SU(2)_\mathrm{L}$ representation. We use the following notation to shorten the expression:

$$\begin{aligned}
T_{(\mu\nu)}&=\frac{1}{2}\left(T_{\mu\nu}+T_{\nu\mu}\right), & |T_{\mu\nu}|^2&=T^*_{\mu\nu}T^{\mu\nu},\\
T_{[\mu\nu]}&=\frac{1}{2}\left(T_{\mu\nu}-T_{\nu\mu}\right), & |T_\mu|^2&=T^*_\mu T^\mu,\\
T_{,\mu}&=\partial_\mu T, & |T_\mu U^\mu|^2&=(T_\mu U^\mu)^*T_\nu U^\nu=T^*_\mu U^{*\mu}T_\nu U^\nu,\\
(\alpha T+\beta U)^\mu&=\alpha T^\mu+\beta U^\mu, & (W^\pm)^*&=W^\mp,\\
(\alpha T+\beta U)^{\mu,\nu}&=\alpha T^{\mu,\nu}+\beta U^{\mu,\nu}, & Z^*,\,A^*&=Z,\,A,
\end{aligned}\tag{2.61}$$

where T and U are some arbitrary fields with Lorentz indices, and α and β are some arbitrary numbers. The field-strength tensors of the physical gauge fields read:

$$\begin{aligned}
W^\pm_{\mu\nu}&=\partial_\mu W^\pm_\nu-\partial_\nu W^\pm_\mu=-2W^\pm_{[\mu,\nu]},\\
Z_{\mu\nu}&=\partial_\mu Z_\nu-\partial_\nu Z_\mu=-2Z_{[\mu,\nu]},\\
A_{\mu\nu}&=\partial_\mu A_\nu-\partial_\nu A_\mu=-2A_{[\mu,\nu]},
\end{aligned}\tag{2.62}$$

where we use the notation (2.61).

Let us examine the resulting expression (2.60). The third line describes the kinetic terms of the physical gauge fields, the fourth line the gauge field self-interactions involving three fields (*triple gauge couplings*, or *TGCs*), and the fifth and sixth lines the gauge field self-interactions involving four fields (*quartic gauge couplings*, or *QGCs*).

Note that the TGC terms are proportional to the first power of the coupling constants $\mathcal{O}(g)$ and $\mathcal{O}(e)$ while the QGC terms are proportional to the second power of the coupling constants $\mathcal{O}(g^2)$ and $\mathcal{O}(e^2)$. This effectively suppresses the reaction rates of the QGCs w.r.t. the TGCs.

Also note that for the TGCs, there is no term involving the product of Z_μ and A_μ. This means that the photon and the Z^0 boson do not couple to each other directly. The perturbative expansion of an LHC collision includes Feynman diagrams with the Z^0 and γ in the final state. However, they always consist of either a QGC vertex or multiple vertices due to the absence of the TGC term involving a direct product of Z_μ and A_μ. We say that there exist higher order processes that lead to the simultaneous $Z\gamma$ production. Their corresponding cross sections are suppressed by multiple orders of the coupling constants thus being relatively small. The (direct) $Z\gamma$ coupling is not allowed in the SM at the tree level.

2.7 Standard Model

The SM Lagrangian follows from the Lagrangians of QCD $\mathcal{L}_{\text{QCD}}$ (2.7) and the Electroweak Theory $\mathcal{L}_{\text{EW}}$ (2.18) including the Higgs-field terms $\mathcal{L}_\phi$ (2.26) expressed in terms of the physical fields after the spontaneous symmetry breaking. It is nearly equal to the sum $\mathcal{L}_{\text{QCD}} + \mathcal{L}_{\text{EW}} + \mathcal{L}_\phi$ except for the kinetic terms of the quarks and the treatment of the quark color in the electroweak interactions. The kinetic terms of the quarks are included fully in $\mathcal{L}_{\text{QCD}}$ and partially in $\mathcal{L}_{\text{EW}}$ (where we made no distinction between the quarks of different colors.) They should be included fully and only once in the SM. As for the color charge of the quarks, we ignored it completely in $\mathcal{L}_{\text{EW}}$ for simplicity as it is conceptually not necessary. Here, we sum all the quark terms over the tree color charges denoted by an additional index denoting the quark fields.

Another important notational difference pertains the mass eigenstates of fermions. In section 2.6 we used a prime (') to distinguish them from the interaction eigenstates. Here, we use the mass eigenstates only and we drop the prime.

Grouping together terms describing the same type of interactions, we write the SM Lagrangian after the symmetry breaking as:

$$\mathcal{L}_{\mathrm{SM}} = \mathcal{L}_{0\psi} + \mathcal{L}_{\mathcal{G}\psi} + \mathcal{L}_{\mathcal{G}} + \mathcal{L}_{\mathrm{TGC}} + \mathcal{L}_{\mathrm{QGC}} + \mathcal{L}_{0H} + \mathcal{L}_{\mathrm{I}H}. \tag{2.63}$$

where:

- $\mathcal{L}_{0\psi}$ describes the free fermions,
- $\mathcal{L}_{\mathcal{G}\psi}$ the interactions of the fermions with the gauge bosons,
- $\mathcal{L}_{\mathcal{G}}$ the free gauge bosons and the gluon self-interactions,
- $\mathcal{L}_{\mathrm{TGC}}$ the triple gauge coupling (TGC) self-interactions of the electroweak gauge bosons,
- $\mathcal{L}_{\mathrm{QGC}}$ the quartic gauge coupling (QGC) self-interactions of the electroweak gauge bosons,
- $\mathcal{L}_{0h}$ the free physical Higgs field, and finally
- $\mathcal{L}_{\mathrm{I}h}$ the dynamics of the physical Higgs field, i.e. its interactions with other particles.

The free fermions are described by their kinetic and mass terms:

$$\mathcal{L}_{0\psi} = \sum_{\psi} \overline{\psi} \left(i\partial\!\!\!/ - m_{\psi} \right) \psi, \tag{2.64}$$

where we sum ψ over all mass eigenstates of the fermions. These include six terms for the three generations of leptons and eighteen terms for the three colors times six flavors of the quarks: $\psi \in \{\nu^i, e^i\}_{i=1}^{3} \cup \{u_a^i, d_a^i\}_{a,i=1}^{3}$. The kinetic terms are included in the QCD Lagrangian $\mathcal{L}_{\mathrm{QCD}}$ (2.7) and also partially in the electroweak Lagrangian $\mathcal{L}_{\mathrm{EW}}$ (2.18). The mass terms are generated through the interaction with the Higgs field (2.48).

The interaction of the fermions with the gauge fields follow from the covariant derivative of the QCD Lagrangian (2.8) and the coupling of the physical electroweak gauge fields to the fermions (2.43):

$$\mathcal{L}_{\mathcal{G}\psi} = -g_{\mathrm{s}} G^{\mathcal{A}}_{\mu} J^{\mu\mathcal{A}}_{G} - g\left(W^{+}_{\mu} J^{\mu+}_{W} + W^{-}_{\mu} J^{\mu-}_{W} + Z_{\mu} J^{\mu}_{Z}\right) - eA_{\mu} J^{\mu}_{\mathrm{EM}}, \tag{2.65}$$

where we sum the superscript $\mathcal{A}$ over the eight gluon color states. The currents in terms of the fermion mass eigenstates are:

$$\begin{aligned}
J^{\mu\mathcal{C}}_{G} &= \sum_{a,b,i=1}^{3} \left(\overline{u}^{i}_{a}\gamma^{\mu} t^{\mathcal{C}}_{ab} u^{i}_{b} + \overline{d}^{i}_{a}\gamma^{\mu} t^{\mathcal{C}}_{ab} d^{i}_{b}\right), \\
J^{\mu+}_{W} &= \frac{1}{\sqrt{2}}\left(\sum_{i,j=1}^{3} \overline{\nu}^{i}_{\mathrm{L}}\gamma^{\mu} V^{ij}_{\mathrm{PMNS}} e^{j}_{\mathrm{L}} + \sum_{a,i,j=1}^{3} \overline{u}^{i}_{a\mathrm{L}}\gamma^{\mu} V^{ij}_{\mathrm{CKM}} d^{j}_{a\mathrm{L}}\right), \\
J^{\mu-}_{W} &= \left(J^{\mu+}_{W}\right)^{*}, \\
J^{\mu}_{Z} &= \frac{1}{\cos\theta_{\mathrm{W}}} \sum_{i=1}^{3} \left[\overline{\nu}^{i}_{\mathrm{L}}\gamma^{\mu}\left(\frac{1}{2}\right)\nu^{i}_{\mathrm{L}}\right. \\
&\qquad \left. \overline{e}^{i}_{\mathrm{L}}\gamma^{\mu}\left(-\frac{1}{2} + \sin^{2}\theta_{\mathrm{W}}\right) e^{i}_{\mathrm{L}} + \overline{e}^{i}_{\mathrm{R}}\gamma^{\mu}\left(\sin^{2}\theta_{\mathrm{W}}\right) e^{i}_{\mathrm{R}}\right] + \\
&\quad \frac{1}{\cos\theta_{\mathrm{W}}} \sum_{a,i=1}^{3} \left[\overline{u}^{i}_{a\mathrm{L}}\gamma^{\mu}\left(\frac{1}{2} - \frac{2}{3}\sin^{2}\theta_{\mathrm{W}}\right) u^{i}_{a\mathrm{L}} + \overline{u}^{i}_{a\mathrm{R}}\gamma^{\mu}\left(-\frac{2}{3}\sin^{2}\theta_{\mathrm{W}}\right) u^{i}_{a\mathrm{R}} + \right. \\
&\qquad \left. \overline{d}^{i}_{a\mathrm{L}}\gamma^{\mu}\left(-\frac{1}{2} + \frac{1}{3}\sin^{2}\theta_{\mathrm{W}}\right) d^{i}_{a\mathrm{L}} + \overline{d}^{i}_{a\mathrm{R}}\gamma^{\mu}\left(+\frac{1}{3}\sin^{2}\theta_{\mathrm{W}}\right) d^{i}_{a\mathrm{R}}\right], \\
J^{\mu}_{\mathrm{EM}} &= \sum_{i=1}^{3} \overline{e}^{i}\gamma^{\mu}\left(-1\right) e^{i} + \sum_{a,i=1}^{3} \left[\overline{u}^{i}_{a}\gamma^{\mu}\left(+\frac{2}{3}\right) u^{i}_{a} + \overline{d}^{i}_{a}\gamma^{\mu}\left(-\frac{1}{3}\right) d^{i}_{a}\right],
\end{aligned} \tag{2.66}$$

where a, b label the quark colors, $\mathcal{C}$ the gluon color states and i, j the lepton generations.

The propagation of free gauge bosons together with the gluon self-interactions are given by the terms:

$$\mathcal{L}_{\mathcal{G}} = \sum_{\mathcal{G}} \left(-\frac{1}{4}|\mathcal{G}_{\mu\nu}|^{2} + \frac{1}{2} m^{2}_{\mathcal{G}} |\mathcal{G}_{\mu}|^{2}\right), \tag{2.67}$$

where $\mathcal{G}$ runs over all the gauge bosons $\mathcal{G} = G^1, G^2, \ldots, G^8, W^+, W^-, Z, A$. The gluon field-strength tensors $G^{\mathcal{A}}_{\mu\nu}$ are given by (2.11), and the electroweak field-strength tensors by (2.62). The masses $m_W = m_{W^\pm}$ and m_Z are given by (2.36) while the photon is massless (2.37), and so is the gluon:

$$m_{G^{\mathcal{A}}} = 0 \qquad \text{for } \mathcal{A} = 1, 2, \ldots, 8. \tag{2.68}$$

The gluon self-interactions due to the non-abelian structure of $SU(3)_{\mathrm{C}}$ are embedded in the gluon field-strength tensor.

The self-interactions of the physical electroweak gauge bosons (2.60) arise from the self-interactions of the electroweak gauge bosons W^1, W^2, W^3, B (2.18), (2.21) and the transformations of the physical fields (2.34). The TGC terms of (2.60) read:

$$\begin{aligned}\mathcal{L}_{\mathrm{TGC}} = {} & ig\cos\theta_{\mathrm{W}}\left[(W^-_\mu W^+_\nu - W^-_\nu W^+_\mu)\partial^\mu Z^\nu + (W^+_{\mu\nu}W^{-\mu} - W^-_{\mu\nu}W^{+\mu})Z^\nu\right] + \\ & ie\left[(W^-_\mu W^+_\nu - W^-_\nu W^+_\mu)\partial^\mu A^\nu + (W^+_{\mu\nu}W^{-\mu} - W^-_{\mu\nu}W^{+\mu})A^\nu\right],\end{aligned} \tag{2.69}$$

while the QGC terms of (2.60) read:

$$\begin{aligned}\mathcal{L}_{\mathrm{QGC}} = {} & g^2\cos^2\theta_{\mathrm{W}}\left(W^+_\mu W^-_\nu Z^\mu Z^\nu - W^+_\mu W^{-\mu} Z_\nu Z^\nu\right) + \\ & e^2\left(W^+_\mu W^-_\nu A^\mu A^\nu - W^+_\mu W^{-\mu} A_\nu A^\nu\right) + \\ & eg\cos\theta_{\mathrm{W}}\left[W^+_\mu W^-_\nu (Z^\mu A^\nu + A^\mu Z^\nu) - 2W^+_\mu W^{-\mu} Z_\nu A^\nu\right] + \\ & \frac{1}{2}g^2\, W^+_\mu W^-_\nu \left(W^{+\mu}W^{-\nu} - W^{+\nu}W^{-\mu}\right).\end{aligned} \tag{2.70}$$

The free propagation of the physical Higgs field follows from the expansion of the kinetic and potential terms of the Higgs field Lagrangian $\mathcal{L}_\phi$ (2.26) around the vacuum state (2.31) in the unitarity gauge as given by eqs. (2.32) and (2.58). The relevant terms are:

$$\mathcal{L}_{0h} = \frac{1}{2}(\partial_\mu h)^2 - \frac{1}{2}m_h^2 h^2, \tag{2.71}$$

where the m_h is the mass of a quantum of the Higgs field (2.59) — the Higgs boson.

Similarly, the Higgs interactions with fermions, bosons, and itself follow from the expansion of $\mathcal{L}_\phi$. Collecting the relevant terms of eqs. (2.32), (2.48), and (2.58) we obtain:

$$\begin{aligned}\mathcal{L}_{\mathrm{I}h} = &-\sum_\psi m_\psi \overline{\psi}\psi \frac{h}{v} \\ &+ \frac{1}{2}\left(m_W^2 |W^{\mu+}|^2 + m_W^2 |W^{\mu-}|^2 + m_Z^2 |Z^\mu|^2\right)\left(\frac{2h}{v} + \frac{h^2}{v^2}\right) \\ &- \frac{1}{2} m_h^2 h^2 \left(\frac{h}{v} + \frac{h^2}{4v^2}\right).\end{aligned} \tag{2.72}$$

This completes the description of the SM Lagrangian after spontaneous electroweak symmetry breaking in terms of the mass eigenstates of the physical fields.

2.8 Parameters of the Standard Model

The SM depends on a number of parameters whose values are not specified by the theory. The total number of these parameters depends on the treatment of neutrino masses and lepton mixings. There are feasible ways to include massive neutrinos other than treating them as Dirac particles as presented in Section 2.6.4, e.g. treating them as Majorana fermions [10, 11] within the framework of the so-called *see-saw mechanism* [12–16]. There is not enough experimental evidence to narrow down the list of hypotheses. More details on the inclusion of massive neutrinos in the SM would go beyond the scope of this work.

Treating the neutrinos as Dirac fermions, there are total of seven related parameters:

- three neutrino masses, see Table 2.1,
- three PNMS mixing angles θ_{12}, θ_{13}, θ_{23}, and CP violating phase δ.

These seven parameters may or may not be considered in the list as, in the original formulation of the SM, neutrinos are massless and leptons do not mix.

The SM predicts a set of relations between its parameters and the observable quantities. For instance, (2.36) gives the gauge boson masses m_W and m_Z in terms

of the electroweak coupling constants g, g' (2.20), and the Higgs vacuum expectation value v (2.30), which in turn depends on the parameters λ and μ^2 of the Higgs-field potential $V(\phi)$ (2.29). Such relations enable us to express the SM parameters in terms of measurable quantities and, with enough knowledge, they can be used to predict results of other measurements thus over-constraining and testing the SM.

In addition to the neutrino-related parameters, there are further eighteen parameters in the SM introduced in this Chapter (see Tables 2.1 and 2.5):

- the masses of the remaining nine fermions excluding neutrinos,
- the Higgs boson mass m_{H} and vacuum expectation value v,
- the couplings g_{s}, g and g' corresponding to the gauge groups $SU(3)_{\mathrm{C}}$, $SU(2)_{\mathrm{L}}$ and $U(1)_{\mathrm{Y}}$,
- the CKM mixing angles θ_{12}, θ_{13}, θ_{23}, and CP violating phase δ.

A correct description of the QCD vacuum requires the introduction of an additional dimensionless parameter [17, 18]:

- the *QCD vacuum angle* θ_{QCD}.

This parameter is related to the so-called *strong CP problem*. We mention it here only for completeness but further details would go beyond the scope of this work. They can be found for example in [19].

This brings the total number of the SM parameters to 26 (19) including (excluding) massive neutrinos as Dirac fermions.

To constrain the SM parameters g, g', λ and μ^2, it is convenient to use α, v, m_{Z} and m_{H} since they are well estimated from experiments. Here, α is the *fine structure constant* defined as:

$$\alpha = \frac{e^2}{4\pi}, \tag{2.73}$$

Symbol	Parameter	Renor-malization	Value
M_H	Higgs mass		~ 125 GeV
v	Higgs vacuum expectation value		246 GeV
$g_{\rm s}$	strong coupling	$\mu_{\overline{\rm MS}} = M_Z$	1.221
g	weak isospin coupling	$\mu_{\overline{\rm MS}} = M_Z$	0.625
g'	weak hypercharge coupling	$\mu_{\overline{\rm MS}} = M_Z$	0.357
θ_{12}	CKM 12-mixing angle		13.1°
θ_{13}	CKM 23-mixing angle		2.4°
θ_{23}	CKM 13-mixing angle		0.2°
δ	CKM CP violating phase		0.995
$\theta_{\rm QCD}$	QCD vacuum angle		$\sim 0^\circ$

Table 2.5: Parameters of the Standard Model [3]. The SM dynamics depend also on the fermion masses that are listed in Table 2.1, and possibly on the unknown values of the four parameters describing the PNMS lepton-mixing matrix.

where e is the QED coupling constant (2.41), or, equivalently, the *(positive) elementary charge*. The fine structure constant is important in its own right because the QED perturbative expansion is carried out in orders of α.

The $g-2$ measurements of the electron anomalous magnetic moment [20–22] together with its theoretical calculation including tenth-order QED contributions involving 12,672 Feynman diagrams [23] give the value of the fine structure constant α with an unprecedented precision reaching a relative uncertainty of 2.5×10^{-10}.

The Higgs vacuum expectation value v is known to high precision through its relation to the *Fermi coupling constant* $G_{\rm F}$ introduced by Enrico Fermi in 1933 to describe beta decay as an effective coupling in the contact interaction $\mathrm{d} \to \mathrm{u}\,\mathrm{e}^-\,\overline{\nu}_{\rm e}$ [24, 25]. It can be defined in terms of g and $m_{\rm W}$, or v, as [26]:

$$G_{\rm F} = \frac{\sqrt{2}}{8}\frac{g^2}{m_W^2} = \frac{\pi\alpha}{\sqrt{2}}\frac{1}{m_W^2 \sin^2\theta_{\rm W}} = \frac{1}{\sqrt{2}v^2}, \tag{2.74}$$

where the first expression on the right is the definition of $G_{\rm F}$, the second expression follows from substitution for g from (2.41) and for e from (2.73), and the third expression follows from substitution for g from (2.36). The most recent measurement

of the positive muon lifetime gives G_F with a relative uncertainty of 6×10^{-7} [27].

The Z^0 boson mass is known to a relative uncertainty of 2.3×10^{-5} from the measurement of Z^0 production at the Large Electron-Positron Collider (LEP) [28–32]. The H boson mass has recently been independently measured by the ATLAS and CMS collaborations at the Large Hadron Collider (LHC). Both measurements reach a relative uncertainty of 5×10^{-3} [33,34]. The precision of the m_H measurements will likely improve dramatically in the coming years as the LHC collects more data.

In order to fully exploit the accuracy of these measurements and to perform the most stringent tests of the SM, the connection between the measured quantities and the SM parameters has to take into account higher orders of the electroweak perturbative expansion known as *electroweak radiative corrections*. This significantly complicates the relations between the measurements and the parameters. The exact form of such corrections depends on the details of the adopted renormalization scheme. Here we follow the approach of [35]. We formally introduce the radiative correction Δr as a relative change of the expression for G_F (2.74) which is usually written in the denominator as $1 + \Delta r \to \frac{1}{1-\Delta r}$:

$$G_\mathrm{F} = \frac{\pi\alpha}{\sqrt{2}} \cdot \frac{1}{m_W^2 \sin^2\theta_\mathrm{W}} \cdot \frac{1}{1-\Delta r}. \tag{2.75}$$

Evaluating the muon decay transition amplitude to the first order gives the radiative correction as:

$$\Delta r = \frac{\hat{\Sigma}_{WW}(0)}{m_W^2} + \frac{\alpha}{4\pi \sin^2\theta_\mathrm{W}} \left(6 + \frac{7 - 4\sin^2\theta_\mathrm{W}}{2\sin^2\theta_\mathrm{W}} \cdot \ln\cos^2\theta_\mathrm{W} \right) \tag{2.76}$$

where $\hat{\Sigma}_{WW}(0)$ is the renormalized W self energy. This is a rather complicated function of $\sin\theta_\mathrm{W}$, $\cos\theta_\mathrm{W}$, m_W, m_Z and Σ_{ij}, with $i, j \in \{\gamma, W^\pm, Z\}$. Here, Σ_{ij} are amputated one-particle irreducible 2-point functions representing a certain class of Feynman diagrams [36]. Other corresponding relations between the experimental and theoretical parameters can be found in [35].

2.9 Zγ Production

In the lowest order of perturbation theory, the Z^0 boson couples to a pair of fermions which are antiparticles of each other. These are quarks coming from the colliding protons for the case of Z^0 boson production at a proton-proton collider like the Large Hadron Collider (LHC). Due to its large mass, the Z^0 boson is very short-lived and decays again via the same coupling that led to its production, where the final state particle-antiparticle pair consists of both quarks and leptons. Figure 2.1 shows the lowest order Feynman diagram for Z^0 boson production and decay in the SM at the LHC. The nature of the final state is random among the fermion flavors and

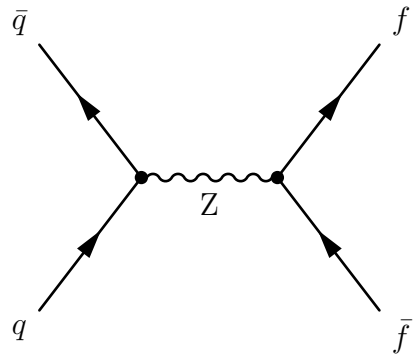

Figure 2.1: Z boson production and decay at a hadron collider to leading order in the SM.

generations, and differs event-by-event. The probabilities of the different fermion flavors are however fixed by the theory, and have been confirmed experimentally with high precision.

The photon interaction with fermions is very similar to the one of the Z^0 boson except it couples only to q charged fermion. The associated production of the photon and the Z^0 boson is from the combination of the two processes. Figure 2.2 shows the tree-level Feynman diagrams for the Zγ production in the SM, through the initial state radiation (ISR) mechanism.

Of the different Z^0 boson final states, the decays to charged leptons are particularly important from the experimental point of view. Unlike decays to quarks, neutrinos and taus, the decays to electrons and muons are particularly easy to identify in the detector and to separate from other processes producing similar signatures. The Zγ

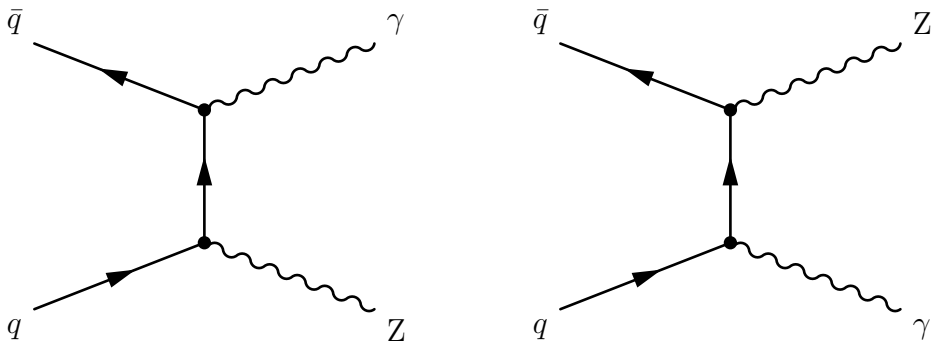

Figure 2.2: Zγ production at a hadron collider in the SM.

final state is $\ell^+\ell^-\gamma$ where ℓ is a charged lepton. Figure 2.3 shows the tree-level Feynman diagrams for the process $q\overline{q} \to \mathrm{Z}\gamma \to \ell^+\ell^-\gamma$ in the SM. We refer to it

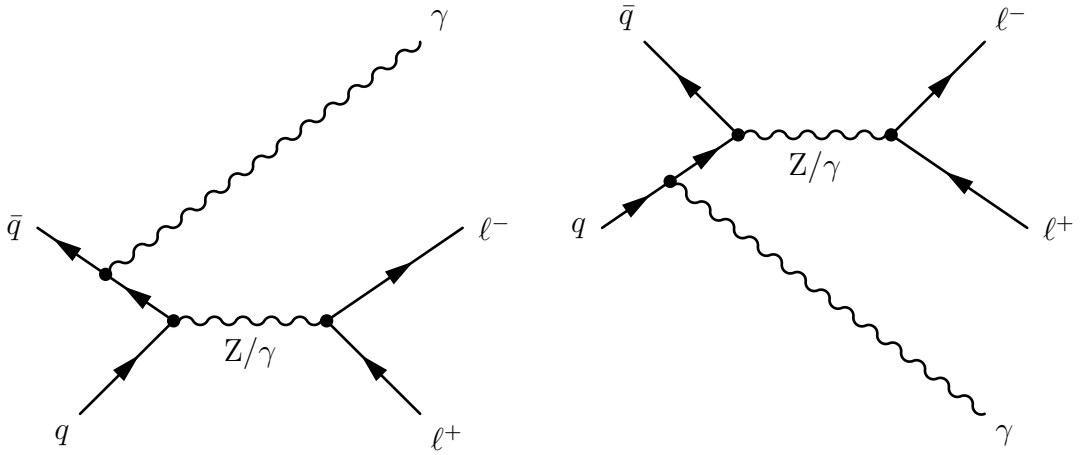

Figure 2.3: Initial state radiation $\ell^+\ell^-\gamma$ production in the SM.

as *initial state radiation* (ISR) since the photon is emitted by one of the incoming quarks.

Figure 2.4 shows the tree-level Feynman diagrams for the process $q\overline{q} \to \mathrm{Z} \to \ell^+\ell^-\gamma$ in the SM, the *final state radiation* (FSR) mechanism. This is a different process with the same final state that constitutes an irreducible background in the measurement of Zγ production.

Due to the identity of the final states, both the ISR and FSR processes contribute to the quantum-mechanical amplitude for $\ell^+\ell^-\gamma$ production including a term arising from their interference.

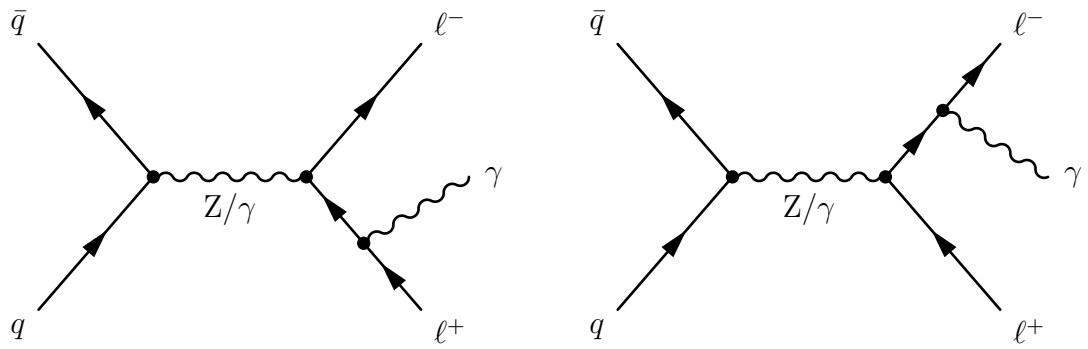

Figure 2.4: Final state radiation $\ell^+\ell^-\gamma$ production in the SM.

2.10 Anomalous Triple Gauge Couplings

The gauge boson self-interactions are a direct consequence of the non-Abelian structure of the electroweak sector of the SM. Elements of a non-Abelian group do not commute. This causes the structure constants f^{abc} in eq. (2.5) to acquire non-zero values. The last term in eq. (2.6) then leads to non-vanishing terms involving products of the gauge field and its derivatives in the Lagrangian. However, Z$\gamma\gamma$ and ZZγ couplings vanish in the SM at the tree level as discussed in Section 2.6.6.

Such anomalous triple-gauge couplings can be described by an effective theory that includes higher-dimension operators [37–39]. Figure 2.5 shows a Feynman diagram of a resulting generic VZγ ATGC vertex with an off-shell $V = \gamma^*$, Z* and on-shell Z and γ.

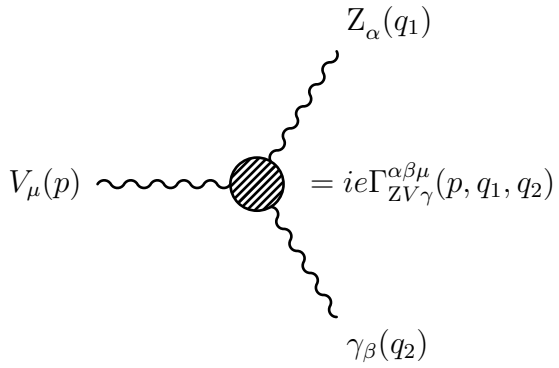

Figure 2.5: Feynman diagram of a generic VZγ ATGC vertex with an off-shell $V = \gamma^*$, Z* and on-shell Z and γ.

Using the notation from Figure 2.5, the corresponding ZZγ ATGC vertex function reads [37, 38]:

$$\begin{aligned}\Gamma^{\alpha\beta\mu}_{\mathrm{ZZ}\gamma}(p,\, q_1,\, q_2) \;=\; \frac{p^2-q_1^2}{m_{\mathrm{Z}}^2}\Bigg[\; & h_1^{\mathrm{Z}}(q_2^\mu g^{\alpha\beta} - q_2^\alpha g^{\mu\beta}) + \\ & \frac{h_2^{\mathrm{Z}}}{m_{\mathrm{Z}}^2} p^\alpha \left[(p\cdot q_2) g^{\mu\beta} - q_2^\mu p^\beta\right] + \\ & h_3^{\mathrm{Z}} \epsilon^{\mu\alpha\beta\rho} q_{2\rho} + \\ & \frac{h_4^{\mathrm{Z}}}{m_{\mathrm{Z}}^2} p^\alpha \epsilon^{\mu\beta\rho\sigma} p_\rho q_{2\sigma} \;\Bigg],\end{aligned} \tag{2.77}$$

where h_1^{Z} through h_4^{Z} are complex couplings characterizing the ZZ$^*\gamma$ interaction.

The Z$\gamma\gamma$ ATGC vertex function is related to the ZZγ one through the symmetry:

$$\begin{aligned}\frac{p^2-q_1^2}{m_{\mathrm{Z}}^2} &\to \frac{p^2}{m_{\mathrm{Z}}^2} \qquad \text{and} \\ h_i^{\mathrm{Z}} &\to h_i^\gamma, \qquad i = 1,\, \ldots,\, 4,\end{aligned}$$

where h_1^γ through h_4^γ are, again, some complex couplings characterizing the Z$\gamma^*\gamma$ interaction. This Z$\gamma\gamma$ vertex function vanishes identically when both photons are on the mass shell due to the Landau-Yang theorem [40, 41].

These are the most generic vertex functions for a time-like virtual $V = \mathrm{Z}^*, \gamma^*$ and on-shell Z and γ constrained by:

- Lorentz invariance,
- gauge symmetry,
- the coupling of the off-shell V to essentially massless fermions, which implies that effectively $\partial_\mu V^\mu = 0$, $V = Z$, A, and
- the omission of terms proportional to p_μ and q_1^α that do not contribute to the cross section.

Using similar constraints, further anomalous couplings can be introduced. They

may involve off-shell photons and Z^0 bosons [37], $W^{\pm}$ bosons [37], or quartic gauge boson vertices [42–49]. Further details on these other couplings would go beyond the scope of this work.

All of the h_i^V, $i = 1, \ldots, 4$ couplings vanish in the SM at leading order, see Section 2.6.6. The $i = 1, 2$ couplings are P-even, the other two are CP-even. All of the couplings are C-odd. $h_{1,3}^V$ receive contributions from operators of dimension ≤ 6, $h_{2,4}^V$ receive contributions from operators of dimension ≥ 8.

Increasing the timelike-virtual-boson energy $\sqrt{\hat{s}}$, the anomalous contributions to the $Z\gamma$ helicity amplitudes grow like $\left(\sqrt{\hat{s}}/m_Z\right)^3$ for $h_{1,3}^V$, and $\left(\sqrt{\hat{s}}/m_z\right)^5$ for $h_{2,4}^V$. Tree-level unitarity requires that the anomalous couplings h_i^V vanish at asymptotically high energies [50–54] since otherwise the $Z\gamma$ production cross section would grow without bound. The unitarity can be restored by introducing $\hat{s}$-dependent form factors [38]:

$$h_i^V = \frac{h_{i0}^V}{\left(1 + \frac{\hat{s}}{\Lambda^2}\right)^n}, \quad i = 1, \ldots, 4, \quad V = \mathrm{Z}, \gamma, \tag{2.78}$$

where $h_{i0}^V = \lim_{\hat{s}\to 0} h_i^V$ are the low energy limits of h_i^V, $\Lambda \gg m_Z$ is a cut-off scale, and $n > 3/2$ for $h_{1,3}^V$ and $n > 5/2$ for $h_{2,4}^V$. This functional form is not uniquely defined by the unitarity requirement. This particular choice is motivated by the well-known nuclear form factors [55]. It has the feature that the h_i^V are essentially constant at low energies $\hat{s} \ll \Lambda^2$ and Λ sets the scale at which they start to decrease with growing $\hat{s}$. This is consistent with a scenario in which non-SM values of h_i^V are a low-energy consequence of some new physics at the mass scale Λ.

The goal of the this work is to constrain, or measure if nonzero, the values of h_{i0}^V. In order to perform the measurement, we must adopt a particular choice of Λ and n. We choose to extract the bare couplings without a form factor:

$$\begin{aligned} \Lambda &\to \infty, \\ h_i^V &\to h_{i0}^V. \end{aligned} \tag{2.79}$$

This has the advantage that we avoid ad-hoc assumptions about the functional form (2.78), the values of the cut-off Λ, and exponents n. It simplifies the inter-

pretation of the measurements, facilitates their comparison with other results, and avoids possible energy-dependent biases. We argue that we need not worry about the unitarity violation since we assume that we probe energies $\hat{s} \ll \Lambda^2$. This assumption is based on the lack of an observation of novel interactions at the scale $\hat{s}$ that we probe.

In full generality, the differential cross section is a real bilinear form in the anomalous couplings $h_{1,\dots,4}^{\gamma,\mathrm{Z}}$:

$$\begin{aligned} \mathrm{d}\sigma = \mathrm{d}\sigma_{\mathrm{SM}} &+ \sum_{V}^{\{\gamma,\mathrm{Z}\}} \sum_{i=1}^{4} \left(\Re h_i^V \, \mathrm{d}\sigma_{i,\Re}^V + \Im h_i^V \, \mathrm{d}\sigma_{i,\Im}^V \right) \\ &+ \sum_{U,V}^{\{\gamma,\mathrm{Z}\}} \sum_{i,j=1}^{4} |h_i^U h_j^V| \, \cos(\arg h_i^U - \arg h_j^V + \Delta\phi_{ij}^{UV}) \, \mathrm{d}\sigma_{ij}^{UV}, \end{aligned} \tag{2.80}$$

where $\mathrm{d}\sigma_{\mathrm{SM}}$ is the SM contribution $\mathrm{d}\sigma_{i,\Re}^V$, $\mathrm{d}\sigma_{i,\Im}^V$, and $\mathrm{d}\sigma_{ij}^{UV}$ are the non-SM contributions after factoring out their h_i^V dependences, and $\Delta\phi_{ij}^{UV}$ are some phases depending on the relative phases of the underlying interfering matrix elements.

Without loss of generality, we are free to redefine the couplings $h_{1,\dots,4}^{\gamma,\mathrm{Z}}$with some constant phase shifts $h_i^V \to \mathrm{e}^{\mathrm{i}\phi_i^V} h_i^V$ such that most of the phases $\Delta\phi_{ij}^{UV}$ in (2.80) vanish. Moreover, the form of (2.80) is such that all of these phases vanish:

$$\Delta\phi_{ij}^{UV} = 0 \tag{2.81}$$

as the anomalous matrix elements have the same relative phases.

All the terms linear in $h_{3,4}^V$ vanish to leading order and to next-to-leading order, after summing over the fermion helicities and photon polarizations because of the antisymmetry of $\epsilon^{\mu\alpha\beta\rho}$ in (2.77):

$$\begin{aligned} \mathrm{d}\sigma_{i,\Re}^V = \mathrm{d}\sigma_{i,\Im}^V &= 0 && \text{for } i = 3,\, 4, \\ \mathrm{d}\sigma_{ij}^{UV} = \mathrm{d}\sigma_{ji}^{VU} &= 0 && \text{for } (i,j) \in \{1,2\} \times \{3,4\}, \end{aligned} \tag{2.82}$$

where $U, V = \gamma, \mathrm{Z}$. Therefore, the CP-violating couplings $h_{1,2}^V$ and the CP-conserving couplings $h_{3,4}^V$ do not interfere.

All the remaining terms linear in $h_{1,2}^V$ are proportional $\cos\theta^*$:

$$\begin{aligned} \mathrm{d}\sigma_{i,\mathfrak{C}}^V \propto \cos\theta^* \qquad & \text{for } i = 1,\ 2,\ \text{and} \\ & \mathfrak{C} = \Re,\ \Im, \end{aligned} \tag{2.83}$$

where θ^* is the scattering angle of the photon in the center-of-mass frame of the incoming partons. These terms vanish after the phase-space integration which is symmetric with respect to $\cos\theta^*$ at the LHC. Therefore, only the quadratic terms of (2.80) contribute to the non-SM cross section.

Furthermore, the cross sections, and thus the sensitivities, are nearly identical for the same values of $h_{1,2}^V$ and $h_{3,4}^V$ [39]:

$$\begin{aligned} \mathrm{d}\sigma_{ij}^{UV} \approx \mathrm{d}\sigma_{kl}^{UV} \qquad & \text{for } i, j \in \{1,\ 2\},\ \text{and} \\ & (k,\ l) = (i+2,\ j+2), \end{aligned} \tag{2.84}$$

where $U, V \in \{\gamma,\ \mathrm{Z}\}$. Therefore, in the following, we focus on the CP-conserving couplings $h_{3,4}^V$ only.

We continue the discussion of the experimental sensitivity to the couplings $h_{3,\ldots,4}^{\gamma,\mathrm{Z}}$, the method of the limit extraction and the results in Sections 5.2 and 6.2.

Chapter 3

Experimental Apparatus

3.1 The Large Hadron Collider

As of this writing, the Large Hadron Collider (LHC) [56–58] is the world's largest and highest-energy accelerator and collider of elementary particles. The European Organization for Nuclear Research (CERN) constructed it from 1998 to 2008, and has been operating it since 2009. It lies in a tunnel 50 to 175 meters underground and 27 km in circumference at the Franco-Swiss border near Geneva, cf. Figure 3.1. The tunnel was originally built for the Large Electron-Positron Collider (LEP) accelerator [59, 60]. The LHC was designed to collide proton pairs (pp) every 25 ns at the center-of-mass energies $\sqrt{s} = 14\,\text{TeV}$, and lead ions of center-of-mass energies up to 5.5 TeV per nucleon-pair.

The LHC is a part of a multi-stage complex. It consists of a number of accelerators leading into each other, cf. Figure 3.2. The protons come from a hydrogen flask, whose molecules are broken up by a high electric field of a duoplasmatron source. The linear accelerator Linac-2 then boosts them to energies of 50 MeV and injects them into the Proton Synchrotron Booster (PSB) as ca. 120 µs-long bunches. The PSB, a circular accelerator, splits the proton bunches in four parallel identical rings, accelerates them to 1.4 TeV, and combines them back again to a single bunch. The bunches keep together and accelerate as they "surf ride" the downhill slopes of electromagnetic waves (buckets) of a Radio Frequency (RF) system. The Proton Synchrotron (PS), the next ring in the injection chain, accelerates the proton bunches to 25 GeV. Next,

Figure 3.1: Aerial view of CERN with the LHC tunnel near Geneva and the Geneva Lake (lac Leman). The red line shows the location of the LHC tunnel, red circles mark its access points. The French Alps with Mont Blanc can be seen in the background [61]. Photo courtesy of CERN.

the bunches travel in the Super Proton Synchrotron (SPS), an accelerator of 6.9 km in circumference. Finally, the SPS accelerates the bunches to 450 GeV before filling them in the LHC in two opposite directions.

The lead ion injection chain shares the PS and the SPS with the protons. It differs in the source, the linear pre-injector, and the second accelerator, which are the Electron Cyclotron Resonance Ion Source (ECRIS), the Linac3, and the Low Energy

Ion Ring (LEIR), respectively.

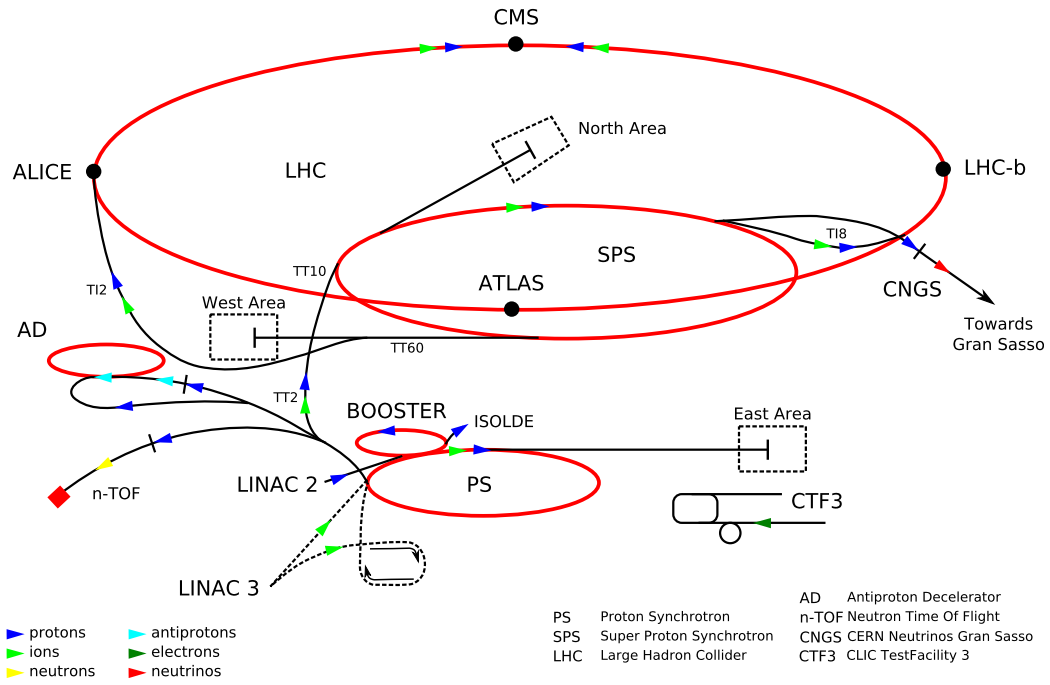

Figure 3.2: The CERN accelerator complex. The LHC is the largest ring in a multi-stage chain of accelerators leading one into another and starting with the linear accelerators LINAC2 and LINAC3 [62].

The performance requirements on the LHC magnets and its cryogenic and vacuum systems combined with their large scale present significant engineering challenges and are at the edge of the current technology. The LEP tunnel houses two rings with proton beams circulating in opposite directions. 1232 dipole and 392 quadrupole magnets keep the protons and lead ions on circular trajectories in two narrow beams of opposite directions. Further sextupole and octupole magnets correct and control the properties of the particle beams. The bending of the trajectories involves the 1232 superconducting dipole magnets of 15 m length and 40 tonne weight. To save space, the two rings for the clockwise and anti-clockwise beams are dual bore two-in-one magnets inside a common cryostat, cf. Figure 3.3. They are designed to reach the magnetic field of 8.3 T, about 100,000 times the magnitude of the Earth's magnetic field. To reach such high fields, the Nb-Ti magnets have to be chilled using superfluid helium-II down to 1.9 K, colder than outer space. This requires a presence

of three separate vacuum systems: one for the insulation of cryomagnets, one for the insulation of the helium distribution line, and one for the beam pipe. Of the three, the requirements on the last one are the most stringent to ensure sufficient beam lifetime and tolerable beam halo background for the experiments. This calls for the equivalent room temperature pressure values as low as $(1 \times 10^{-8}$ to $1 \times 10^{-9})$ Pa making the volume inside the LHC beam pipe not only colder but also emptier than outer space.

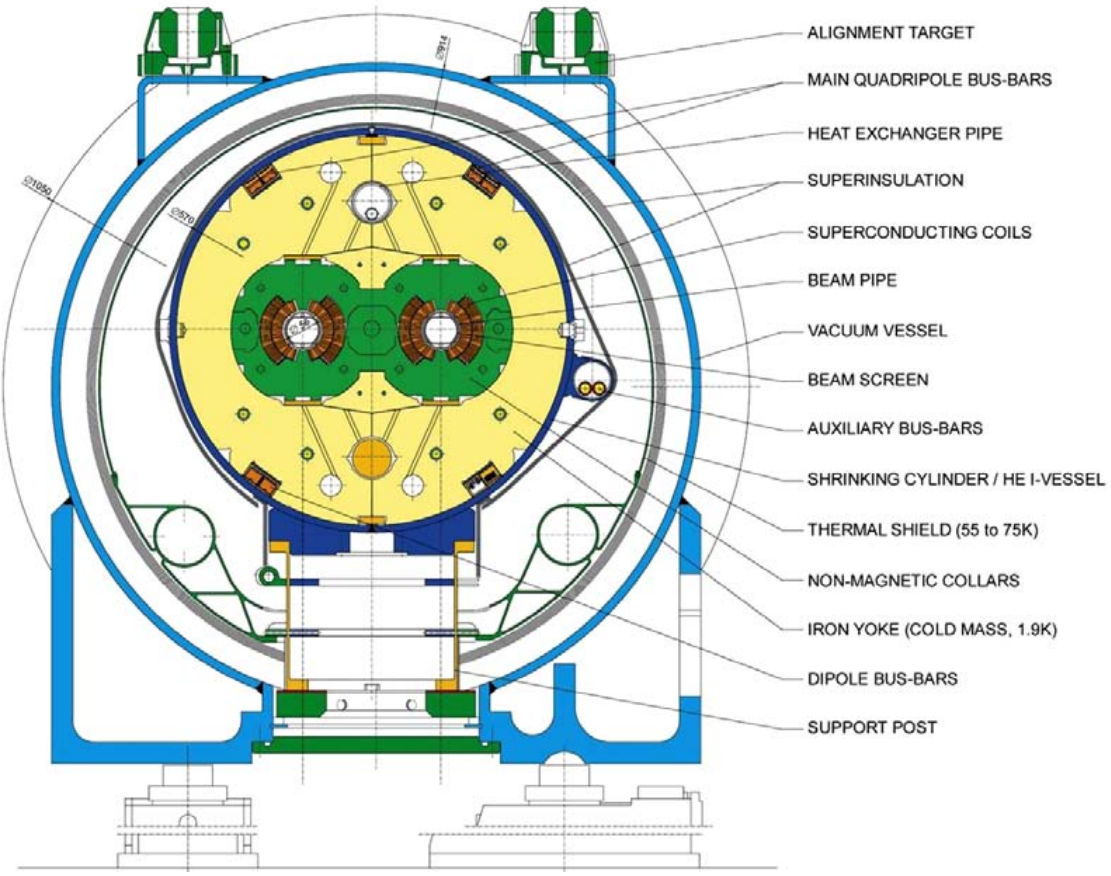

Figure 3.3: A schematic cross sectional view of a main LHC dipole.

The 392 quadrupole magnets of (5 to 7) m length focus the particle bunches to maintain a narrow beam about the equilibrium orbit. There are four main interaction regions along the LHC tunnel where the beams cross. Large cavities surround them housing particle detectors that record the resulting collision products. Two of them are general-purpose high-luminosity detector experiments optimized to search

for the SM Higgs boson and new yet-unknown particles in proton-proton collisions: A Toroidal LHC Apparatus (ATLAS) and the Compact Muon Solenoid (CMS). The LHC-beauty (LHCb) experiment specializes in physics of the bottom (beauty) quark, and finally A Large Ion Collider Experiment (ALICE) designed to study the heavy ion collisions, see Figure 3.4.

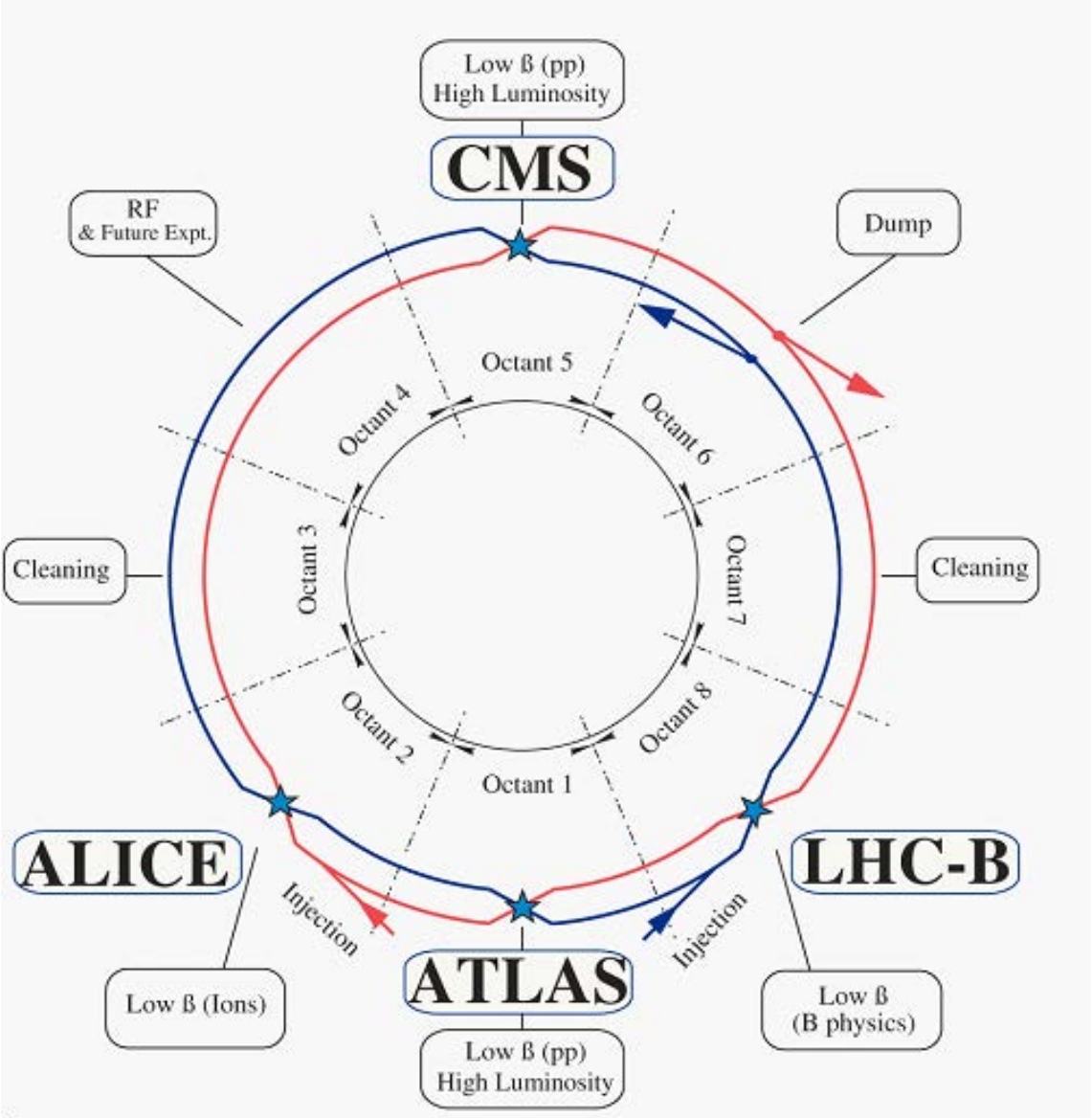

Figure 3.4: layout of the LHC interaction points and experiments.

In addition to the center-of-mass energy, another important parameter of an accelerator is its *luminosity*. It is a measure of how frequently collisions occur. Higher

luminosity provides more collisions which increases the statistical power of searches for rare processes. The production rate of collision events of certain type is [63]:

$$\frac{dN_{\text{event}}}{dt} = \mathscr{L}\,\sigma_{\text{event}}, \tag{3.1}$$

where $\mathcal{L}$ is the *instantaneous luminosity* of the machine and σ_{event} the production cross section for that particular type of event. The instantaneous luminosity varies with time as the beam conditions change during a fill. The total number of events is then obtained as:

$$N_{\text{event}} = \sigma_{\text{event}} \int \mathscr{L}\,\mathrm{d}t, \tag{3.2}$$

where $L = \int \mathscr{L}\,\mathrm{d}t$ is the *integrated luminosity*. Figure 3.5 shows the integrated luminosity of pp collisions delivered to CMS as a function of time. In addition to the proton-proton collisions, the LHC also delivered lead-lead collisions in 2011 and proton-lead collisions in 2013. The running campaigns involving lead collisions were significantly shorter than the proton-proton ones lasting only about 3 weeks each.

The luminosity can be expressed in terms of the beam parameters as [63]:

$$\mathscr{L} = \frac{N_{\text{b}}^2 n_{\text{b}} f_{\text{rev}} \gamma_{\text{r}}}{4\pi\epsilon_{\text{n}}\beta^*}\,F,$$

where N_{b} is the number of particles per bunch, n_{b} the number of bunches per beam, f_{rev} the beam revolution frequency, γ_{r} the relativistic gamma factor, and ϵ_{n} is the normalized transverse beam emittance, which is a measure of the average spread of a particle beam bunch in the position and momentum phase-space. β^* is the beta function at the Interaction Point (IP), a measure of the amount of beam "squeezing" by the focusing magnets, and F is the geometric factor due to the crossing angle of the beams. ϵ_{n} and β^*

The beam revolution frequency depends on the size of the accelerator. At the LHC, it is $f_{\text{rev}} = f_{\text{LHC}} = 11.245\,\text{kHz}$. The relativistic gamma factor is a ratio of the energy E and the mass m of the accelerated beam particles. The particle energy is in

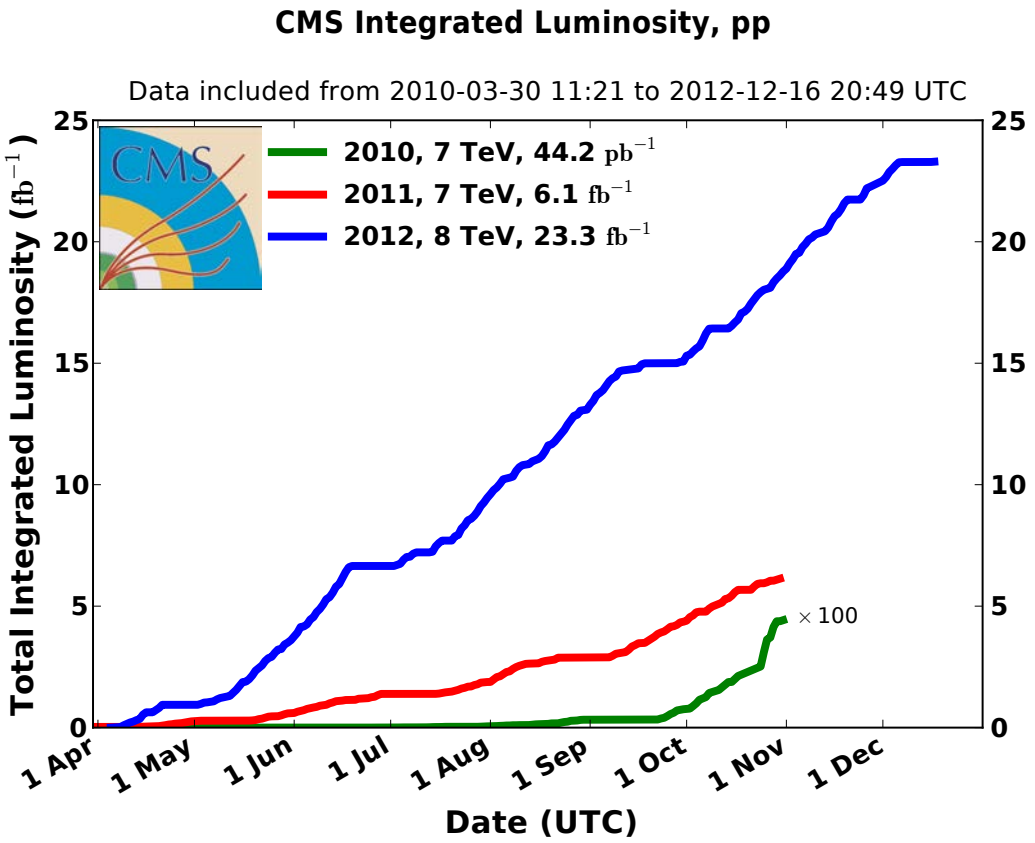

Figure 3.5: Tolal integrated luminosity delivered to CMS [64].

turn half of the the center-of-mass energy of a collision $E = \frac{1}{2}\sqrt{s}$. The relevant mass for the LHC pp collisions is the proton mass $m_{\mathrm{p}} = 938.272\,046 \pm 0.000\,021\,\mathrm{MeV}$ [3]. The relativistic gamma factor then reads:

$$\gamma_{\mathrm{r}} = \frac{E}{m} = \frac{\sqrt{s}}{2m_{\mathrm{p}}}. \tag{3.3}$$

In Table 3.1, we list the LHC beam parameters for data collected in 2009-2012 along with their design values. The bunch intensity and size expressed by N_{b} and the product $\epsilon_{\mathrm{n}}\beta^*$ have exceeded their design values during 2011 and 2012 operation. The bunch spacing, which has to be a multiple of the size of the LHC RF buckets corresponding to the design value of 25 ns, was 75 ns and 50 ns during 2011 and 2012. These next higher values resulting in lower luminosities were chosen to mitigate the effects of the electron cloud and high pileup. The latter one refers to the average num-

Parameter	Design	2009	2010	2011	2012
$\sqrt{s}$ (TeV)	14	0.9-2.36	0.9-7	7	8
N_b (10^{10} p/bunch)	11.5	0.05-5	12	15	16
n_b (bunches/beam)	2808	1-9	368	up to 1380	1368-1380
Bunch spacing (ns)	25	312-2808	150	75, 50	50
f_rev (kHz)	11.245	11.245	11.245	11.245	11.245
γ_r	7460	480-1260	480-3730	3730	4263
ϵ_n (µm rad)	3.75	2-4	1.5-10	1.9-2.4	2.2-2.5
β^* (m)	0.55	11	2-11	1.5-1	0.6
F	0.836	≈ 1	≈ 1	≈ 1	≈ 1
$\mathscr{L}$ ($\mathrm{cm}^{-2}\,\mathrm{s}^{-1}$)	10^{34}	3×10^{26}	2×10^{32}	4×10^{33}	7.6×10^{33}
$\langle N_\mathrm{evt} \rangle$ (per x-ing)	23	0	0-3	19	35
$\int \mathscr{L}\,\mathrm{d}t$ (per IP)	200-300 fb^{-1}	≈ 0	44 pb^{-1}	6 fb^{-1}	20 fb^{-1}

Table 3.1: LHC proton beam parameters. $\sqrt{s}$ is the center-of-mass energy of a pp collision, N_b the number of particles per bunch, n_b the number of bunches per beam, f_rev the beam revolution frequency, γ_r the relativistic gamma factor, ϵ_n the normalized transverse emittance, β^* the beta function at the Interaction Point, F the geometric factor due to the crossing angle of the beams, L the instantaneous luminosity, $\langle N_\mathrm{evt} \rangle$ the average number of inelastic interactions per bunch crossing, and $\int \mathscr{L}\,\mathrm{d}t$ the total delivered integrated luminosity per experiment.

ber of multiple inelastic proton-proton interactions occurring simultaneously during a bunch crossing. This can be significantly greater than one and can be expressed as:

$$\langle N_\mathrm{evt} \rangle = \frac{\sigma_\mathrm{inel} \mathscr{L}}{n_\mathrm{b} f_\mathrm{LHC}} \tag{3.4}$$

where σ_inel is the total pp inelastic cross section whose value depends on the collision center-of-mass energy. It is around $\sigma_\mathrm{inel} \approx 68\,\mathrm{mb}$ at $\sqrt{s} = 7\,\mathrm{TeV}$ [65]. High values of pileup reduce the efficiency of particle reconstruction and identification, which deteriorates the statistical power of the data. This is one of the limiting factors for reaching high luminosity values.

3.2 The Compact Muon Solenoid

The Compact Muon Solenoid (CMS) detector [66,67] is together with ATLAS [68,69] one of the two main general-purpose detectors at the LHC. As of this writing, the CMS collaboration consists of 2585 physicists (of which 845 are graduate students), 790 engineers, 690 undergraduates, and 281 technicians representing 182 institutes and 42 countries [70], see Figure 3.6. The CMS collaboration built the detector between

Figure 3.6: A part of the CMS Collaboration in front of a real size CMS poster at the surface hall above the LHC Point 5 where the CMS detector elements were assembled [71]. Photo courtesy of CERN.

1992 and 2008 at Point 5 of the LHC, 100 m underground near Cessy, France [72], and have been operating it since then.

CMS was designed to explore the physics at the TeV scale, elucidate the mechanism of electroweak symmetry breaking, find evidence of the SM Higgs boson's existence or non-existence, search for physics beyond the SM including supersymmetry, extra dimensions, other new and potentially not-yet-thought-of interactions and heavy particles, and study heavy ion collisions [73]. To meet these goals, CMS

must have the ability to reconstruct and identify leptons, photons, jets, and missing transverse energy with high precision, efficiency and geometric hermeticity over a wide angular range. The challenge of CMS is to operate in the harsh environment of approximately 20 inelastic pp collisions producing about 1000 charged particles every 25 ns. CMS also has to be able to reduce the total interaction rate from the 1 GHz delivered by the LHC by a factor of nearly 10^6 down to about 1.5 kHz that can affordably be processed and stored. This requires a very fast, granular, and radiation resistant apparatus whose large number of channels are well synchronized.

CMS consists of several sub-systems with different roles, see Figure 3.7. They

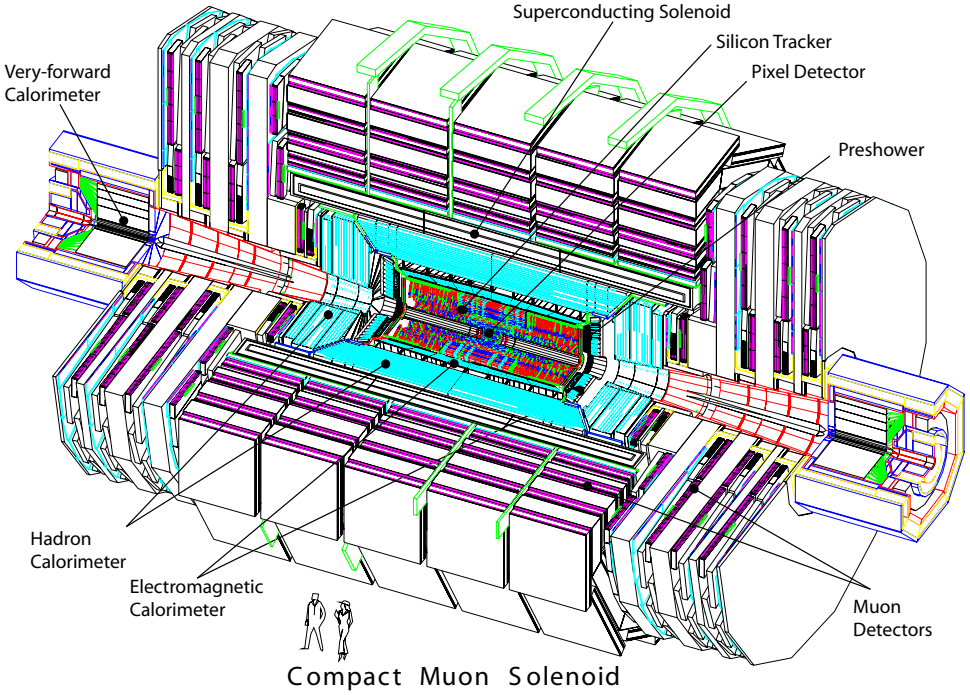

Figure 3.7: A schematic overview of the CMS detector with average-sized physicists [67].

are arranged in an onion-like layered structure around the nominal interaction point. Particles produced in collisions at the geometrical center of CMS cross these layers as they propagate from the inside out. The presence or lack of signals along their trajectories depends on the type of the particle and of the given subsystem. Combining information from the various detectors enables inferences about the underlying particle trajectory, kinematics and types, cf. Figure 3.8.

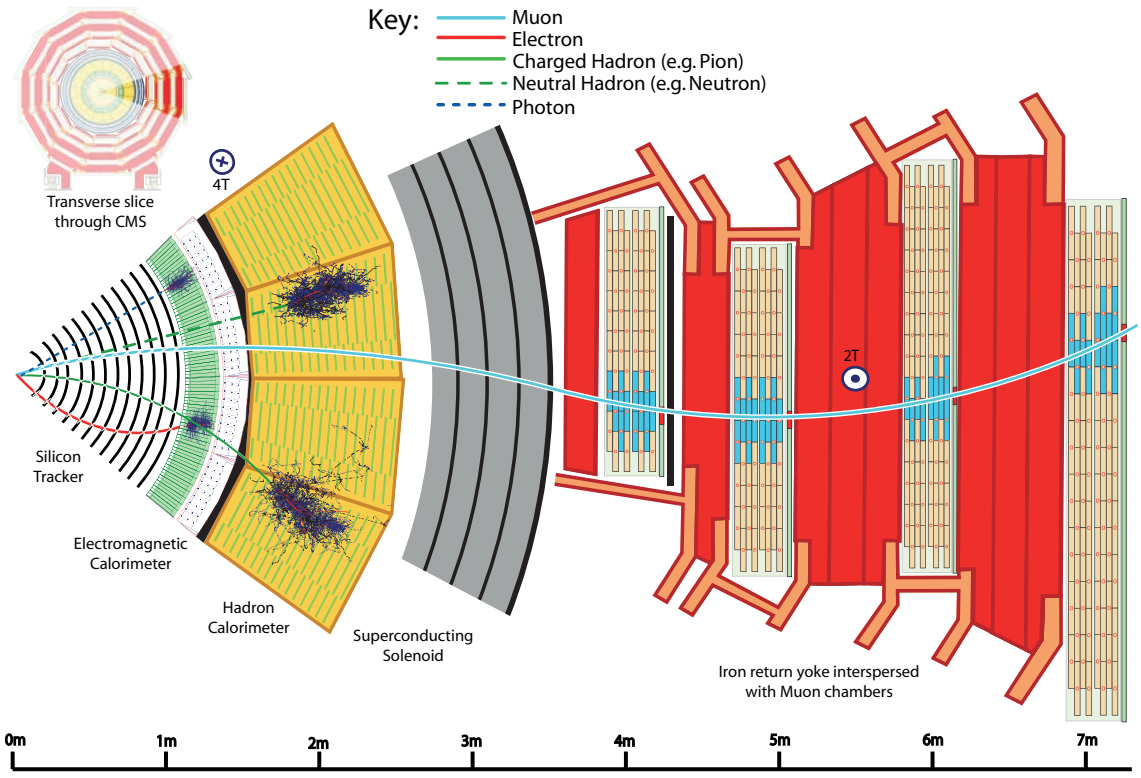

Figure 3.8: Transverse slice of the CMS detector depicting interaction of particles of different types with the various sub-systems [74].

A characteristic feature of the CMS design is the arrangement of its magnetic field. To reach sufficient bending power for precise momentum measurement of charged particles, and unambiguous charge assignment for muons of transverse momentum up to $p_{\mathrm{T}} \approx 1\,\mathrm{TeV}$, CMS chose a large superconducting solenoid. To reduce the amount of material in front of the calorimeters, they are located inside of the solenoid together with the inner tracking system. The size of the solenoid limits the size of the calorimeters, leading to a use of very dense materials in their active volume that can contain electrons, photons and hadrons with sufficiently high efficiencies. So it is the *design* of CMS that is compact in contrast to ATLAS rather than its overall dimensions of 21.6 m length, 14.6 m diameter, and 12.5 kt.

The CMS design is not only compact, it is also modular. The various CMS detector elements were constructed on the surface, lowered into the experimental cavern, and then assembled in a fashion resembling *LEGO* building blocks.

CMS uses a right-handed Cartesian coordinate system with the origin at the nominal interaction point at the geometrical center of the detector. The x-axis points inward to the center of the LHC ring, the y-axis upward, and the z-axis tangentially to the direction of the beams. The right-handedness leads to a counter-clockwise direction of the z-axis looking from above.

Based on the Cartesian coordinates, we define cylindrical ones with the radial distance from the beam $r = \sqrt{x^2 + y^2}$, the azimuthal angle $\phi = \arctan(y/x)$ measured from the positive end of the x-axis, and the z-axis. We also define a spherical coordinate system with the radial distance to the origin $\rho = \sqrt{x^2 + y^2 + z^2}$, the azimuthal angle ϕ, and the polar angle $\theta = \arccos(z/r)$ measured from the positive end of the z-axis.

Another often used coordinate is the *pseudorapidity* defined as:

$$\eta = -\ln \tan \frac{\theta}{2}, \tag{3.5}$$

which, in the limit $E \to |\mathbf{p}|$, is equal to the *rapidity*:

$$y = \frac{1}{2} \ln \frac{E + p_z}{E - p_z}. \tag{3.6}$$

It has the advantage that particle production rate is roughly constant as a function of it, in the region around $\eta = 0$, and its differences are Lorentz invariant with respect to boosts along the beam axis. This is especially important at hadron colliders where the center-of-mass momentum component along this direction is unknown and differs event-by-event. Pseudorapidity $\eta = 0$ corresponds to the x-y plane and it tends to $\eta \to +\infty$ for the direction along the positive z-axis and $\eta \to -\infty$ for the negative z-axis with most of the fiducial volume covered by small numerical values of η.

3.3 CMS Superconducting Solenoid

The superconducting solenoid [75], is one of the important design features of the CMS detector, hence the "S" for "Solenoid" in CMS. It surrounds the silicon tracker,

ECAL and majority of HCAL, see Figure 3.9. This is important for the minimization of the material budget in front of the calorimetry which maximizes the momentum and energy resolution.

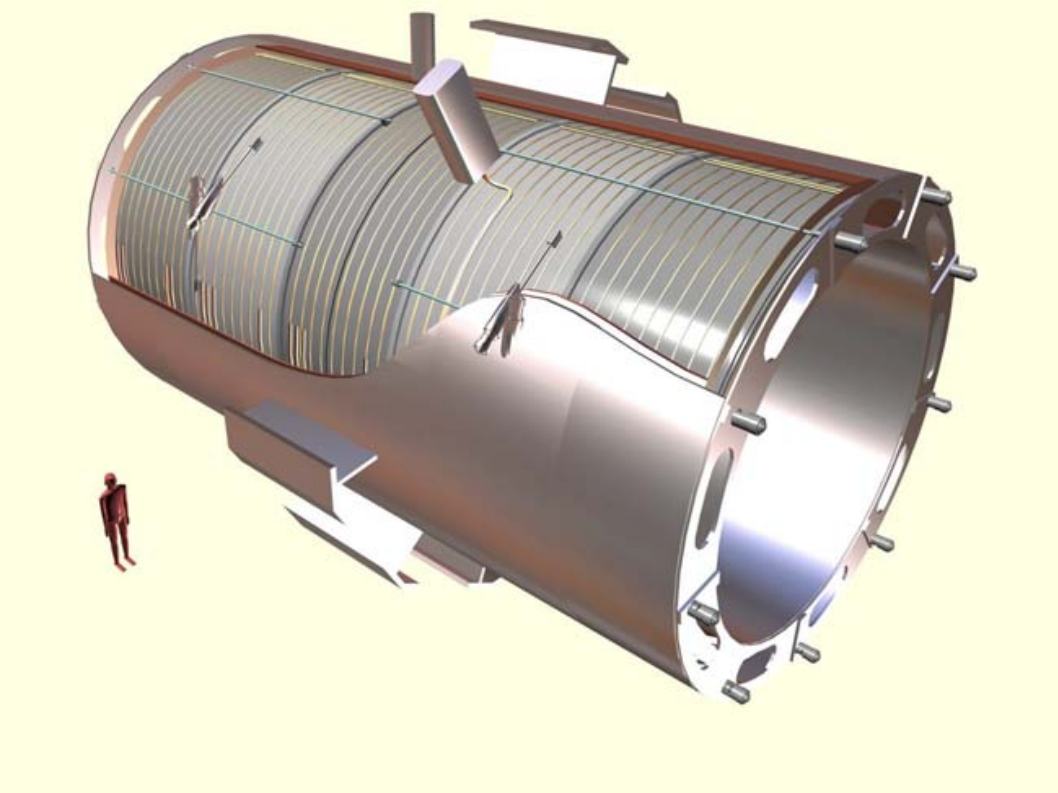

Figure 3.9: Artist's rendition of the CMS solenoid cold mass with details of the supporting system and an average-sized physicist [67].

The performance requirements on the bending power of the magnet derive from the requirements on the muon system and its spatial resolution. To enable reconstruction of narrow states decaying into muons and unambiguously determine the sign of muons up to momenta of $p_{\mathrm{T}} \approx 1\,\mathrm{TeV}$, a momentum resolution of $\frac{\sigma(p_{\mathrm{T}})}{p_{\mathrm{T}}} \approx 10\,\%$ is needed, and has been achieved.

The solenoid was designed to reach a field of 4 T but it is operated at a lower value of 3.8 T to lower the risk of damage and increase its longevity. It has a cold bore of 6.3 m, a length of 12.5 m, a mass of 220 t and stores energy of 2.7 GJ at full current of 19.5 kA corresponding to 4 T.

Compared to previous experiments, the CMS magnet is new in a number of ways.

The winding consists of 4 layers instead of the usual single layer due to the required number of ampere-turns of 41.7 MA turn. The conductor is structurally strengthened with an aluminum alloy to withstand the larger pressures. The large dimensions of the solenoid combined with its narrow radial extent represent a challenge for its mechanical integrity. This is exemplified in Figure 3.10 showing the energy-over-mass ratio E/M versus the stored energy E with CMS at extreme ends of both spectra.

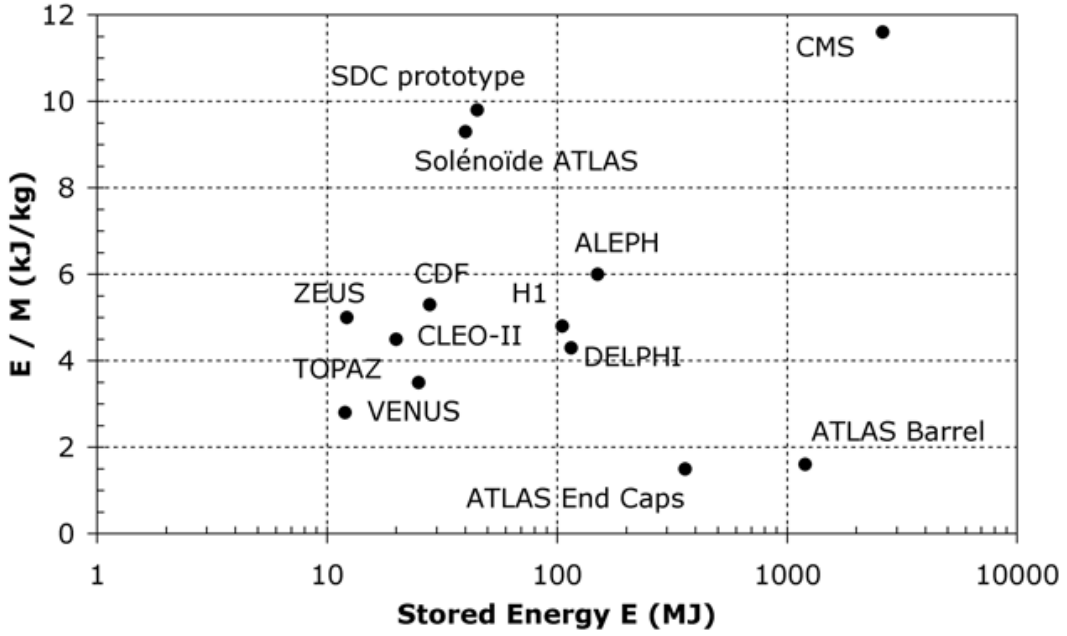

Figure 3.10: Comparison of the magnet energy-over-mass ratio E/M for a number of particle detectors [67].

3.4 CMS Inner Tracker

The CMS inner tracker [76, 77] constitutes the inner-most detection layer closest to the interaction vertex. Its purpose is to measure the trajectories of charged particles in space and time, thus enabling inferences about their charge, momentum and impact parameters. These are important for identification and precise kinematic reconstruction of electrons, muons and charged hadrons.

The tracker is located in the center of CMS and extends to nearly 2.2 m in diameter

and approximately 5.4 m in length providing coverage up to $|\eta| < 2.4$. It is composed of the inner silicon pixel detector and the outer silicon strip detectors [76]. Together, they comprise 75.6 million channels with a total active silicon area of approximately 200 m^2. The spatial granularity of the different components varies with the distance to the beam to keep the average occupancy low enough as the average charge particle fluxes change.

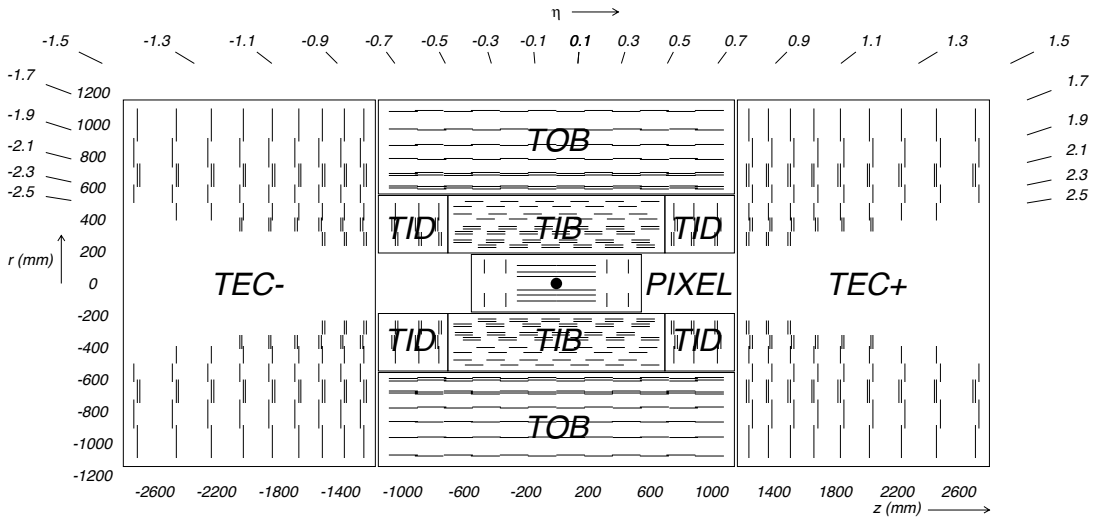

Figure 3.11: Longitudinal-sectional schematic of the CMS tracker layout depicting the various subsystems: the Pixel Detector (PIXEL), the Tracker Inner Barrel and Disks (TIB and TID), Tracker Outer Barrel (TOB), and the Tracker End Caps (TEC+ and TEC- with the sign designating the location along the z axis) [67].

Compared to alternative tracking technologies, the silicon technology has the advantage of high granularity, sensitivity and temporal resolution at the price of higher material budget, cf. Figure 3.12.

Figure 3.13 illustrates the dependence of the tracker reconstruction efficiency and transverse momentum resolution on the pseudorapidity η and transverse momentum p_{T}. It shows the resolution for muons as a function η for $p_{\mathrm{T}} = 1$, 10, and 100 GeV. Similarly, Figure 3.14 shows the resolution of the transverse and longitudinal impact parameters.

The CMS Pixel Detector constitutes the inner-most detection layer closest to the beam line. It is composed of 66 million silicon pixels of dimensions $100 \times 150\,\mu\mathrm{m}^2$

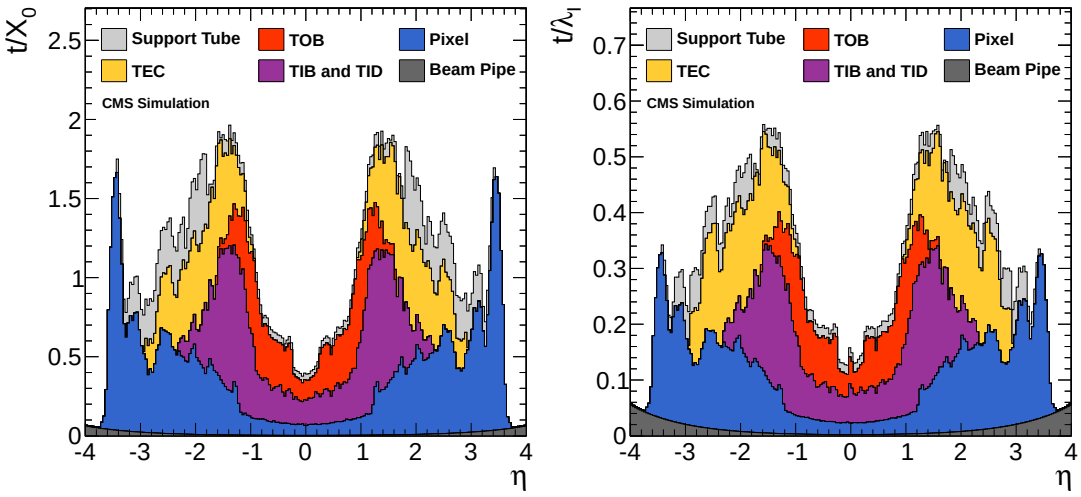

Figure 3.12: The CMS tracker material budget in units of radiation length X_0 (left) and nuclear interaction length λ_I (right) [78]. The contributions from the individual tracker subsystems are shown, as well as the contributions from the beam pipe at the center of the tracker, and the support tube surrounding the tracker.

with a total active area of $\approx 1\,\mathrm{m}^2$. The pixels are arranged into three barrel layers and two endcap disks on each side. The barrel layers are 53 cm in length and lie at mean radii of $r = 4.4\,\mathrm{cm}$, 7.3 cm and 10.2 cm, while the endcap disks are from 6 cm of the annular inner radius to 15 cm of the annular outer radius and lie at $|z| = 34.5\,\mathrm{cm}$ and 46.5 cm on each side. The large number of pixel detector channels places high demands on its services, such as the low voltage power supply and the cooling system. These in turn result in a contribution to the total material budget of the tracker in front of ECAL, cf Figure 3.12. It is $0.05\,\mathrm{X}_0$ at $\eta = 0$ rising to $\approx 0.18\,\mathrm{X}_0$ at $|\eta| = 1.5$ and dropping again to $\approx 0.13\,\mathrm{X}_0$ at $|\eta| = 2.4$, see Figure 3.15.

The Silicon Strip Tracker complements the Pixel Detector in the detection of trajectories of charged particles coming from the interaction point. It comprises 9.6 million silicon strips of various sizes with a total active area of $200\,\mathrm{m}^2$. The strips are arranged into 15,400 modules which are in turn organized in a number of sub-detectors. The inner subsystems are the Tracker Inner Barrel and Disks (TIB and TID), while the outer subsystems are the Tracker Outer Barrel and the Tracker End Caps (TOB and TEC), cf. Figure 3.11. To reduce the radiation damage to the active silicon, the entire system is cooled and operated at a lower temperature.

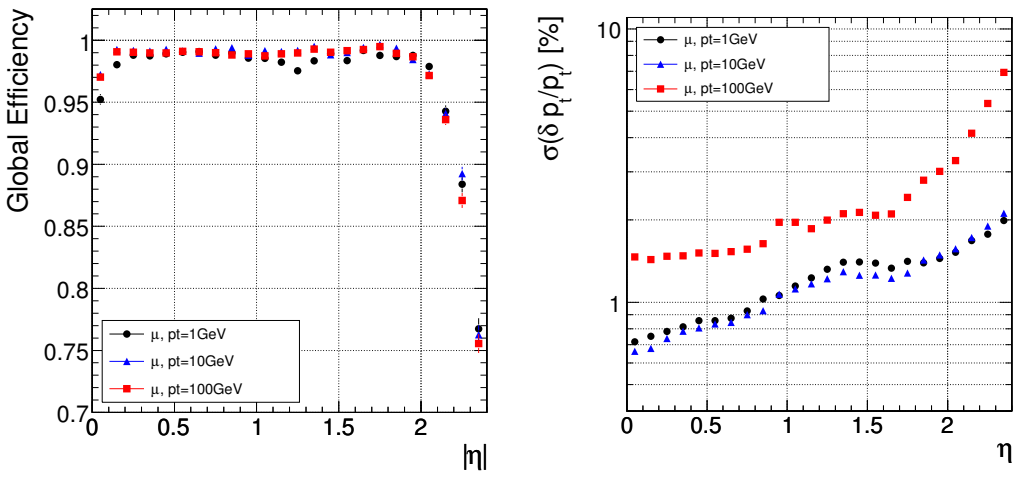

Figure 3.13: CMS tracker reconstruction efficiency (left) [66] and transverse momentum resolution (right) [67] as functions of pseudorapidity η for muons of transverse momentum $p_{\mathrm{T}} = 1\,\mathrm{GeV}$ (black circles), $10\,\mathrm{GeV}$ (blue triangles), and $100\,\mathrm{GeV}$ (red squares).

3.5 CMS Electromagnetic Calorimeter

The CMS Electromagnetic Calorimeter (ECAL) [79, 80] is a hermetic, homogeneous calorimeter that constitutes the next detection layer after the inner tracking system. Its purpose is two fold: to measure the time, location, and amount of energy deposits of electromagnetically interacting particles; and to fully contain electrons and photons inside of its volume. This enables their identification, precise estimates of their momenta and the ability to trigger on high energetic electrons and photons, and large missing transverse energy.

The ECAL is 3.5 m in diameter, 6.1 m in length and more than 93 t in weight. It consists of three main subsystems: the ECAL barrel (EB), the two ECAL endcaps (EE+ and EE-), and the two ECAL preshower detectors (ES+ and ES-), cf. Figure 3.16.

The ECAL active material consists of 75,848 lead tungstate ($PbWO_4$) crystals, including 61,200 in the barrel, and 14,648 in the two endcaps. The preshower detector is composed of two lead absorber layers interleaved with two active silicon layers. The barrel crystals have the form of a tall, narrow a truncated pyramid. The endcap

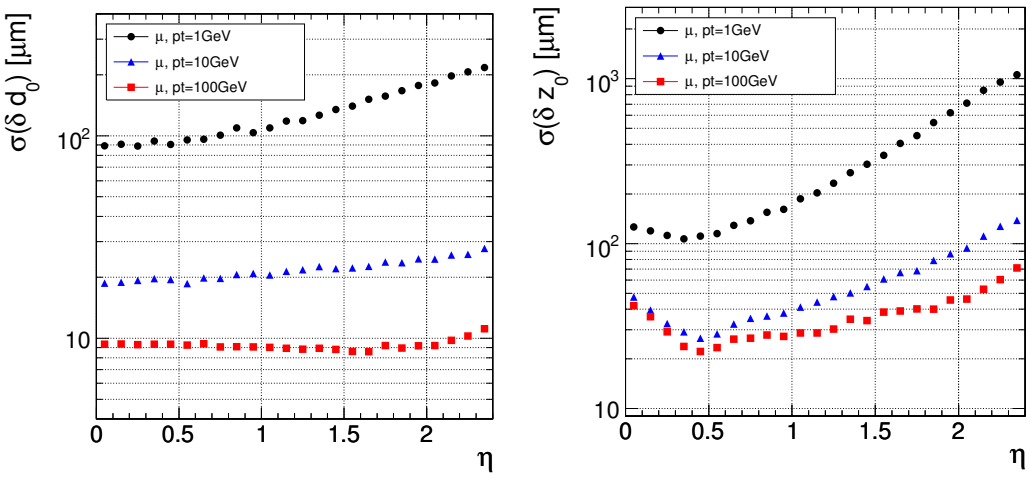

Figure 3.14: CMS Tracker resolution on the transverse (left) and longitudinal (right) impact parameter as a function of pseudorapidity η for muons of transverse momentum $p_{\mathrm{T}} = 1\,\mathrm{GeV}$ (black circles), $10\,\mathrm{GeV}$ (blue triangles), and $100\,\mathrm{GeV}$ (red squares) [67].

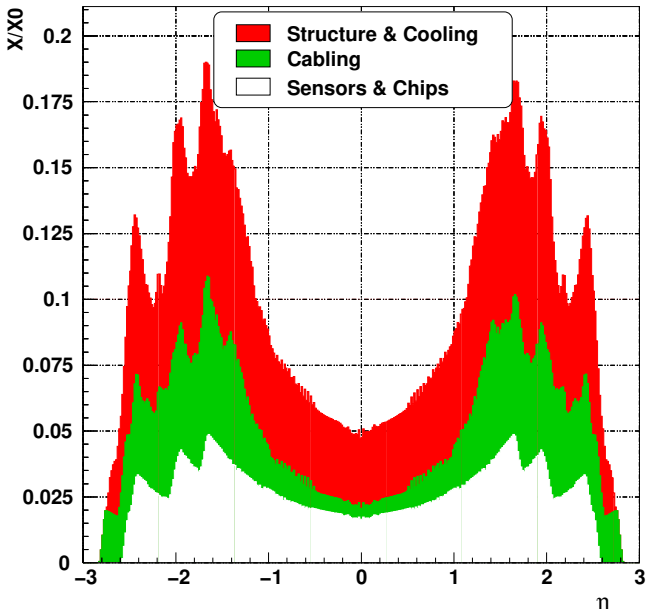

Figure 3.15: The CMS pixel detector material budget [67].

crystal geometry is nearly parallelepipedic.

When an electron or photon traverses the $PbWO_4$ crystals, it interacts with the material. Electrons and positrons emit bremsstrahlung photons while photons in-

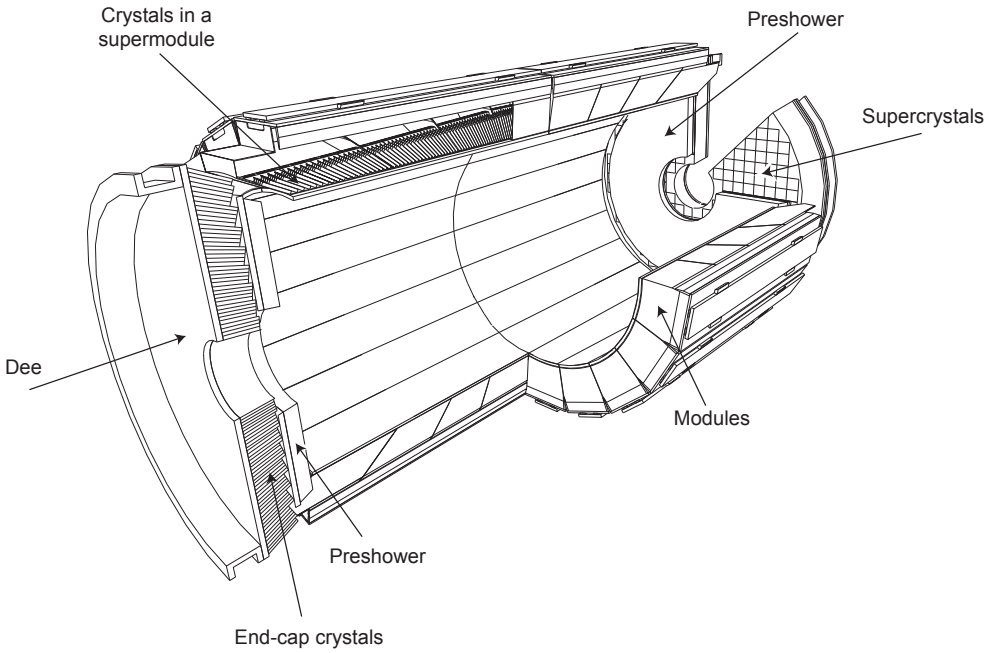

Figure 3.16: A diagram of the CMS electromagnetic calorimeter layout [79].

turn convert to electron-positron pairs, producing an exponential number of electrons, positrons and photons in a cascade fashion with the total number of particles multiplying at each step. An electromagnetic shower develops eventually stopping all the energetic particles within the crystal volume. In the process, the crystals emit blue-green scintillation light with a broad maximum at 420 nm whose overall intensity is proportional to the deposited energy. This scintillation light is collected by photodetectors attached to their back side, see Figure 3.17. There are two different photodetector technologies employed for the Barrel and the Endcaps. The avalanche photodiodes are used in the Barrel, the vacuum phototriodes in the Endcaps.

The high density $d = 8.28\,\mathrm{g\,cm^{-3}}$ and high average atomic number of the $PbWO_4$ crystals is key to their short radiation length of 0.89 cm and a small Molière radius of 2.19 cm which are necessary to achieve the required granularity thickness. Their response is also reasonably fast compared to the LHC design bunch spacing interval of 25 ns as they emit 80 % of the scintillation light from a charged particle within that period of time. Their light output is subject to change with varying temperature by about $-1.9\,\%/^{\circ}\mathrm{C}$ at 18 °C requiring the presence of a system that cools the read-

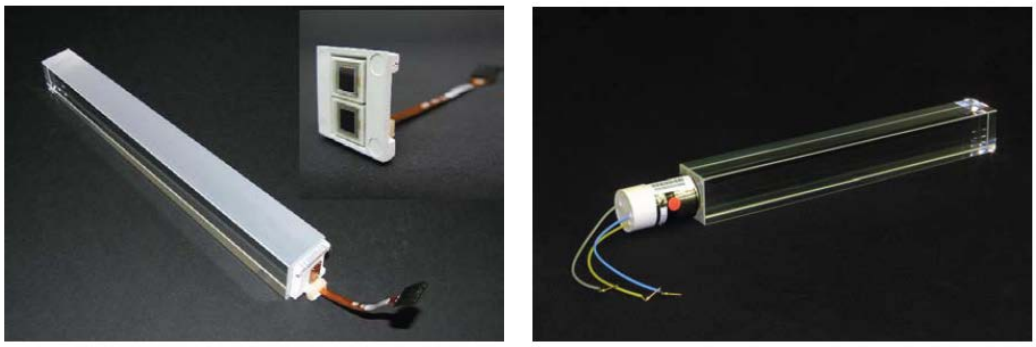

Figure 3.17: The ECAL $PbWO_4$ Crystals with Photodetectors. Left: A barrel crystal with two avalanche photodiodes. Right: An endcap crystal with a vacuum phototriode [67].

out electronics and maintains the crystal temperature stable within $\pm 0.05\,^{\circ}\mathrm{C}$. The crystals are also sufficiently radiation hard. However, their response decreases in the harsh environment during LHC operation due to their exposure to high radiation dose rates [81]. The Caltech group developed, constructed and operates a laser monitoring system that continuously tracks and corrects these changes to maintain the excellent energy resolution. Figure 3.18 shows the time evolution of the relative crystal transparency to the laser light (440 nm) averaged over the barrel for some fills in 2011. It illustrates the loss of the response during a fill and its corresponding recovery during the time between fills. Figure 3.19 shows the history of the relative crystal response to the laser light in both 2011 (440 nm) and 2012 (447 nm) averaged over groups in crystals by regions of the pseudorapidity absolute values $|\eta|$.

The EB has an inner radius of 124 cm, a length of 609 cm, and a thickness of 31 cm. It covers the fiducial volume of $|\eta| < 1.48$. It has a granularity of $170 \times 360 = 61,200$ crystals folded in $\eta \times \phi$. It is composed of two halves, each on one side of the x-y plane (EB+ and EB-). Each half is structured into 18 identical *supermodules* folded in the ϕ direction with each supermodule containing 85×20 crystals in $\Delta\eta \times \Delta\phi$. Each supermodule is in-turn made of 4 modules with the module 1 (the most central one at lowest η) being 25×20 crystals, and modules 2-4 20×20 crystals in $\Delta\eta \times \Delta\phi$. To improve the ECAL hermeticity by mitigating the shower leakage through inter-crystal

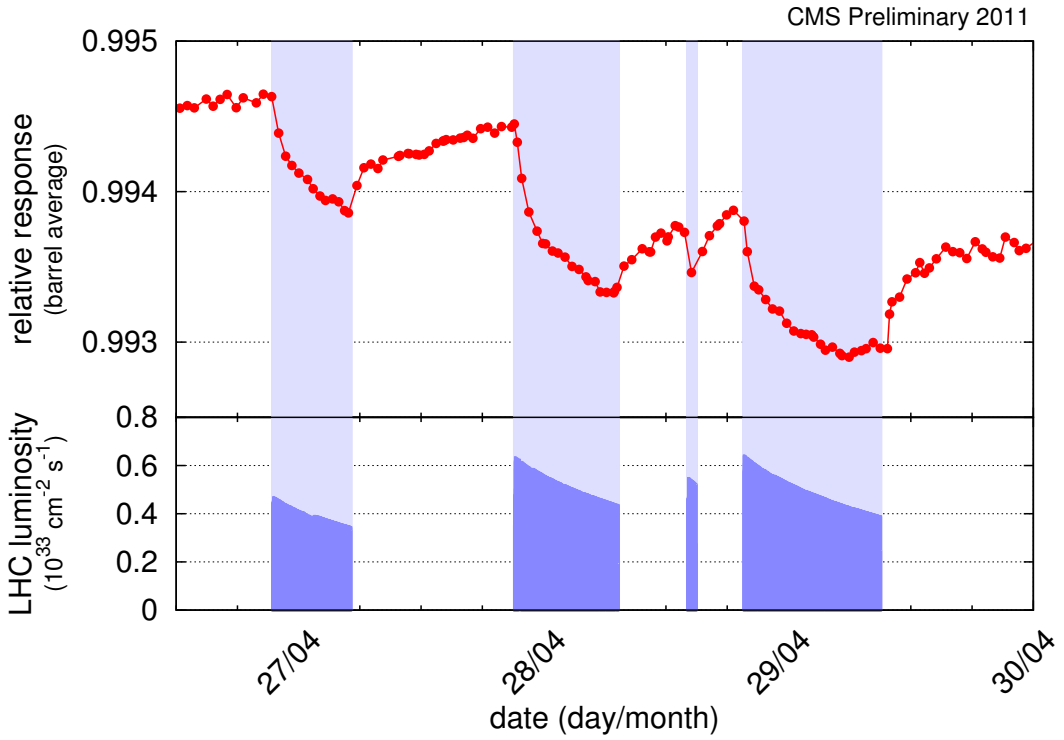

Figure 3.18: CMS ECAL relative mean laser response in the barrel for some fills in 2011 [82]. The loss of the response is clearly visible during the fills. So is the corresponding recovery in the mean time. The physics data is corrected crystal-by-crystal using these measurements.

gaps, the crystals are mounted in a quasi-projective geometry: their axes are tilted at 3° with respect to a line from the nominal interaction vertex. Each EB crystal covers 0.0174×0.0174 in $\Delta\eta \times \Delta\phi$ ($1° \times 1°$ in $\Delta\theta \times \Delta\phi$), has a front face cross-sectional area of $\approx 22 \times 22\,\mathrm{mm}^2$ (about 1 Molière radius squared), and a length of 230 mm corresponding to $25.8\,\mathrm{X}_0$ radiation lengths.

Seen from the nominal interaction vertex, the front faces of the EE disks are annuli with inner and outer radii of 32 cm and 171 cm. They are located on each side at $|z| = 317\,\mathrm{cm}$, and are 73 cm thick. Each EE disk is composed of two "Dees" symmetric with each other by a reflection in the y-z plane. The EE covers a fiducial volume of $1.5 < |\eta| < 3.0$. Compared to the barrel, the endcap crystal are wider and shorter. They have a front face area of $28.6 \times 28.6\,\mathrm{mm}^2$ and a length of 200 mm corresponding to $24.7\,\mathrm{X}_0$. The preshower detectors are mounted in front of the endcaps and cover

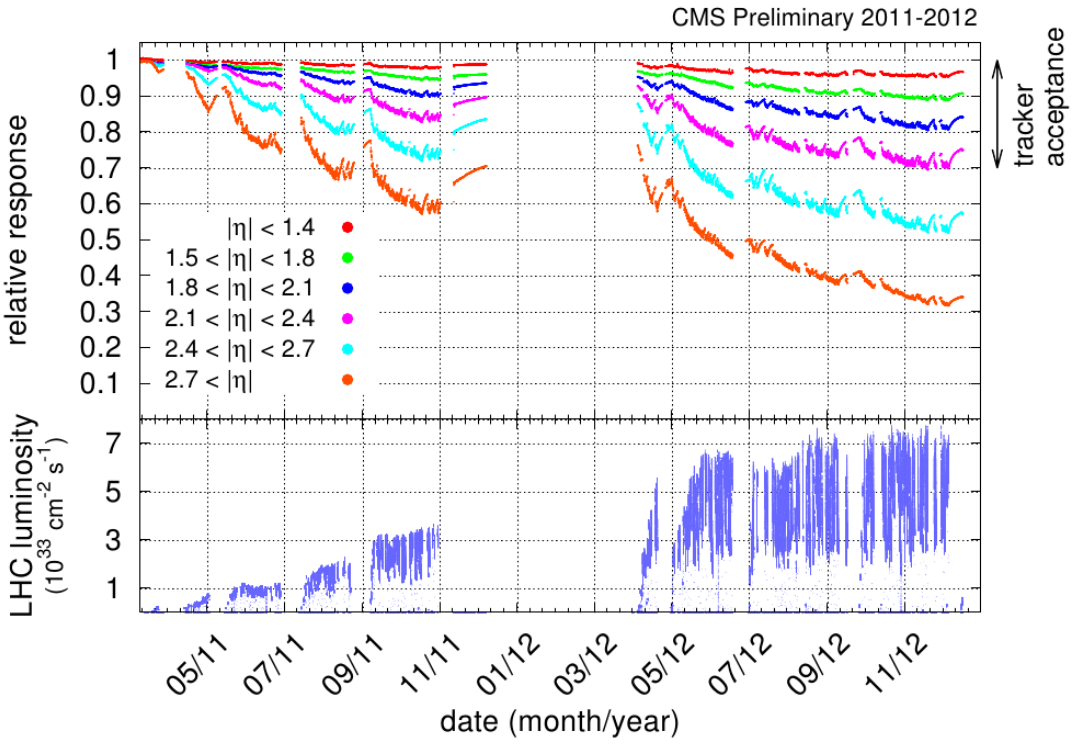

Figure 3.19: CMS ECAL relative mean laser response histories in 2011 and 2012 for groups of crystals in categories of $|\eta|$ [82].

the pseudorapidity region of $1.65 < |\eta| < 2.6$. The two disks of the lead absorber are located at $2\,X_0$ and $3\,X_0$. See Figure 3.20 for a schematic diagram of a longitudinal sectional view in the y-z plane of an ECAL quadrant showing the location and arrangement of its subsystems and crystals.

The energy resolution $\sigma(E)$ of the ECAL as a function of the total energy E of the incident particle is [79]:

$$\frac{\sigma(E)}{E} = \frac{N}{E} \oplus \frac{S}{\sqrt{E}} \oplus C, \tag{3.7}$$

where N, S, and C are the *noise*, *stochastic*, and *constant terms*, and the operator $\oplus$ denotes *addition in quadrature*:

$$x \oplus y = \sqrt{x^2 + y^2}. \tag{3.8}$$

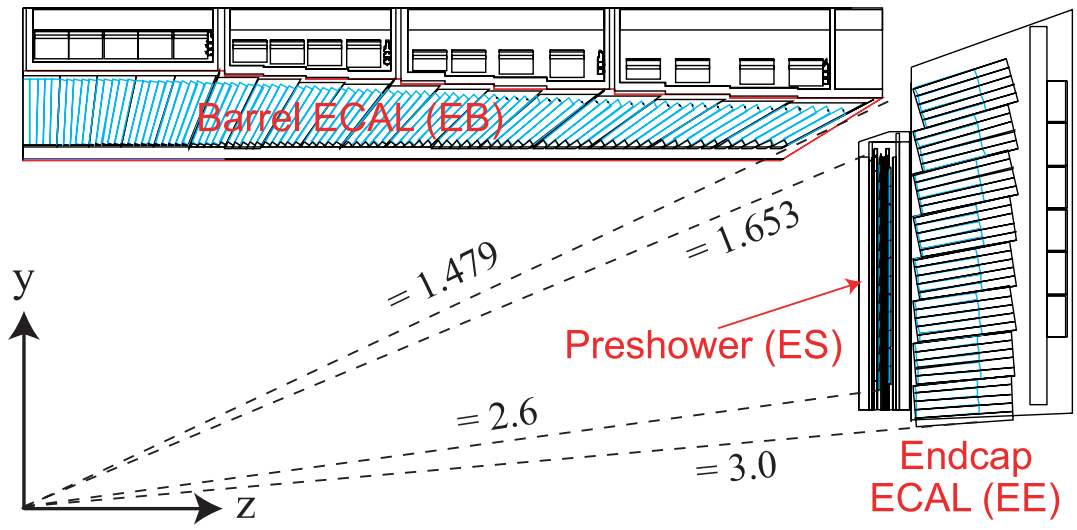

Figure 3.20: A schematic diagram of a longitudinal-sectional view in the y-z plane of an ECAL quadrant showing the location and arrangement of its subsystems and crystals. [66].

The three terms correspond to a sum of three statistically independent quantities. The parameters S, N, and C depend on the properties of the crystals, detector electronics, calibration, and other factors, see Table 3.5.

The stochastic term describes the fluctuation in the number of photons and electrons in the electromagnetic shower due to its lateral containment, endcap preshower absorber, and Poisson fluctuations (ca. 2.3 % $\sqrt{\text{GeV}}$).

The noise term refers to the noise due to pileup deposits from multiple inelastic collisions and readout electronics including the preamplifier and the readout.

Finally, the constant term represents fluctuations in the calibration and other smaller effects that are proportional to the total deposited energy like non-uniformity of the longitudinal light collection, shower leakage from the back of the crystal, geometrical effects, etc.

The ECAL energy resolution has been measured using test beams of high energetic electrons with minimal material in front of crystals, absence of magnetic field and with beams centered on the crystal faces. The measured resolution for energies

Term	Contribution	Barrel ($\eta = 0$)	Endcaps ($\lvert\eta\rvert = 2$)	Unit
Noise at low luminosity	Electronics noise (at start-up)	15	75	% GeV
	Leakage current noise	3	–	
	Pileup noise	3	18	
	Total Noise Term	**16**	**77**	
Noise at high luminosity	Electronics noise (at start-up)	15	75	% GeV
	Leakage current noise	11	–	
	Pileup noise	10	53	
	Total Noise Term	**21**	**92**	
Stochastic	Containment	1.5	1.5	$\% \sqrt{\text{GeV}}$
	Photo-statistics	2.3	2.3	
	Preshower sampling	–	5.0	
	Total Stochastic Term	**2.7**	**5.7**	
Constant	Inter-calibration	0.4	0.4	%
	Longitudinal non-uniformity	0.3	0.3	
	Others	< 0.2	< 0.2	
	Total Constant Term	**0.55**	**0.55**	

Table 3.2: CMS ECAL resolution design parameters [79] broken down into different contributions to the various terms of (3.7)

reconstructed in 3×3 crystals under such ideal conditions is [83]:

$$\frac{\sigma(E)}{E} = \frac{12.7\,\%}{E\,(\text{GeV})} \oplus \frac{2.8\,\%}{\sqrt{E\,(\text{GeV})}} \oplus 0.3\,\%$$

Figure 3.21 illustrates the ECAL energy resolution as a function of the incident particle energy. The left panel shows the magnitude of the various contributions according to the design [79], the right panel shows the measurement using a test beam of electrons [83].

3.5.1 CMS ECAL In Situ Performance

The energies and directions of prompt electrons and photons from pp collisions in CMS are identified and reconstructed starting from the energies deposited in each crystal in the ECAL. These deposits are clustered by algorithms discussed in Section 4.4, and

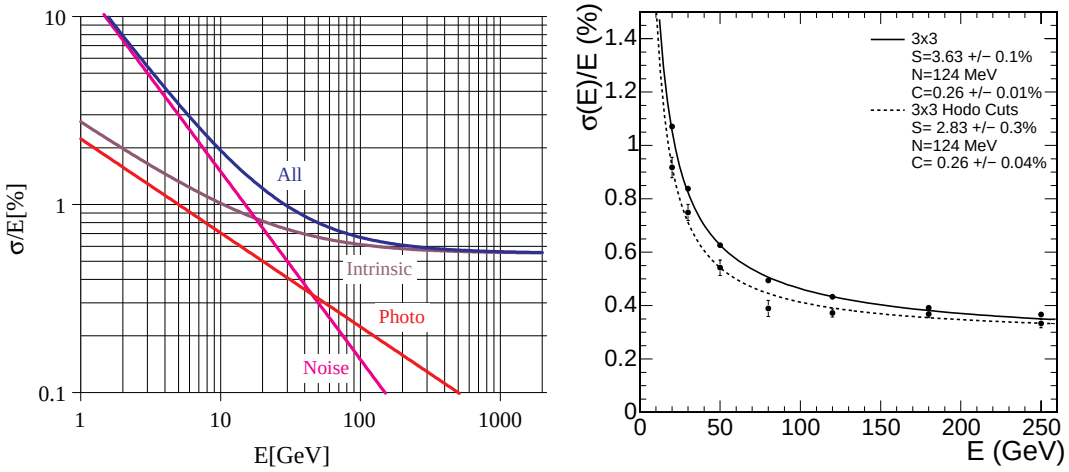

Figure 3.21: CMS ECAL energy resolution as a function of energy. Left: Different contributions according to the design [79]: the noise term (magenta line labeled "Noise"), the stochastic term (red line labeled "Photo"), the sum in quadrature of the stochastic and constant terms (brown line labeled "Intrinsic"), and the total resolution (blue line labeled "All"). Right: Measurement for a 3×3 array of crystals with electrons from a test beam incident in an area of $20 \times 20\,\mathrm{mm}^2$ (solid line) and $4 \times 4\,\mathrm{mm}^2$ (dashed line) in the center of the front face of an arbitrary crystal. [66, 83].

associated with hypotheses as to the nature of the particles that produced them, as discussed in Sections 4.5 and 4.6. The energy deposited in each crystal, together with other properties of the clusters are then used to estimate the energy of the electrons and photons originating at the interaction point. As discussed in more detail in the remainder of this section, the reconstructed electron and photon energy resolution is significantly worse than the resolution measured in test beams.

This is due to several factors, the most important of which is the material of the tracker, its cables and services in front of the ECAL, and the additional material of the preshower in front of the ECAL endcap. Other factors contributing to the resolution in situ include the energy scale determination using $\mathrm{Z} \to \mathrm{e}^+\mathrm{e}^-$ and $\mu\mu\gamma$ events, the crystal-by-crystal calibration accuracy, the electronic noise, and the accuracy of the GEANT4 simulation [84].

As discussed in detail in Section 4.4, the in-situ reconstruction of electrons takes into account electron showering and photon conversions in the tracker material, that lead to a spread of the electromagnetic showers along the ϕ-direction due to the

bending of electrons and positrons in the magnetic field. As a result of the spreading of energy over a larger angular range, there is a greater likelihood that part of the shower goes into the inter-crystal, inter-module and inter-supermodule cracks, and so more of the energy is lost on average and the fluctuations in these losses contribute to the resolution. In addition, since the energy is spread among a greater number of crystals, the overall contribution to the resolution from electronic noise is increased for showering electrons relative to non-showering electrons.

In addition to the effects of translating the detector energies to the particle energies and the associated changes in clustering, there are further effects that worsen the energy resolution. In the ECAL barrel ($|\eta| < 1.5$), the per-crystal electronics noise has risen due to the rise in the dark current in the avalanche photodiodes (APDs) caused by irradiation (see Figures 3.22 and 3.23), and there is an additional small effect due to the radiation-induced loss of transparency of the crystals (see Figure 3.19) that amplifies the noise relative to the signal for a given particle energy.

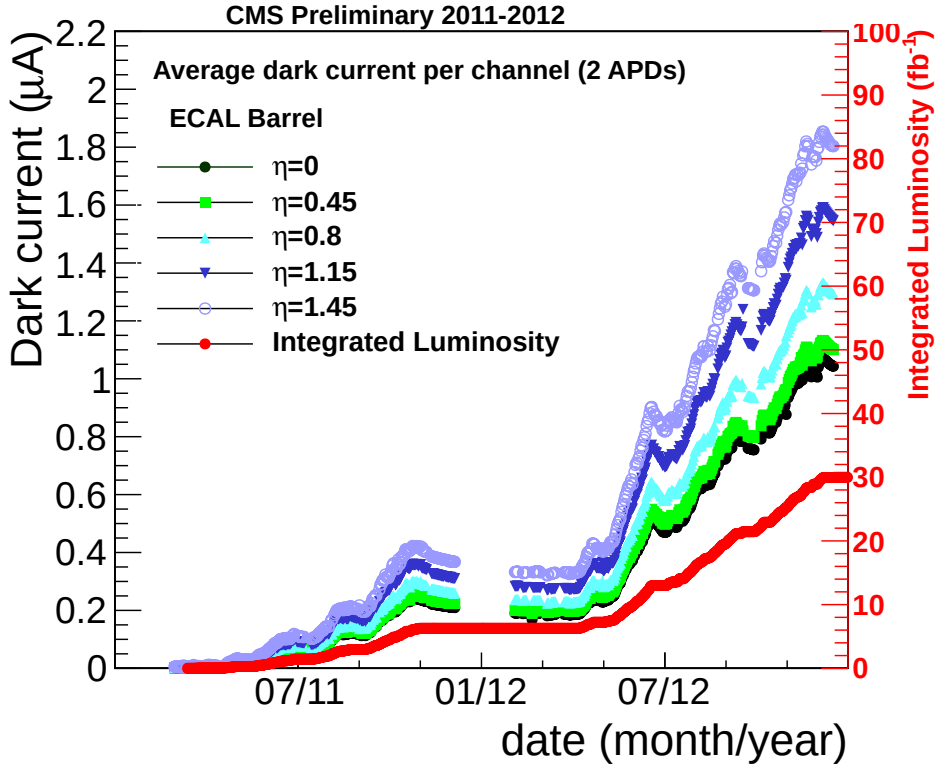

Figure 3.22: CMS ECAL APD dark current evolution in time [82].

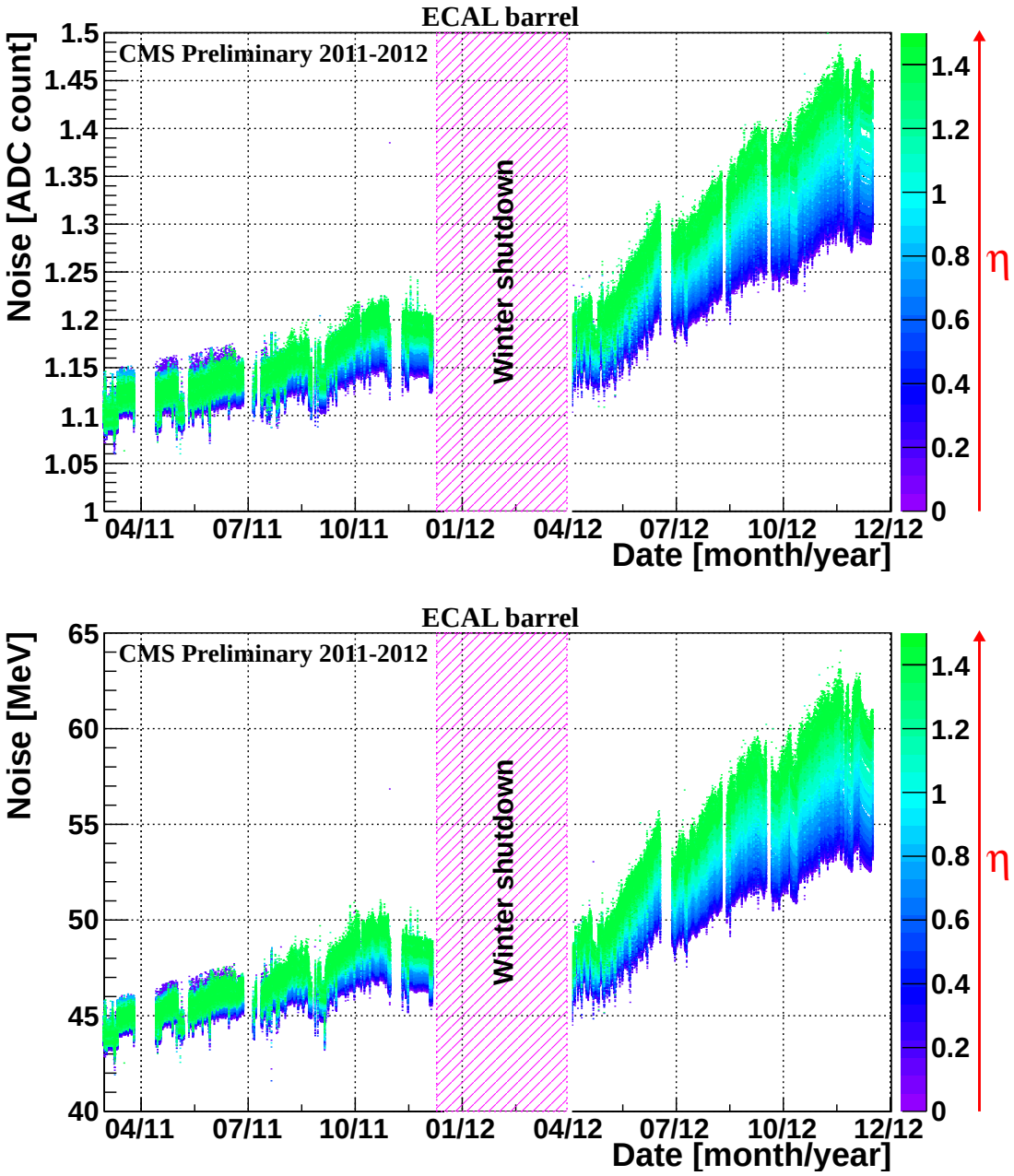

Figure 3.23: CMS ECAL APD noise in the barrel in ADC counts (top) and MeV (bottom) [82]. Colors are used to represent the pseudorapidity magnitude $|\eta|$ with low values of $|\eta|$ at the violet end of the spectrum and high values of $|\eta|$ at the green end of the spectrum as indicated by the color palette on the right side of the panels.

In the ECAL endcaps, the vacuum phototriodes used are immune to the leakage current effect, but the endcaps are substantially more susceptible to the noise amplification effect (see Figure 3.24), since the loss of transparency in the endcap crystals,

especially those at the larger values of $|\eta|$, is considerably larger as a result of the higher radiation doses, as shown in Figure 3.19. These time-dependent noise effects

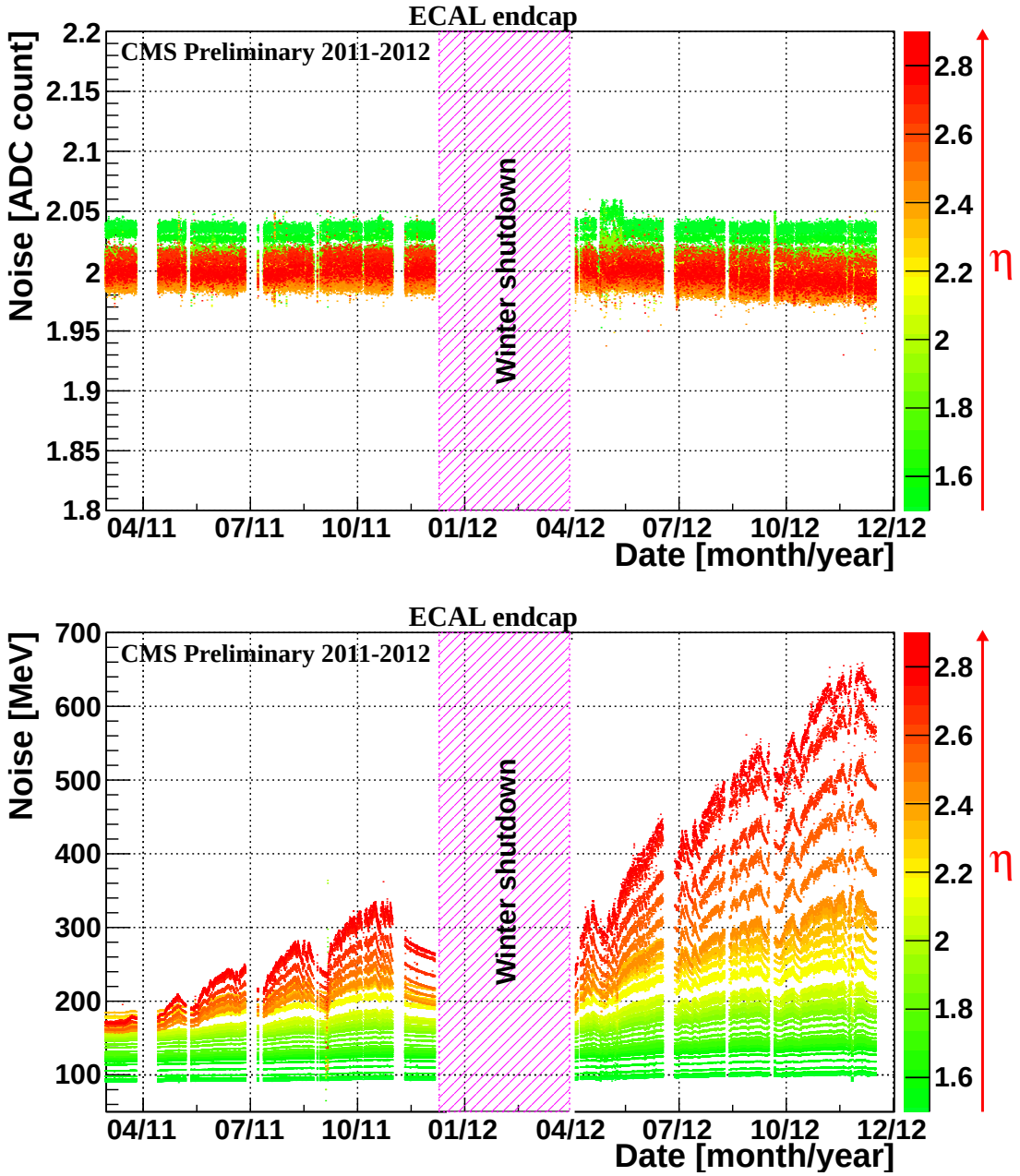

Figure 3.24: CMS ECAL VPT noise in the endcaps in ADC counts (top) and MeV (bottom) [82]. Colors are used to represent the pseudorapidity magnitude $|\eta|$ with low values of $|\eta|$ at the green end of the spectrum and high values of $|\eta|$ at the red end of the spectrum as indicated by the color palette on the right side of the panels.

are not well-represented in the simulation.

The in-situ electron and photon resolution is also affected by the accuracy of the calibration and the cluster corrections (the energy reconstruction algorithm). Both of these have evolved since 2010 and several different versions and combinations of the two have been used since then. Figure 3.25 shows the relative photon energy resolution unfolded in bins of transverse energy E_{T} using photons from $\mathrm{Z} \to \mu^{+}\mu^{-}\gamma$ decays collected in 2011. Figures 3.26 and 3.27 show the relative electron energy resolution unfolded in bins of pseudorapidity $|\eta|$ using electrons from $\mathrm{Z} \to \mathrm{e}^{+}\mathrm{e}^{-}$ decays collected in 2011 and 2012, respectively.

The CMS simulation attempts to describe the resolution as realistically as possible, taking into account all the known effects, including e.g. the estimated intercalibration precision and its dependence on η and the data-taking period. In 2012, this precision was approximately 0.35 % in the central region of the barrel up to $|\eta| < 0.7$, rising with $|\eta|$ in the outer region of the barrel with $0.7 < |\eta| < 1.5$ to approximately 0.9 % at its ends, see Figure 3.28. In the endcaps, it was approximately 3 % at the outer edges near $|\eta| = 1.5$, dropping down to approximately 2 % in the range $1.6 < |\eta| < 2.3$, and rising again to approximately 5 % at $|\eta| = 2.5$.

Despite the efforts to realistically simulate the ECAL, it is clearly visible from Figures 3.26 and 3.27 that the electron resolution in situ is worse than in simulation. Among the known causes of this discrepancy are:

- the description of the material in front of the crystals,
- the increase of the APD electronics noise due to radiation damage discussed above, and
- the scaling of the resolution by the transparency correction described above.

As of this writing, there is an ongoing effort in the CMS collaboration to improve the simulation with respect to the above aspects. Whether there are further effects contributing to the observed difference in the particle energy resolution in data and simulation remains to be seen.

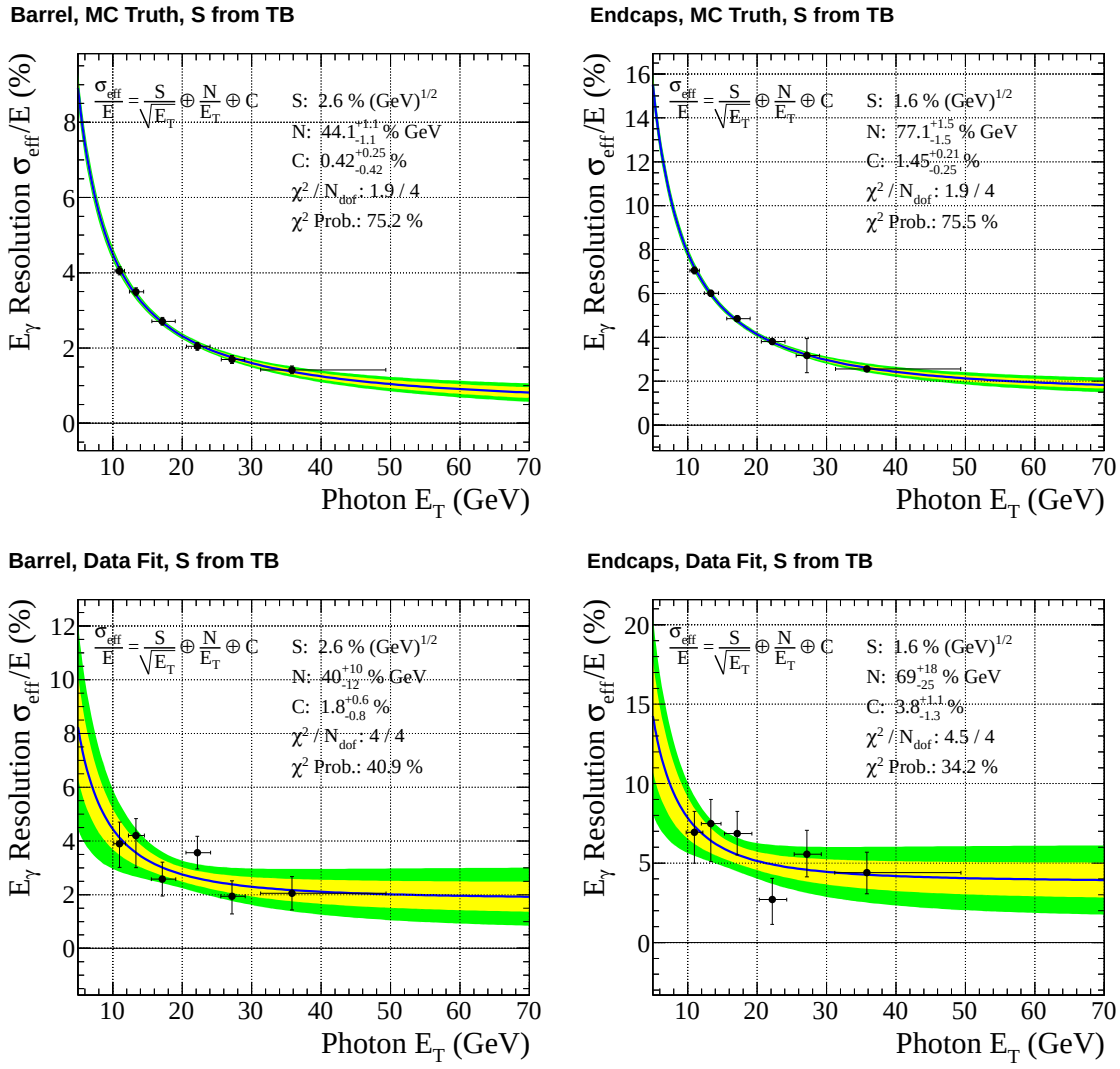

Figure 3.25: Photon energy resolution (black points with error bars) unfolded in bins of transverse energy E_{T} using photons from $\mathrm{Z} \to \mu^+\mu^-\gamma$ decays collected in 2011 overlaid with a fit (solid blue line). Top row: simulation, bottom row: data, left column: barrel, right column: endcaps. The fitted function has a similar form to (3.7) but it uses transverse energy E_{T} instead of the energy E. The parameter S is fixed to its value estimated from the test beam with electrons after adjusting for the E_{T}/E ratio of the sample at hand. The light yellow and light green bands represent $\pm 1\sigma$ and $\pm 2\sigma$ uncertainties on the fit, respectively.

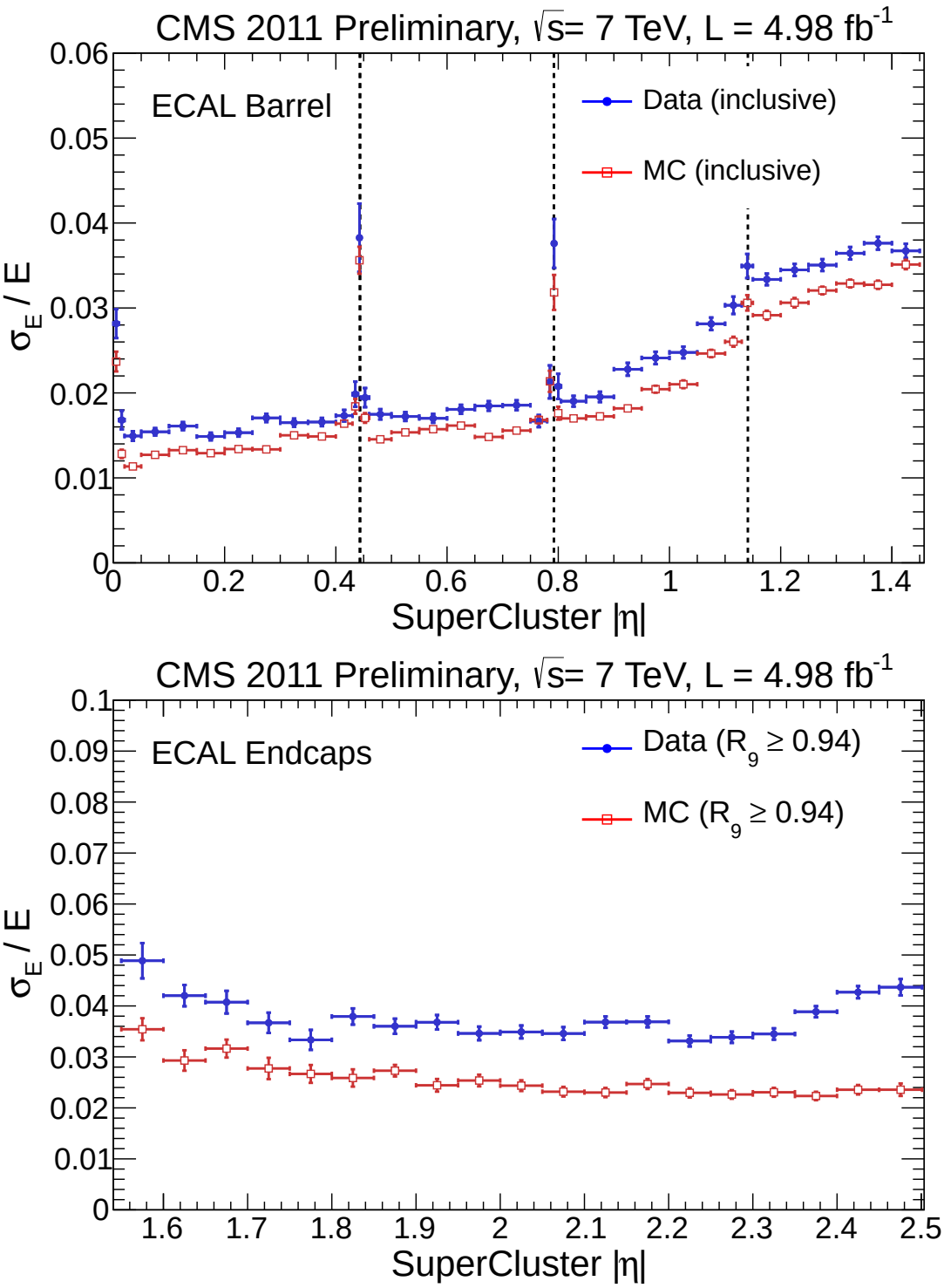

Figure 3.26: Electron energy resolution unfolded in bins of pseudorapidity $|\eta|$ using electrons from $Z \to e^+e^-$ decays collected in 2011 [85].

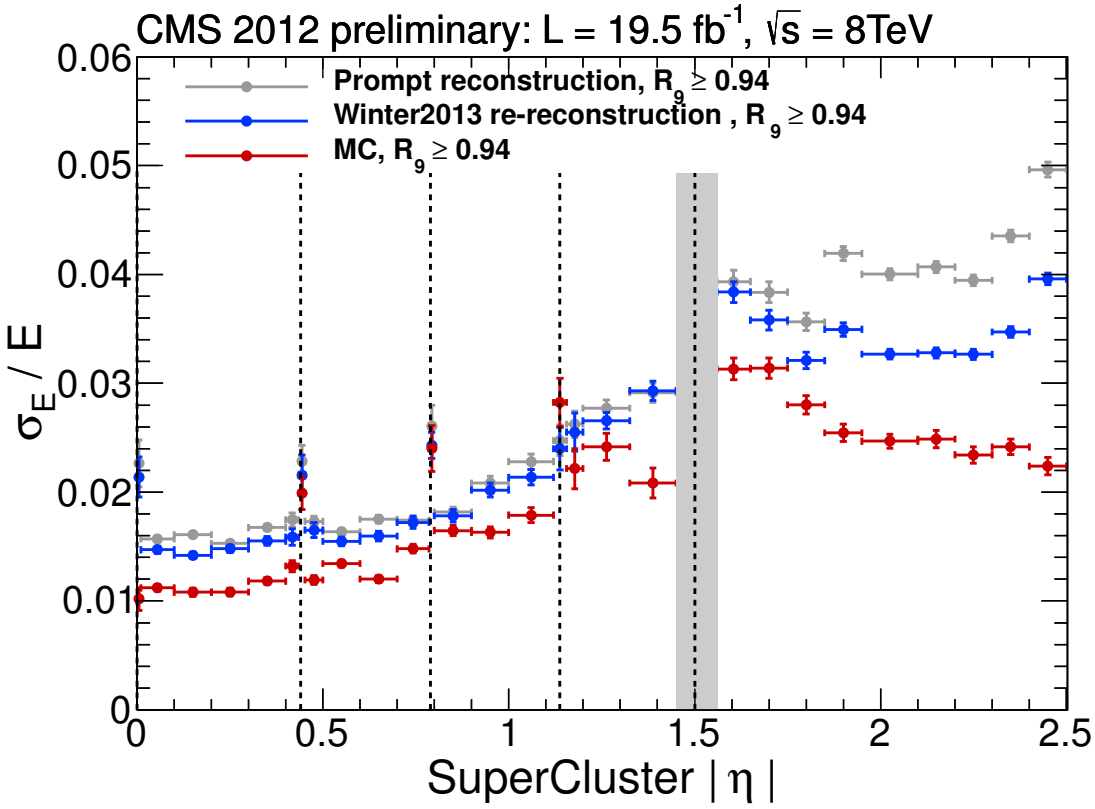

Figure 3.27: Electron energy resolution unfolded in bins of pseudorapidity $|\eta|$ using electrons from $Z \to e^+e^-$ decays collected in 2012 [82].

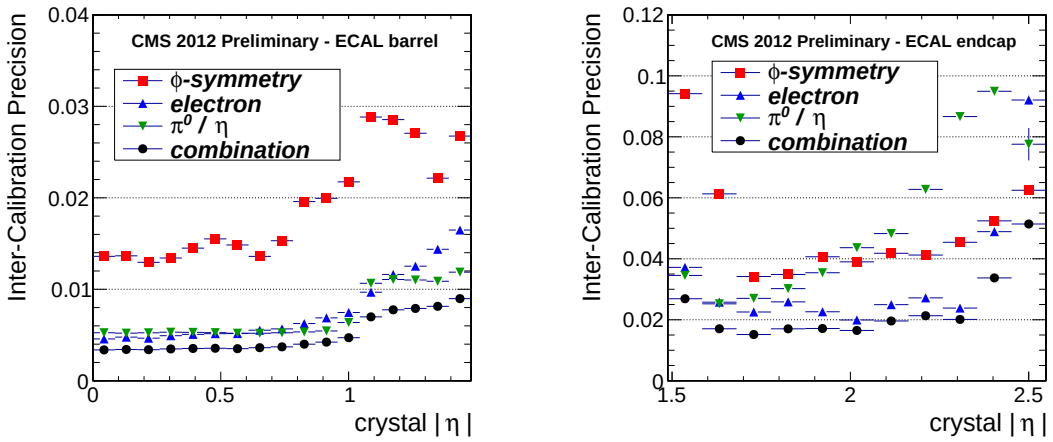

Figure 3.28: CMS ECAL intercalibration precision in 2012 for the barrel (left) and the endcaps (right) in bins of pseudorapidity $|\eta|$ [82]. The red squares corresponds to calibration based on the ϕ-symmetry of the energy deposits, the blue upward-pointing triangles correspond to calibration using electrons from $Z \to e^+e^-$ and $W \to e\nu$ decays, the green downward-pointing triangles correspond to calibration using photons from $\pi^0 \to \gamma\gamma$ and $\eta \to \gamma\gamma$ decays, and the black circles correspond to a combination of the results from all the three methods.

3.6 CMS Hadron Calorimeter

The CMS hadron calorimeter [86] (HCAL) surrounds the ECAL and the inner tracking system and is partially installed inside of the superconducting solenoid and partially outside of it. Similarly to the ECAL, its primary purpose is to measure and fully contain certain particles. It complements the ECAL by further absorbing hadrons. It is designed to (a) acquire the location, time and magnitude of the energy deposited by the incident particles and (b) capture all hadrons so that the only particles originating from the collisions and traveling past the HCAL are muons and neutrinos. It directly contributes to muon identification and precise measurements of jet kinematics and missing transverse energy. It also contributes to the rejection of jets faking prompt isolated leptons and photons. It is vital for a number of important trigger paths including hadronic activity, large missing transverse energy, etc.

The CMS HCAL is a sampling calorimeter. Its active volume consists of 70,000 scintillating plastic tiles interleaved with absorber plates. The short nuclear interaction length of $\lambda_I = 16.42\,\text{cm}$, non-magneticity and reasonable cost were the key

properties making brass alloy the absorber material of choice for the compact design of HCAL placed in a strong magnetic field. Brass is complemented by steel for greater structural strength. Wavelength shifting fibers transmit the signal to Hybrid Photodiodes for readout.

The CMS HCAL consists of 4 sub-systems, the HCAL barrel (HB), the HCAL endcap (HE), the hadron outer calorimeter (HO), and the hadron forward calorimeter (HF). The HE and HB lie inside the magnet and the HO and HF outside of it, see Figure 3.29.

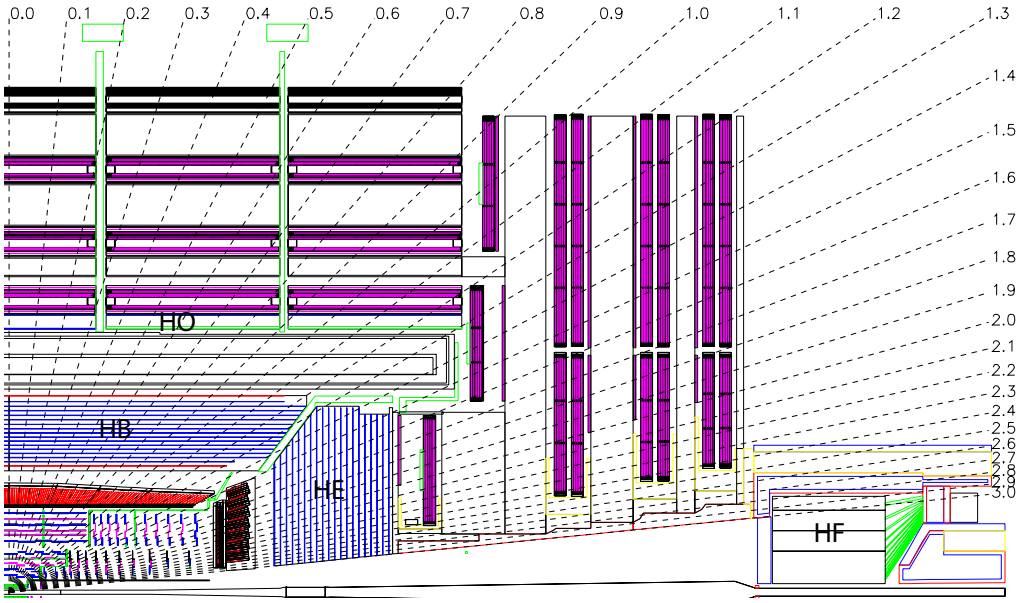

Figure 3.29: Longitudinal-sectional diagram of the HCAL layout depicting the positions of the four sub-detectors [67].

The HB covers the central region up to pseudorapidity of $|\eta| < 1.4$. It is radially restricted at $r = 1.77\,\mathrm{m}$ by the extent of the ECAL from the inside and at $r = 2.95\,\mathrm{m}$ by the extent of the solenoid from the outside. It comprises 2,304 separately-readout towers with a granularity of $\Delta\eta \times \Delta\phi = 0.087 \times 0.087$ ($\Delta\theta \times \Delta\phi = 5^\circ \times 5^\circ$). Each tower is composed of 17 scintillator tiles interleaved with 16 absorber plates. Traversing HB from the inside out, the absorber consists of a steel front plate 40 mm in thickness, eight brass plates 50.5 mm in thickness, six brass plates 56.5 mm in thickness, and finally a steel back plate 75 mm in thickness. The total absorber thickness is 5.82 λ_I at

pseudorapidity $\eta = 0$ and grows to $10.6\,\lambda_\mathrm{I}$ at pseudorapidity $|\eta| = 1.3$. The scintillator tiles are 3.7 mm thick, with the exception of the front and back tiles which are 9 mm thick.

The HB is complemented by an additional absorber-scintillator layer, called HO, outside the solenoid for improved hermeticity and containment. The HO matches the coverage and segmentation of the HB. The HO scintillators are 10 mm thick. The absorber is made of iron and is 18 cm thick. It serves as a "tail-catcher" containing hadron showers leaking through the HB and the solenoid. It increases the total effective thickness of the hadron calorimetry including ECAL to $\approx 10\,\lambda_\mathrm{I}$.

The HE covers the forward regions with pseudorapidities of $1.3 < |\eta| < 3.0$. It comprises 20,916 scintillator tiles in 18 layers with a granularity of $\Delta\eta \times \Delta\phi = 0.087 \times 0.087$ for $|\eta| < 1.6$ and of $\approx 0.17 \times 0.17$ for $1.6 \leq |\eta| < 3.0$. The absorber plates are made of brass and are 79 mm thick. The front scintillator tile is 10 mm, all the others are 3.7 mm thick. The total effective thickness of the hadron calorimetry is approximately $10\,\lambda_\mathrm{I}$ — the same as for the HB + HO.

The HF is composed of 900 towers and 1,800 channels shared among two modules, one on each side. The modules are cylindrical structures with outer diameters of 1.3 m. They sit at $|z| = 11.2$ m and extend the pseudorapidity coverage to $|\eta| < 5.2$. They use a steel absorber with a depth of 1.65 m. Quartz fibers constitute the active volume. They emit Čerenkov light and transmit it to photomultipliers for readout. They have a diameter of 0.6 mm and are arranged in a square grid with a pitch of 5 mm. The tower segmentation varies from $\Delta\eta \times \Delta\phi = 0.175 \times 0.175$ at $|\eta| = 3.0$ to $\Delta\eta \times \Delta\phi = 0.3 \times 0.35$ at $|\eta| = 5.0$.

The total resolution of the CMS hadronic calorimetry including both ECAL and HCAL can be expressed as a function of the incident particle energy as:

$$\frac{\sigma(E)}{E} = \frac{S}{\sqrt{E}} \oplus C, \tag{3.9}$$

where S is the stochastic term and C the constant term. The values of these terms were estimated experimentally in test beams [87, 88]. We summarize the results in

Parameter	HB, HE	HF	Unit
Stochastic term S	84.7	198	$\% \sqrt{GeV}$
Constant term C	7.4	9	%

Table 3.3: CMS HCAL calorimetry performance from beam tests.

Table 3.6.

Figure 3.30 shows the jet p_{T} resolution as a function of the jet p_{T} for jets reconstructed using two different algorithms: the so-called *calo-jets* based solely on calorimeter deposits, and the so-called *PF jets* based on the *particle flow* (PF) algorithm that combines information from all the subsystems including the inner tracking. The calo-jet reconstruction is generally more robust while the PF-jet reconstruction is generally more performant. The measured relative jet p_{T} resolution ranges between approximately 18 % for low-p_{T} calo-jets ($p_{\mathrm{T}} \sim 50\,\mathrm{GeV}$), and approximately 8 % for high-p_{T} PF jets ($p_{\mathrm{T}} > 200\,\mathrm{GeV}$).

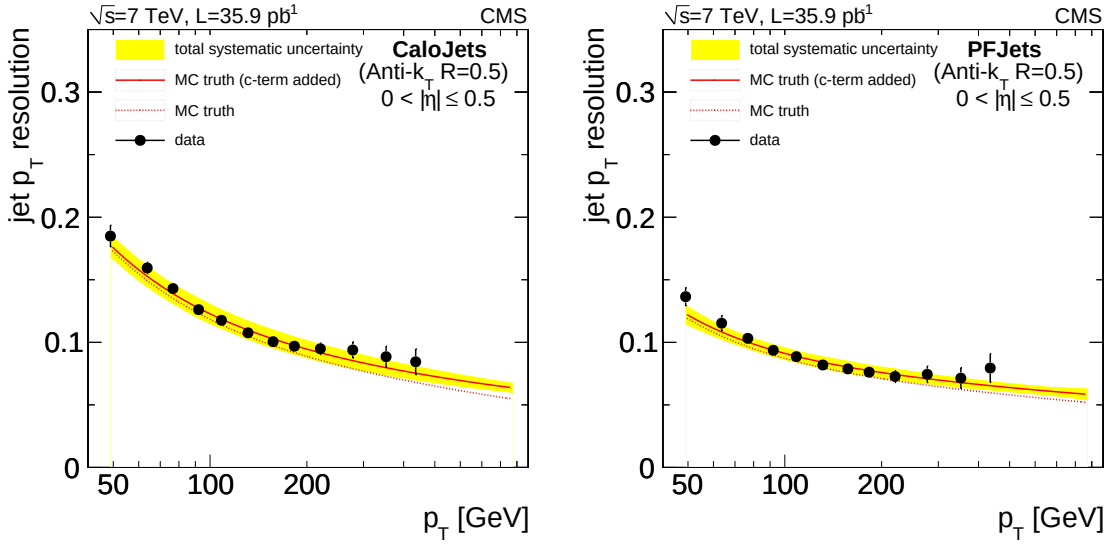

Figure 3.30: Jet p_{T} resolution in bins of jet p_{T} for jets with pseudorapidities $|\eta| < 0.5$ as measured in dijet events selected in $35.9\,\mathrm{pb}^{-1}$ of pp collisions at $\sqrt{s} = 7\,\mathrm{TeV}$ collected in 2010 (black dots with error bars), compared to the so-called *MC truth*, the generator-level simulation before and after applying a correction based on the data measurements (dashed and solid red lines, respectively) [89]. The yellow bands represent the total systematic uncertainty on the corrected MC truth. The left panel corresponds to calo-jets, the right panel corresponds to PF jets.

3.7 CMS Muon System

The CMS muon system [90] represents together with the return yoke the outermost layer of the various CMS components. Its design was driven by three primary objectives: triggering, momentum measurement and identification.

Of the various particles reaching CMS, muons are extraordinary in the way they interact with matter. Similar to electrons, they lose energy though the bremsstrahlung radiation as they propagate through material. However, compared to electrons, the rate of this process is suppressed by a factor of $\sim 4 \times 10^4$ as it is inversely proportional to the square of the mass, and muons are 200 times heavier. As a result, muons can escape the calorimeters with relatively small energy losses while simultaneously depositing enough energy to enable their detection (unlike neutrinos). Consequently, they can be reconstructed and identified with very high efficiency and very low background contamination, making them a great tool for studying rare and otherwise difficult-to-reconstruct processes.

CMS uses three different types of gaseous detectors to register muons. This is a result of optimizing the performance in regions with different magnetic field intensities, particle fluxes, and neutron background dose rates. The drift tube chambers (DTs) used in the barrel region up to $|\eta| < 1.2$ provide the best spatial resolution. The cathode strip chambers (CSCs) used in the endcap region up to $|\eta| < 2.4$ can cope with the higher intensities of the magnetic field and higher rates of muons, and neutron background. The resistive plate chambers (RPCs) used in both the barrel and endcap regions complement the DTs and CSCs with an excellent temporal resolution thus improving the triggering performance and reducing ambiguities in the correct bunch-crossing assignment. Together, the three systems contain approximately $25\,000\,\mathrm{m}^2$ of active detection planes, and nearly 10^6 electronic channels. Figure 3.31 depicts the layout of the muon detectors and their η coverage.

The DT system consists of 250 chambers inside the magnet return yoke. They are arranged in 4 stations — concentric cylindrical layers interleaved with the magnet return yoke at radii of approximately $r = 4.0\,\mathrm{m}$, $4.9\,\mathrm{m}$, $5.9\,\mathrm{m}$ and $7.0\,\mathrm{m}$ from the beam.

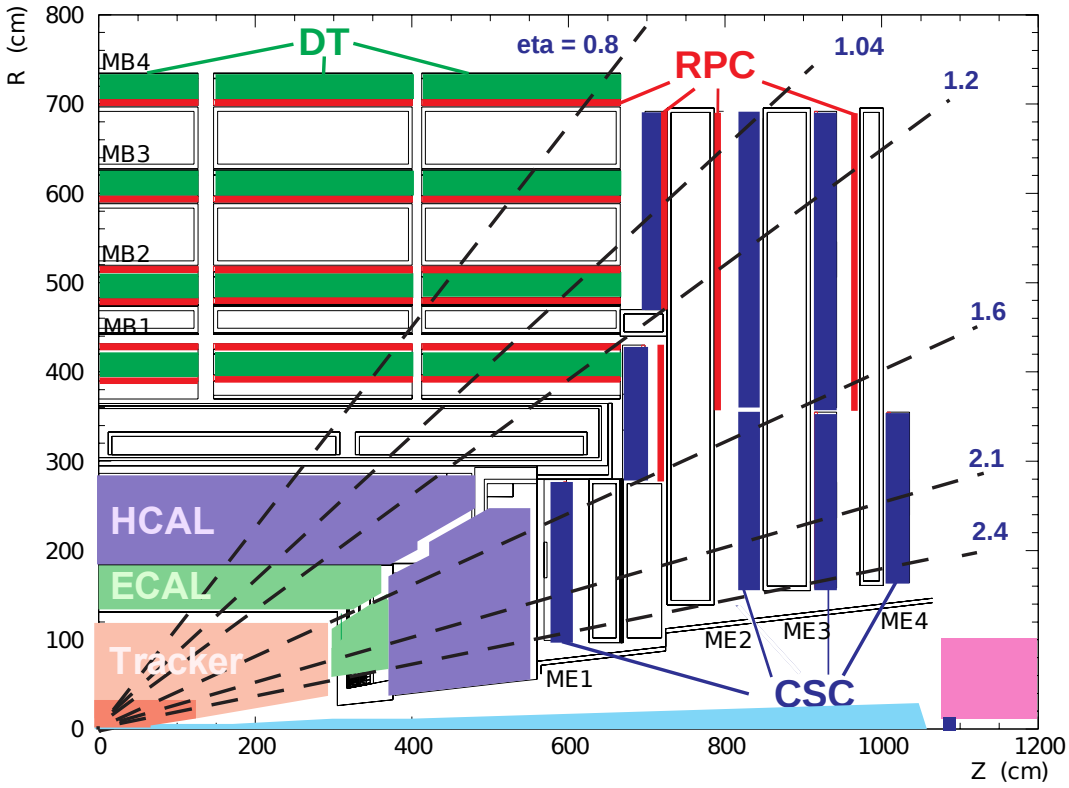

Figure 3.31: The longitudinal sectional diagram of a upper-right quarter of the muon system with the locations of the drift tubes (DT), resistive plate chambers (RPC), and cathode strip chambers (CSC) [91].

Along the z direction, they are segmented into 5 wheels each spanning approximately 2.7 m, and along the ϕ direction into 12 sectors, each covering an azimuthal angle of $\Delta\phi = 30°$. To avoid gaps in the coverage, the chambers are staggered among the different stations. Figure 3.32 shows a layout of the drift tube chambers for one of the 5 wheels.

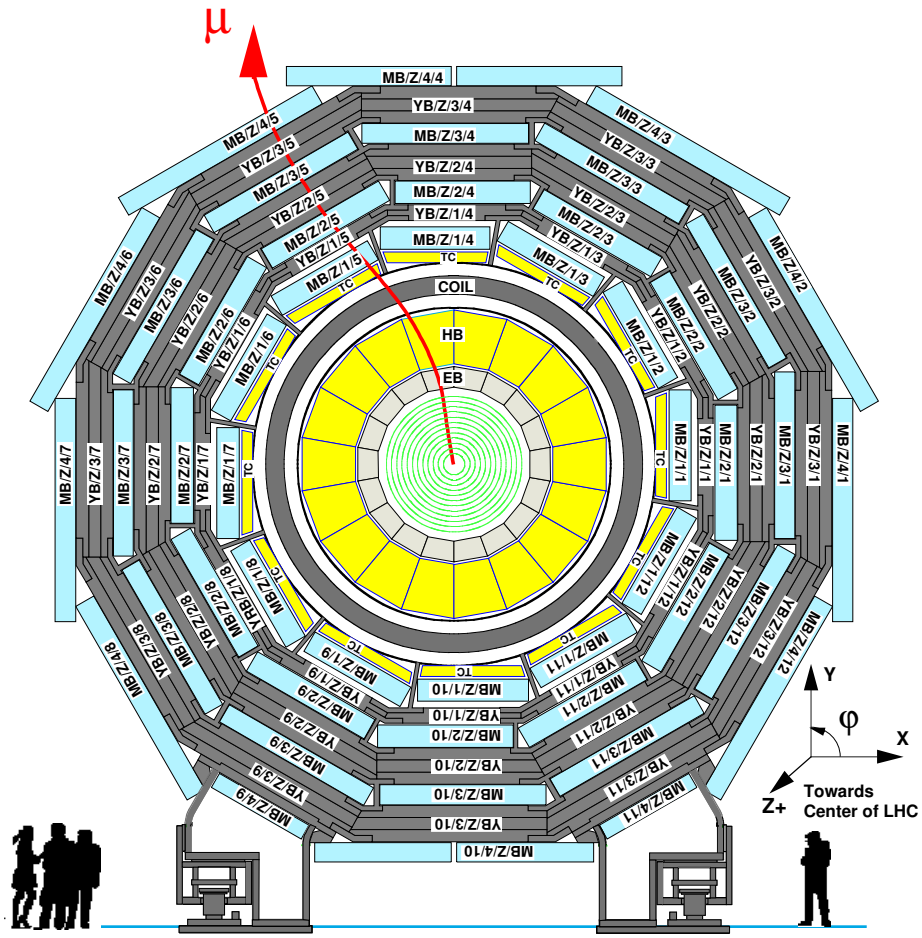

Figure 3.32: Layout of the CMS barrel muon drift-tube chambers for one of the 5 wheels. The layout of the other wheels is identical with the exception of wheels -1 and $+1$ which have shorter chambers in two sectors to allow for cryogenic chimneys of the solenoid [67].

The CSC system consists of 468 chambers in the 2 endcaps covering a region of $0.9 < |\eta| < 2.4$. Their position resolution is coarser than for the DTs but they are fast, finely segmented and radiation hard.

Figure 3.33 shows the muon momentum resolution as a function of the momentum measured by the inner tracking system only, the muon system only, and the full system including the combination of both. The precision of the measurement is fully dominated by the inner tracking system up to approximately $p = 200\,\text{GeV}$. For higher momenta, the muon system starts contributing significantly to the overall precision.

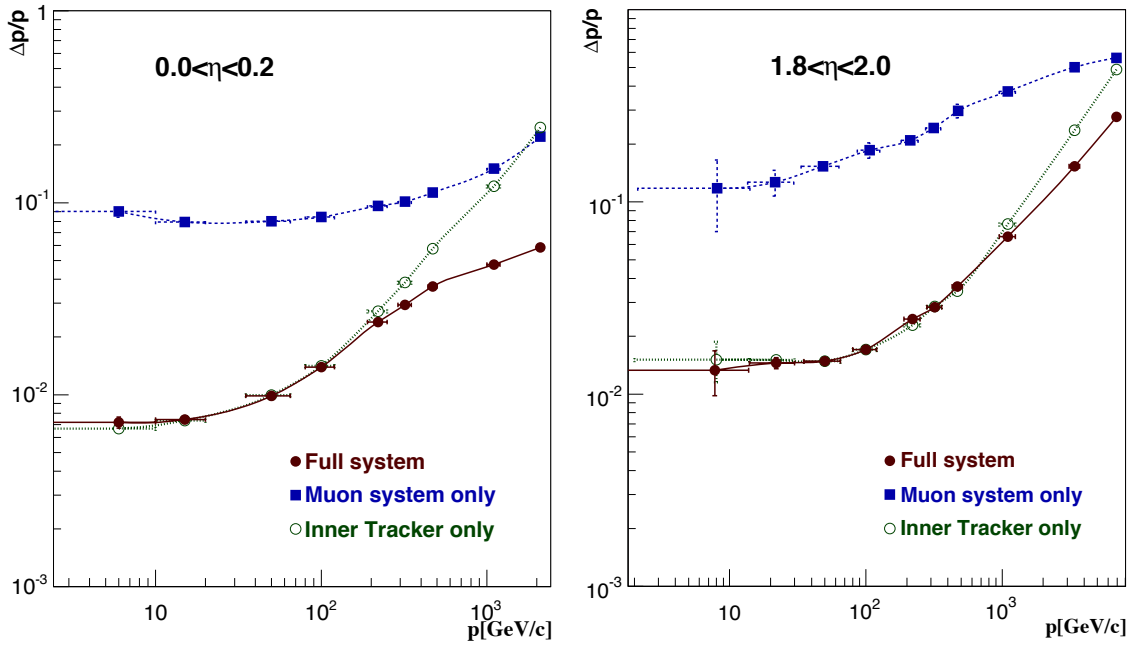

Figure 3.33: Muon momentum resolution as a function of p measured by the inner tracking system only (green circles), the muon system only (blue solid squares), and the full system including the combination of both (solid red circles). Left panel shows the performance in the region $0 < |\eta| < 0.2$, right panel in the region $1.8 < |\eta| < 2.0$. (right) [66].

Chapter 4

Reconstruction and Identification

The goal of this analysis is to measure the production rate of $Z\gamma \to \mu^+\mu^-\gamma$ and $Z\gamma \to e^+e^-\gamma$ events. The strongest discrimination of these events from the backgrounds comes from the identification of electrons, muons and photons. In this chapter, we discuss how the final state particles in these events are reconstructed and identified.

A particle traversing CMS typically produces a signal in multiple channels of several detector subsystems. To compare measurements with theory we need to make conclusions about the underlying physical processes that lead to its production. The question to ask is: "What particle is it, where was it produced, and with what momentum?" To combine all the relevant information from all channels of all subsystems in an optimal way, a set of standard algorithms is employed. These are organized in several steps.

First, the *local reconstruction* collects the relevant information for the individual subsystems. For instance, tracks are reconstructed from individual hits in the tracker, electromagnetic clusters and superclusters are reconstructed from ECAL deposits in individual crystals, etc.

Then, the *global reconstruction* combines information from multiple subsystems and associates it with particle candidates of specific types. For example, electron candidates are reconstructed from tracks and ECAL superclusters.

Finally, the *particle identification* selects candidates of a certain type with high efficiency while rejecting most candidates due to false signals, e.g. the electron identification selects electrons coming from $Z \to e^+e^-$ decays while suppressing most of

the electron candidates due to quarks and gluons hadronizing into jets with a high electromagnetic fraction.

4.1 Tracks

The goal of the CMS track reconstruction [66, 78, 92] is to collect all the signals (*hits*) due to a single charged particle and combine them in an estimate of the track parameters and their incertainties including the impact parameter, charge, and momentum at the interaction vertex. The challenge of the track reconstruction is to do this with high efficiency and low fake rate, while meeting the physics goals of CMS [67, 73] at the per-bunch-crossing track multiplicity corresponding to the design luminosity and bunch intensity of the LHC [56].

Searches for heavy dilepton resonances require the reconstruction of hard tracks with transverse momenta of up to $p_{\mathrm{T}} = 1\,\mathrm{TeV}$. Simultaneously, hadron production rate measurements and optimal missing-transverse-energy and jet-energy resolutions require an efficient reconstruction of very soft tracks with transverse momenta of down to $p_{\mathrm{T}} \approx 100\,\mathrm{MeV}$ [92]. Also, precise estimates of the interaction vertex locations and b-jet identification require excellent resolutions on the transverse and longitudinal impact parameters. Finally, the reconstruction of certain processes, like the 3-prong tau decay, require the ability to resolve very close tracks.

At the LHC design luminosity of $\mathscr{L} = 10^{34}\,\mathrm{cm}^{-2}\,\mathrm{s}^{-1}$, multiple inelastic pp collisions will produce on the order of 1000 charged particles at each bunch crossing every 25 ns. The CMS tracking must be able to process the bunch crossing events at sufficient rates at both the offline reconstruction and the HLT trigger, given the CPU resources available.

The dedicated piece of software used for track reconstruction by CMS is called the *Combinatorial Track Finder* (CTF) [93]. The CTF runs in an iterative fashion. Early iterations search for easier-to-reconstruct tracks (relatively harder p_{T}, originating near the interaction region). After each iteration, the CTF removes hits assigned to the reconstructed tracks. This reduces the combinatorial complexity so that further

iterations can search for harder-to-reconstruct tracks (relatively softer p_{T}, originating from displaced vertices).

The CTF starts by obtaining parameters for initial track candidates, *seeds*, using triplets of tracker hits near the beam pipe, or pairs of tracker hits near the beam pipe together with a third constraint from the known position of a vertex or the nominal beam spot [94].

The CTF then extrapolates the seeds outward along their expected trajectories of charged particles in a magnetic field. At each additional detector surface, it searches for hits consistent with the current track estimate employing a technique known as the Kálmán filter [95–97]. This takes into account material effects of multiple scattering and energy losses, as well as the current track parameters and their uncertainties, allowing for branching of individual tracks into multiple track hypotheses. The CTF assigns compatible hits to the current track, and updates accordingly the track parameters and their uncertainties at the current detector layer. The search stops when it reaches the limit of the tracker fiducial volume, or the number of missing expected hits reaches a specified maximum, or the transverse momentum drops below a specified minimum. Tracks with too few hits are then discarded.

Starting with the collection of the found hits excluding the seed hits, the search is then repeated in the opposite — inward — direction. This enables finding additional hits in the seeding layers and other layers closer to the interaction vertex.

This track finding algorithm may lead to duplicate track candidates resulting from a passage of a single charged particle, as well as incidental "fake" track candidates resulting from ambiguous hit configurations corresponding to no actual particles. To reduce these effects, the CTF discards tracks that share too many hits while having a low total number of hits or a high fit χ^2 value. This concludes the track search, yielding a collection of track candidates and their associated hits.

In the next step, the CTF improves the estimates of the track parameters by a Kálmán filter and smoother. It refits the tracks using all available hits. Compared to the track finding, this avoids possible biases from the hit selection during the seeding stage. Similarly to the track finding, the track fitting step accounts for material

effects, namely multiple scattering and energy losses. However, in contrast to the track finding, it uses a *Runge-Kutta propagator* [98] to account for the inhomogeneity of the magnetic field by numerically solving the equations of motion.

Due to the sequential nature of Kálmán's algorithm, the fit is performed twice. First, it propagates the track from the inside out (the Kálmán filter), then from the outside in (the Kálmán smoother). Both fits yield track parameters at each detector layer using the information from the previous layers. Their average at each layer then optimally combines the information from all the available layers.

Finally, the CTF selects a subset of track candidates to reduce the fraction of "fakes." It uses the following quantities to define quality criteria that depend on the track p_{T} and η:

- the number of layers with at least one associated hit,
- the number of layers with at least one associated "3D" hit constraining all three spatial coordinates, i.e. hits in the pixel tracker or "matched hits" in the strip tracker,
- the number of layers with missing expected hits surrounded from both sides by layers that do contain associated hits,
- the normalized χ^2 of the track fit: the ratio χ^2/n_{dof} of the χ^2 and the number of degrees of freedom n_{dof} of the fit,
- the transverse $|d_0|/\delta d_0$ and longitudinal $|z_0|/\delta z_0$ impact parameter significances, and
- the alternative transverse $|d_0|/\sigma_{d_0}$ and longitudinal $|z_0|/\sigma_{z_0}$ impact parameter significances,

where d_0 and z_0 are the transverse and longitudinal impact parameters, δd_0 and δz_0 their uncertainties, and σ_{d_0} and σ_{z_0} their alternative uncertainties. For the purposes of the track selection, d_0 is defined as the distance from the beam spot in the plane

transverse to the beam line (x-y), and z_0 as the distance along the beam line (z-axis) from the closest pixel primary vertex, if present, or the beam spot, otherwise. δd_0 and δz_0 come from the covariance matrix of the track fit, while σ_{d_0} and σ_{z_0} are parametrized as functions of the track p_{T}. Tracks that fail the selection are discarded, and their associated hits are reused in the next iteration.

In each iteration, the CTF repeats the above four steps: the seed generation, the track search, the track fit, and the track selection. It performs six iteration passes in total. Individual CTF iterations differ mainly in the requirements on the seed-generation hits, and the criteria on the track selection, as well as the collection of available hits that contains only those that have not been associated with any tracks yet.

In addition to the general CMS tracking, the same algorithm with different configurations is used to produce other specialized track collections. These include the tracks reconstructed at the *High Level Trigger* (HLT), electron tracks and tracks in the muon systems. The HLT configuration emphasizes speed over precision. For example, it stops the track finding sooner, when enough hits have been found. We discuss the specialized muon and electron tracking below in the respective Sections 4.7 and 4.6.

4.2 Event Vertices

The goal of the event vertex reconstruction is to partition the reconstructed tracks into groups, each originating from a single inelastic pp collision, and to estimate the spatial coordinates of the corresponding interactions. It is organized into three steps: first, the selection of the tracks to be used, second, the clustering of the selected tracks according to the z-coordinate of the point of their closest approach to the beam spot, and third, the fitting of the vertex position.

The purpose of the first step, the track selection, is to remove tracks that are displaced and not prompt (secondary decays). The tracks are required to pass a set of criteria based on the significance of their transverse impact parameter with respect

to the beam spot, the number of pixel and strip hits, and the value of the normalized χ^2 of their track fit.

In 2010, the number of pileup interactions per bunch crossing was relatively low. A simple gap algorithm [99] was sufficient to assign tracks to vertices since the individual vertices were relatively well separated along the beam direction (z-axis) compared to the longitudinal impact parameter uncertainties of the tracks. The tracks were sorted according to the z-coordinates of the points of their closest approach to the beam spot. When a distance in the z-coordinates between any two closest tracks reached a value greater than a given large gap, it defined a boundary separating the tracks into groups belonging to different vertices.

Thanks to the great performance of the LHC in delivering higher instantaneous luminosities, the number of pileup interactions increased significantly in 2011. This required the introduction of a different, more sophisticated, algorithm for the track clustering: *deterministic annealing* (DA) [100]. Similarly to the gap algorithm, it is based on a clustering according to the z-coordinate of the points of their closest approach to the nominal beam spot position, as defined in the next section. It is inspired by an analogy to statistical mechanics. The collection of tracks is treated as a thermodynamical system. The assignment of the tracks to vertices is not unique. It is 'soft' with each track i at z_i^{T} with an uncertainty σ_i having a certain probability p_{ik} of originating from a given vertex k at z_k^{V}. The χ^2 pull of the distance of the track i from the vertex k along the z-axis plays the role of the potential energy $E_{ik} = (z_i^{\mathrm{T}} - z_k^{\mathrm{V}})^2/\sigma_i^2$. The vertex locations z_k^{V} and weights w_k at a given "temperature" T are given by minimizing what is the equivalent of the system's free energy in statistical thermodynamics (using natural units in which the Boltzmann constant is $k = 1$). It is defined as [78]:

$$F = -T \sum_i p_i \log \sum_k w_k \mathrm{e}^{-E_{ik}/T}, \tag{4.1}$$

where the p_i are the track weights reflecting their compatibility with the beam spot and the w_k are the vertex weights. The track-to-vertex assignment probabilities p_{ik}

are then given by:

$$p_{ik} = \frac{w_k \mathrm{e}^{-E_{ik}/T}}{\sum_l w_l \mathrm{e}^{-E_{il}/T}}. \tag{4.2}$$

The track-to-vertex assignments are "soft" in the sense that a track may be compatible with multiple vertices. They become "hard" in the limit $T \to 0$ at which each track corresponds to exactly one vertex $z_i^{\mathrm{T}} = z_k^{\mathrm{V}}$ and there is as many vertices as tracks.

The DA algorithm starts at a very high T with a single vertex prototype $k = 1$ and equal track assignments $p_{ik} = 1$ all compatible with the vertex. As the temperature decreases, the minimum of F (4.1) reaches a saddle point at a critical temperature given by:

$$T_c^k = 2 \frac{\sum_i \frac{p_i p_{ik}}{\sigma_i^2} E_{ik}}{\sum_i \frac{p_i p_{ik}}{\sigma_i^2}}. \tag{4.3}$$

At that temperature, the single vertex is split, a new vertex prototype is added and the vertex positions z_k^{V} and vertex weights ρ_k are re-optimized.

The starting temperature is chosen to be above the first critical temperature calculated for $p_{ik} = \rho_k = 1$. It is decreased at every step by a cooling factor of 0.6 until a minimal temperature of $T_{\mathrm{min}} = 4$ is reached. This value of minimal temperature corresponds to an optimal compromise between the power to resolve two nearby vertices and the danger of accidentally splitting vertices due to outliers in the measurements of the track z_i^{T}.

To assign the tracks uniquely to vertices, the annealing is then continued down to $T = 1$ without further vertex splitting. During this cool-down, an outlier rejection is used to reduce the bias from tracks that are displaced by more than 4-σ from the nearest vertex candidate. This completes the clustering of the selected tracks by the DA algorithm.

Finally, an *adaptive vertex fitter* [101] is used to estimate the vertex parameters for vertex prototypes with at least two tracks. These include:

- the vertex position in all three dimensions,

- the vertex fit covariance matrix,
- the weights $\omega_i \in [0, 1]$ of the associated tracks describing their statistical compatibility with the vertex (0 meaning incompatible, 1 meaning perfectly compatible), and
- the *number of degrees of freedom* defined as:

$$n_{\text{dof}} = -3 + 2 \sum_{i}^{n_{\text{tracks}}} \omega_i, \tag{4.4}$$

  where the sum runs over all tracks assigned to the vertex and ω_i is the weight of the i^{th} track.

The number of degrees of freedom is a good estimator of the total number of tracks compatible with the interaction region and is therefore a useful quantity to identify events with real proton-proton inelastic collisions.

4.3 Beam Spot

The beam spot (BS) is the luminous region where pp collisions occur. It is evaluated for time periods corresponding to up to 60 individual *luminosity sections*. The so-called luminosity sections (LSs) are time intervals of 26 s length into which the CMS data taking is divided.

The BS is a property of the LHC beam while the vertex position is specific to individual events. The BS is important since it is a good approximation of the vertex, it is known already before the event reconstruction, and its determination is robust. It is therefore used, for example, during the triggering for track identification.

The BS has approximately a 3-dimensional (3D) multivariate Gaussian probability density. It is characterized by its location and width along the x, y, and z directions.

There are two independent methods used to determine the BS location (x_0, y_0, z_0). The *likelihood fit* maximizes the likelihood of the Gaussian density with respect to the 3D locations of the reconstructed vertices. The d_0-ϕ *fit* exploits a known cor-

relation in the perturbations of the track transverse impact parameter d_0 and the track azimuthal angle ϕ due to small displacements of the BS location. The d_0-ϕ fit iteratively minimizes the χ^2 of a large number of tracks from multiple collisions [102]. The advantage of the d_0-ϕ fit is that it does not require the reconstruction of vertices. Both the likelihood and the d_0-ϕ fit methods yield consistent results.

There are also two independent methods used to determine the BS width parameters σ_x, σ_y and σ_z. The same likelihood fit used for the BS location returns also the BS width parameters. The second method infers them from the measurement of the "event-by-event correlations between the transverse impact parameters of two tracks from the primary event vertex [78]." Averaged over an LHC fill, both methods yield compatible results within a few µm [99].

4.4 ECAL Superclusters

The primary purpose of the ECAL *superclusters* is to identify and characterize the sets of energy deposits in the CMS ECAL due to single prompt energetic electrons, positrons and photons (e/γ). The superclusters group together relevant crystals and their deposits and combine the information to estimate the location in the ECAL and hence the direction as well as the total energy of the incident particle. The spatial topology of the individual crystal deposits enables further inferences on the size of the estimated uncertainties and the incident particle's identity. Superclusters are used for triggering, and in the reconstruction and identification of electrons and photons.

Due to the strong magnetic field and presence of the tracker material, electrons and positrons from pp collisions tend to radiate bremsstrahlung photons before they reach the ECAL. Photons, on the other hand, tend to convert into electron-positron pairs. Therefore, superclusters consist of one or more spatially contiguous *clusters* of ECAL crystals. These clusters correspond to individual e/γ particles entering the ECAL. They can be both *prompt*, originating at the event vertex, and *non-prompt* or *secondary*, originating from showering and conversions inside of the tracker volume. Clusters composing a supercluster form a typical footprint spreading along the ϕ

direction, due to the bending of electron and positron trajectories in the magnetic field. We refer to the most energetic cluster of a supercluster as the *seed cluster*.

The supercluster reconstruction is organized into several steps. First, the *rec-hit reconstruction* converts detector signals to energy deposits in individual pre-shower (ES) channels and in individual barrel (EB) and endcap (EE) crystals, so-called *rec hits*. Then, the *clustering* identifies groups of crystals creating clusters, and groups of clusters creating superclusters. Finally, the location and energy of the so-formed superclusters is estimated taking into account associated deposits in the ES in the EE.

The supercluster reconstruction starts with the ECAL rec-hit reconstruction. The same 12-bit analogue-to-digital converters (ADC) sample the signals from the silicon sensors of the ES and the signals from the photodetectors of the EB and the EE at a rate of 40 MHz. Three consecutive samples (*time slices*) are used for the rec-hit energy estimate in ES, while ten samples are used in EB and EE. The readout pipeline is delayed such that the signal pulse should begin from the second sample in ES and from the fourth sample in EB and EE. This allows for pedestal estimation from the first sample in the ES and from the first three samples in the EB and EE. In all ECAL subdetectors, the pulse amplitude A in ADC counts is then reconstructed as a linear combination of the individual sample counts S_j [103]:

$$A = \sum_j w_j S_j,$$

where j runs over the time slices (three in the ES, ten in the EB and EE), and the w_j are the weights, which are optimized by using the measured pulse shapes averaged separately in the EB, the EE and the ES. For each individual channel i, the amplitude A_i is then multiplied by an ADC-to-GeV conversion factor G_d and an intercalibration constant C_i. Here, d labels the subdetectors EB, EE and ES. The intercalibration constants are defined so as to uniformize the response of the individual channels, while giving unity on average.

The clustering starts by identifying *seed crystals* as maxima in the spatial array

of individual crystal energy deposits. The clusters and superclusters are then built around these seeds. In the absence of the magnetic field and the tracker material, the best energy resolution is obtained by clustering a 5×5 fixed-size matrix of crystals around the seed crystal. This was shown in tests with beams of highly energetic electrons under such ideal conditions [104]. In CMS however, the situation is more challenging. To take into account the spread of the secondary e/γ particles due to the bending of the CMS magnetic field, the cluster sizes are dynamically adjusted supercluster-by-supercluster rather than remaining fixed. There are two different clustering algorithms used in CMS, one in the EB and one in the EE.

The *hybrid algorithm* clusters the crystals in the EB by searching along the ϕ direction for deposits of fixed width in η centered on the seed crystal.[1] "Dominoes" of 3×1 or 5×1 crystals in $\eta \times \phi$ are iteratively added to the supercluster if they pass a given energy threshold, until a given maximum distance from the seed crystal of N_{step} crystals along the ϕ is reached in both the positive and the negative directions, cf. Figures 4.1 and 4.2.

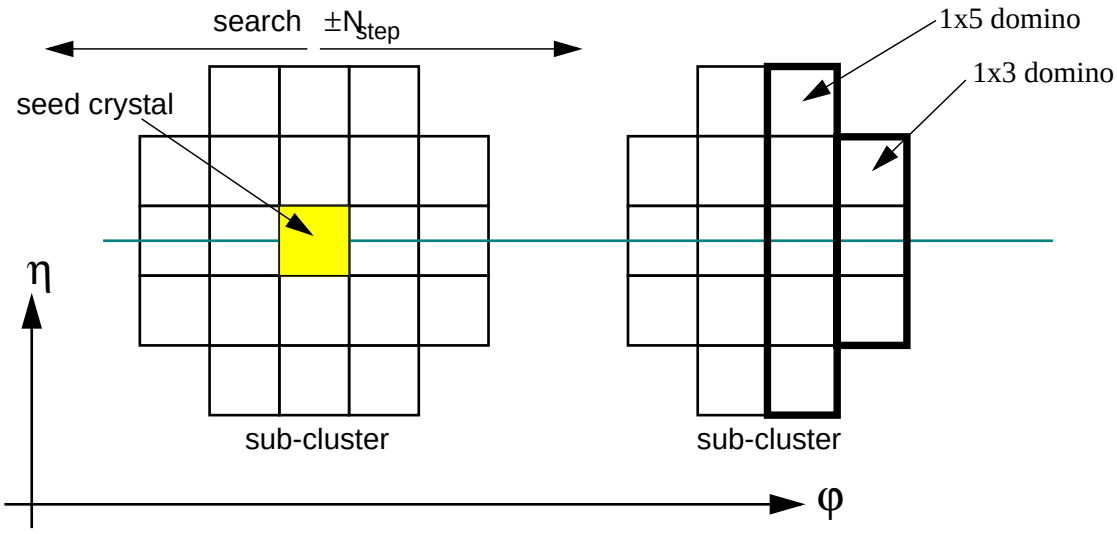

Figure 4.1: The ECAL hybrid clustering algorithm "dominoes" [105].

The arrangement of the EE crystals does not match the symmetry of magnetic field lines as nicely as in the EB. Therefore a different approach is closer to optimal in

[1] Hence the name "hybrid" as the supercluster size is fixed in η and dynamic in ϕ, so it is neither fixed nor dynamic, but something in between.

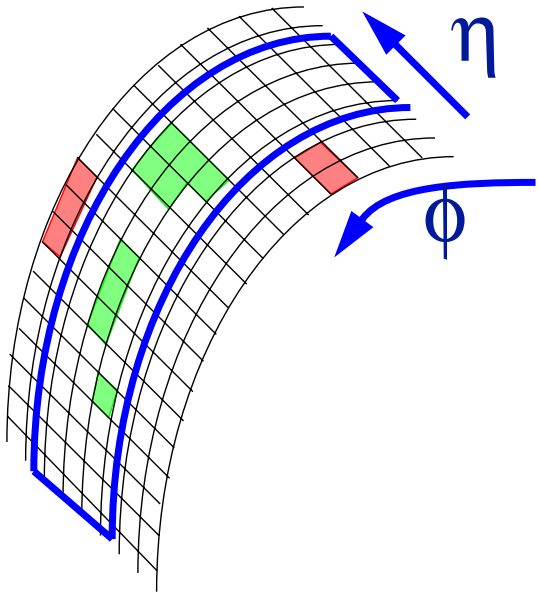

Figure 4.2: The ECAL hybrid clustering algorithm search path [105]. Green squares indicate clustered deposits, red squares unclustered deposits.

EE. The *multi*-5×5 *algorithm* clusters the crystals in the ECAL endcaps by iteratively merging regions of 5×5 crystals centered on the seeds and removing already-clustered crystals.

The supercluster position is estimated as an energy-weighted average over its crystals. A simple averaging is complicated by the following two aspects:

- The lateral (η-ϕ) location of the crystals varies along their depth (r) as they are arranged in a quasi-projective geometry and do not point to the nominal interaction point, see Figure 4.3. This is taken into account by estimating the crystal location at the average depth of the center of the shower $t_{\max}$. This depth depends logarithmically [106] on the shower energy. It also depends on the incident particle type: it is about one radiation length X_0 deeper for photons than for electrons and positrons[2].

- The energy deposition in the shower is non-uniform among the crystals. It falls off approximately exponentially [106] with the lateral distance from the

[2]In terms of technical implementation, the dependence on the particle type is ignored at this stage and all superclusters are treated as electron deposits. It is then taken into account during the photon reconstruction.

center of the shower. This is taken into account by applying weights based on the logarithms of the crystal energies $\log E_i$ rather than the crystal energies directly E_i.

The supercluster position x then reads [105]:

$$x = \frac{\sum_i w_i \cdot x_i}{\sum_i w_i},$$

where we sum over all supercluster crystals i at positions x_i, and the weights w_i are given by:

$$w_i = \max\left\{0,\ w_0 + \log\left(\frac{E_i}{\sum_i E_i}\right)\right\}.$$

Here, the parameter w_0 controls the smallest fraction of energy $E_i / \sum_i E_i$ that the crystal i must contribute to be taken into account for the position measurement. The default value of $w_0 = 4.2$ found by optimization corresponds to $E_i / \sum_i E_i \approx 1.5\,\%$ [105].

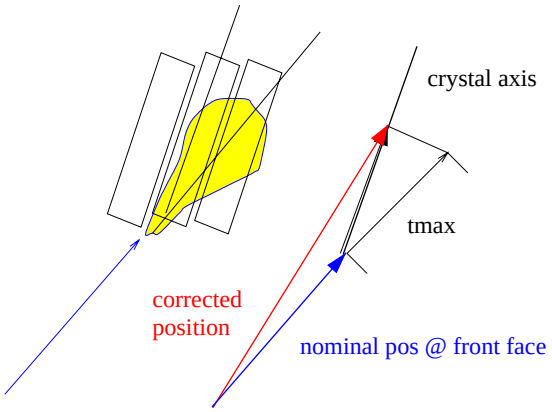

Figure 4.3: A diagram of the ECAL crystal quasi-projective geometry illustrating the impact of the crystal off-pointing with respect to the nominal interaction point on the dependence of its lateral position on the depth of the shower maximum $t_{\max}$ [105].

The supercluster energy is then estimated as:

$$E = F\left[G_d \sum_i S_i(t)\, C_i\, A_i + E_{\mathrm{ES}}\right]$$

where we sum over all crystals of the supercluster labeled by the index i. The factor F corrects for the η- and ϕ-dependent geometry and material effects, the factor $S_i(t)$ corrects for time-dependent radiation-induced channel response changes, the term E_{ES} stands for the eventual corresponding ES energy, and we continue our notation of G_d and C_i introduced above in the discussion of the rec-hit reconstruction.

Figure 4.4 illustrates the impact of the clustering and correction algorithms on the energy scale and resolution of superclusters produced by electrons from $\mathrm{Z} \to \mathrm{e}^+\mathrm{e}^-$ decays. The invariant mass of the electron-positron pair is calculated using the electron energies estimated in three (four in the endcaps) different ways with an increasing level of sophistication: (i) the energy of the 5×5 cyrstals centered on the seed crystal, (ii) the uncorrected supercluster energy, (iii) the sum of the uncorrected supercluster energy including the preshower energy (for the endcaps only), and (iv) the corrected supercluster energy. The intercalibration constants and laser-monitoring transparency corrections are applied in all cases. The peak in the invariant mass becomes narrower and shifts to higher value with each step, with the last step peaking at the known mass of the Z^0 bosons and having the smallest width. This illustrates that both the per-electron energy scale and the resolution in data improve with each step. This indicates that the superclustering algorithm successfully identifies energy deposits outside the 5×5 crystals and that the corrections compensate well for the energy lost in the material in front of the crystals, and the inter-crystal gaps. The width of the mass peak using the currected supercluster energy is consistent with the per-electron energy resolution shown in Figure 3.27, folded with the pseudorapidity spectrum of the electrons.

Similarly, Figure 4.5 illustrates the impact of the intercalibration and transparency corrections of the laser monitoring system. This time, the corrected supercluster energy of the electrons from the $\mathrm{Z} \to \mathrm{e}^+\mathrm{e}^-$ decays is used in all three cases; however, the energies of the individual crystals are evaluated differently.

For the purposes of triggering and e/γ reconstruction, it is useful to introduce the transverse energy of the supercluster E_{T}. It is a good approximation to the transverse momentum of the underlying e/γ particle. Its advantage is that it is known before the

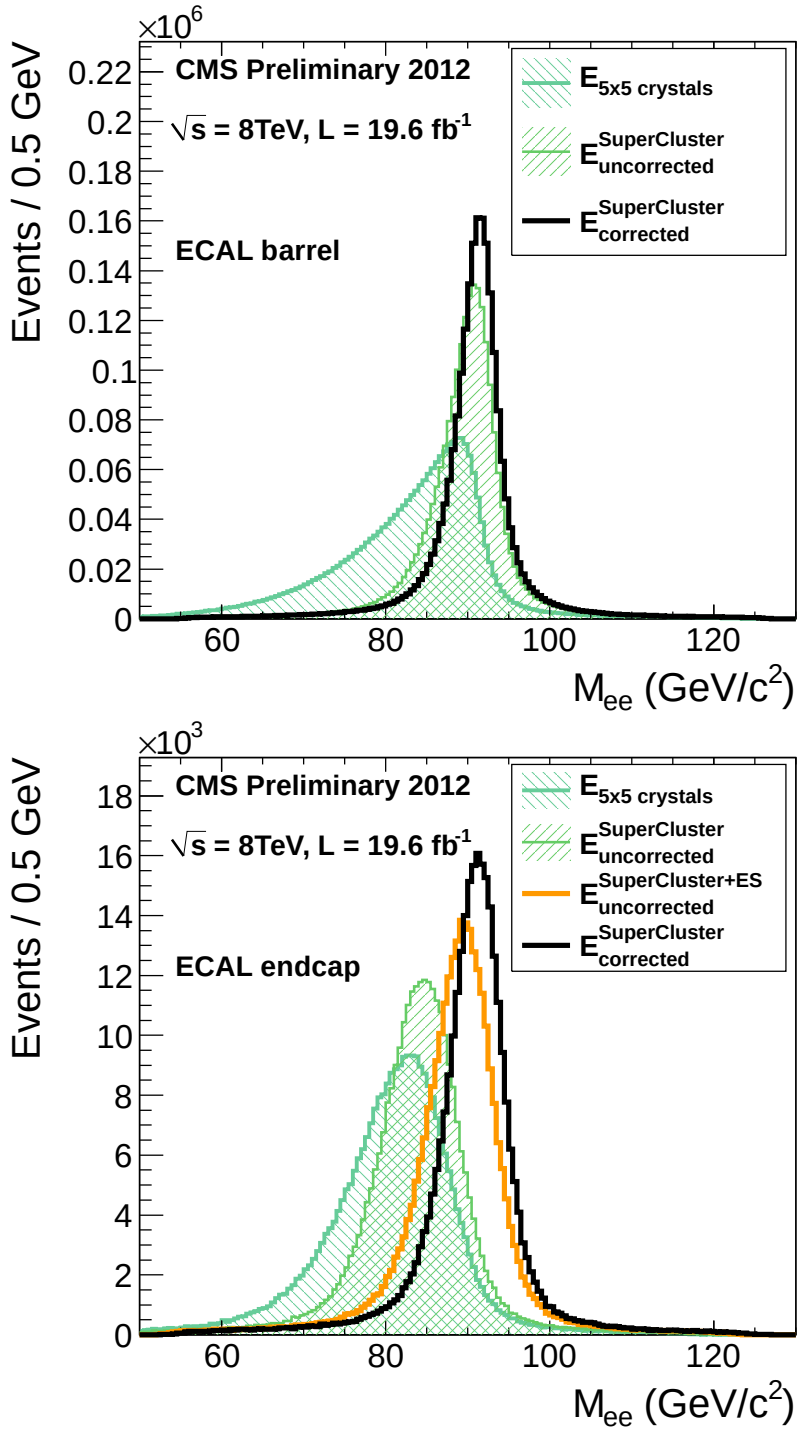

Figure 4.4: Impact of the ECAL clustering and energy correction algorithms on the energy scale and resolution of superclusters produced by electrons from $Z \to e^+e^-$ decays [82]. Top: ECAL barrel, bottom: ECAL endcaps.

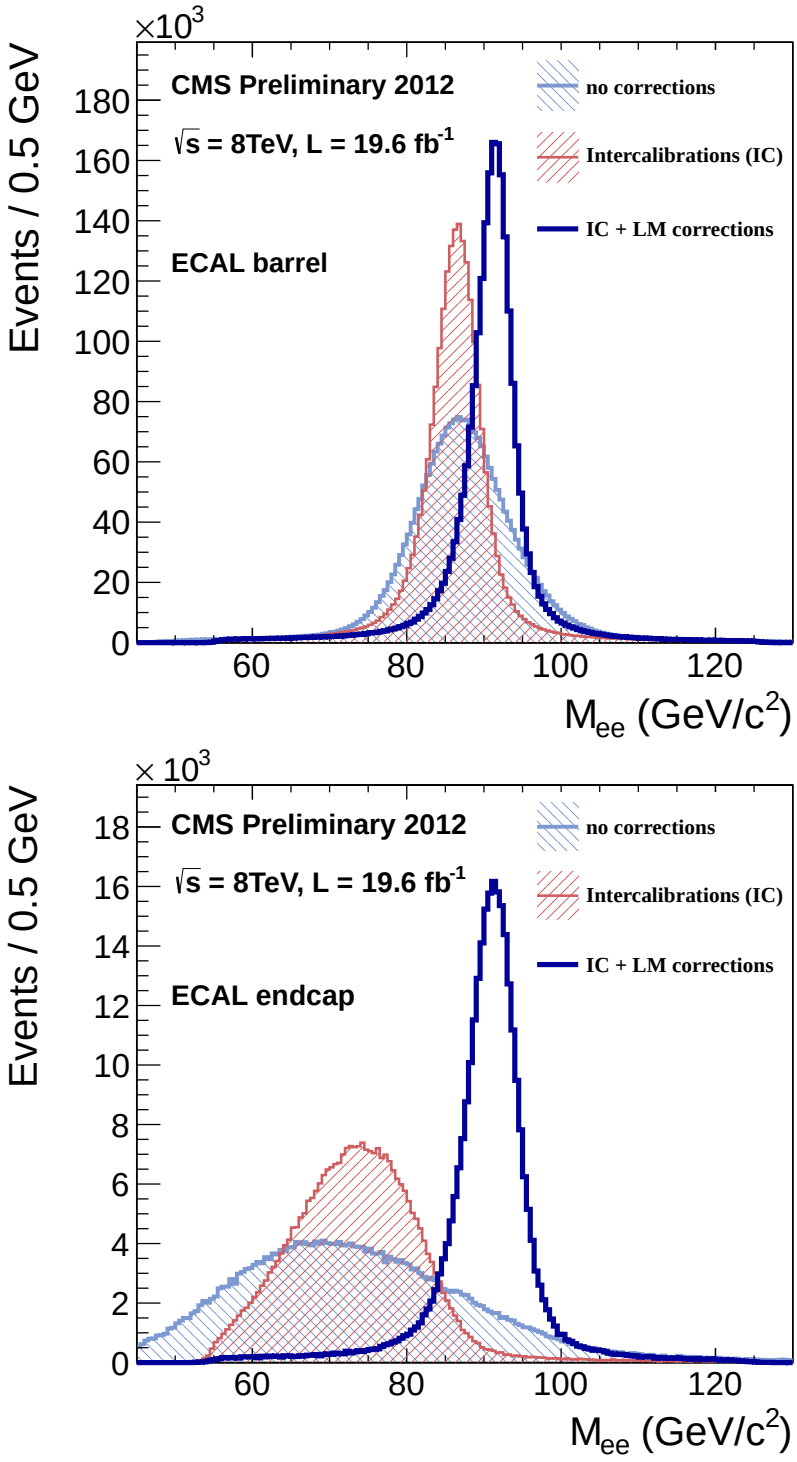

Figure 4.5: Impact of the ECAL intercalibration and transparency corrections of the laser monitoring system on the energy scale and resolution of superclusters produced by electrons from $Z \to e^+e^-$ decays [82]. Top: ECAL barrel, bottom: ECAL endcaps.

electron and photon reconstruction. It is estimated from the supercluster η position and energy E, assuming that it corresponds to a particle originating at the nominal interaction point:

$$E_{\mathrm{T}} = \frac{E}{\cosh \eta}.$$

Other variables characterizing the shower shape of the electromagnetic cluster are powerful in discriminating backgrounds coming from jet production. This analysis uses the following variables:

Shower width $\sigma_{i\eta i\eta}$, the log-energy weighted η-width of the electromagnetic cluster defined by:

$$\sigma^2_{i\eta i\eta} = \frac{\sum_i (\eta_i - \overline{\eta})^2 w_i}{\sum_i w_i}, \quad \text{with}$$
$$\overline{\eta} = \frac{\sum_i \eta_i w_i}{\sum_i w_i} \quad \text{and}$$
$$w_i = \max\left\{0,\ w_0 + \ln \frac{E_i}{\sum_j E_j}\right\}$$

where the summing index i labels ECAL crystals in the 5×5 matrix centered on the seed crystal, the η_i denotes the pseudorapidity of the crystal i in units of crystals, $\overline{\eta}$ the pseudorapidity of the 5×5 cluster, w_i the crystal log-weight, and the E_i the uncalibrated energy deposit in the crystal i. The "i" notation in $\sigma_{i\eta i\eta}$ stands for the crystals being used as the unit for the pseudorapidity. In the same way as for the supercluster position reconstruction, the parameter w_0 controls the smallest fraction of the energy $E_i / \sum_j E_j$ that the crystal i must contribute to be taken into account. Here, we use a value of $w_0 = 4.7$ corresponding to $E_i / \sum_j E_j \approx 0.9\%$. This value is chosen to optimize the background rejection power of the $\sigma_{i\eta i\eta}$ variable. It is greater than the value of $w_0 = 4.2$ used in the position reconstruction since the fluctuations are lower due to the following two differences. First, we only consider crystals in the 5×5 cluster around the seed crystal and, second, we effectively average over five crystals at the same η.

Comparisons of the cluster width spectra with data using superclusters from electrons in $Z \to e^+e^-$ events and photons from $Z \to \mu^+\mu^-\gamma$ events revealed that this variable was mismodeled in the simulation. To restore the agreement we correct this variable in simulation by subtracting a correction term derived using $Z \to e^+e^-$ events, cf. Figures 4.6, 4.7, 4.8 and 4.9. This correction term has the value of $\Delta\sigma_{i\eta i\eta} = 1.1 \times 10^{-4}$ in the barrel and $\Delta\sigma_{i\eta i\eta} = 1.6 \times 10^{-4}$ in the endcaps.

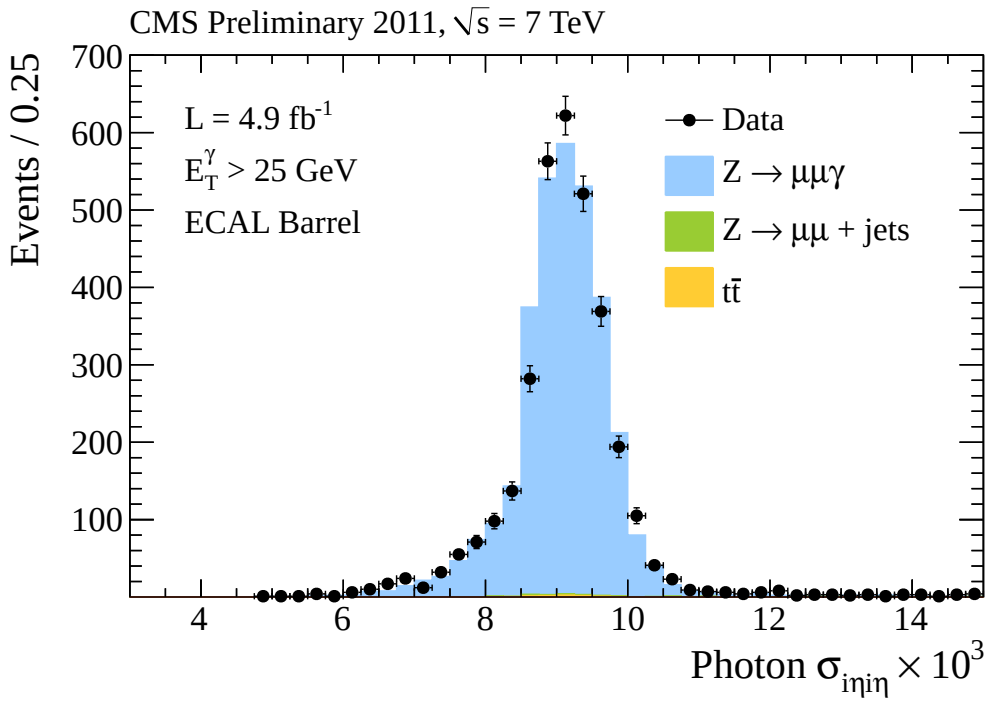

Figure 4.6: Shower width $\sigma_{i\eta i\eta}$ spectrum in data (black points with error bars) and simulation (blue histogram) for ECAL barrel superclusters from photons in $Z \to \mu^+\mu^-\gamma$ events. The green and orange histograms (which are hardly visible in the figure) represent the expected background contributions from $Z \to \mu^+\mu^- +$ jets and $t\bar{t}$ events, respectively.

Hadronic-over-electromagnetic ratio H/E, the ratio of the energy deposits in the HCAL inside of a $\Delta R = \sqrt{(\Delta\eta)^2 + (\Delta\phi)^2} \leq 0.15$ cone around the position of the supercluster and the clustered ECAL energy.

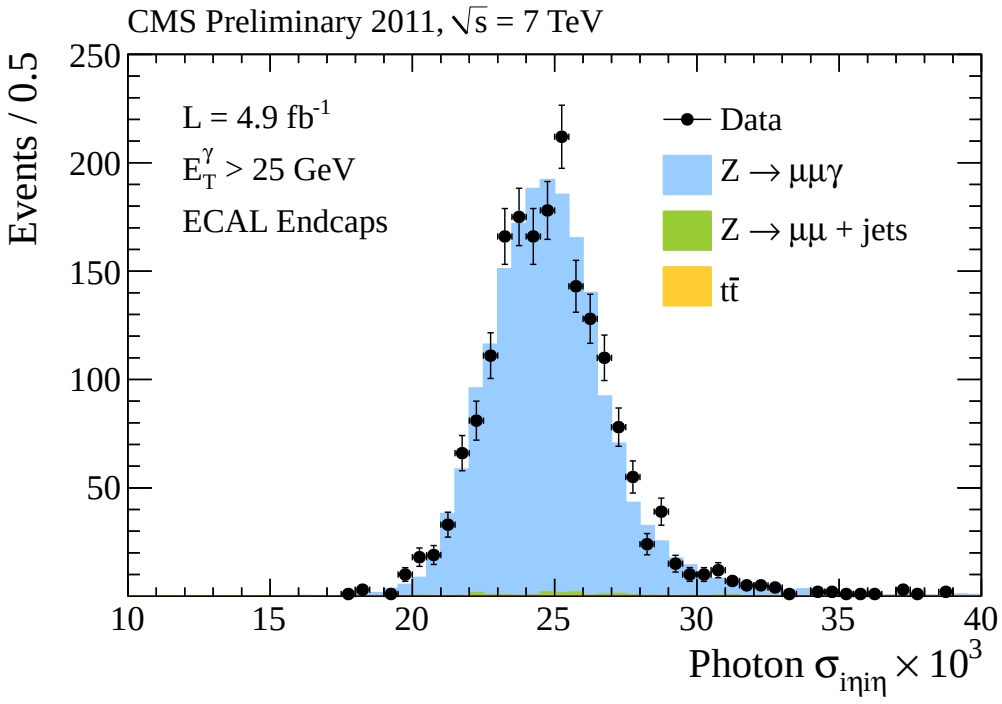

Figure 4.7: Shower width $\sigma_{i\eta i\eta}$ spectrum in data (black points with error bars) and simulation (blue histogram) for ECAL endcap superclusters from photons in $Z \to \mu^+\mu^-\gamma$ events. Green and orange histograms represent expected background contributions from $Z \to \mu^+\mu^-$ + jets and $t\bar{t}$ events, respectively.

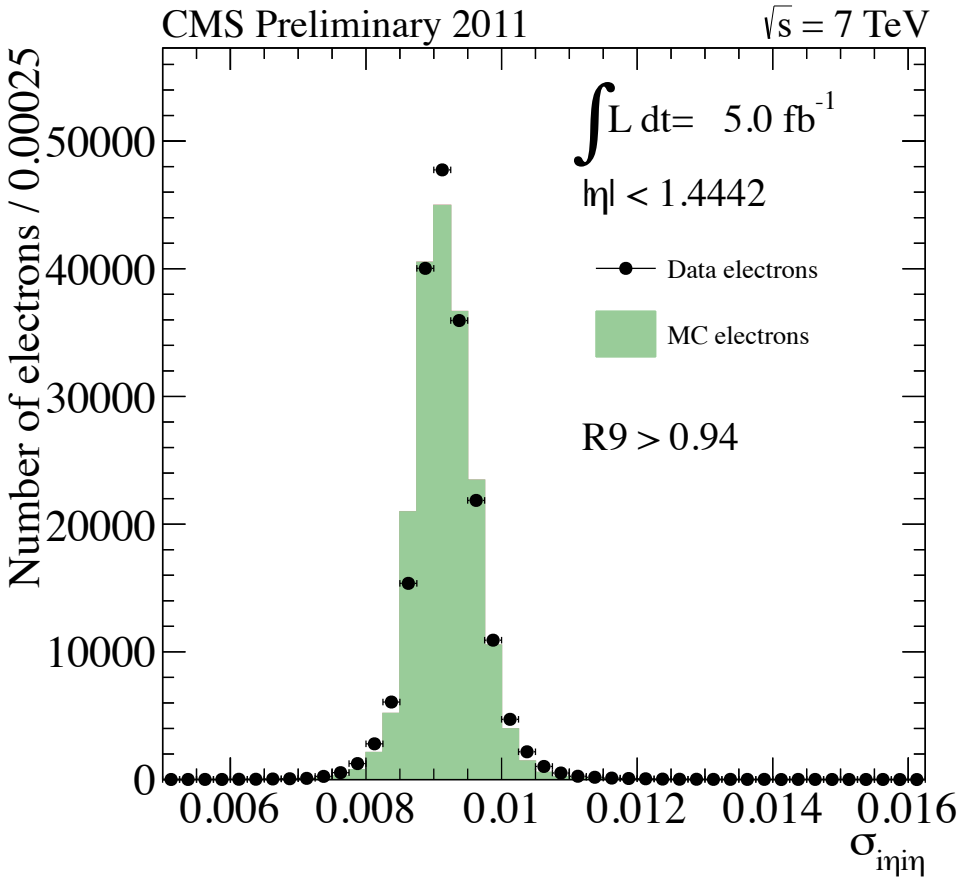

Figure 4.8: Shower width $\sigma_{i\eta i\eta}$ spectrum in data (black points with error bars) and simulation (green histogram) for ECAL barrel supercluster deposits from electrons in $Z \to e^+e^-$ events [107].

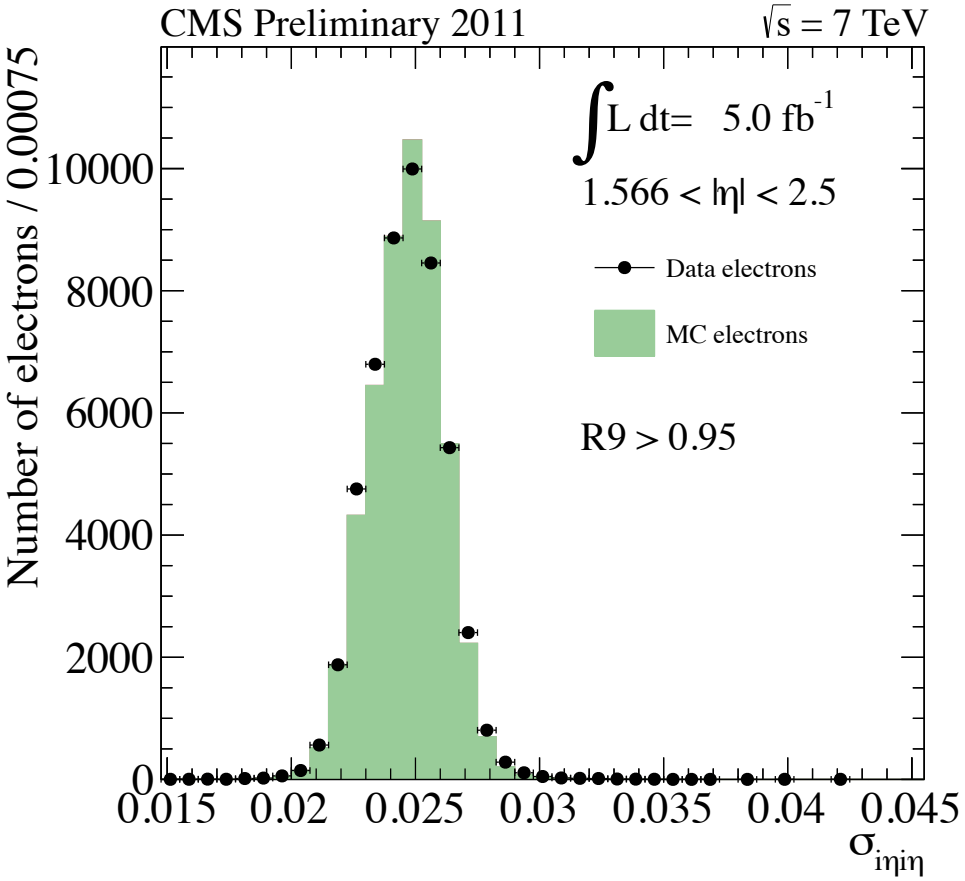

Figure 4.9: Shower width $\sigma_{i\eta i\eta}$ spectrum in data (black points with error bars) and simulation (green histogram) for ECAL endcap superclusters from electrons in $Z \to e^+e^-$ events [107].

4.5 Photons

Photon candidates are reconstructed as high energy superclusters in the ECAL. For each candidate, the magnitude of the photon energy is given by the total energy of its electromagnetic superclusters, and its direction is given by the position of the supercluster with respect to the primary event vertex. Such candidates correspond to a mixture of real signal photons and mis-identified background objects coming mainly from two sources: real isolated electrons and jets. Further photon identification criteria are driven by improving the signal-to-background ratio while keeping the signal efficiency high.

The hadronization process can sometimes fluctuate to yield a large fraction of the overall momentum being carried by neutral hadrons π^0 and/or η^0 decaying to a small number of highly energetic and collimated photons. Such jets can then lead to photon candidates with ECAL clusters whose characteristics are similar to primary isolated photons. On average, they tend to produce wider clusters in the η direction, and be less isolated from other jet constituents leaving deposits in the tracker, ECAL and HCAL subdetectors.

As for the primary isolated electrons, their footprint in the calorimeter is very similar to the one of a photon in terms of the cluster shape, isolation and the lack of HCAL deposits. However, unlike unconverted photons, they interact with the tracker material producing a number of hits and, with high probability, a reconstructed track. The presence, or lack of, such a track that is consistent with the electromagnetic cluster in the direction and magnitude of the momentum discriminates electrons and photons.

The photon identification consists of a list of criteria applied to a number of variables designed to capture the differences between the signal and background photon candidates:

Shower width $\sigma_{i\eta i\eta}$ as defined above for superclusters in Section 4.4,

Hadronic-over-electromagnetic ratio H/E, also as defined above for superclusters in Section 4.4,

Pixel seed match m_{ps}, the presence or absence of a pixel track of a momentum consistent in direction and magnitude with a prompt electron creating the given supercluster.

In addition to these identification variables, the following isolation variables used in this analysis enable us to further suppress the jet-fake background:

Photon tracker isolation I^{γ}_{TRK} , the scalar sum of the transverse momenta of tracks originating from the same primary vertex, with $p_{\text{T}} > 1.5$ GeV, within an annulus of $0.04 < \Delta R < 0.4$ around the photon momentum direction, and excluding a rectangular strip of $\Delta\eta \times \Delta\phi = 0.015 \times 0.4$ to protect the isolation sum from the inclusion of signal photon conversion tracks.

Photon ECAL isolation I^{γ}_{ECAL}, the scalar sum of transverse energy of ECAL crystal deposits within a $0.06 < \Delta R < 0.4$ annulus around the supercluster ECAL location, excluding a rectangular strip of $\Delta\eta \times \Delta\phi = 0.04 \times 0.4$ to protect the isolation sum from the inclusion of energy deposits of converted signal photons.

Photon HCAL isolation I^{γ}_{HCAL}, the scalar sum of the transverse energy of HCAL tower deposits within a $0.15 < \Delta R < 0.4$ annulus around the supercluster ECAL location.

To minimize the impact of the energy deposits from pileup events, the isolations are corrected using an average energy density per unit area ϱ_{FJ} as:

$$I^{\text{corr}} = I - \varrho_{\text{FJ}} \times A^{\text{eff}} \tag{4.5}$$

where A^{eff} is an effective area of the isolation cone specific to the isolation type, see Table 4.1.

4.6 Electrons

The CMS particle reconstruction process produces electron candidates from pairs of tracks and ECAL superclusters whose position and energies match well.

	Effective Area A^{eff}	
Isolation	Barrel	Endcaps
Tracker	0.0167	0.032
ECAL	0.183	0.090
HCAL	0.062	0.180

Table 4.1: Effective areas A^{eff} for the pileup correction of the photon isolation.

Due to their low mass, electrons radiate bremsstrahlung photons in the tracker material significantly more often than other charged particles. The default CTF track reconstruction algoritm assumes a Gaussian distribution for the fractional energy loss in the tracker material — not a suitable assumption for electrons. Their energy loss is better described by a distribution based on the Bethe-Heitler formula [108]. Therefore, the electron reconstruction uses tracks from a special collection produced with the same algorithm as the default tracks but with a different configuration that takes this into account. This is the so-called *Gaussian-sum filter* (GSF) technique [109,110]. It approximates the correct energy loss distribution by a sum of Gaussian distributions rather than a single Gaussian distribution. It also uses ECAL superclusters with E_{T} above a certain threshold to seed the tracks. Figures 4.10 and 4.11 show the electron reconstruction efficiency for the 2011A run period in the barrel and endcaps, respectively. Similarly, Figures 4.12 and 4.13 show it for the 2011B run period.

We use electron identification variables designed to select highly energetic prompt electrons from Z decays with high efficiency, and simultaneously suppresses background electron candidates due to prompt charged hadrons, non-prompt electrons from early photon conversions, non-prompt electrons from hadron decays possibly embedded in jets, and random coincidences of unrelated tracks and ECAL deposits. The identification variables can be organized into four groups: (i) ECAL supercluster variables, (ii) track-cluster compatibility variables, and (iii) conversion rejection variables [111].

Similarly to photons, for electron identification, we use the following variables defined above for ECAL superclusters in Section 4.4:

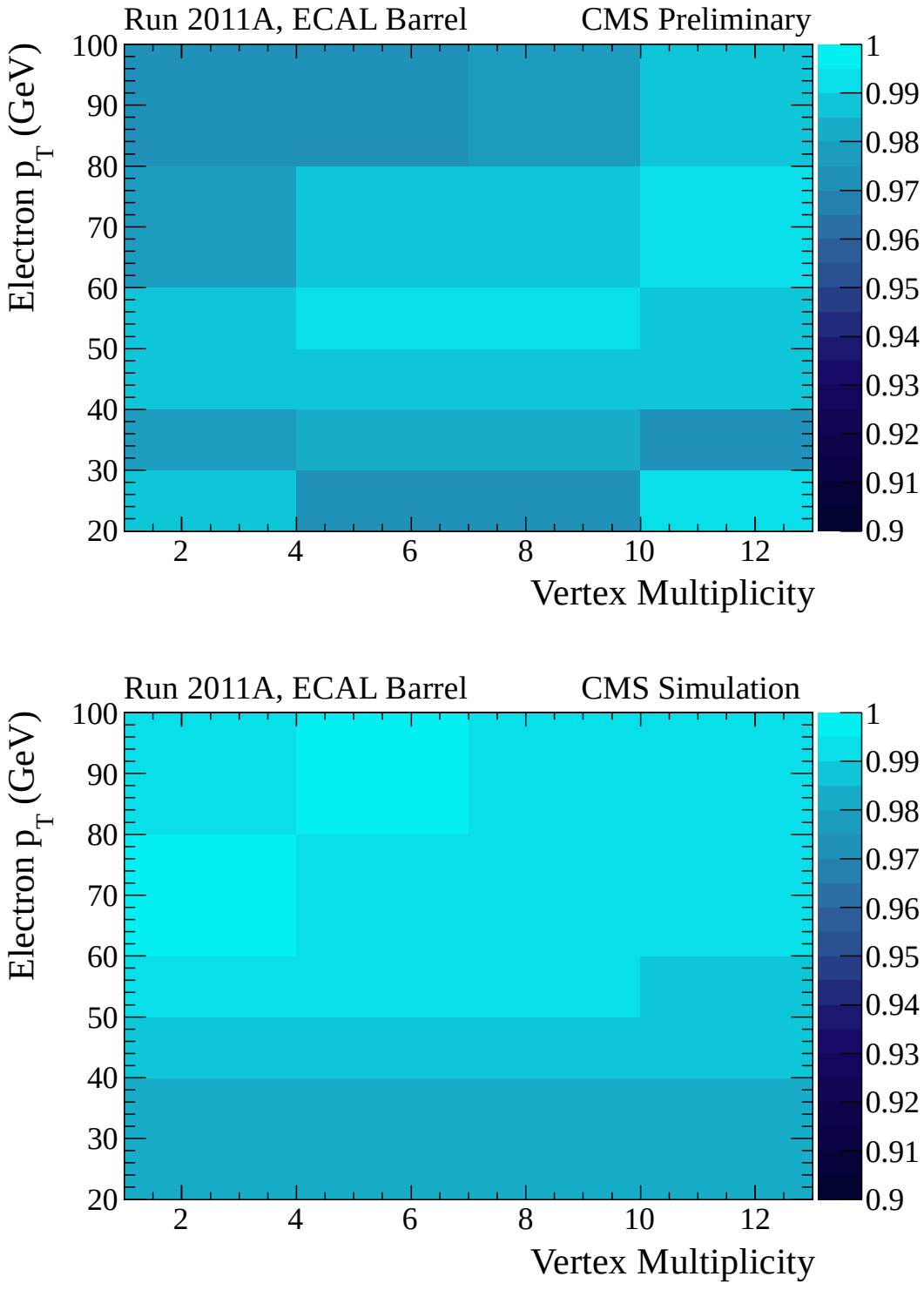

Figure 4.10: Electron reconstruction efficiency in the barrel for the 2011A run period [107]. Top: data, bottom: simulation.

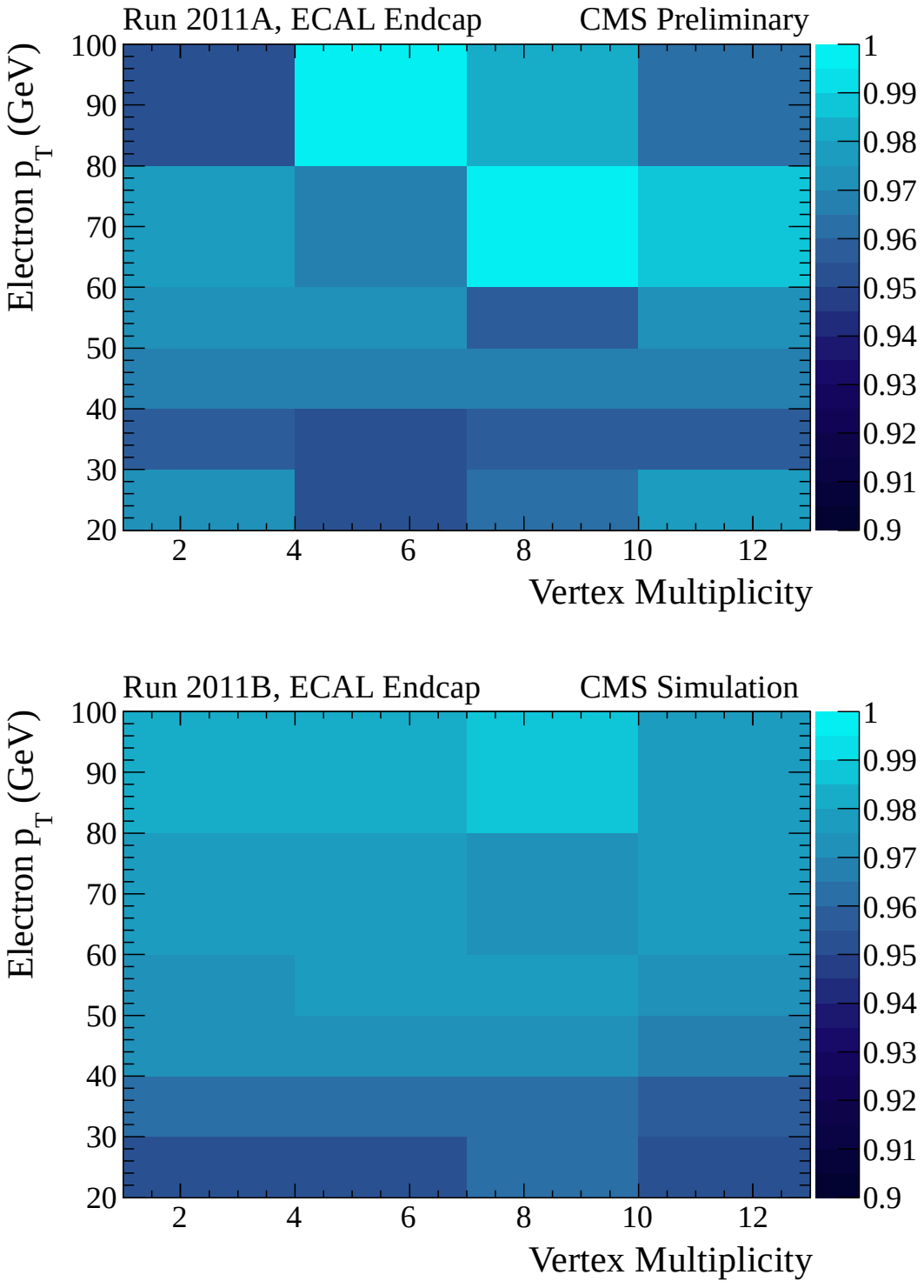

Figure 4.11: Electron reconstruction efficiency in the endcaps for the 2011A run period [107]. Top: data, bottom: simulation.

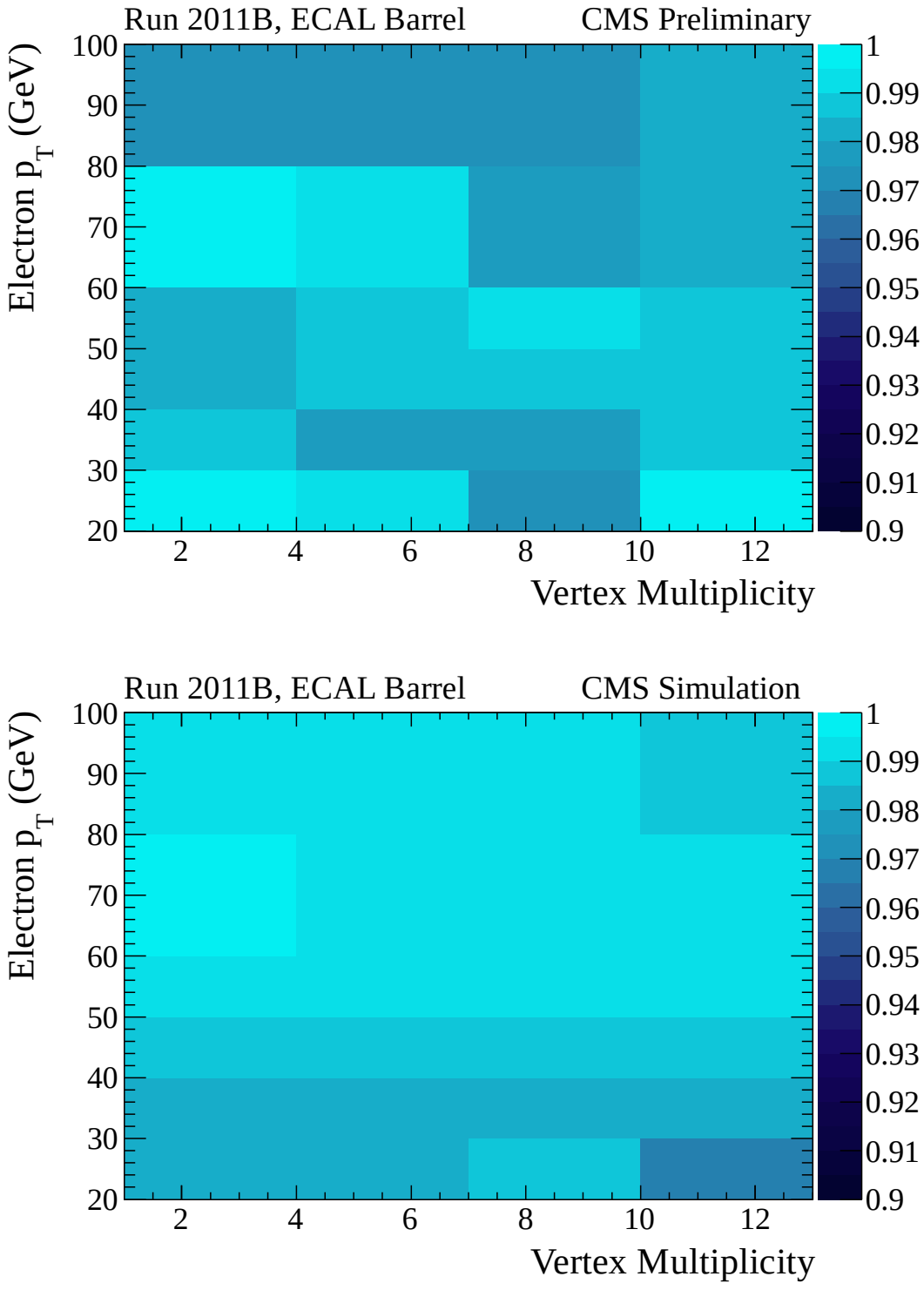

Figure 4.12: Electron reconstruction efficiency in the barrel for the 2011B run period [107]. Top: data, bottom: simulation.

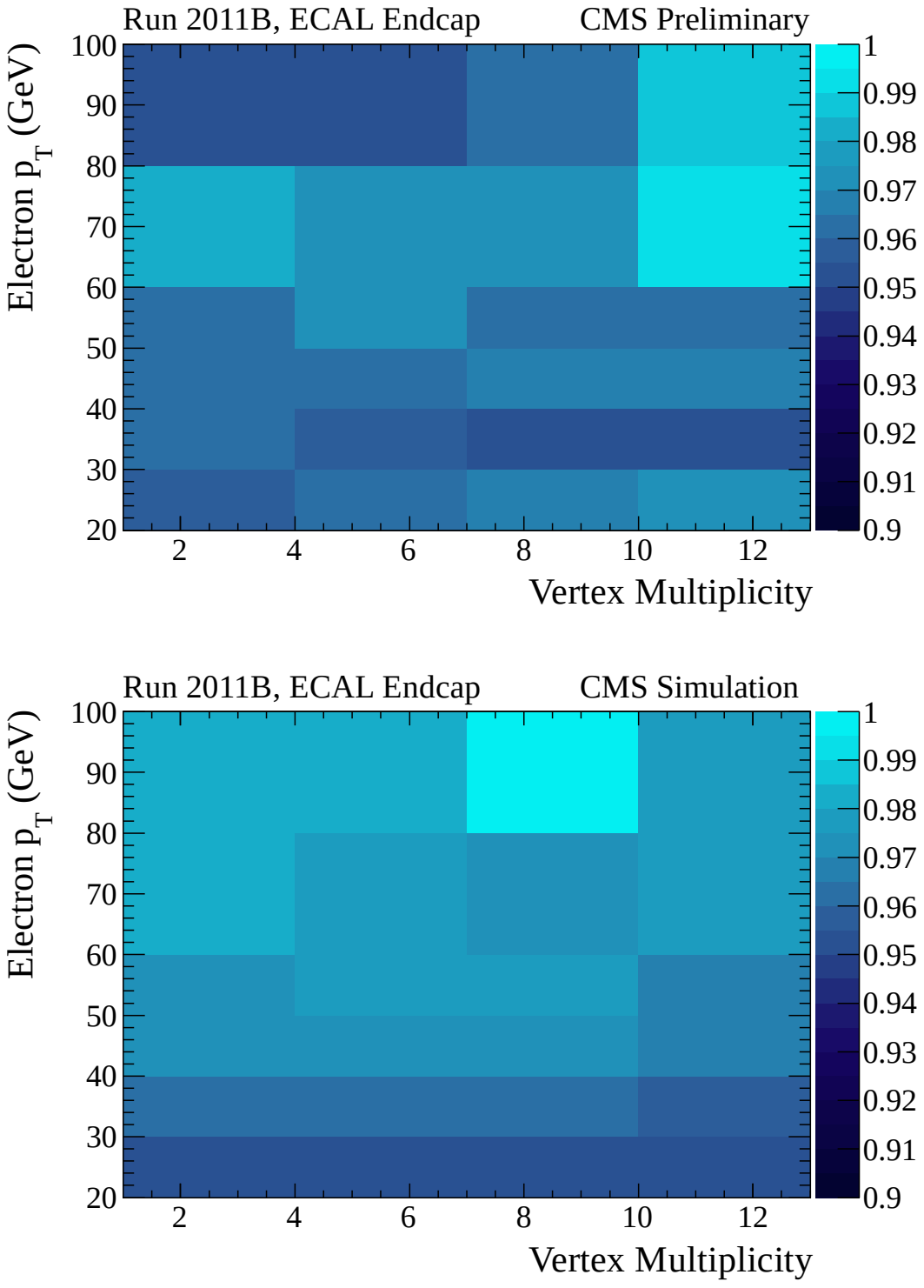

Figure 4.13: Electron reconstruction efficiency in the endcaps for the 2011B run period [107]. Top: data, bottom: simulation.

Shower width $\sigma_{i\eta i\eta}$, and

Hadronic-over-electromagnetic ratio H/E.

These variables are useful for suppressing background due to hadrons and electrons embedded in jets.

We use the following electron identification variables describing the spatial compatibility of the GSF track and the matching supercluster:

Track-cluster compatibility $\Delta\eta_{\text{in}}$, the difference in the η coordinates between the supercluster position and the expected electron incidence extrapolated from the innermost track momentum measurement.

Track-cluster compatibility $\Delta\phi_{\text{in}}$, the difference in the ϕ coordinates between the supercluster position and the expected electron incidence extrapolated from the innermost track momentum measurement.

These variables are useful in suppressing background due to random coincidences of unrelated tracks and ECAL deposits.

We use the following electron identification variables to suppress electrons originating from early conversions of primary prompt photons:

Number of missing hits n_{miss}, the number of missing hits before the first valid hit of the electron track.

Conversion opening angle $\cot\Delta\theta$, the cotangent of the opening angle between the electron track and a track corresponding to a potential conversion partner of opposite charge.

Conversion track distance d_{conv}, the transverse distance between the electron track and a track corresponding to a potential conversion partner at the point were the two tracks become parallel.

In addition to these electron identification variables, we use the following isolation variables to further suppress electrons and background from jets and hadron decays:

Electron tracker isolation $I^{\mathrm{e}}_{\mathrm{TRK}}$, the scalar sum of the transverse momenta of tracks originating from the same primary vertex, with $p_{\mathrm{T}} > 0.7\,\mathrm{GeV}$, within an annulus of $0.015 < \Delta R < 0.3$ around the electron momentum direction, excluding a rectangular region of 0.03×0.3 in $\Delta\eta \times \Delta\phi$ centered on the electron to protect the isolation sum from the inclusion of the electron track and conversion tracks of eventual bremsstrahlung photons [112, 113].

Electron ECAL isolation $I^{\mathrm{e}}_{\mathrm{ECAL}}$, the scalar sum of transverse energy of ECAL crystal deposits within a $3\Delta\eta_0 < \Delta R < 0.3$ cone around the supercluster ECAL location, excluding a rectangular strip of $3\Delta\eta_0 \times 0.3$ in $\Delta\eta \times \Delta\phi$ to protect the isolation sum from the inclusion of energy deposits due bremsstrahlung showers and secondary conversions. Here, $\Delta\eta_0$ is the size of a single crystal in units of pseudorapidity η. In the ECAL barrel, only deposits with energies $E > 80\,\mathrm{MeV}$ are included in the sum. In the ECAL endcaps, only deposits with transverse energies $E_T > 100\,\mathrm{MeV}$ are included [114, 115].

Electron HCAL isolation $I^{\mathrm{e}}_{\mathrm{HCAL}}$, the scalar sum of the transverse energy of HCAL tower deposits within a solid cone of $\Delta R < 0.3$ around the ECAL supercluster location.

Electron combined relative isolation $I^{\mathrm{rel,\,e}}_{\mathrm{comb}} = (I^{\mathrm{e}}_{\mathrm{TRK}} + I^{\mathrm{e}}_{\mathrm{ECAL}} + I^{\mathrm{e}}_{\mathrm{HCAL}})/p_{\mathrm{T}}$, the sum of the tracker, ECAL and HCAL isolations divided by the electron transverse momentum.

Similarly to photons, to minimize the impact of the pileup energy deposits on the isolation, we correct the combined isolation by subtracting the average energy deposited by the pileup using eq. (4.5). Here, the effective area is given by $A^{\mathrm{eff}} = \pi R^2$ with $R = 0.3$.

4.7 Muons

In CMS, muons are reconstructed as tracks in the inner silicon tracker and matching signals in the outer muon systems. The signals in the outer systems can be either

isolated hits or a reconstructed track. There are two algorithms used. The *tracker muon* reconstruction starts with the inner tracks. It propagates them through the muon system using the known track parameters and the magnetic field map, and searches for consistent hits in the muon system. The *global muon* reconstruction requires that a global track can be fitted to the hits in both the tracker and the muon system simultaneously.

Figure 4.14 shows the reconstruction efficiency for muons in the inner tracker from $Z \rightarrow \mu^+\mu^-$ decays, measured in both data and simulation with the tag-and-probe method. Similarly, Figures 4.15 and 4.16 show the efficiencies of the outer track reconstruction and inner-outer track matching of the global muon reconstruction algorithm, respectively.

The reconstruction is optimized to have a very high efficiency. However, it can happen that signals that do not originate from primary isolated muons are also reconstructed. These may come from a number of sources:

- hadronic punch-through,
- decays in flight,
- accidental track-to-segment matches, potentially involving pile-up tracks,
- cosmic muons.

A set of requirements serves to reject such undesired muon candidates and to identify signal muons with high efficiency.

We use the following muon identification and isolation variables:

Global muon - the candidate is reconstructed as a global muon.

Reduced χ squared χ^2/n_{dof}, the ratio of the χ^2 and the number of degrees of freedom n_{dof} of the global track fit. Requiring low values of χ^2/n_{dof} suppresses hadronic punch-through and muons from decays in flight.

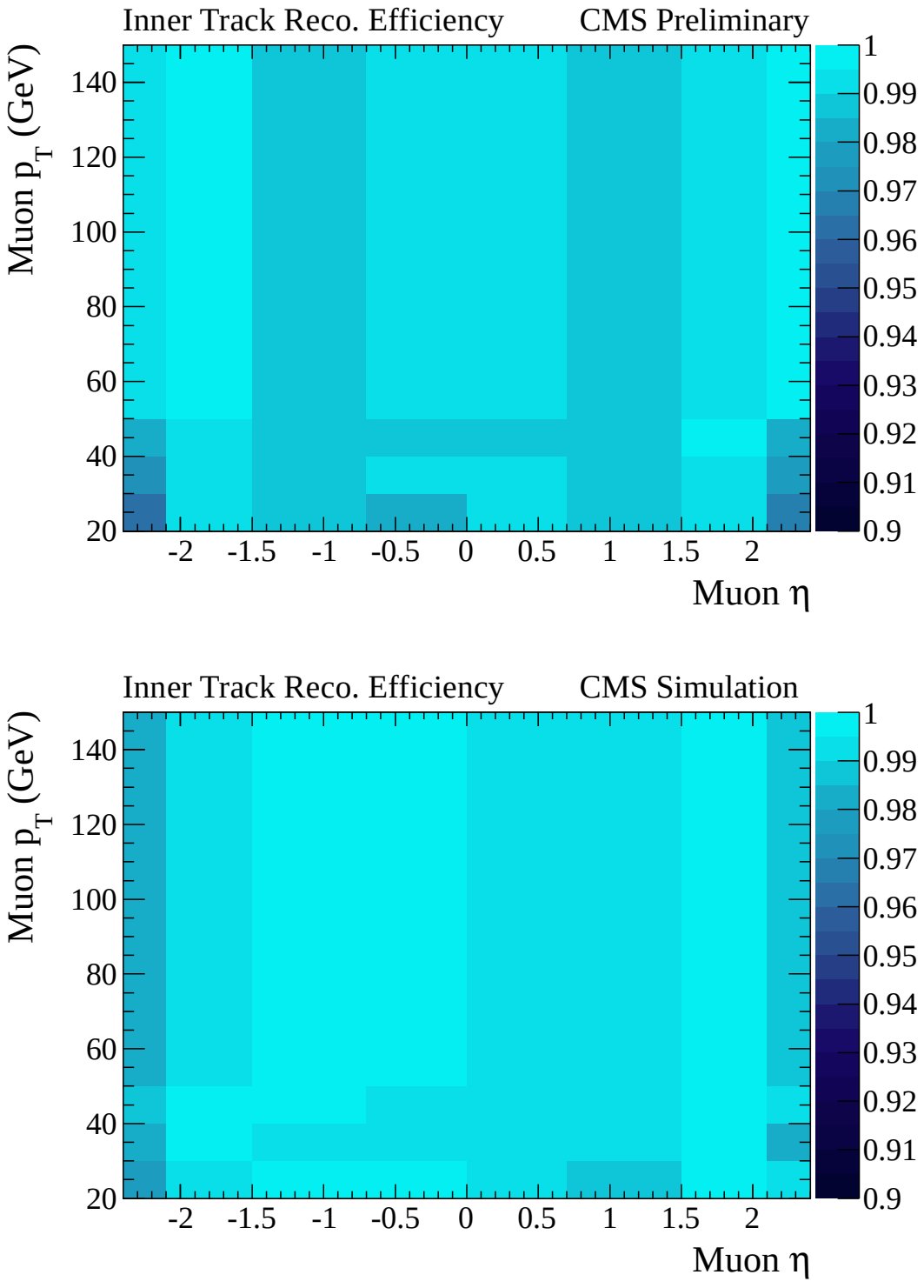

Figure 4.14: Muon inner track reconstruction efficiency map in the p_T-η plane [107]. Top: data, bottom: simulation.

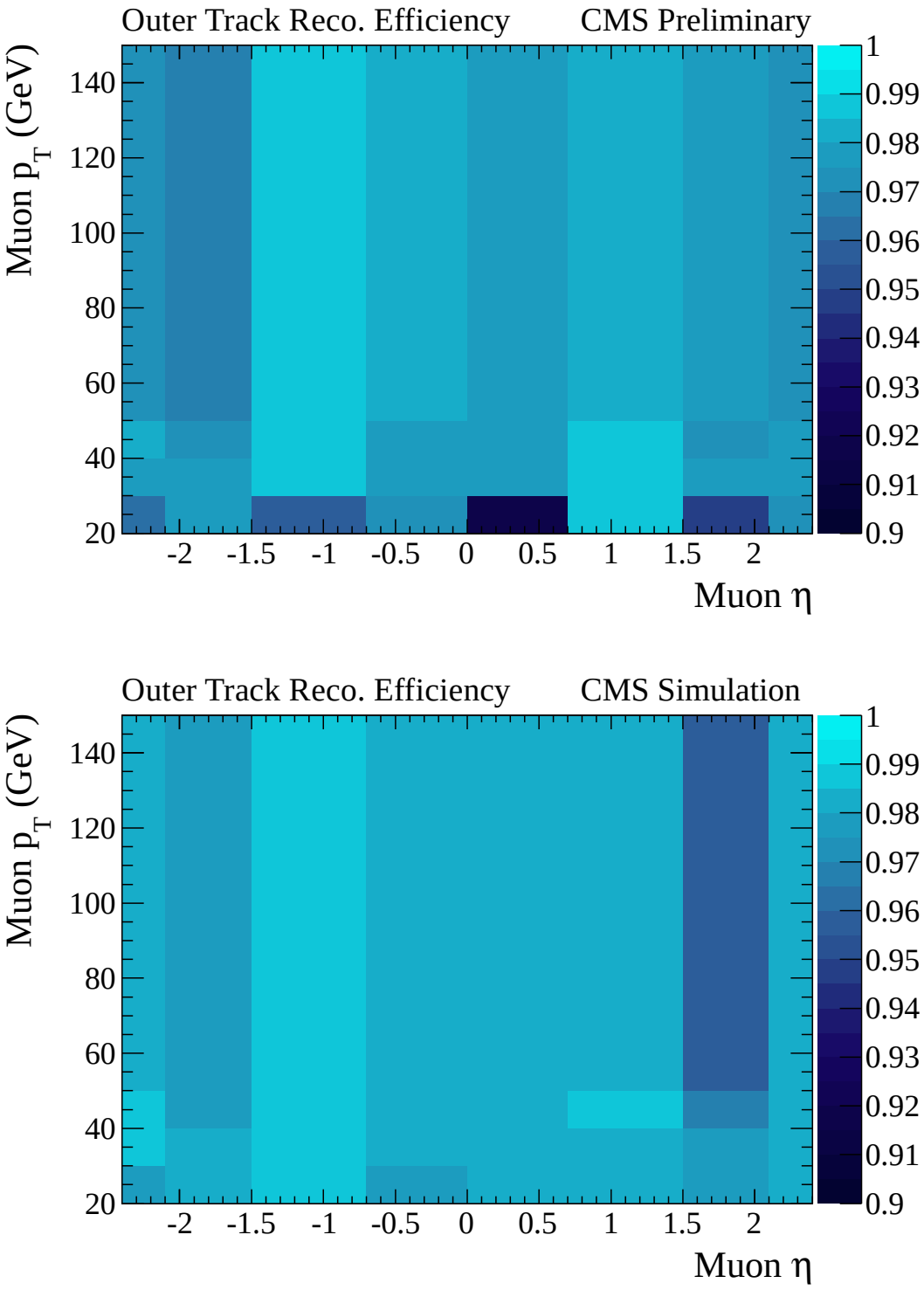

Figure 4.15: Muon outer track reconstruction efficiency map in the p_{T}-η plane [107]. Top: data, bottom: simulation.

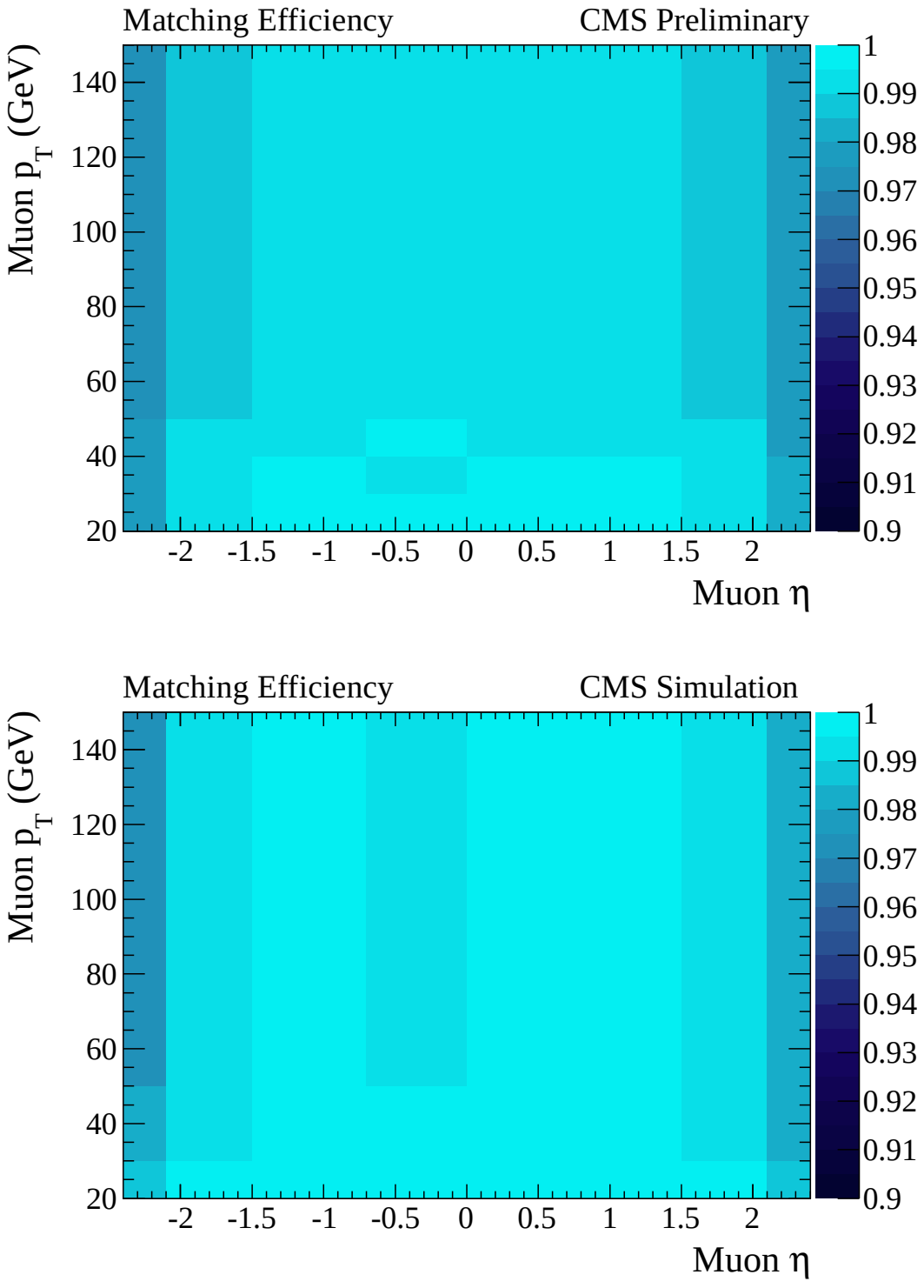

Figure 4.16: Muon inner-outer track matching efficiency map in the p_T-η plane [107]. Top: data, bottom: simulation.

Number of muon chamber hits n_{hits}, the total number of valid muon chamber hits included in the global track fit, for which a high value further discriminates signal muons from hadronic punch-through and muons from decays in flight.

Number of matched stations n_{stations}, the total number of muon stations with muon segments. Requiring higher values of n_{stations} suppresses punch-through and accidental track-to-segment matches. This also guarantees the consistency between the offline selection and the muon trigger selection, since the same criterion is used in the trigger to establish that the muon transverse momentum estimate is reasonably accurate.

Transverse impact parameter d_{xy}, the signed minimum distance in the xy plane of the extrapolated muon inner track and the primary vertex. Signal muons tend to have lower values of $|d_{xy}|$ than cosmic muons and those from decays in flight.

Longitudinal impact parameter d_z, the signed minimum distance along the z coordinate of the extrapolated muon inner track and the primary vertex. As for d_{xy}, requiring low values of $|d_z|$ contributes to rejecting cosmic muons and muons from decays in flight.

Number of pixel hits n_{pixel}, the total number of reconstructed hits in the pixel detector. The signal muons tend to record more hits in the pixel detector than the muons from decays in flight.

Number of tracker hits n_{tracker}, the total number of the hits in the inner tracker including the silicon pixel and strip detectors. Requiring greater values of n_{tracker} further suppresses muons from decays in flight and ensures a reasonable estimate of the inner track muon transverse momentum estimate.

In addition to the muon identification variables, this analysis uses the following muon isolation variables:

Muon Tracker Isolation I^{μ}_{TRK} , the scalar sum of the transverse momenta of tracks originating from the same primary vertex, with $p_{\mathrm{T}} > 1.5$ GeV, and within an annulus of $0.015 < \Delta R < 0.3$ around the muon momentum direction.

Muon ECAL Isolation I^{μ}_{ECAL}, the scalar sum of transverse energy of ECAL rec hits within a cone of $\Delta R < 0.3$ around the muon direction.

Muon HCAL Isolation I^{μ}_{HCAL}, the scalar sum of the transverse energy of HCAL towers within a cone of $\Delta R < 0.3$ around the near muon direction.

Muon Combined Relative Isolation $I^{\mathrm{rel},\mu}_{\mathrm{comb}} = (I^{\mu}_{\mathrm{TRK}} + I^{\mu}_{\mathrm{ECAL}} + I^{\mu}_{\mathrm{HCAL}})/p_{\mathrm{T}}$, the sum of the tracker, ECAL and HCAL isolations divided by the muon transverse momentum.

Hadronic punch through and decays in flight tend to have higher isolation values on average than the signal muons. The tracker isolation is very robust with respect to the pileup. The ECAL isolation is efficient in rejecting events with hard radiative photons that tend to be collinear. The combined relative isolation has greater signal-to-background rejection power due to reduced fluctuation coming from jet hadronization and detector noise.

Chapter 5

Analysis

In this chapter we first describe in Section 5.1 how we measure the cross section of associated Zγ production, and in Section 5.2 how we set limits on the Zγ anomalous triple-gauge couplings. In the following sections, we describe in more detail the needed quantitative input variables and their estimates.

5.1 Cross Section Extraction

We estimate the value of the measured cross section as:

$$\sigma = \frac{S}{A \cdot \epsilon \cdot L} \tag{5.1}$$

where S is the total number of recorded signal events passing the selection, A is the geometric and kinematic *acceptance* of the signal events, ϵ is the overall efficiency of reconstruction, triggering and selection for signal events in the acceptance, and $L = \int \mathscr{L}\, \mathrm{d}t$ is the total integrated luminosity. Here, the acceptance A is the probability that all the final state particles of a signal event cross the detector fiducial volume.

In practice, we only determine the product $\mathcal{F} = A \cdot \epsilon$ without explicitly decomposing it into its factors. We estimate A only indirectly through corrections derived from the data and applied to simulation. In the simulation, the product of acceptance-times-efficiency $\mathcal{F}_{\mathrm{MC}}$ is equal to the ratio of the selected signal events S_{sel} over the

total number of simulated signal events within the kinematic acceptance S_{gen}:

$$\mathcal{F}_{\text{MC}} = \frac{S_{\text{sel}}}{S_{\text{gen}}}. \tag{5.2}$$

This follows from (5.1) substituting:

$$S_{\text{gen}} = \sigma \cdot L.$$

To avoid singularities in the differential cross section, we define the phase space of the kinematic acceptance by requiring that

- the photon transverse energy be $E_T^{\gamma} > 15\,\text{GeV}$,
- the photon be separated from both leptons in the plane of pseudorapidity and azimuthal angle by $\Delta R_{\ell\gamma} > 0.7$, and
- the invariant mass of the dilepton system be $M_{\ell\ell} > 50\,\text{GeV}$.

To proceed, we formally assume that the acceptance in simulation A_{MC} is the same as in data $A_{\text{data}} = A_{\text{MC}} = A$. In practice, this assumption does not hold precisely. However, our treatment will still be correct as we will release the assumption again later in Section 5.8 and include the tolerance within which it holds as a systematic uncertainty. We write the product of acceptance-times-efficiency in data as:

$$\begin{aligned} \mathcal{F}_{\text{data}} &= A_{\text{data}} \cdot \epsilon_{\text{data}} \\ &= A_{\text{MC}} \cdot \epsilon_{\text{data}} \\ &= A_{\text{MC}} \cdot \epsilon_{\text{MC}} \cdot \rho_{\text{eff}} \\ &= \mathcal{F}_{\text{MC}} \cdot \rho_{\text{eff}}, \end{aligned} \tag{5.3}$$

where $\mathcal{F}_{\text{MC}}$ is evaluated from the definition (5.2), and ρ_{eff} is the ratio of the efficiencies in data and in simulation:

$$\rho_{\text{eff}} = \frac{\epsilon_{\text{data}}}{\epsilon_{\text{MC}}}.$$

We can then write the measured cross section as:

$$\sigma = \frac{N - B}{\mathcal{F}_{\mathrm{MC}} \cdot \rho_{\mathrm{eff}} \cdot L}\,, \tag{5.4}$$

where N is the total number of observed events passing the selection in data and $B_{\mathrm{Z+jets}}$ is the estimate of their subset corresponding to background events.

We assume that the efficiencies of the final state objects are mutually independent. We then evaluate the event efficiency ϵ as a product of the efficiencies of the final state objects:

$$\epsilon = \epsilon_{\ell^+} \cdot \epsilon_{\ell^-} \cdot \epsilon_{\gamma}, \tag{5.5}$$

where ℓ stands for a lepton ℓ = e, μ. We describe the measurements of the object efficiencies in both data and simulation in more detail together with their selection in Section 5.4.

In practice the efficiencies $\epsilon_{\ell^\pm}$ and ϵ_{γ} depend on kinematic and other variables and so does the data/simulation efficiency ratio ρ_{eff}. To take this into account, we measure the ρ_{eff} dependencies. We then generalize (5.3):

$$\begin{aligned} \mathcal{F}_{\mathrm{MC}} \cdot \rho_{\mathrm{eff}} &= \frac{1}{S_{\mathrm{gen}}} \cdot S_{\mathrm{sel}} \cdot \rho_{\mathrm{eff}} \\ &= \frac{1}{S_{\mathrm{gen}}} \cdot \sum_{i}^{S_{\mathrm{sel}}} \rho_{\mathrm{eff}} \\ &= \frac{1}{S_{\mathrm{gen}}} \cdot \sum_{i}^{S_{\mathrm{sel}}} \rho_{\mathrm{eff}}^{(i)}, \end{aligned} \tag{5.6}$$

where we use the superscript (i) on the last line to denote that $\rho_{\mathrm{eff}}^{(i)}$ is specific for the given simulated event i passing the selection and includes all the dependencies on kinematic and other variables.

The luminosity L is integrated over the period of time corresponding to the acquisition of the dataset used in this analysis, as discussed in detail in Section 5.3. The goal of the selection is to achieve a high signal-to-background ratio. We discuss it in

detail in Section 5.4 together with the corresponding selection efficiencies.

The leading source of background events comes from inclusive Z^0 boson production, $pp \to Z + X \to \ell^+\ell^- + X$, with the reconstructed photon candidate originating from fake signals X, mainly related to jet production. We estimate the amount of such events directly from the selected data, using two independent methods as described in Section 5.5. The other sources of background events are due to one of the leptons originating from fake signals. Their contributions are minor and we estimate them from simulation.

5.2 Anomalous Triple-Gauge Coupling Limits

Here we discuss the method we use to set limits on the anomalous triple-gauge couplings (ATGCs) as introduced in Section 2.10. All of the coupling constants h_i^V vanish at the tree-level approximation in the Standard Model (SM). Here, $i = 1, \ldots, 4$ labels the different terms in the vertex function (2.77) and $V = Z, \gamma$ label the $ZZ\gamma$, $Z\gamma\gamma$ vertices. Nonzero values of the couplings with $i = 1, 2$ violate the CP symmetry, while nonzero values of those with $i = 3, 4$ do not violate it.

Nonzero values of the ATGC couplings would cause an enhancement in the rate of associated $Z\gamma$ production at higher $\hat{s}$. This would manifest itself by an observed excess of Z and γ bosons with high momenta. To set the limits on the ATGC values, we use the p_T^γ spectrum of the photon as it is more sensitive than the one of the Z^0 boson.

To extract the limits on h_i^V we perform a counting experiment based on bins of p_T^γ. We set 95% C.L. upper limits on the values of couplings using a modified frequentist hypothesis testing technique known as *CLs* [3, 116].

To explain the method, we denote the parameter(s) of interest $\boldsymbol{\theta}$. In the case of the one-dimensional limits, this denotes one of the coupling constants $\boldsymbol{\theta} = h_i^V$ with $i = 3, 4$ and $V = Z, \gamma$. In the case of the two-dimensional limits, this denotes a pair of the couplings $\boldsymbol{\theta} = (h_3^V, h_4^V)$ with $V = Z, \gamma$.

In addition to $\boldsymbol{\theta}$, the photon p_T spectrum and its expectation depend on other

parameters whose values are not known precisely, but are constrained through auxiliary measurements. These so-called *nuisance parameters* include the total integrated luminosity $\mathcal{L}$ and the total number of observed signal and background events S and B. We express them in terms of their fractional differences $f_X = X/\hat{X}$ of their true and expected values X and $\hat{X}$ as:

$$\mathcal{L} = f_{\mathcal{L}}\hat{\mathcal{L}}\,,$$
$$S = f_S\hat{S}\,,$$
$$B = f_B\hat{B}\,.$$

We denote these nuisance parameters collectively as:

$$\boldsymbol{\nu} = (f_{\mathcal{L}},\, f_S,\, f_B)\,.$$

The upper limits are defined by excluding points in the space of $\boldsymbol{\theta}$ for which:

$$\mathrm{CLs} < \alpha,$$

where $1 - \alpha = 0.95$ is the chosen confidence level. Here, CLs is defined as:

$$\mathrm{CLs} = \frac{p_{\boldsymbol{\theta}}}{1 - p_0},$$

where $p_{\boldsymbol{\theta}}$ is the p-value under the signal hypothesis corresponding to the specific point in the $\boldsymbol{\theta}$ space, and p_0 is the p-value of the SM hypothesis where all the ATGC couplings vanish $h_i^V = 0$. The p-value is defined for an observed value of the *test statistic* $t_{\boldsymbol{\theta}}$, a quantity describing the compatibility of the observed data and the assumed hypothesis. Small values of $t_{\boldsymbol{\theta}}$ correspond to good compatibility, while large values of $t_{\boldsymbol{\theta}}$ correspond to poor compatibility. The p-value is the probability that for an independent repetition of the measurement $t_{\boldsymbol{\theta}}$ attains a value equal or greater than the one observed $t_{\boldsymbol{\theta},\mathrm{obs}}$. In terms of the probability density function (PDF) of

the test statistic $f(t_{\boldsymbol{\theta}}|\boldsymbol{\theta})$, we write:

$$p_{\boldsymbol{\theta}} = \int_{t_{\boldsymbol{\theta},\mathrm{obs}}}^{\infty} f(t_{\boldsymbol{\theta}}|\boldsymbol{\theta})\,\mathrm{d}t_{\boldsymbol{\theta}}\,.$$

The CLs procedure defines the test statistic as:

$$t_{\boldsymbol{\theta}} = -2\ln\lambda(\boldsymbol{\theta})\,,$$

where $\lambda(\boldsymbol{\theta})$ is the *profile likelihood ratio*:

$$\lambda(\boldsymbol{\theta}) = \frac{L(\boldsymbol{\theta},\hat{\hat{\boldsymbol{\nu}}}(\boldsymbol{\theta}))}{L(\hat{\boldsymbol{\theta}},\hat{\boldsymbol{\nu}})}\,.$$

Here, $L(\boldsymbol{\theta},\boldsymbol{\nu})$ is the *likelihood function*, $\hat{\boldsymbol{\theta}}$ and $\hat{\boldsymbol{\nu}}$ are the *maximum-likelihood* estimates of $\boldsymbol{\theta}$ and $\boldsymbol{\nu}$ that maximize $L(\boldsymbol{\theta},\boldsymbol{\nu})$, and $L(\boldsymbol{\theta},\hat{\hat{\boldsymbol{\nu}}}(\boldsymbol{\theta}))$ is the *profile likelihood*, where $\hat{\hat{\boldsymbol{\nu}}}(\boldsymbol{\theta})$ is the value of $\boldsymbol{\nu}$ that maximizes the likelihood $L(\boldsymbol{\theta},\boldsymbol{\nu})$ for a given fixed value of $\boldsymbol{\theta}$.

The likelihood $L(\boldsymbol{\theta},\boldsymbol{\nu})$ reads:

$$L(\boldsymbol{\theta},\boldsymbol{\nu}) = L(\boldsymbol{\nu})\prod_{j=1}^{N}\mathcal{P}(n_j|\nu_j(\boldsymbol{\theta},\boldsymbol{\nu})) \tag{5.7}$$

where $L(\boldsymbol{\nu})$ is a likelihood factor describing our known constraints on the nuisance parameters from auxiliary measurements and $P(n_j|\nu_j(\boldsymbol{\theta},\boldsymbol{\nu})$ is the likelihood to observe n_j events in the bin $j = 1,\,\ldots,\,N$ of the photon p_{T} with its corresponding expectation of $\nu_j(\boldsymbol{\theta},\boldsymbol{\nu})$. Here, $\mathcal{P}(n|\nu)$ is the *Poisson probability distribution*:

$$\mathcal{P}(n|\nu) = \frac{\nu^n\,\mathrm{e}^{-\nu}}{n!}\,.$$

For each bin of the photon p_{T} spectrum, we write the expected number of events as:

$$\nu(\boldsymbol{\theta},\boldsymbol{\nu}) = s(\boldsymbol{\theta},\boldsymbol{\nu}) + b(\boldsymbol{\nu}),$$

where $s(\boldsymbol{\theta}, \boldsymbol{\nu})$ and $b(\boldsymbol{\nu})$ are the expected number of signal and background events in that bin:

$$s(\boldsymbol{\theta}, \boldsymbol{\nu}) = f_{\mathcal{L}} f_S \hat{s}(\boldsymbol{\theta}) \,,$$
$$b(\boldsymbol{\nu}) = f_{\mathcal{L}} f_B \hat{b} \,.$$

Here, we factor out explicitly the dependence on the nuisance parameters.

Let us discuss the inclusion of our knowledge of the values of the nuisance parameters $\boldsymbol{\nu}$ from independent measurements. To simplify the calculation, we use the *log-normal* PDF $\phi_{\ln}(y \,|\, \mu, \sigma)$ to approximate the true likelihood constraining $\boldsymbol{\nu}$ in (5.7). This density provides a model for the error of a process that involves many small multiplicative errors [117]. The resulting likelihood then reads:

$$L(\boldsymbol{\nu}) \approx \prod_{y \in \boldsymbol{\nu}} \phi_{\ln}(y \,|\, \hat{y}, \hat{\sigma}_y) \,,$$

where $\hat{y}$ and $\hat{\sigma}_y$ characterize the estimate of the nuisance parameter y and its uncertainty from the auxiliary measurement. Here, the log-normal PDF reads:

$$\phi_{\ln}(y \,|\, \mu, \sigma) = \frac{1}{y\sigma\sqrt{2\pi}} \, \mathrm{e}^{-\frac{(\ln y - \mu)^2}{2\sigma^2}} \,.$$

5.3 Dataset and Trigger

This analysis uses all data acquired by CMS during the course of the year 2011. During that period, LHC delivered a total integrated luminosity of 6.1 fb^{-1} of which CMS recorded 5.6 fb^{-1} and certified for analysis 5.0 fb^{-1}. There was a period of no data taking due to a technical stop in August separating the 2011 dataset into two periods. They are referred to as 2011A and 2011B, and correspond to certified integrated luminosities of 2.3 fb^{-1} and 2.7 fb^{-1}. These are further split into five periods corresponding to different calibrations and detector conditions used for the reconstruction.

The instantaneous luminosity was significantly lower during 2011A than during

2011B, corresponding to a significantly lower average number of simultaneous inelastic collisions during a single bunch crossing (pileup). This leads to differences in the efficiency of the event selection. The selection efficiencies of photons and leptons were measured separately for the 2011A and 2011B data taking periods and then taken into account accordingly.

This analysis employs triggers based on two reconstructed leptons without requiring the presence of a photon. The trigger configuration was continuously updated to reflect the increasing luminosity and pileup.

For the eeγ final state we use unprescaled isolated double-electron triggers with asymmetric p_{T} thresholds of 17 GeV and 8 GeV. The isolation requirements changed in 2011B to cope with the greater amount of background and to keep the trigger rate at acceptable levels.

For the $\mu\mu\gamma$ final state we use unprescaled double-muon triggers that — in contrast to the electron final state — do not require isolation. They also require different thresholds on their transverse momenta to keep the rate within a reasonable window. The thresholds on the leading and subleading muons were 7 and 7 GeV at the beginning of 2011, increasing to 13 and 8 GeV, and finally 17 and 8 GeV as the instantaneous luminosity ramped up.

5.4 Selection

The greatest discrimination power of the signal selection comes from the requirement of two isolated leptons and an isolated photon. The background is further suppressed with kinematic cuts on the invariant masses of the dilepton system and of the three final state objects. In this section, we list the selection criteria used for the Zγ production cross section measurement and the setting of the limits on anomalous triple gauge couplings (ATGCs). These selection requirements are specified in terms of the identification and isolation variables introduced in the previous chapter.

5.4.1 Selection of Photons

We list the numerical requirements on the identification and isolation variables in Table 5.1. They were chosen to simultaneously maximize the signal selection efficiency, the background suppression, and the statistical uncertainty on the estimated signal production rate [118].

	Requirement	
Criterion	Barrel	Endcaps
Transverse momentum	$p_{\mathrm{T}} > 15\,\mathrm{GeV}$	
Pseudorapidity	$\lvert\eta\rvert < 1.4442$	$1.556 < \lvert\eta\rvert < 2.5$
Shower width	$\sigma_{i\eta i\eta} < 0.11$	$\sigma_{i\eta i\eta} < 0.30$
Pixel seed match	absent	
Tracker isolation	$I^{\gamma}_{\mathrm{TRK}} - 0.001 \times p_{\mathrm{T}} - \varrho_{\mathrm{FJ}} \times A^{\mathrm{eff}}_{\mathrm{TRK}} < 2.0$	
ECAL isolation	$I^{\gamma}_{\mathrm{ECAL}} - 0.006 \times p_{\mathrm{T}} - \varrho_{\mathrm{FJ}} \times A^{\mathrm{eff}}_{\mathrm{ECAL}} < 4.2$	
HCAL isolation	$I^{\gamma}_{\mathrm{HCAL}} - 0.0025 \times p_{\mathrm{T}} - \varrho_{\mathrm{FJ}} \times A^{\mathrm{eff}}_{\mathrm{HCAL}} < 2.2$	

Table 5.1: Photon identification and isolation requirements. See section 4.5 for the definition of the variables.

The efficiencies of the photon identification and isolation requirements are measured in the data with the tag-and-probe method using $\mathrm{Z} \to \mathrm{e}^{+}\mathrm{e}^{-}$ events, except for the pixel match veto which is measured using $\mathrm{Z} \to \mu^{+}\mu^{-}\gamma$ events.

The tag-and-probe method is based on a measurement of the signal yield for events from the decay of a resonance, such as $\mathrm{Z} \to \ell^{+}\ell^{-}$. The events are "tagged" by requiring stringent selection criteria for one of the decay legs. The other leg of the decay then serves as a probe of a particular requirement. The yield is then extracted for probes both passing P and failing F the given requirement. These yields can be estimated from a fit of the sum of signal and background models to the invariant mass data. The efficiency of the requirement can then be estimated as $\epsilon = P/(P + F)$.

Figures 5.1 and 5.2 show the barrel and endcaps data/MC efficiency ratio scale factors as two-dimensional maps of photon transverse momentum and primary vertex multiplicity for the 2011A and 2011B data taking periods.

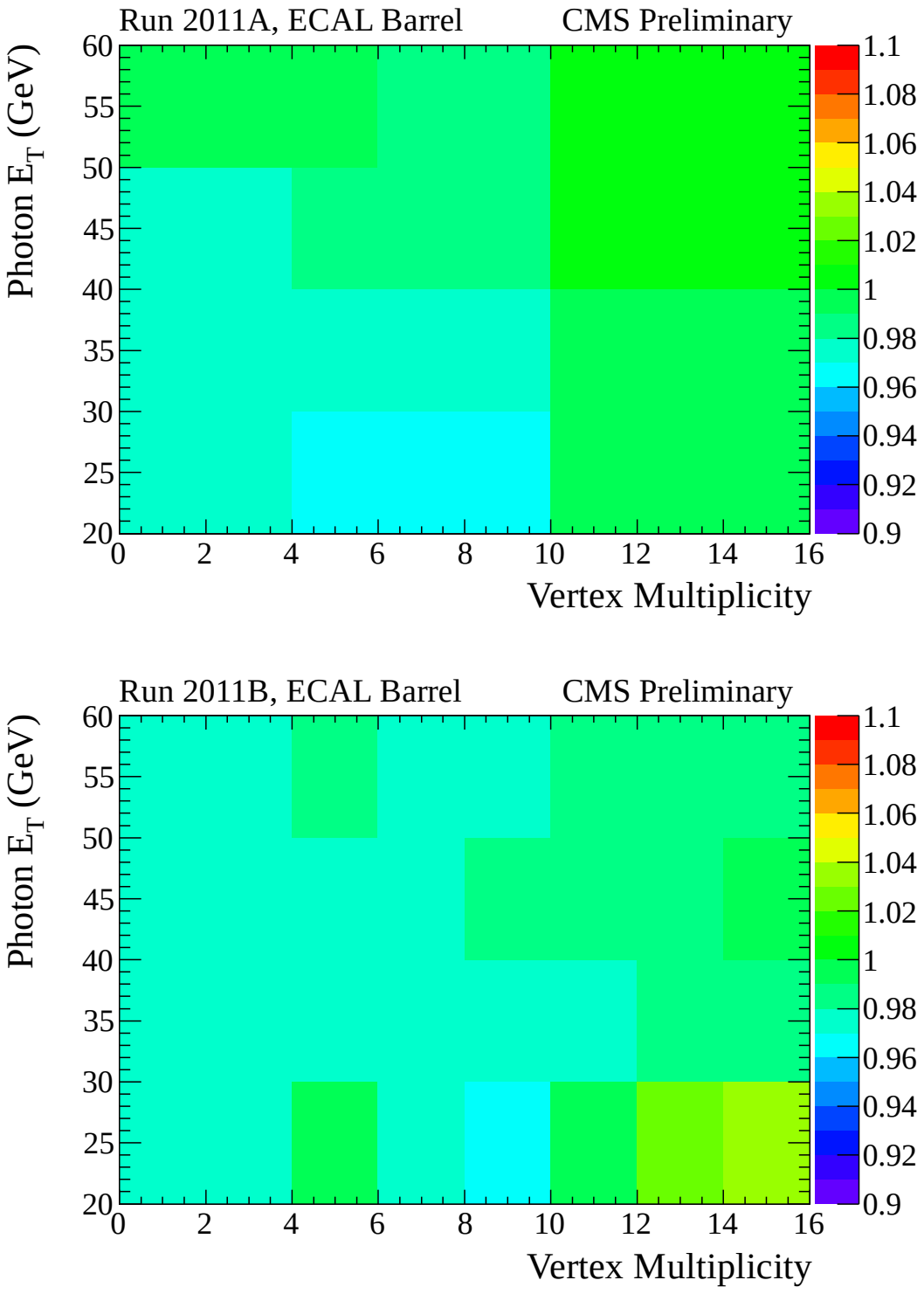

Figure 5.1: Photon efficiency scale factors in the barrel. Top: the 2011A run period, bottom: the 2011B run period.

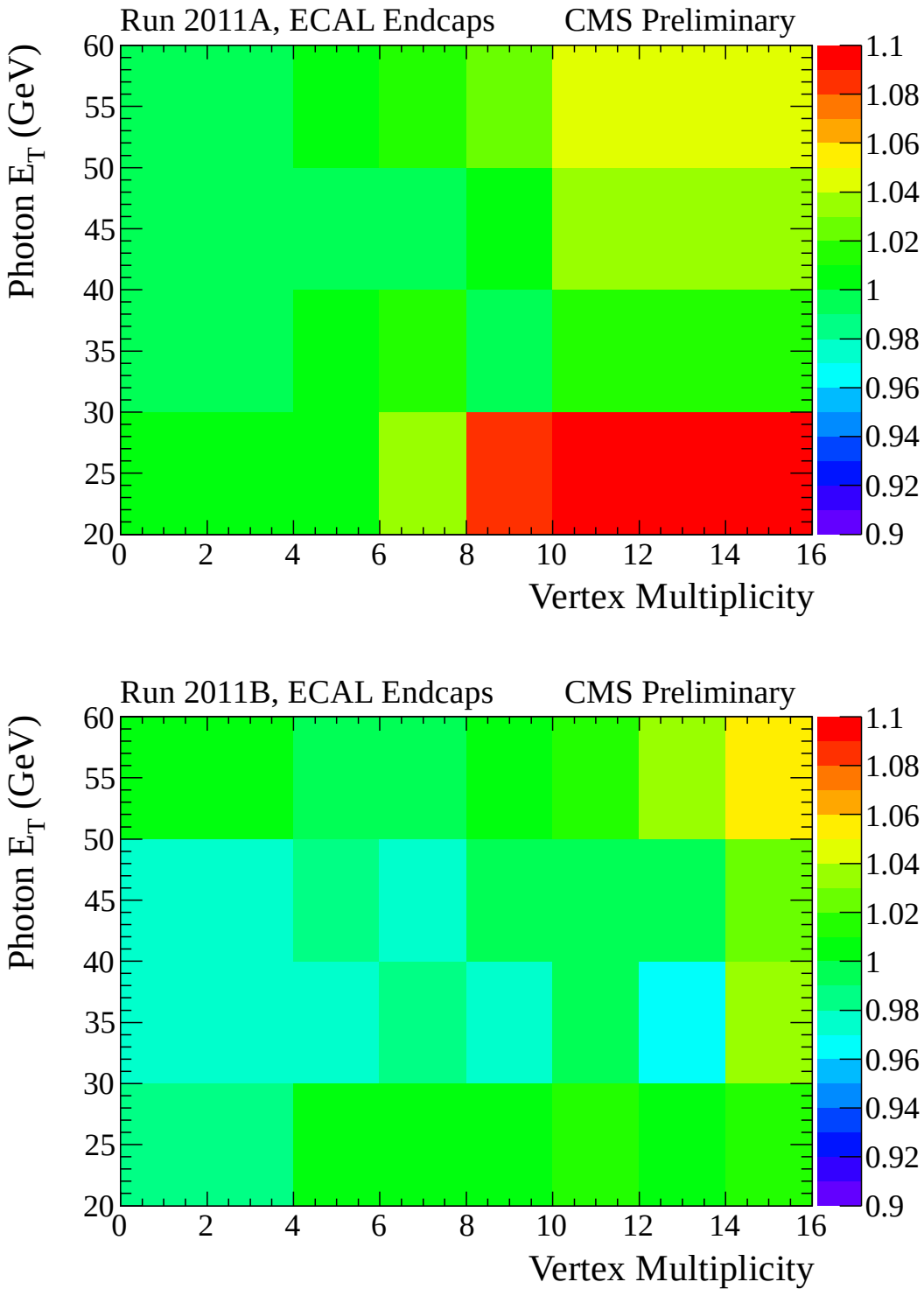

Figure 5.2: Photon efficiency scale factors in the endcaps. Top: the 2011A run period, bottom: the 2011B run period.

5.4.2 Selection of Electrons

We list the numerical requirements on the electron identification and isolation variables in Table 5.2. They were chosen to simultaneously maximize the signal selection efficiency, the background suppression, and the statistical uncertainty on the estimated rate of inclusive $Z \to e^+e^-$ production [119].

	Requirement	
Criterion	Barrel	Endcaps
Transverse momentum	$p_T > 20\,\text{GeV}$	
Pseudorapidity	$\lvert\eta\rvert < 1.4442$	$1.556 < \lvert\eta\rvert < 2.5$
Track-cluster compatibility	$\lvert\Delta\eta_{in}\rvert < 0.005$	$\lvert\Delta\eta_{in}\rvert < 0.007$
	$\lvert\Delta\phi_{in}\rvert < 0.039\,\text{rad}$	$\lvert\Delta\phi_{in}\rvert < 0.028\,\text{rad}$
Shower width	$\sigma_{i\eta i\eta} < 0.010$	$\sigma_{i\eta i\eta} < 0.031$
Number of missing hits	$n_{miss} = 0$	
Conversion opening angle	$\lvert\cot\Delta\theta\rvert < 0.02$	
Conversion track distance	$\lvert d_{conv}\rvert < 0.02\,\text{cm}$	
Combined relative isolation	$I_{comb}^{rel,\,e} < 0.053$	$I_{comb}^{rel,\,e} < 0.042$

Table 5.2: Electron identification and isolation requirements. See Section 4.6 for the definition of the variables.

Figures 5.3 and 5.4 show the barrel and endcaps data/MC efficiency ratio scale factors as two-dimensional maps of electron transverse momentum and primary vertex multiplicity for the 2011A and 2011B data-taking periods as measured with the $Z \to e^+e^-$ tag-and-probe method.

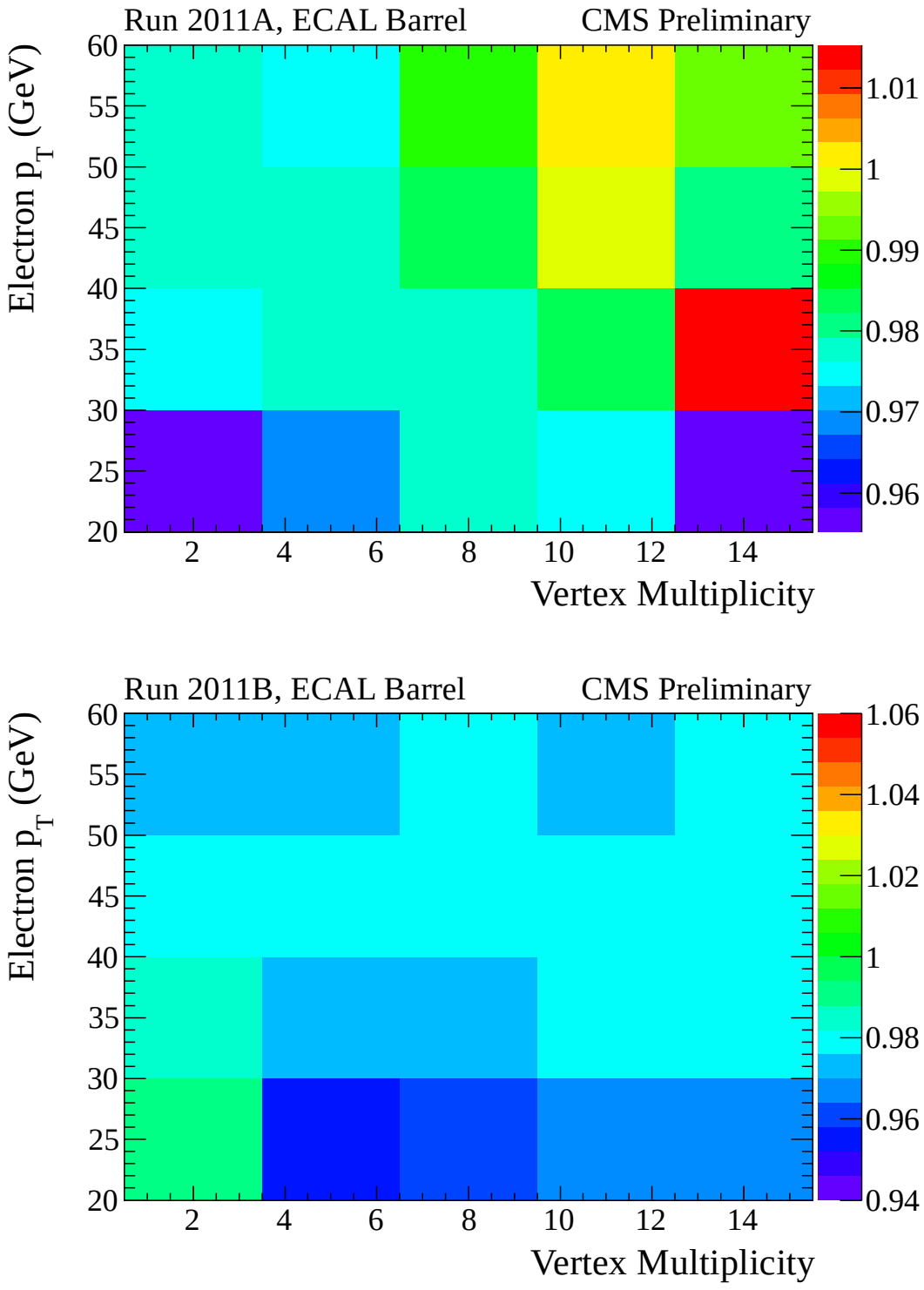

Figure 5.3: Electron efficiency scale factors in the barrel. Top: the 2011A run period, bottom: the 2011B run period.

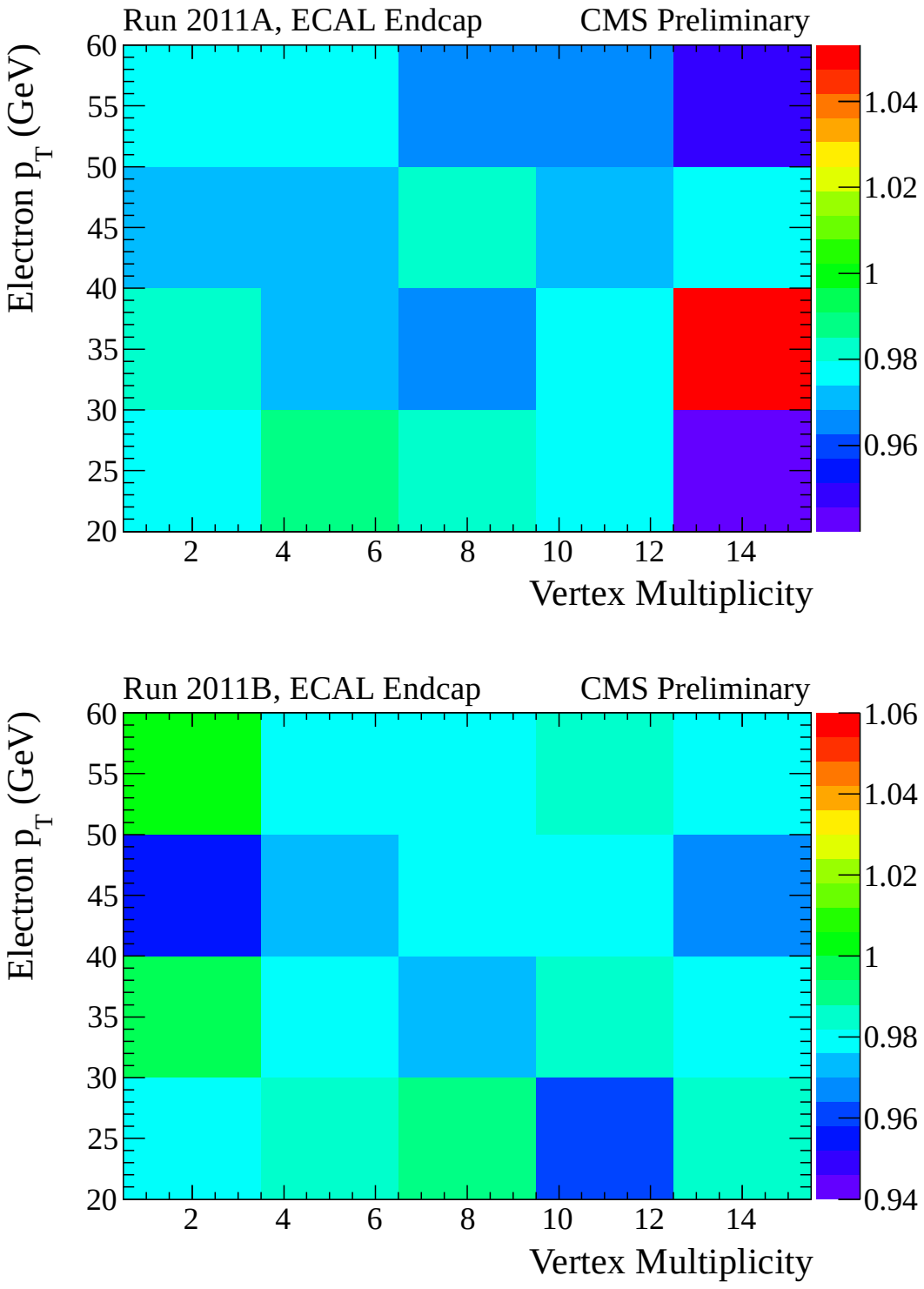

Figure 5.4: Electron efficiency scale factors in the endcaps. Top: the 2011A run period, bottom: the 2011B run period.

5.4.3 Selection of Muons

We require the muons to be reconstructed as global muons as discussed in Section 4.7. We list the numerical values of further requirements on the identification and isolation variables in Table 5.3. Similarly to the electrons, they were chosen to simultaneously maximize the signal selection efficiency, the background suppression, and the statistical uncertainty on the estimated rate of inclusive $Z \to \mu^+\mu^-$ production [119].

Criterion	Requirement
reduced χ-squared	$\chi^2/n_{\text{dof}} < 10$
number of muon chamber hits	$n_{\text{hits}} \geq 1$
number of matched stations	$n_{\text{stations}} \geq 2$
transverse impact parameter	$\lvert d_{xy}\rvert < 0.02\,\text{cm}$
transverse impact parameter	$\lvert d_z\rvert < 0.1\,\text{cm}$
number of pixel hits	$n_{\text{pixel}} \geq 1$
number of tracker hits	$n_{\text{tracker}} \geq 11$
relative combined isolation	$I_{\text{comb}}^{\text{rel},\mu} < 0.1$

Table 5.3: Muon identification and isolation requirements. See the text in Section 4.7 for the definition of the variables.

The efficiencies of the muon identification and isolation requirements are measured in data with the tag-and-probe method using $Z \to \mu^+\mu^-$ events. Figure 5.5 shows the data/MC efficiency scale factors as two-dimensional maps of muon transverse momentum and pseudorapidity measured separately for the 2011 A and B data-taking periods.

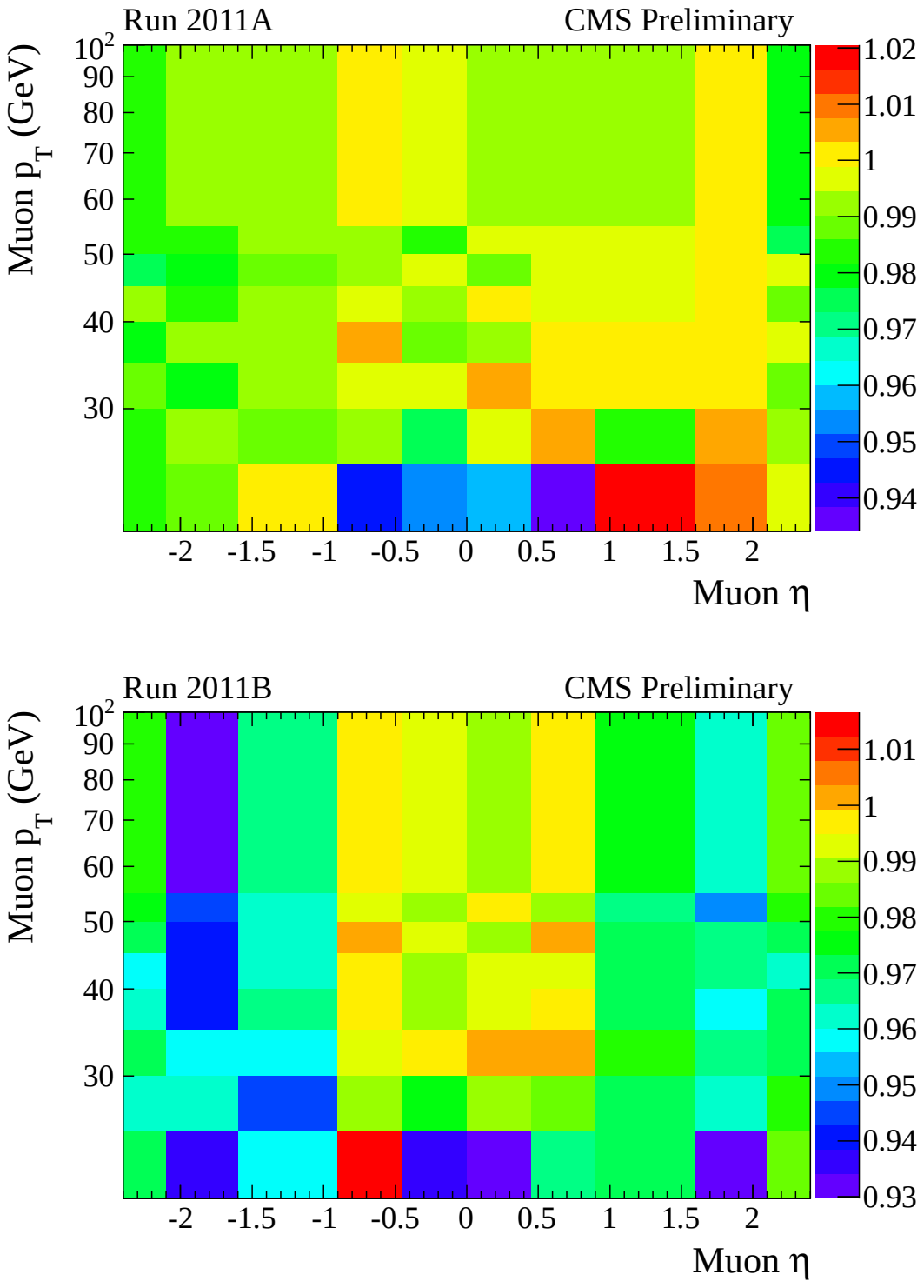

Figure 5.5: Muon data/MC efficiency ratios for the 2011 A (top) and B (bottom) data-taking periods.

5.4.4 Selection of pp $\to \ell\ell\gamma$ Events

The selected Zγ event candidates are required to have at least two leptons and one photon passing the selection criteria described in Sections 5.4.1, 5.4.2, and 5.4.3. A number of requirements on the kinematics of these three objects ensures that the cross section is well-defined and improves the signal-to-background yield ratio. These requirements are arbitrary to the extent that their exact numerical values are chosen such to agree with similar measurements carried out at Tevatron and by the the Atlas collaboration at the LHC.

- The invariant mass of the dilepton system is required to be greater than:

$$m_{\ell^+\ell^-} > 50\,\text{GeV}.$$

  This reduces the contribution of dilepton production through the photon propagator and avoids the divergence of the differential cross section for vanishing dilepton mass values.

- The distance in the η-ϕ plane between the photon and the nearest lepton is required to be greater than:

$$\min \Delta R(\ell^{\pm}, \gamma) = \sqrt{\Delta\eta^2 + \Delta\phi^2} > 0.7.$$

  This avoids the collinear divergence of the differential cross section due to the radiative decays Z $\to \mu^+\mu^-\gamma$.

In Figures 5.6 and 5.7 we show the kinematic distributions of photon candidates in the selected event samples, compared with the predictions from the simulation for the electron and muon channel respectively. In Figures 5.8 and 5.9 we show the corresponding invariant mass distributions.

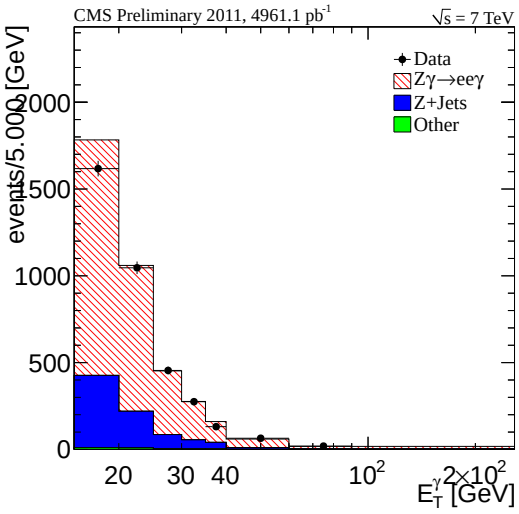

(a) Photon candidate E_T

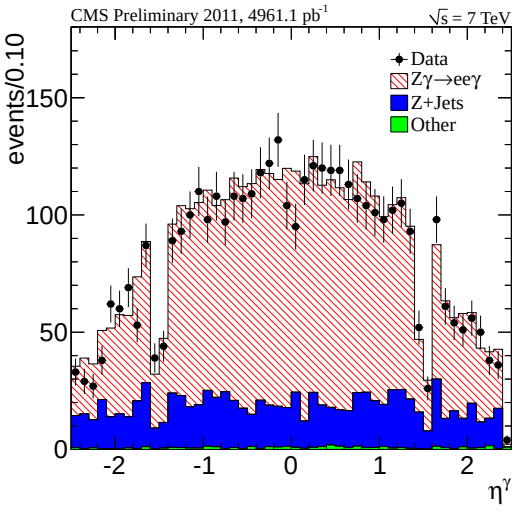

(b) Photon candidate pseudorapidity η

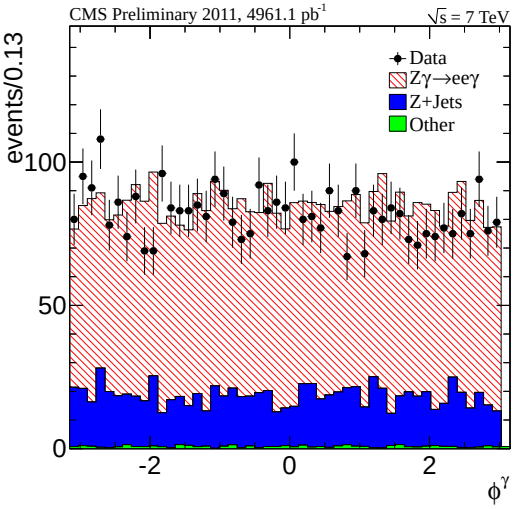

(c) Photon candidate ϕ

Figure 5.6: Photon candidate kinematic distributions for selected events in the channel with electrons: data (black dots), Zγ signal (white histogram), Z/γ^*+jets and other backgrounds are given as red and green filled histograms respectively.

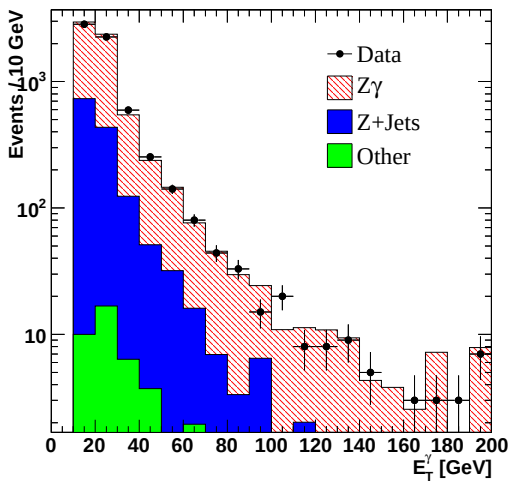

(a) Photon candidate E_T

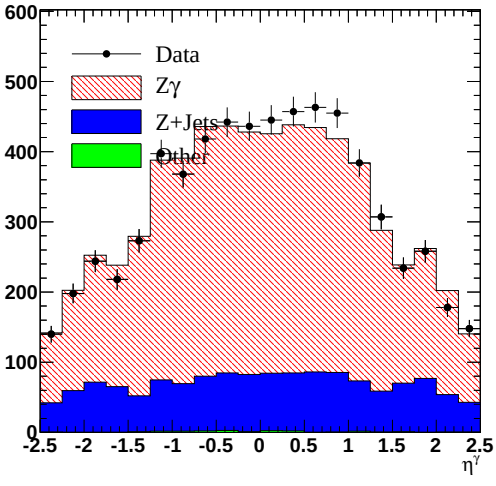

(b) Photon candidate pseudorapidity η

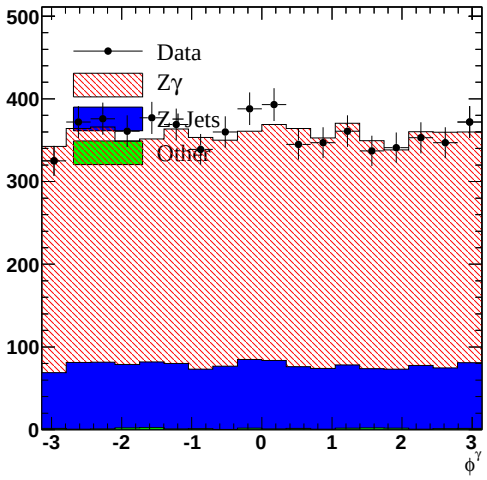

(c) Photon candidate ϕ

Figure 5.7: Photon candidate kinematic distributions for selected events in the channel with muons: data (black dots), Zγ signal (white histogram), Z/γ^*+jets and other backgrounds are given as red and green filled histograms respectively.

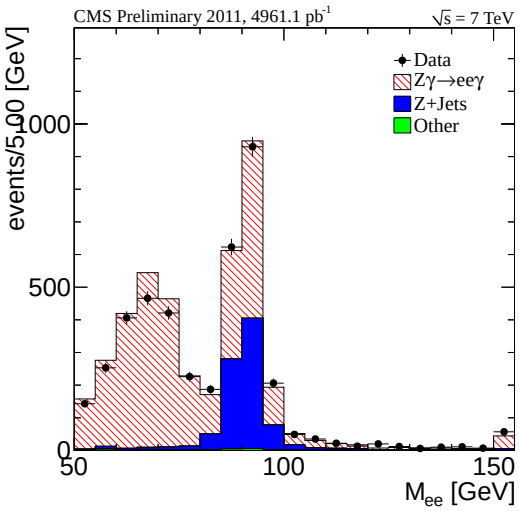

(a) Dielectron invariant mass

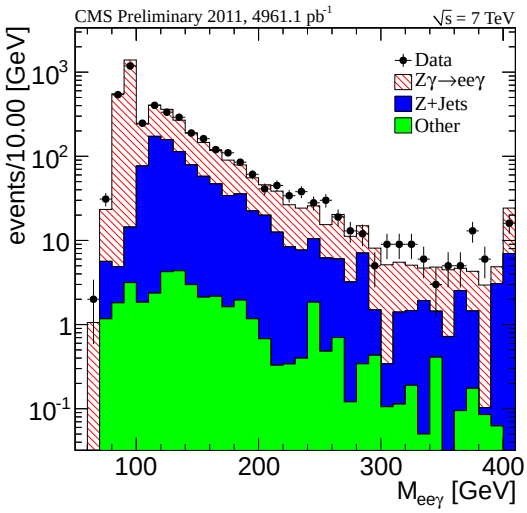

(b) Dielectron + photon invariant mass

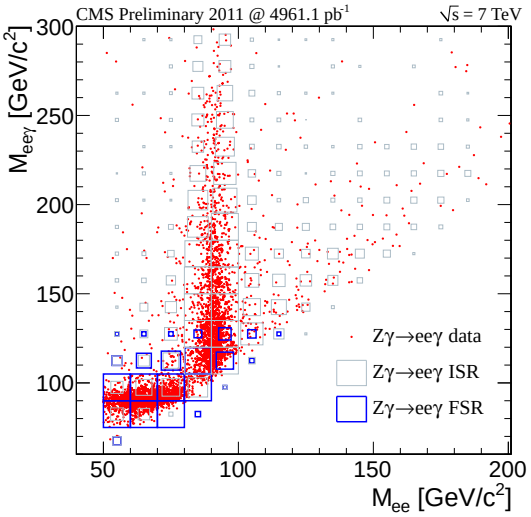

(c) Two-dimensional plot

Figure 5.8: Mass distributions for the selected Z/γ events in the electron channel. Top row: data (black points with error bars) overlaid with the simulation (histograms). The dielectron invariant mass (left) peaks at m_Z for the initial state radiation (ISR). The eeγ invariant mass (right) peaks at m_Z for the final state radiation (FSR). Bottom panel: data (red dots) overlaid with simulation (solid squares; grey for the ISR contribution and blue for the FSR contribution). The size of the squares denotes the density of the events. The ISR and FSR contributions are clearly visible as vertical and horizontal bands at $M_{\mathrm{ee}} \approx m_Z$ and $M_{\mathrm{ee}\gamma} \approx m_Z$, respectively.

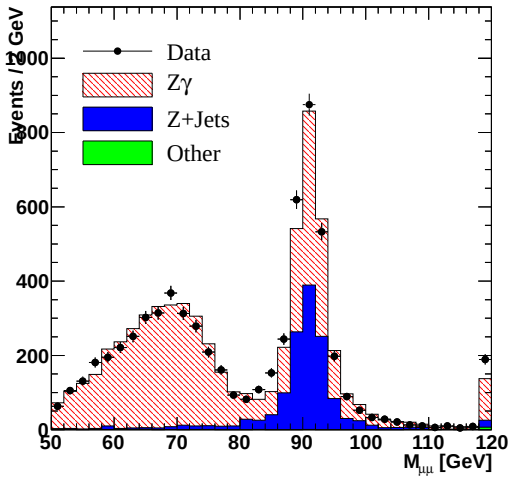

(a) Dimuon invariant mass

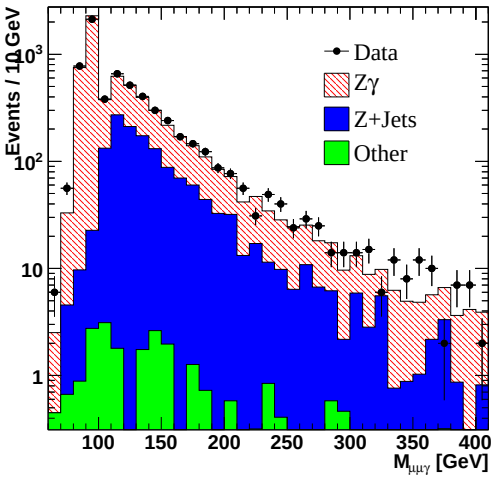

(b) Dimuon + photon invariant mass

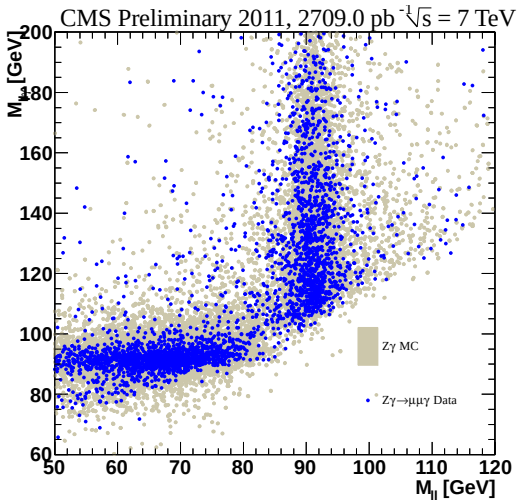

(c) Two-dimensional plot

Figure 5.9: Mass distributions for the selected Z/γ events in the muon channel. Top row: data (black points with error bars) overlaid with the simulation (histograms). Similarly to the electron channel, the dimuon invariant mass (left) peaks at m_Z for the initial state radiation (ISR). The $\mu\mu\gamma$ invariant mass (right) peaks at m_Z for the final state radiation (FSR). Bottom panel: data (solid blue dots) and simulation (solid grey dots). The ISR and FSR contributions are clearly visible as vertical and horizontal bands at $M_{\ell\ell} \approx m_Z$ and $M_{\ell\ell\gamma} \approx m_Z$, respectively.

5.5 Background Estimation

The dominant background comes from inclusive pp $\rightarrow$ Z$+X$ production where a final state jet is misidentified as a photon. We measure the contribution of this background in data, exploiting the difference between the real photons and misidentified jets in the spectrum of the photon candidate shower width $\sigma_{i\eta i\eta}$. We obtain the background yield estimate from an unbinned maximum likelihood fit to a sum of the signal and background components. The signal component is taken from the simulation and corrected by a scaling factor derived from Z $\rightarrow$ e$^+$e$^-$ events. The background component shape is derived from data using photon candidates from a tracker isolation sideband:

$$2\,\mathrm{GeV} < I_{\mathrm{TRK}} - 0.001 p_{\mathrm{T}}^{\gamma} - 0.0167 \varrho_{\mathrm{FJ}} < 5\,\mathrm{GeV} \quad \text{in the Barrel, and}$$
$$2\,\mathrm{GeV} < I_{\mathrm{TRK}} - 0.001 p_{\mathrm{T}}^{\gamma} - 0.0320 \varrho_{\mathrm{FJ}} < 3\,\mathrm{GeV} \quad \text{in the Endcaps.}$$

The templates are built in bins of p_{T}^{γ} since the shower width $\sigma_{i\eta i\eta}$ depends on it slightly. The bin boundaries are at p_{T}^{γ} = 15, 20, 25, 30, 35, 40, 60, 90, 120 and 500 GeV.

Figure 5.10 shows an example of the fit result for photons with $p_{\mathrm{T}}^{\gamma} \in [15, 20)$ GeV.

5.6 PHOSPHOR Fit

The PHOSPHOR Fit is a method to extract the PHOton energy Scale and PHOton energy Resolution in-situ measurement using radiative muonic Z^0 boson decays Z $\rightarrow \mu^+\mu^-\gamma$. It is based on an unbinned maximum likelihood fit of a model for the $\mu\mu\gamma$ invariant mass model $m_{\mu\mu\gamma}$ to the $m_{\mu\mu\gamma}$ values in selected Z $\rightarrow \mu^+\mu^-\gamma$ events in the data. The photon energy scale s and resolution r are parameters of the signal components of the model. They are floated in the fit, together with the signal purity f_{S}, and two more parameters describing the background components of the the model.

We use these measurements to apply corrections to the photon momenta in both

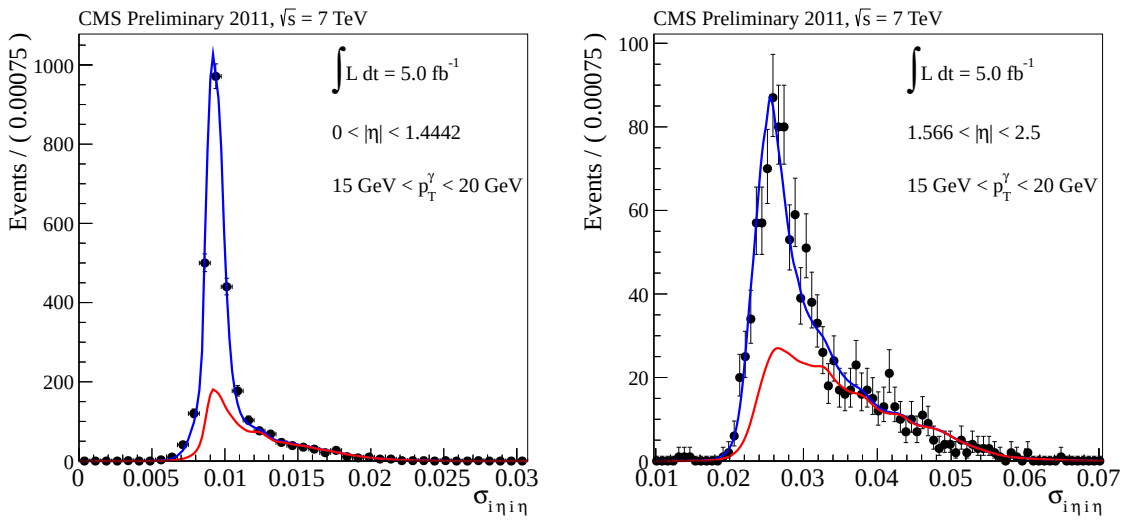

Figure 5.10: An example of a background estimate using the template fit to the shower width $\sigma_{i\eta i\eta}$ for photons in the ECAL barrel (left) and endcaps (right) with $p_{\mathrm{T}} \in [15, 20]$GeV. The black points with error bars represent the data, the solid blue line shows the fitted sum of the signal and background components, the solid red line shows the background component.

the data and the simulation. These corrections improve the photon energy scale for both, and correct the energy resolution in the simulation to match the one in the data. This is important for the cross section measurement because of the cut on the photon p_{T} and the related systematic uncertainty on the acceptance-times-efficiency estimate $\mathcal{F}_{\mathrm{MC}}$.

The goal of the PHOSPHOR fit is to characterize the in-situ ECAL response to photons by two parameters: the photon energy scale s and the photon energy resolution r. Conceptually, this is an ill-defined problem. The ECAL response is a probability density function and as such it has an infinite number of degrees of freedom considering full generality. To deal with this problem, we give up on the generality and restrict ourselves to a subset of considered responses. We use the simulation as a starting point in the description of our response-density phase space. We build its so-called *kernel density estimator* (KDE) [120, 121], and then let its *location* and *scale* vary. We choose the *mode* and the *effective sigma* as the location and scale parameters and interpret them as the photon energy *scale* and *resolution*.[1] Below, we introduce

[1]Mind the clash of the statistical and experimental terminology here: The *scale* parameter of the

this language formally along with other related concepts to specify explicitly what we mean.

5.6.1 Definitions

We define the *photon energy response* (E^γ response) x as:

$$x = \frac{E^\gamma}{E^\gamma_{\text{true}}} - 1$$

where E^γ is the reconstructed photon energy and E^γ_{true} is the true photon energy – the generator level energy in the case of simulation.

The E^γ response is a random variable. We call its probability distribution function the *photon energy response distribution* (*photon energy response density*, E^γ *response distribution*, or E^γ *response density*) and denote it $f(x)$.

The *photon energy scale* s is then the mode — the most probable value or the position of the peak if you like — of $f(x)$:

$$s := \arg\max_x f(x), \tag{5.8}$$

where the *argument of the maximum* operator arg max gives the value of the given argument x for which the given function f attains its maximum value:

$$\arg\max_x f(x) := \{x \,|\, \forall y : f(y) \leq f(x)\}\,.$$

By *photon energy resolution* r we mean the effective sigma — half of the minimum interval of the E^γ response distribution that contains $\approx 68.3\,\%$ of the area under the curve, the same as the area under a Gaussian distribution $\pm 1\sigma$ around its mean.

Strictly speaking, the definition of *signal* as a final state radiation event is ambiguous since (a) every event is radiative and (b) there is interference with the initial state radiation. We define signal through the matching to the generator level topology

photon energy response probability density in the statistical sense refers to the E^γ *resolution* in the experimental sense, **not** the E^γ *scale* as the naming may suggest.

as any event with a photon radiated off of one of the Z legs by the electromagnetic component of the parton shower with a sufficiently large p_{T} to pass our selection criteria. All other events passing our selection criteria are considered *background*.

For most practical purposes of the E^{γ} scale and resolution measurement, the $\mathrm{Z}+\mathrm{jets}$ background has to be considered separately from backgrounds coming from other sources. This is because its invariant mass spectrum peaks at $\approx m_Z + p_{\mathrm{T}}^{\mathrm{cut}}$. Here, $p_{\mathrm{T}}^{\mathrm{cut}}$ is the minimum photon p_{T} threshold. This feature of the $\mathrm{Z}+\mathrm{jets}$ background mass spectrum would bias the measurement of the photon energy scale and resolution if we did not model this background correctly.

Other backgrounds coming from QCD fakes, $W+\mathrm{jet}$ production, $t\bar{t}$ production, and other processes do not have peaking features. Their sum may be well modeled by an exponentially falling distribution.

5.6.2 Monte Carlo Truth

The PHOSPHOR Fit relies on precise knowledge of the true values of the E^{γ} scale and resolution in the simulation. These are also necessary to validate the method. Therefore, a robust and accurate method to extract these values is desirable.

The estimation of the Monte Carlo true E^{γ} scale and resolution would be straightforward if the E^{γ} response followed a simple known density function, like the Gaussian or the Crystal Ball [122]. We could then simply fit it to the simulated E^{γ} response data and interpret its location and scale parameters as the E^{γ} scale and resolution. Unfortunately, this does not seem to be the case.

In Figure 5.11 we fit the Crystal Ball line shape to the E^{γ} response of photons in a subclass of $\mu\mu\gamma$ events. We select only photons in the ECAL barrel with $E_T > 30$ GeV and $R_9 > 0.94$. The fitted function describes the data very poorly due to the tails. The tails are much heavier in the data than the function can model, biasing the fit.

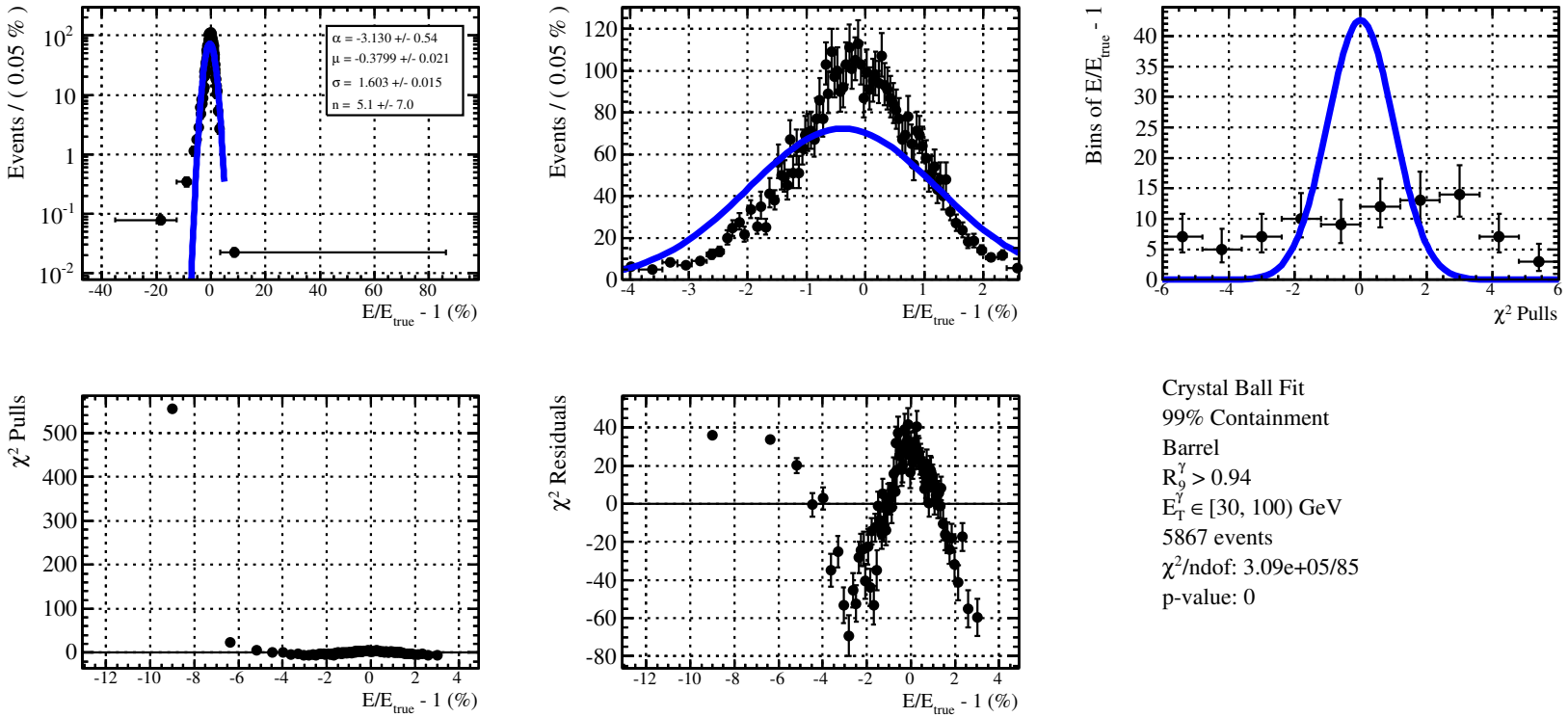

Figure 5.11: An example of E^{γ} response mismodeling by the CB line shape. These events have photons in the ECAL barrel with $E_T > 30$ GeV and $R_9 > 0.94$. The fit range contains 99% of all events. (Top Left) The data and the fitted function on a logarithmic y-axis scale with an x-axis range covering 99.99994% (5-σ) of the data. (Top Middle) The data and the fitted function on a linear y-axis scale with an x-axis range covering 95.4% (2-σ) of the data.

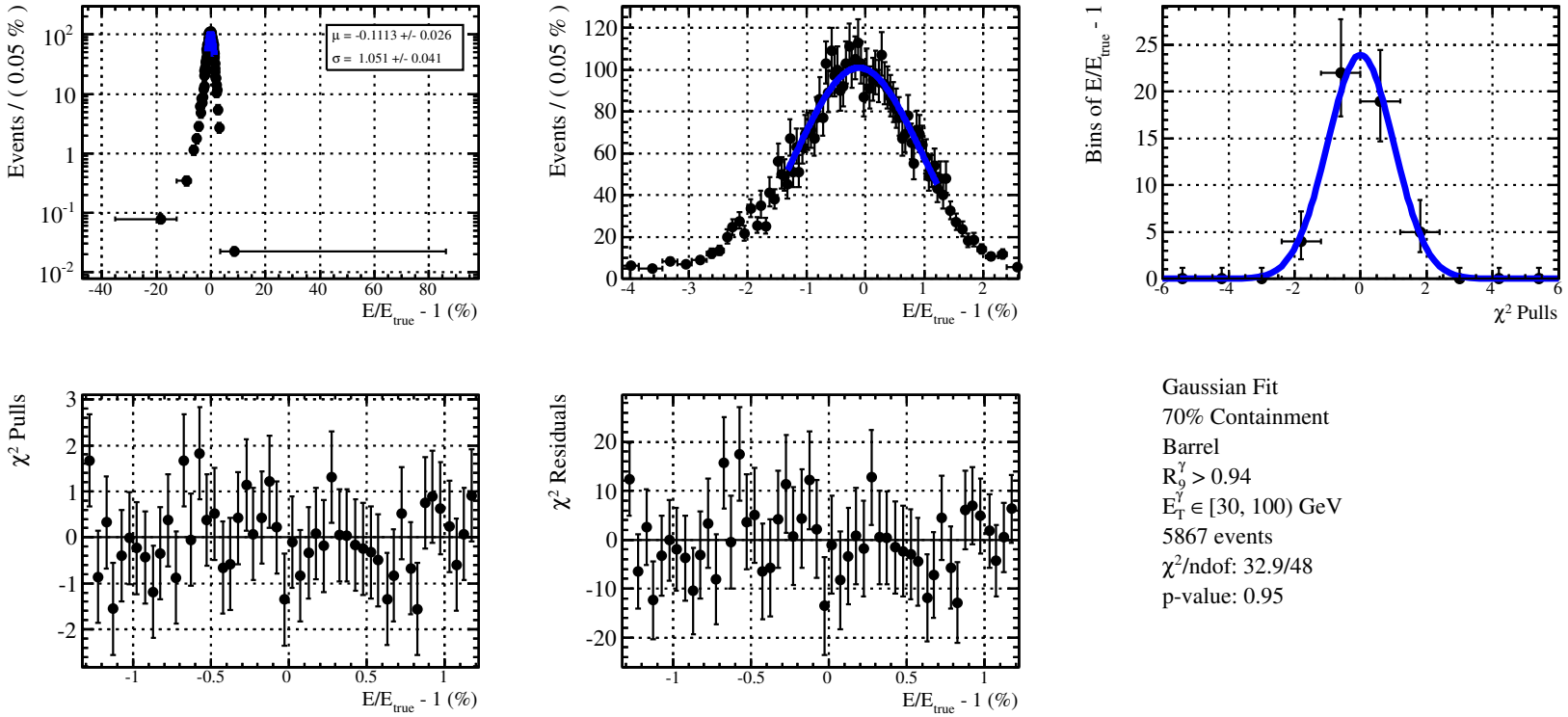

Figure 5.12: An example of a good modeling of the E^{γ} response peak by a Gaussian. (Top Left) The data and the fitted function on a logarithmic y-axis scale with an x-axis range covering 99.99994% (5-σ) of the data. (Top Middle) The data and the fitted function on a linear y-axis scale with an x-axis range covering 95.4% (2-σ) of the data. This fit demonstrates the impact of limiting the range on the goodness of the E^{γ} response modeling. This is to be compared with the reference fit in Figure 5.11. Here, the data is the same (photons in the ECAL barrel with $E_T > 30$ GeV and $R_9 > 0.94$), the model is even simpler (Gaussian instead of the CB line shape) yet — in contrast to the reference fit — the model describes the data reasonably well. The important difference is that the fit range is a modal interval containing only 70% of all events instead of 99%.

To judge the goodness of a fit, we plot the χ^2 residuals and pulls as a function of the observable x. The χ^2 residuals are defined for each bin $i = 1, \ldots, N$ as follows:

$$\Delta n_i = n_i - \nu_i, \tag{5.9}$$

where n_i and ν_i are the numbers of the observed and expected events in the bin i, respectively. Here, the number of the expected events events in the bin i is:

$$\nu_i = \sum_{j=1}^{N} n_j \int_{a_i}^{b_i} f(x|\boldsymbol{\theta})\,\mathrm{d}x, \tag{5.10}$$

where we sum j over all the bins. Here, $f(x|\boldsymbol{\theta})$ is the fitted model depending on P parameters $\boldsymbol{\theta} = \theta_1, \ldots, \theta_P$, and a_i and b_i are the lower and upper boundary of the bin $i = 1, \ldots, N$, respectively. We choose the binning such that $n_i \geq 30$ for $\forall i$. This guaranties that $\nu_i > 5$ for $\forall i$ at a very high confidence level. We define the χ^2 pulls as:

$$\chi_i = \frac{n_i - \nu_i}{\sqrt{\nu_i}} \tag{5.11}$$

High values of the χ^2 residuals and pulls indicate poor compatibility of the model $f(x|\boldsymbol{\theta})$ with the data. For each bin, we plot Δn_i and χ_i at the median x of that bin.

We also plot the distribution of the χ^2 pulls. This should follow a unit Gaussian if the $f(x|\boldsymbol{\theta})$ describes the data well:

$$\chi_i \sim \mathcal{N}(x|0,1). \tag{5.12}$$

Therfore we also overlay the spectrum of χ^2 pulls with a properly normalized unit Gaussian to see their mutual compatibility.

As another goodness-of-fit test, we calculate the χ^2 statistic as [123]:

$$\chi^2 = \sum_{i=1}^{N} \chi_i^2, \tag{5.13}$$

where we sum the index i over all bins. If the data follows the model $f(x|\boldsymbol{\theta})$, the χ^2 statistic approaches a known probability density function (PDF), the so-called χ^2 PDF $f(z|n_\mathrm{d})$. Here, n_d is the *number of degrees of freedom*:

$$n_\mathrm{d} = N - P. \tag{5.14}$$

The χ^2 statistic follows the χ^2 PDF in the limit of high statistic. In practice, the χ^2 PDF is a good approximation of the actual χ^2 distribution when $\nu_i > 5$ for all $i = 1, \ldots, N$ [123]. This condition is satisfied by our choice of the binning. We can thus use the χ^2 PDF to calculate the p-value of the χ^2 statistic as:

$$p = \int_{\chi^2}^{\infty} f(z|n_\mathrm{d})\,\mathrm{d}z. \tag{5.15}$$

The p-value expresses the probability that the χ^2 statistic of a random sample would atain a greater value than the χ^2 statistic of the sample at hand. The p-value should be uniformly distributed. Poor compatibility of the model $f(x|\boldsymbol{\theta})$ with the data leads to low numerical values of the p-value.

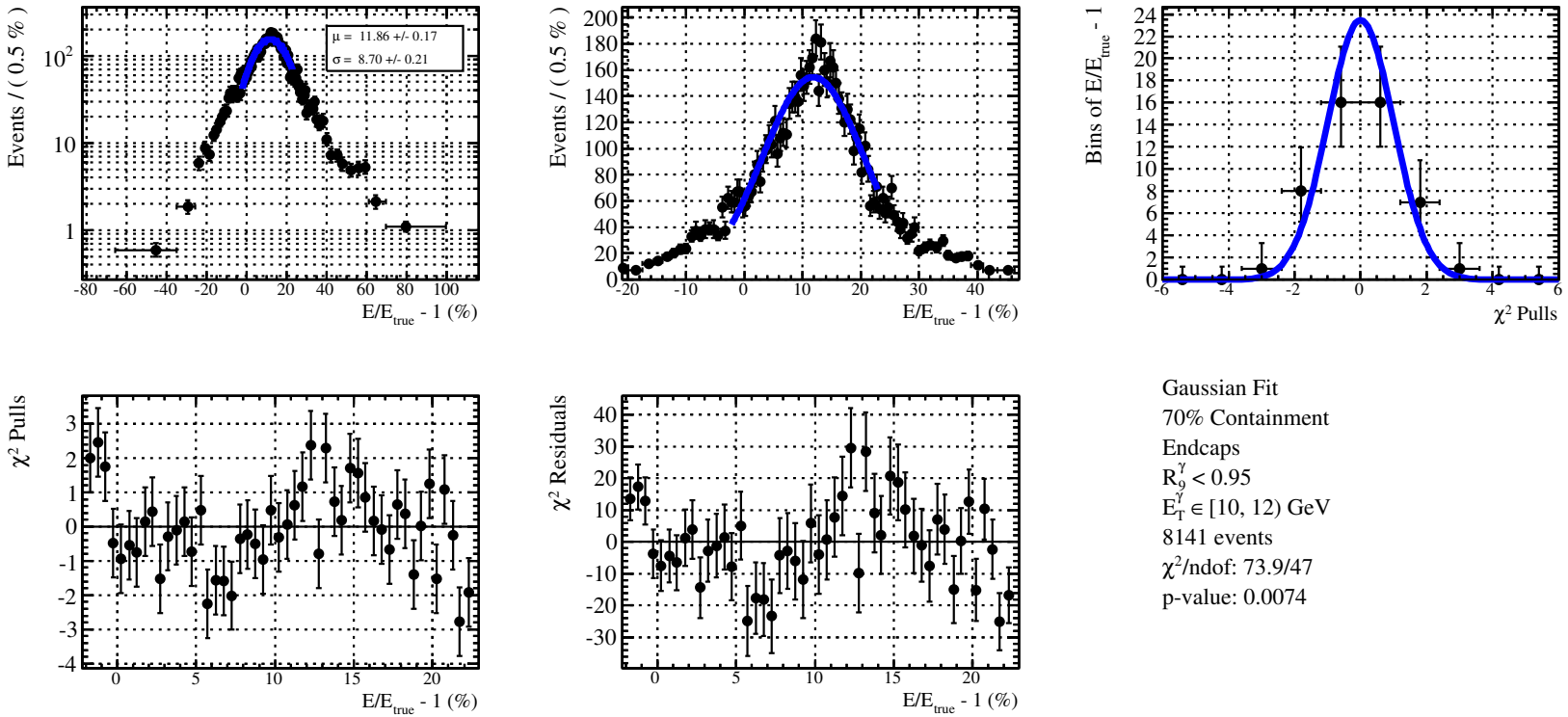

Figure 5.13: An example of the E^{γ} response peak mismodeling by a Gaussian. These events have photons in the ECAL endcaps with E_T =10–12 GeV and $R_9 < 0.94$. The fit range contains 70% of all events. (Top Left) The data and the fitted function on a logarithmic y-axis scale with an x-axis range covering 99.99994% (5-σ) of the data. (Top Middle) The data and the fitted function on a linear y-axis scale with an x-axis range covering 95.4% (2-σ) of the data.

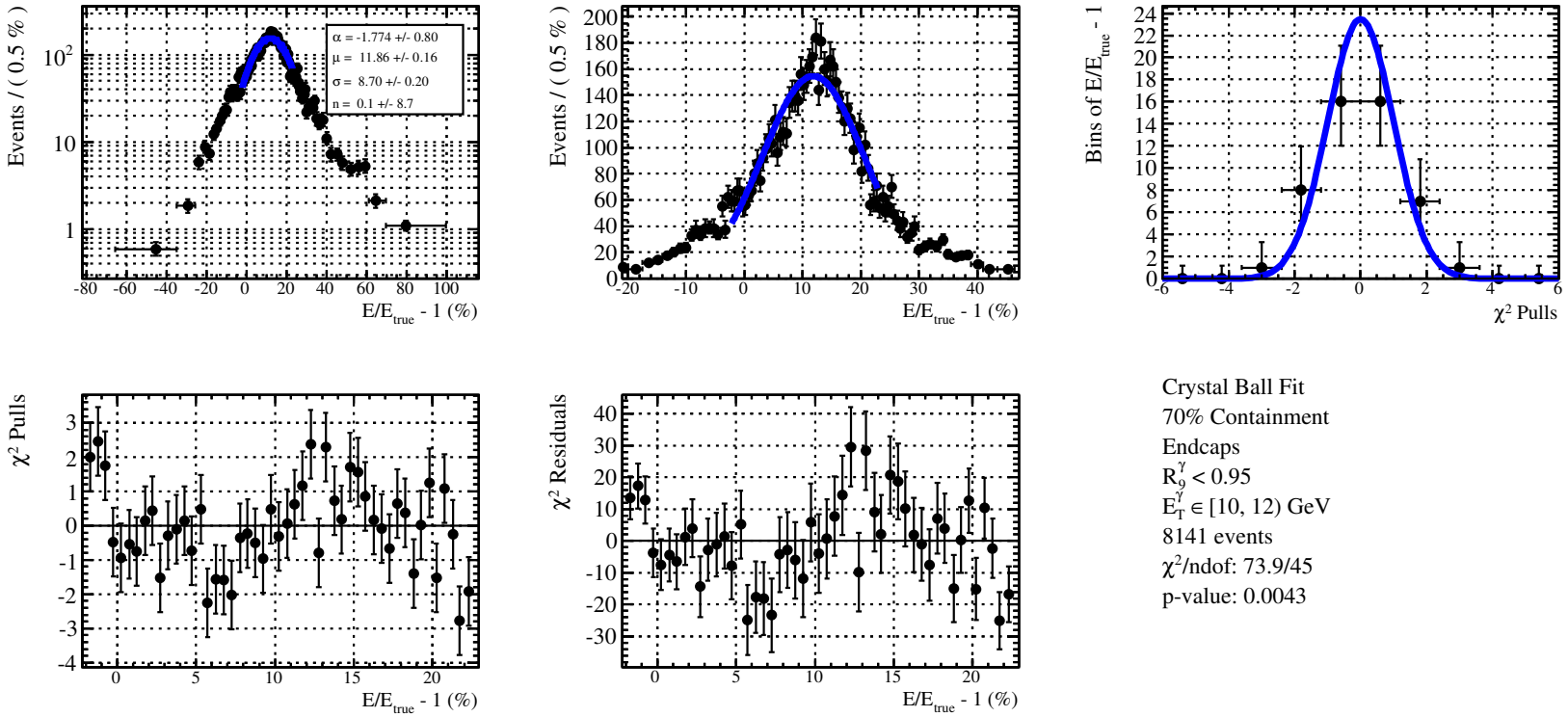

Figure 5.14: An example of the E^{γ} response peak mismodeling by a CB line shape. Same as Figure 5.13 but for the CB line shape instead of a Gaussian.

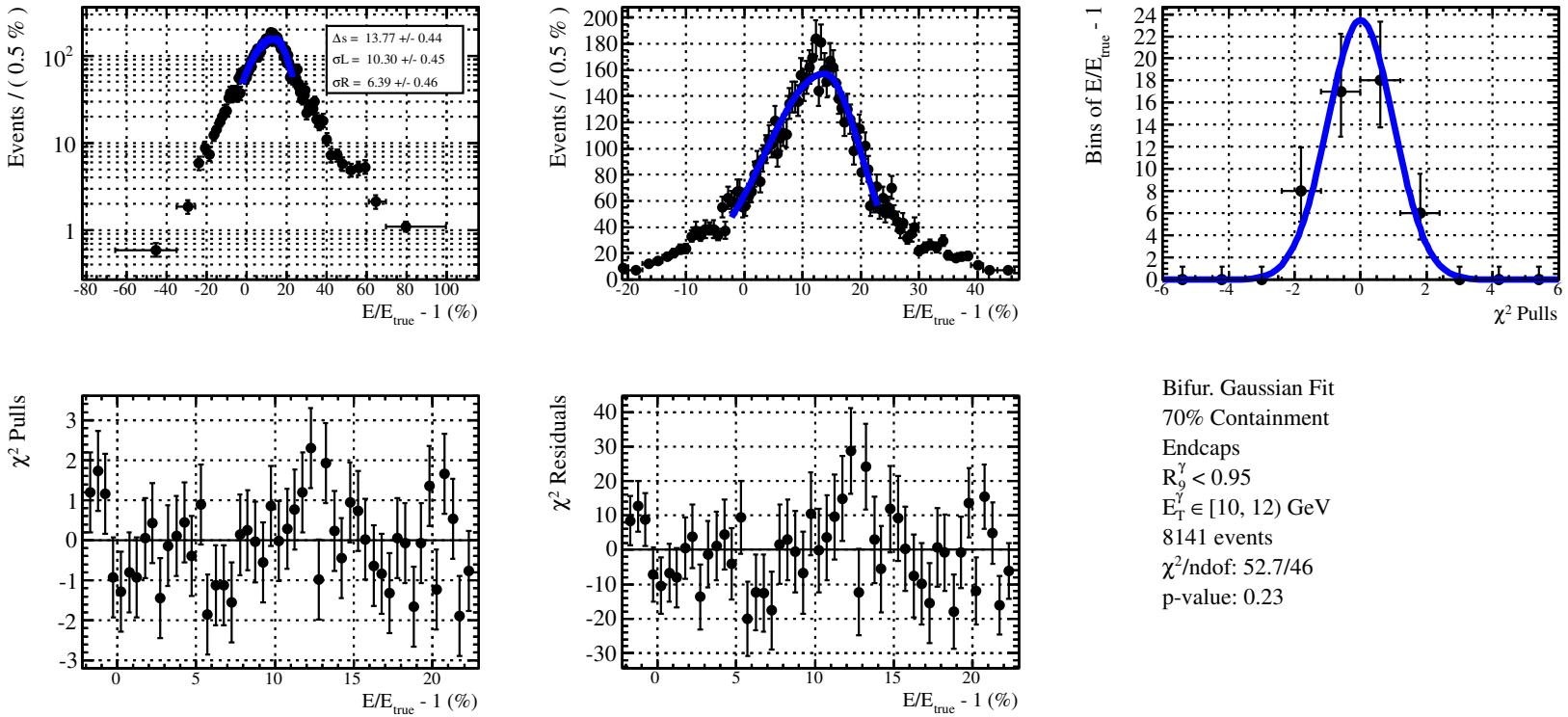

Figure 5.15: An example of the E^{γ} response peak mismodeling by a bifurcated Gaussian. Same as Figure 5.13 but for a bifurcated Gaussian instead of a Gaussian.

The poor modeling of the tails can be mitigated by fitting a subset of the data near the peak, see Figure 5.12. However, reducing the fit range leads to additional systematics due to the fit range and is very fragile since the behavior varies greatly among various photon categories based on the photon p_{T}, η and R_9. Figures 5.13–5.15 demonstrate the limitation of this approach for photons in the endcaps with $E_T \in [10, 20]$ GeV and $R_9 < 0.94$, for increasingly complex analytical models.

5.6.3 Photon Energy Response Model

It turns out that it is more robust and precise to use the sample of the energy responses (from the simulation) to build the model. We smooth it with a kernel density estimator to obtain a non-parametric estimate of the photon energy response density.

We use the so-called *KEYS* estimator developed specifically for applications in high energy physics [124]. It is bin-independent, scale invariant, continuously differentiable, positive definite, and everywhere defined. It employs an adaptive kernel bandwidth which has the advantage that it depends on the data only locally. This enables it to handle a wide variety of distributions.

Given a *training data sample* $\{t_i\}_{i=1}^n$ drawn from some unknown probability density $f(x)$ the estimate of which we seek, the E^γ response distribution in our case, the construction of the KEYS estimator proceeds in two steps. First, a fixed kernel bandwidth h is used to obtain the estimate $\hat{f}_0(x)$. This then serves as an input in the definition of the adaptive kernel bandwidth b_i, $i = 1, \ldots, n$, used to build the final estimator $\hat{f}_1(x)$. The fixed bandwidth is defined as:

$$h = \left(\frac{4}{3}\right)^{1/5} n^{-1/5}\sigma,$$

where σ is the estimate of the standard deviation of $f(x)$:

$$\sigma^2 = \frac{n}{n-1}\left[\frac{1}{n}\sum_{i=1}^{n} t_i^2 - \left(\frac{1}{n}\sum_{i=1}^{n} t_i\right)^2\right].$$

The fixed bandwidth estimate is then:

$$\hat{f}_0(x) = \frac{1}{nh} \sum_{i=1}^{n} K\left(\frac{x - t_i}{h}\right),$$

where K is a Gaussian kernel:

$$K(x) = \frac{1}{\sqrt{2\pi}} e^{-x^2/2}.$$

Using $\hat{f}_0(x)$, the adaptive kernel bandwidth corresponding to a data point $i = 1, \ldots, n$ is:

$$b_i = \varrho_{\mathrm{KEYS}} \left(\frac{4}{3}\right)^{1/5} n^{-1/5} \sqrt{\frac{\sigma}{\hat{f}_0(t_i)}},$$

where ϱ_{KEYS} is a free parameter of the model. Given the bandwidths $\{b_i\}_{i=1}^{n}$, the KEYS estimate reads:

$$\hat{f}_1(x) = \frac{1}{n} \sum_{i=1}^{n} \frac{1}{b_i} K\left(\frac{x - t_i}{b_i}\right). \tag{5.16}$$

The free parameter ϱ_{KEYS} relates the local and global scale of the structure of the data σ_{local} and σ, respectively:

$$\varrho_{\mathrm{KEYS}} = \sqrt{\frac{\sigma_{\mathrm{local}}}{\sigma}}.$$

Its default value is $\varrho_{\mathrm{KEYS}} = 1$. Greater numerical values of ϱ_{KEYS} lead to smoother estimates, while smaller numerical values of ϱ_{KEYS} lead to better estimates of fine details in the structure of the data. The latter may be useful for example for bimodal distributions, for which the σ_{local} and σ may differ significantly. The estimates, in which we are interested, do not depend strongly on the value of ϱ_{KEYS}. We use the value $\varrho_{\mathrm{KEYS}} = 1.5$, which minimizes the fluctuations in the position of the peak, while preserving the width of the distribution. Lower values of ϱ_{KEYS} lead to greater fluctuations in the peak position while greater values of ϱ_{KEYS} lead to estimates with width greater than the training data, see Figure 5.16.

To simplify the notation, we denote the KEYS estimator of the E^{γ} response distribution $f_0(x) := \hat{f}_1(x)$. Here, the subscript "0" signifies that this is the estimator

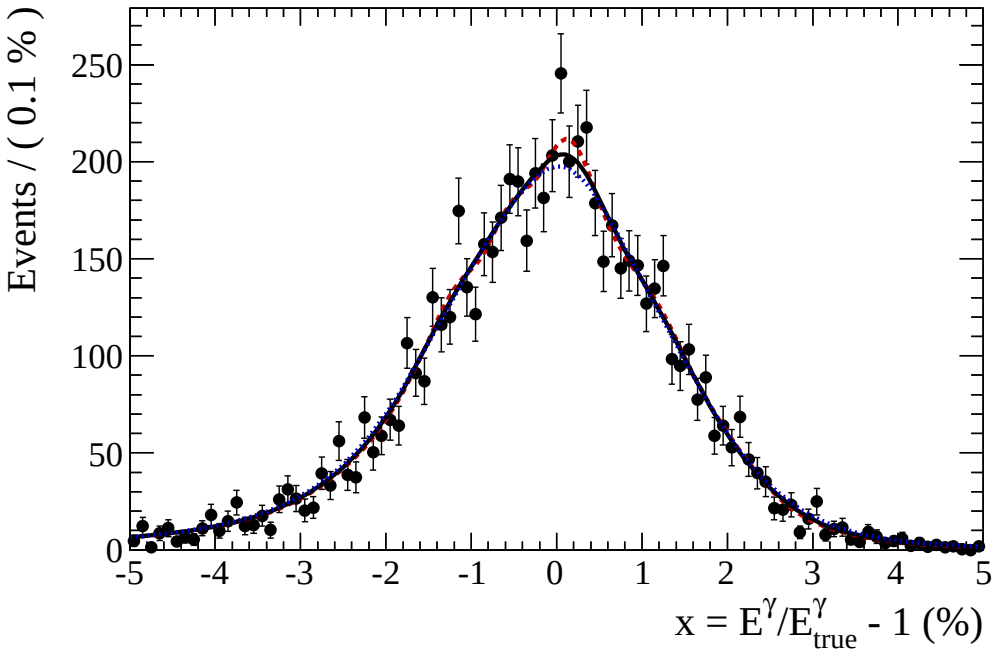

Figure 5.16: An illustration of the dependence of a KEYS estimator of the E^{γ} response density on the parameter ϱ_{KEYS}. The dashed red, solid black, and dotted blue lines correspond to KEYS estimators constructed with values of the parameter $\varrho_{\mathrm{KEYS}} = 1.0$, 1.5 and 2.0, respectively. The black dots with error bars represent the simulated data used to "train" the estimators. The dashed red curve corresponding to $\varrho_{\mathrm{KEYS}} = 1.0$ is slightly more susceptible to random fluctuations of the peak position due to the limited size of the training sample. The dotted blue curve corresponding to $\varrho_{\mathrm{KEYS}} = 2.0$ is slightly broader.

corresponding to the nominal E^γ response in the simulation. We denote the scale and resolution corresponding to the energy response density estimate $f_0(x)$ as s_0 and r_0, respectively. Invoking the definitions introduced in Section 5.6.1, they read:

$$\begin{aligned} s_0 &= \arg\max_x f_0(x), \\ r_0 &= \min\left\{ \frac{|b-a|}{2} \;\middle|\; \int_a^b f_0(x)\,\mathrm{d}x = \frac{1}{\sqrt{2\pi}} \int_{-1}^{1} e^{-x^2/2}\,\mathrm{d}x = \operatorname{erf}\frac{1}{\sqrt{2}} \approx 0.683 \right\}. \end{aligned} \tag{5.17}$$

We then introduce the dependence on the scale s and resolution r by a linear transformation of the observable:

$$\begin{aligned} x \to x' = \alpha(s,r) + \beta(r)\,x = x_0(x,s,r), \\ f_0(x) \to f(x|s,r) = \beta(r) f_0(x_0(x,s,r)), \end{aligned} \tag{5.18}$$

where the transformed photon energy response $x' = x_0(x,s,r)$ is given by:

$$\frac{x-s}{r} = \frac{x_0 - s_0}{r_0}. \tag{5.19}$$

Solving this relation for x_0 gives:

$$\begin{aligned} \alpha(s,r) &= s_0 - s\frac{r_0}{r} = \frac{1}{r}(s_0 r - s r_0) = r_0\left(\frac{s_0}{r_0} - \frac{s}{r}\right), \\ \beta(r) &= \frac{r_0}{r}, \\ x_0(x,s,r) &= s_0 + r_0\frac{x-s}{r}. \end{aligned} \tag{5.20}$$

Plugging (5.20) in the second line of (5.18), we obtain a model for the E^γ response distribution based on a parameterized KEYS PDF estimator that depends on the E^γ scale s and resolution r:

$$f(x|s,r) = \frac{r_0}{r}\, f_0\left(s_0 + r_0\frac{x-s}{r}\right), \tag{5.21}$$

where $f_0(x) := \hat{f}_1(x)$ is the KEYS PDF estimate given by (5.16), s_0 is its corresponding scale given by (5.17), and r_0 is its corresponding resolution given also by (5.17).

Here, s and r play the roles of the scale and resolution corresponding to $f(x|s,r)$, as defined in Section 5.6.1. For the scale s, this can be seen in the following way:

$$\begin{aligned}
f(s|s,r) &= \frac{r_0}{r} f_0(s_0) && && \text{by (5.21)} \\
&\geq \frac{r_0}{r} f_0(y_0) && \text{for } \forall y_0 && \text{by (5.8) and (5.17)} \\
&\geq \frac{r_0}{r} f_0\left(s_0 + r_0 \frac{y-s}{r}\right) && \text{for } \forall y && \text{setting } y_0 = s_0 + r_0 \frac{y-s}{r} \\
&\geq f(y|s,r) && \text{for } \forall y && \text{by (5.21),}
\end{aligned}$$

which matches the definition (5.8) for s being the scale corresponding to $f(x|s,r)$.

To verify that r plays the role of the resolution, we write:

$$\begin{aligned}
\int_a^b f(x|s,r)\,\mathrm{d}x &= \frac{r_0}{r} \int_a^b f_0\left(s_0 + r_0 \frac{x-s}{r}\right)\,\mathrm{d}x && \text{by (5.21)} \\
&= \int_{s_0 + r_0(a-s)/r}^{s_0 + r_0(b-s)/r} f_0(x_0)\,\mathrm{d}x_0 && \text{setting } x_0 = s_0 + r_0 \frac{x-s}{r} \\
&= \int_{a_0}^{b_0} f_0(x_0)\,\mathrm{d}x_0, && && (5.22)
\end{aligned}$$

where we define a_0 and b_0 as:

$$\begin{aligned}
a_0 &= s_0 + r_0 \frac{a-s}{r}, \quad \text{and} \\
b_0 &= s_0 + r_0 \frac{b-s}{r},
\end{aligned}$$

which gives:

$$b_0 - a_0 = \frac{r_0}{r}(b-a). \tag{5.23}$$

Plugging this in the definition of resolution, we obtain:

$$
\begin{aligned}
&\min\left\{\frac{|b-a|}{2}\;\middle|\;\int_a^b f(x|s,r)\,\mathrm{d}x = \operatorname{erf}\frac{1}{\sqrt{2}}\right\} \\
&= \frac{r}{r_0}\min\left\{\frac{|b_0-a_0|}{2}\;\middle|\;\int_{a_0}^{b_0} f_0(x_0)\,\mathrm{d}x_0 = \operatorname{erf}\frac{1}{\sqrt{2}}\right\} && \text{by (5.22) and (5.23)} \\
&= \frac{r}{r_0}\cdot r_0 && \text{by (5.17)} \\
&= r,
\end{aligned}
$$

which is what we wanted to show.

Figures 5.17 and 5.18 show examples of so-constructed E^γ response model and its dependence on the scale and resolution, respectively.

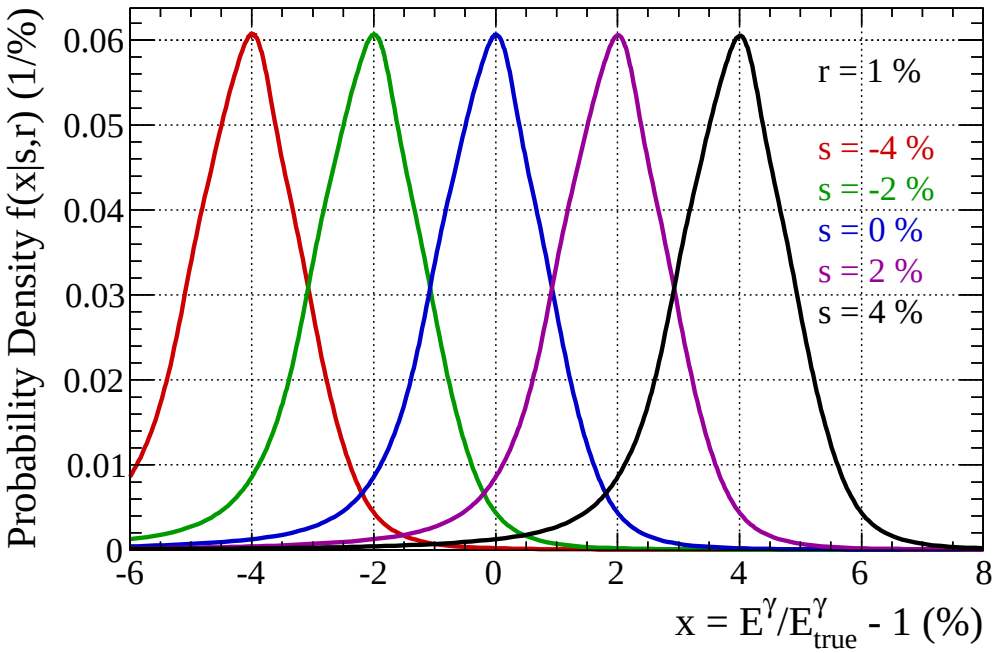

Figure 5.17: An illustration of the scale dependence of a transformed KDE E^γ response model. We plot the model for a fixed value of the resolution $r = 1\,\%$, and five different values of the scale. The solid red, green, blue, magenta and black lines correspond to scale values of $s = -4\,\%$, $-2\,\%$, $0\,\%$, $2\,\%$ and $4\,\%$, respectively. The curves peak at the given values of the scale as expected.

Having constructed a robust E^γ response density model, we can now obtain the

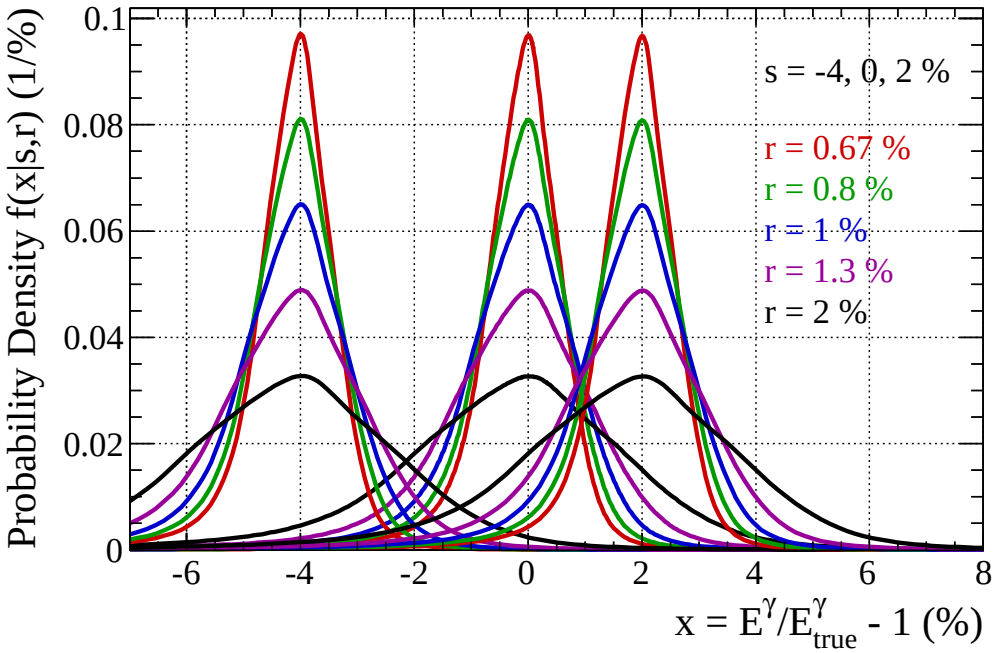

Figure 5.18: An illustration of the resolution dependence of a transformed KDE E^γ response model. We plot the model for different values of scale and resolution. The three sets of five curves peaking at the same location correspond to three different values of the scale. The left, center, and right peaks correspond to scale values of $s = -4\,\%$, $0\,\%$ and $2\,\%$, respectively. The solid red, green, blue, magenta and black lines correspond to resolution values of $r = 0.67\,\%$, $0.8\,\%$, $1.0\,\%$, $1.3\,\%$ and $2.0\,\%$, respectively. The curves become wider with increasing values of r, as expected. Also, all curves corresponding to a given scale peak at the same location, independent of their width. This illustrates that there is no bias on the scale due to the resolution. Conversely, the same-color threesomes of curves, corresponding to the same values of the resolution r, have the same widths, independent of their locations. This illustrates that there is no bias on the resolution due to the scale.

scale and resolution estimates and their uncertainties from an unbinned maximum likelihood fit back to the training sample, see Figure 5.19. Figures 5.20 and 5.21 show further examples of such fits demonstrating that the models describe the data well in the full range, including the tails.

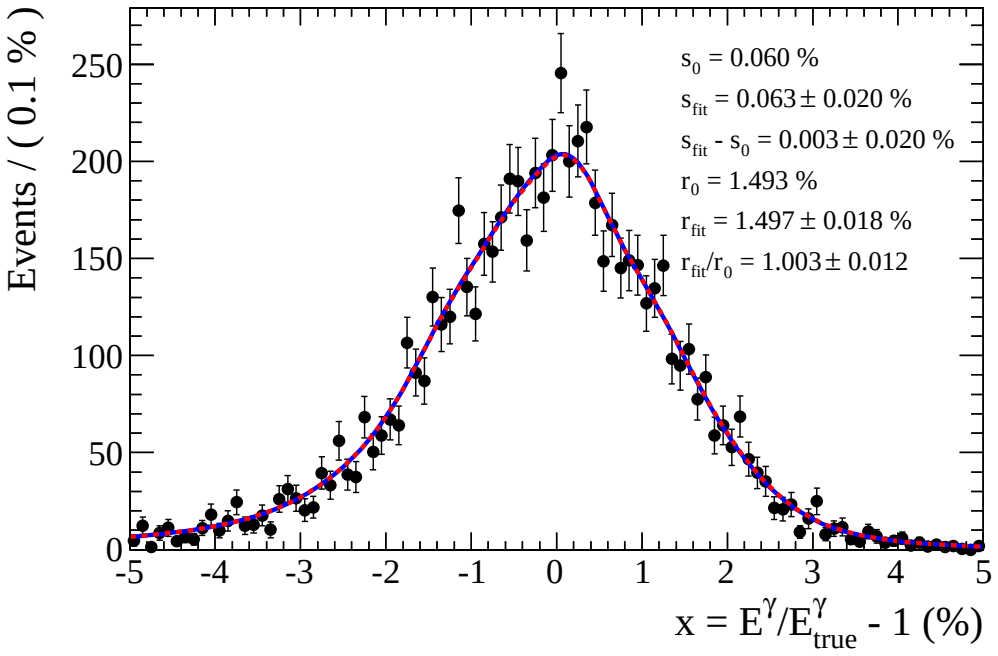

Figure 5.19: An example fit of a parameterized KEYS PDF model of the E^γ response distribution. The black points with error bars represent the training sample $\{t_i\}_{i=1}^n$, the solid blue line shows the KEYS PDF $f_0(x)$ given by (5.16), with the scale s_0 and resolution r_0 from (5.17). The dashed red line shows the parameterized KEYS PDF $f(x|s_{\text{fit}}, r_{\text{fit}})$ given by (5.21). We also show the scale and resolution estimates s_{fit} and r_{fit} and their uncertainties, as obtained from an unbinned maximum likelihood fit of $f(x|s, r)$ to the shown training sample $\{t_i\}_{i=1}^n$. They agree with s_0 and r_0 within their uncertainties. This agreement represents a successful sanity check of both the concept behind the use of a parameterized KEYS PDF to model the E^γ response, as well as its software implementation.

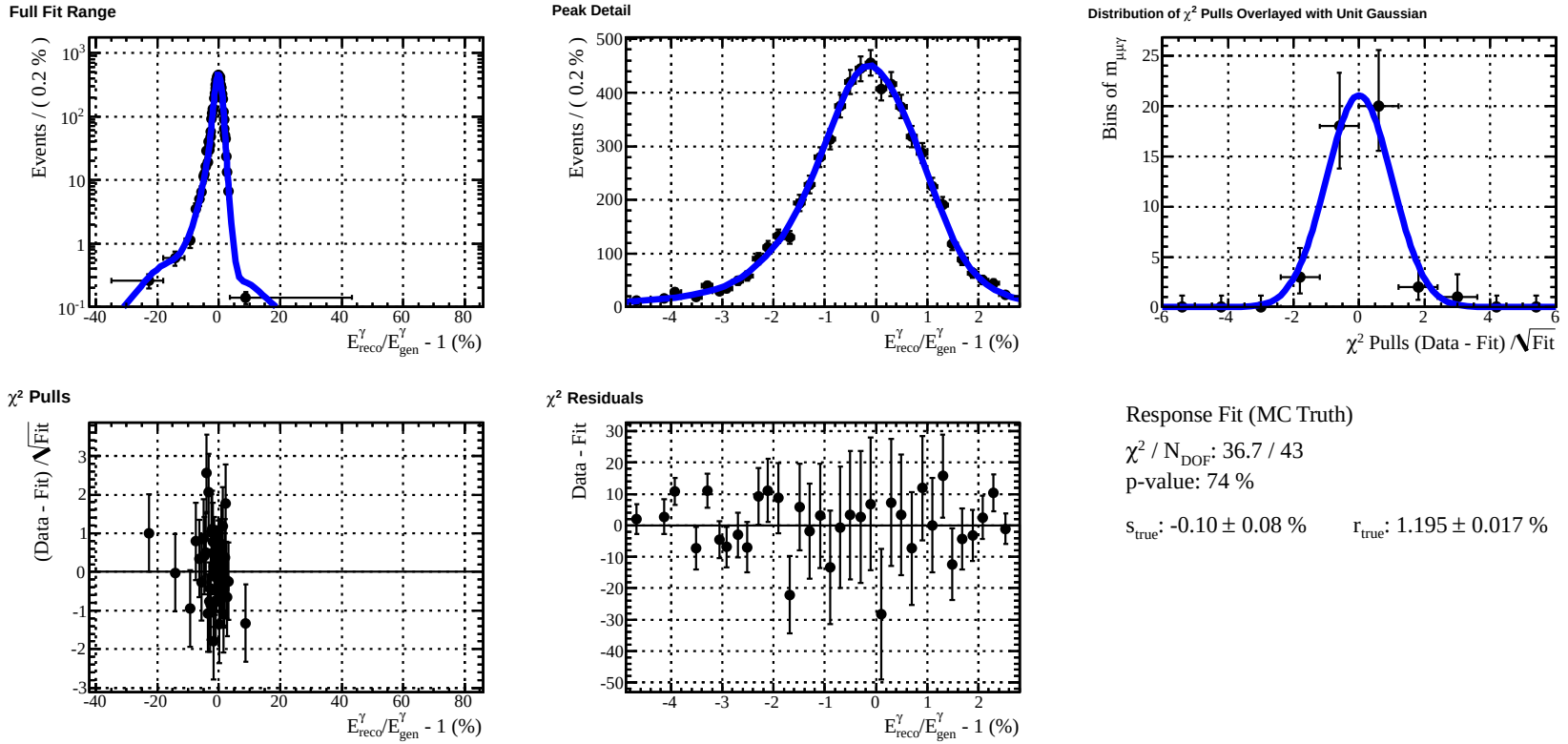

Figure 5.20: An example of the E^{γ} response modeling by a parameterized KEYS PDF for photons in the ECAL barrel with $E_T > 30$ GeV and $R_9 > 0.94$. This is similar to fits shown Figures 5.11 and 5.12 but the model here is fitted in the full range. In contrast to the models shown in the other Figures, the model here describes the data well, including the tails.

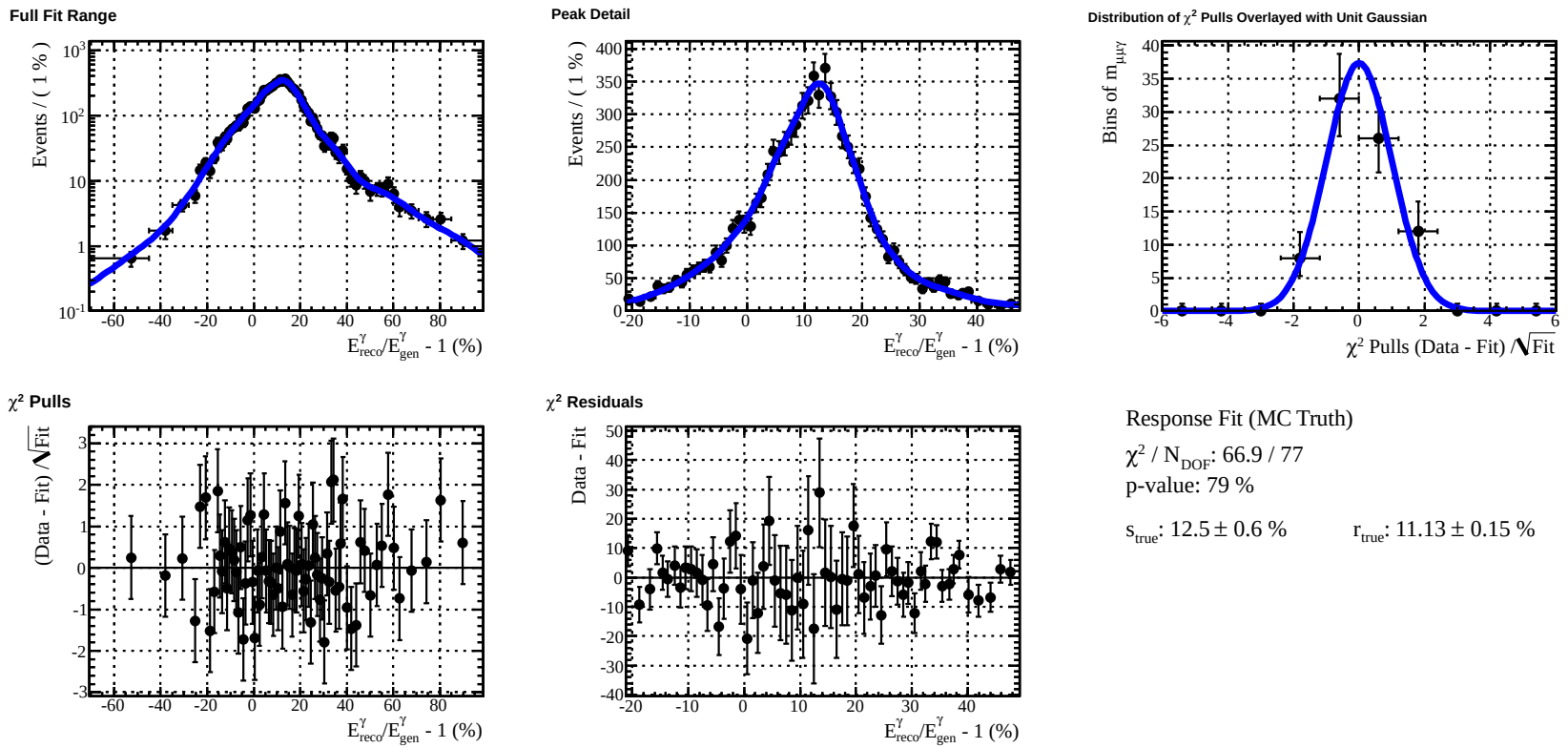

Figure 5.21: Another example of the E^{γ} response modeling by a parameterized KEYS PDF. Here, we show photons in the ECAL endcaps with $E_T \in [10, 12]$ GeV and $R_9 < 0.95$. These photons have a relatively poor resolution compared to those used in Figure 5.20. The sample used here is similar to the one used in Figures 5.13-5.15 but the model here is fitted in the full range. In contrast to the models shown in the other three Figures, the model here describes the data well, including the tails.

5.6.4 Monte Carlo Smearing

The E^γ response in-situ differs from the one in the simulation. It is useful to use a simple parameterization of this difference that provides a prescription to modify the photon energies $\{E_i^\gamma\}_{i=1}^n$ in the simulation for all photon candidates. That way, we can propagate the changes to photon energies to changes in the $\mu\mu\gamma$ invariant mass candidate-by-candidate. Comparing the smeared $\mu\mu\gamma$ mass spectrum with the $\mu\mu\gamma$ data enables us to make inferences about the unknown E^γ response in the data.

One such prescription, which is common in high energy physics, is to inject a Gaussian smearing:

$$E_i^\gamma \to E_i^{\gamma\prime} = E_i^\gamma + \Delta E_i^\gamma, \tag{5.24}$$

where $E_i^{\gamma\prime}$ is the smeared energy of the photon candidate i, and $\Delta E_i^\gamma = E_i^\gamma \Delta e_i$ is the injected energy smearing. Here, Δe_i is a randomly generated dimensionless number, usually following the normal distribution:

$$\Delta e_i \sim \mathcal{N}(x|\Delta s, \Delta r), \tag{5.25}$$

where Δs and Δr are free parameters.

Such a smearing of the simulated energies is equivalent to modifying the response values $x_i = E_i^\gamma / E_{\text{true},i}^\gamma - 1$ to $x_i' = E_i^{\gamma\prime} / E_{\text{true},i}^\gamma - 1$ in the following way:

$$x_i \to x_i' = x_i + \Delta x_i, \tag{5.26}$$

where

$$\begin{aligned} \Delta x_i &= \Delta e_i + \underbrace{x_i \Delta e_i}_{\approx 0} \\ &\approx \Delta e_i. \end{aligned} \tag{5.27}$$

Note that the nominal response values x_i, and the values of the injected response smearing Δx_i are independent, and thus uncorrelated. Therefore, we call this method

of Monte Carlo smearing the *uncorrelated smearing*, or *Gaussian smearing*.

As a consequence of the fact that x_i and Δx_i are independent, the smeared energies $E_i^{\gamma\prime}$ correspond to a smeared response $f'(x)$ which is a convolution of the nominal response $f(x)$ and the injected smearing $\mathcal{N}(x|\Delta s, \Delta r)$:

$$f(x) \to f'(x) \approx \int_{-\infty}^{\infty} f(y)\,\mathcal{N}(x-y|\Delta s, \Delta r)\,\mathrm{d}y, \tag{5.28}$$

where

$$\begin{aligned} x_i &\sim f(x), \quad \text{and} \\ x'_i &\sim f'(x). \end{aligned}$$

The relation for $f'(x)$ (5.28) is not mathematically exact because we neglect the term $x_i \Delta e_i$ in (5.27). In practice however, this is a very good approximation, since both, the nominal resolution r, and the injected smearing Δr, are significantly smaller than unity: $r \ll 1$, $\Delta r \ll 1$. The examples shown in Figures 5.20 and 5.21 correspond to $r = 0.0120 \pm 0.0002$ and $r = 0.111 \pm 0.002$, respectively. These represent extreme values on the opposite ends of the range of typical values of r for photons at CMS. The smearing values are typically even smaller than the resolution values: $\Delta r \lessapprox r$.

If the nominal response $f(x)$ is Gaussian with a nominal scale s and a nominal resolution r, and the smearing is Gaussian as in (5.25), then the smeared response $f'(x)$ is (approximately) also Gaussian:

$$f(x) = \mathcal{N}(x|s, r) \quad \Rightarrow \quad f'(x) \approx \mathcal{N}(x|s', r'), \tag{5.29}$$

which follows from (5.28). This relation would be exact if (5.28) was exact. The corresponding smeared scale s' and the smeared resolution r' are:

$$\begin{aligned} s &\to s' = s + \Delta s \\ r &\to r' = \sqrt{r^2 + (\Delta r)^2}. \end{aligned} \tag{5.30}$$

Despite its straightforwardness and ubiquity, the Gaussian smearing has a number

of features that make it less attractive:

- It can only model resolution values that are greater or equal to the nominal ones $r' \geq r$.
- The generation of the random values Δx_i is computationally expensive.
- The Gaussian smearing (5.25) may not model well the behavior of the tails which are often non-Gaussian, cf. Figures 5.12 and 5.13.
- It is nondeterministic in the sense that repeated calculations involving a smearing of the same sample $\{E_i^\gamma\}_{i=1}^n$ with the same Δs and Δr do **not** lead to the exact same results each time[2]. This may lead to difficulties with the technical implementation, for instance when we use MINUIT [125] to find the values Δs and Δr from a fit of the smeared simulation to the data.
- Finally, the nominal resolution typically varies as a function of kinematics and other variables within the sample. The uncorrelated smearing treats all candidates on the same footing, independent of their "local" scale and resolution. It smears them by the same amount. This may lead to an over-smearing of candidates with relatively good resolution, and an under-smearing of candidates with relatively poor resolution.

To avoid these aspects of the uncorrelated smearing, we choose a different approach to the Monte Carlo smearing.

To smear the simulation, we proceed in analogy to the way we introduced the energy and scale dependence of the response model $f(x|s,r)$ in Section 5.6.3: we linearly transform the response. The difference to the construction of $f(x|s,r)$ is that here we seek a prescription for the modification of the photon energies, an alternative to (5.24). We start with the relation analogous to (5.19) but we rewrite it using the notation introduced in this Section:

$$\frac{x_i' - s'}{r'} = \frac{x_i - s}{r}. \tag{5.31}$$

[2]This issue can be avoided if special care is taken to synchronize the seeds of the random generator with the candidate index i and the smearing parameters Δs and Δr.

This gives the following expression for the smeared response:

$$\begin{aligned} x_i \to x_i' &= x_i + \Delta x_i \\ &= s' + r' \frac{x_i - s}{r}, \end{aligned} \tag{5.32}$$

and for the injected response smearing:

$$\begin{aligned} \Delta x_i &= x_i' - x_i \\ &= s' - \frac{r'}{r} s + \left(\frac{r'}{r} - 1 \right) x_i. \end{aligned} \tag{5.33}$$

Note that here, in contrast to (5.27), the Δx_i depends on x_i, and so x_i and Δx_i are correlated. Therefore, we refer to this way of smearing the Monte Carlo as the *correlated smearing*.

The correlated smearing leads to the following expression for the smearing of the energies:

$$\begin{aligned} \Delta E_i^\gamma &= E_{\text{true},i}^\gamma \Delta x_i \\ &= \left(\frac{r'}{r} - 1 \right) (E_i^\gamma - E_{\text{true},i}^\gamma) + \left(s' - \frac{r'}{r} s \right) E_{\text{true},i}^\gamma, \end{aligned} \tag{5.34}$$

where ΔE_i^γ is to be plugged into (5.24). This relation exposes the challenge of applying the correlated smearing over applying the uncorrelated smearing. To apply the uncorrelated smearing, we only need to choose some values of Δs and Δr. This is equivalent to choosing the target smeared scale s' and the target smeared resolution r' in the case of the correlated smearing. However, for the correlated smearing, we need to know additional quantities, namely the nominal scale s, the nominal resolution r, and the true photon energy $E_{\text{true},i}^\gamma$. This is the price to pay for avoiding the above listed inconveniences of the uncorrelated smearing. We deal with it in the following way. We use the energy of a generator-level photon matched to the reconstructed photon candidate i for the value of $E_{\text{true},i}^\gamma$. We use the method described in Section 5.6.3 to obtain the values of the nominal scale and resolution. This further exemplifies the importance of a robust and precise method for the estimation of MC

true scale and resolution.

The relation for the smeared response density corresponding to the correlated smearing is:

$$f'(x) = \frac{r}{r'} f\left(s + r\frac{x - s'}{r'}\right). \tag{5.35}$$

Similarly to the uncorrelated smearing, a Gaussian nominal response leads to a Gaussian smeared response:

$$f(x) = \mathcal{N}(x|s, r) \quad \Rightarrow \quad f'(x) = \mathcal{N}(x|s', r'). \tag{5.36}$$

Moreover, if the response is a parameterized KEYS PDF $f(x|s, r)$ given by (5.21), then the smeared response is again a parameterized KEYS PDF:

$$f(x) = f(x|s, r) \quad \Rightarrow \quad f'(x) = f(x|s', r'), \tag{5.37}$$

This can be seen in the following way:

$$\begin{aligned}
f'(x) &= \frac{r}{r'} f\left(s + r\frac{x - s'}{r'}\middle| s, r\right) && \text{by inserting } f(x) = f(x|s, r) \text{ in (5.35)} \\
&= \frac{r}{r'}\frac{r_0}{r} f\left(s_0 + r_0\frac{s + r\frac{x-s'}{r'} - s}{r}\right) && \text{by (5.21)} \\
&= \frac{r_0}{r'} f\left(s_0 + r_0\frac{x - s'}{r'}\right) \\
&= f(x|s', r'), && \text{by (5.21)}
\end{aligned}$$

So we see that the our definitions of the correlated smearing (5.34) and the parameterized KEYS PDF model (5.21) are mutual consistent. Figures 5.22 and 5.23 show the effect of the correlated smearing for varying values of target smeared scale s' and resolution r', respectively, as well as an explicit test of this consistency.

To propagate the effect of the photon energy smearing to the change in the $\mu\mu\gamma$

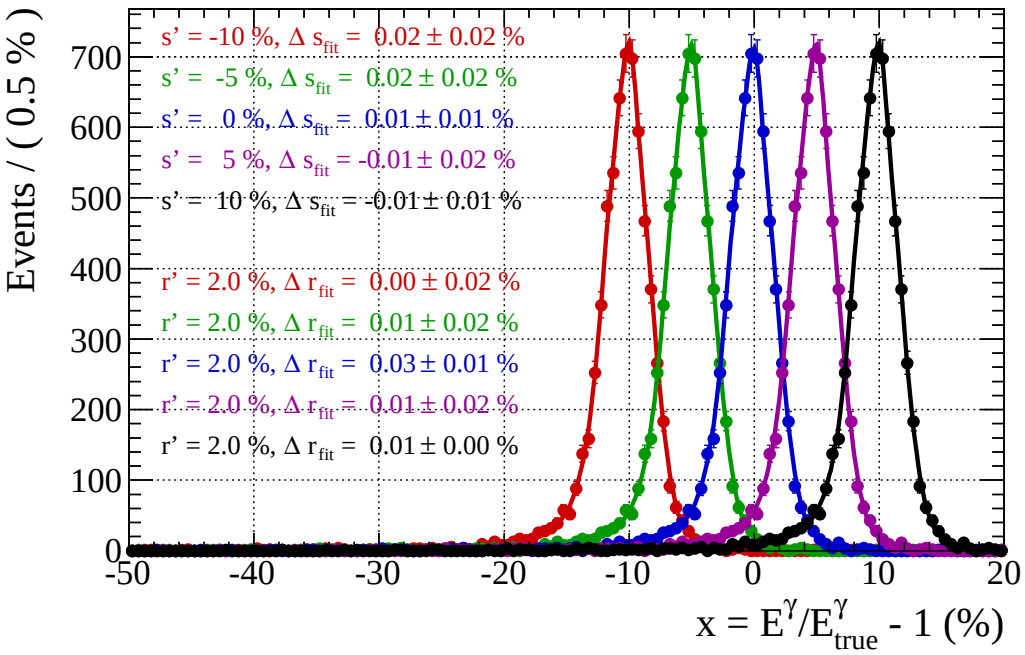

Figure 5.22: An illustration of the scale dependence of the correlated smearing and its consistency with the parameterized KEYS PDF model. In this example, we require photons to be registered in the ECAL barrel, have p_{T} between 20 GeV and 25 GeV, and $R_9 > 0.94$. We plot the smeared response values $\{x'_i\}_{i=1}^n$ as given by (5.32) for different values of the target smeared scale s' and a fixed value of the target smeared resolution $r' = 2.0\,\%$. For each different value of s', we also plot the fitted response model $f(x|s_{\mathrm{fit}}, r_{\mathrm{fit}})$ as given by (5.21), wher s_{fit} and r_{fit} come from the fit. The red, green, blue, magenta and black points with error bars correspond to the responses $\{x'_i\}_{i=1}^n$ smeared to $s' = -10\,\%$, $-5\,\%$, $0\,\%$, $5\,\%$ and $10\,\%$, respectively. The solid red, green, blue, magenta and black lines represent the models fitted to the data of the same color. $\Delta s_{\mathrm{fit}} = s' - s_{\mathrm{fit}}$ denotes the difference between the target scale s' and the fitted scale s_{fit}. Similarly, $\Delta r_{\mathrm{fit}} = r' - r_{\mathrm{fit}}$ denotes the difference between the target resolution r' and the fitted resolution r_{fit}. The different values of Δs_{fit} and Δr_{fit} correspond to models of the same color. In all cases, the target and fitted values of scale and resolution are compatible with each other. This represents an explicit test of the consistency between the correlated smearing and the parametrized KEYS PDF modeling (5.37), as well as a test of their correct software implementation.

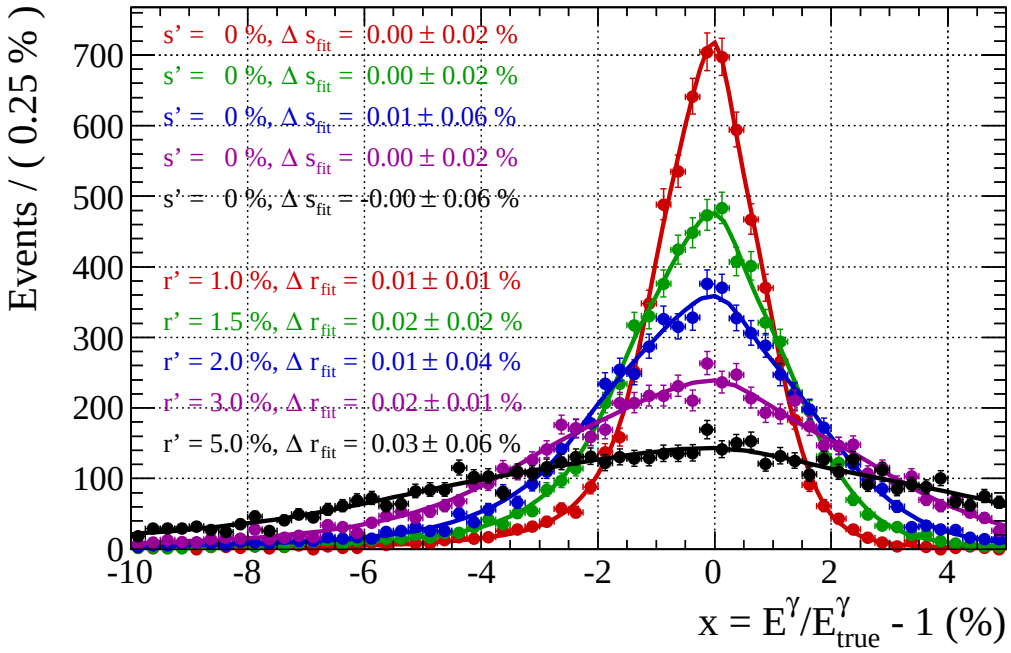

Figure 5.23: An illustration of the resolution dependence of the correlated E^γ response smearing and its consistency with the parameterized KEYS PDF E^γ response model. This is the same as Figure 5.22 except for varying the resolution r' instead of the scale s'. In this example, we require photons to be registered in the ECAL barrel, to have p_T between 20 GeV and 25 GeV, and to have $R_9 > 0.94$. We plot the smeared response values $\{x'_i\}_{i=1}^n$ as given by (5.32) for a fixed value of the target smeared scale $s' = 0\,\%$ and different values of the target smeared resolution r'. For each different value of r', we also plot the fitted response model $f(x|s_\mathrm{fit}, r_\mathrm{fit})$ as given by (5.21), wher s_fit and r_fit come from the fit. The red, green, blue, magenta and black points with error bars correspond to the responses $\{x'_i\}_{i=1}^n$ smeared to $r' = 1.0\,\%$, $1.5\,\%$, $2.0\,\%$, $3.0\,\%$ and $5.0\,\%$, respectively. The solid red, green, blue, magenta and black lines represent the models fitted to the data of the same color. $\Delta s_\mathrm{fit} = s' - s_\mathrm{fit}$ denotes the difference between the target scale s' and the fitted scale s_fit. Similarly, $\Delta r_\mathrm{fit} = r' - r_\mathrm{fit}$ denotes the difference between the target resolution r' and the fitted resolution r_fit. The different values of Δs_fit and Δr_fit correspond to models of the same color. In all cases, the target and fitted values of scale and resolution are compatible with each other. This represents an explicit test of the consistency between the correlated smearing and the parametrized KEYS PDF modeling (5.37), as well as a test of their sound software implementation.

invariant mass, the following expression is useful:

$$m'_{\mu\mu\gamma,i} = \sqrt{m^2_{\mu\mu,i} + \frac{E_i^{\gamma\prime}}{E_i^{\gamma}}(m^2_{\mu\mu\gamma,i} - m^2_{\mu\mu,i})}, \tag{5.38}$$

where $m_{\mu\mu,i}$ is the invariant mass of the muon pair within the $\mu\mu\gamma$ candidate i, $m_{\mu\mu\gamma,i}$ is the invariant mass of the $\mu\mu\gamma$ candidate i, and $m'_{\mu\mu\gamma,i}$ is its corresponding smeared invariant mass.

In order to quantify the effects of such a smearing on the $\mu\mu\gamma$ mass distribution, we estimate its peak position and width. To do so, we use a parameterized KEYS PDF model again, very much the same way as we do for the E^γ response in Section 5.6.3. We plot the smeared invariant mass values $\{m'_{\mu\mu\gamma,i}\}_{i=1}^n$ together with the corresponding fits in Figures 5.24 and 5.25.

Figure 5.24 illustrates the dependence of the $\mu\mu\gamma$ invariant mass on the E^γ scale. We observe that the $\mu\mu\gamma$ mass peak location increases approximately linearly with the increasing E^γ scale, while the absolute peak width remains approximately independent of the E^γ scale.

Figure 5.25 illustrates the dependence of the $\mu\mu\gamma$ invariant mass on the E^γ resolution. We observe that the $\mu\mu\gamma$ mass peak width grows nonlinearly with the increasing E^γ resolution, while the peak location remains approximately independent of the E^γ resolution.

To examine these observations in more detail, we smear the $\mu\mu\gamma$ invariant mass for a finer grid of E^γ scale and resolution values and for a number of photon categories based on the photon p_{T}, η and R_9.

We plot the resulting relative $\mu\mu\gamma$ mass peak location as a function of the E^γ scale for $\mathrm{Z} \to \mu^+\mu^-\gamma$ events requiring photons to be in the barrel and have $R9 > 0.94$ in Figure 5.26 and for events requiring photons to have $R9 < 0.94$ in Figure 5.27. Figures 5.28 and 5.29 correspond to $\mathrm{Z} \to \mu^+\mu^-\gamma$ events requiring photons to be in the endcaps. The shown dependencies reinforce our previous observation that the $\mu\mu\gamma$ mass peak position depends approximately linearly on the E^γ scale. We establish that this dependence holds over a relatively broad range of E^γ scale values. We also

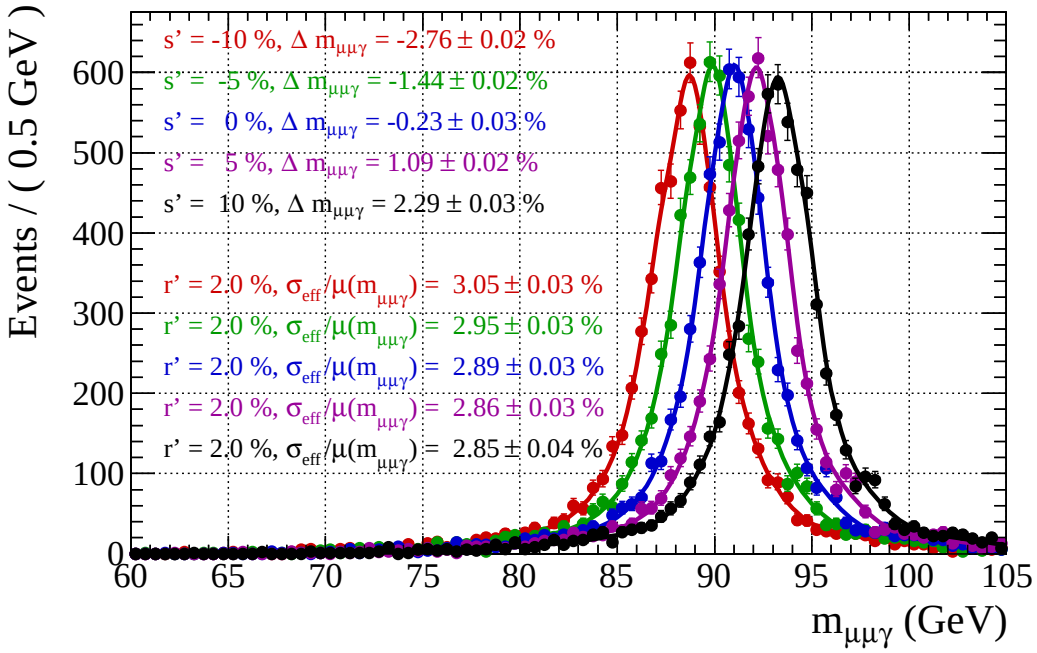

Figure 5.24: An illustration of the $\mu\mu\gamma$ invariant mass dependence on the E^γ scale for $\mathrm{Z} \to \mu^+\mu^-\gamma$ events. This complements Figure 5.22 which shows the dependence of the E^γ response instead of the $\mu\mu\gamma$ mass shown here. The requirements on the photons here the same as in Figure 5.22: they must be registered in the ECAL barrel, have p_T between 20 GeV and 25 GeV, and have $R_9 > 0.94$. We plot the spectrum of the smeared $\mu\mu\gamma$ invariant mass $\{m'_{\mu\mu\gamma,i}\}_{i=1}^n$ as given by (5.38), for different values of the E^γ scale s' and a fixed value of the E^γ resolution $r' = 2.0\,\%$. For each different value of s', we also plot the fitted parameterized KEYS PDF model of the $\mu\mu\gamma$ mass. The red, green, blue, magenta and black points with error bars correspond to the smeared masses $\{m'_{\mu\mu\gamma,i}\}_{i=1}^n$ for $s' = -10\,\%$, $-5\,\%$, $0\,\%$, $5\,\%$ and $10\,\%$, respectively. The solid red, green, blue, magenta and black lines represent parameterized KEYS PDF models fitted to the smeared mass values of the same color. $\Delta m_{\mu\mu\gamma} = \mu(m_{\mu\mu\gamma}) - m_Z$ denotes the difference between the fitted peak location $\mu(m_{\mu\mu\gamma})$ and the Z^0 boson mass m_Z. Similarly, $\sigma_\mathrm{eff}/\mu(m_{\mu\mu\gamma})$ denotes the relative width of the mass peak defined as a ratio of its effective sigma σ_eff and its location $\mu(m_{\mu\mu\gamma})$. The different values of $\Delta m_{\mu\mu\gamma}$ and $\sigma_\mathrm{eff}/\mu(m_{\mu\mu\gamma})$ correspond to curves of the same color. We observe that the $\mu\mu\gamma$ mass peak location increases approximately linearly with the E^γ scale, while the absolute peak width remains approximately independent of it. (The slight decrease of $\sigma_\mathrm{eff}/\mu(m_{\mu\mu\gamma})$ with s' is largely driven by the increase of the denominator $\mu(m_{\mu\mu\gamma})$.)

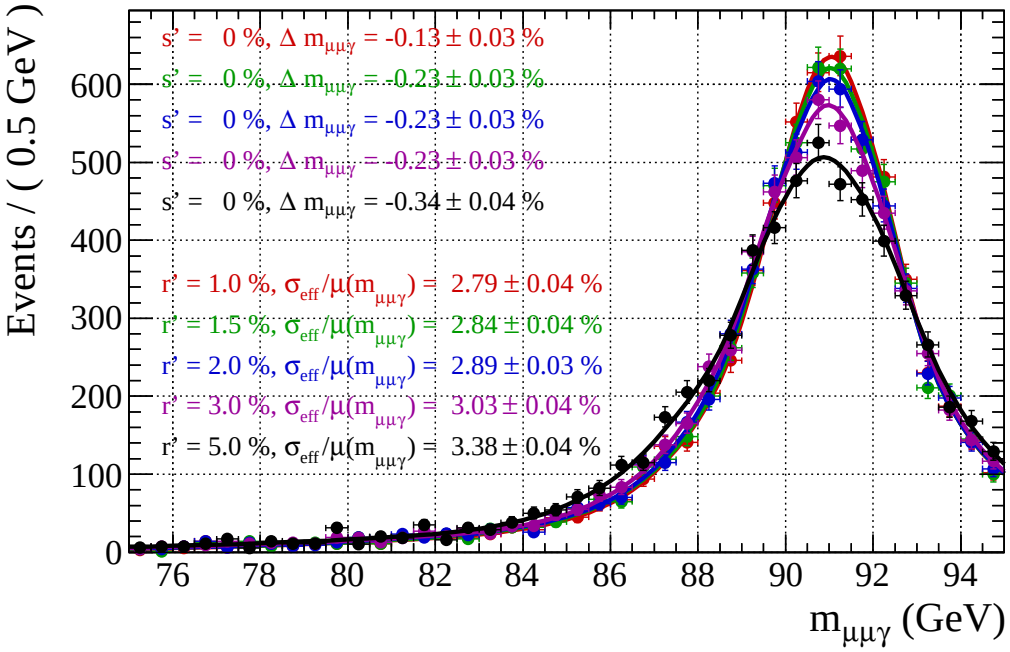

Figure 5.25: An illustration of the $\mu\mu\gamma$ invariant mass dependence on the E^γ resolution for $Z \to \mu^+\mu^-\gamma$ events. This is the same as Figure 5.24 except for varying the resolution r' instead of the scale s'. Also, this complements Figure 5.23 which shows the dependence of the E^γ response instead of the $\mu\mu\gamma$ mass shown here. We require photons to be registered in the ECAL barrel, have p_T between 20 GeV and 25 GeV, and $R_9 > 0.94$. We plot the smeared $\mu\mu\gamma$ invariant mass values $\{m'_{\mu\mu\gamma,i}\}_{i=1}^n$ (5.38) for a fixed value of the E^γ scale $s' = 0\,\%$ and a number of different values of the E^γ resolution r'. For each different value of r', we also plot the fitted parameterized KEYS PDF model of the $\mu\mu\gamma$ mass. The red, green, blue, magenta and black points with error bars correspond to the smeared masses $\{m'_{\mu\mu\gamma,i}\}_{i=1}^n$ for $r' = 1\,\%$, $1.5\,\%$, $2\,\%$, $3\,\%$ and $5\,\%$, respectively. The solid red, green, blue, magenta and black lines represent parameterized KEYS PDF models fitted to the smeared mass values of the same color. $\Delta m_{\mu\mu\gamma} = \mu(m_{\mu\mu\gamma}) - m_Z$ denotes the difference between the fitted peak location $\mu(m_{\mu\mu\gamma})$ and the Z^0 boson mass m_Z. Similarly, $\sigma_{\text{eff}}/\mu(m_{\mu\mu\gamma})$ denotes the relative width of the mass peak defined as a ratio of its effective sigma σ_{eff} and its location $\mu(m_{\mu\mu\gamma})$. The different values of $\Delta m_{\mu\mu\gamma}$ and $\sigma_{\text{eff}}/\mu(m_{\mu\mu\gamma})$ correspond to curves of the same color. We observe that the $\mu\mu\gamma$ mass peak width grows nonlinearly with the increasing E^γ resolution, while the peak location remains approximately independent of the E^γ resolution.

observe that the slope increases significantly with increasing the photon p_{T}. The offset, on the other hand, seems to be anti-correlated with the photon R_9. There does not seem to be a strong dependence on the photon η (barrel vs endcaps).

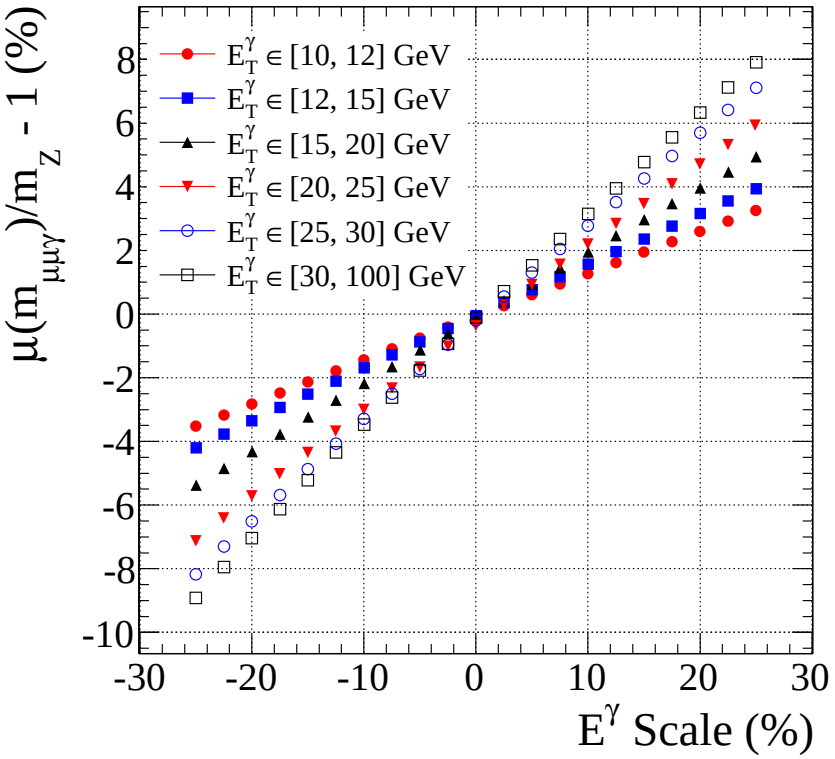

Figure 5.26: Position of the $\mu\mu\gamma$ invariant mass peak as a function of the E^γ scale for $\mathrm{Z} \to \mu^+\mu^-\gamma$ events requiring photons to be in the ECAL barrel and have $R_9 > 0.94$.

We plot the relative $\mu\mu\gamma$ mass peak width as a function of the E^γ resolution for $\mathrm{Z} \to \mu^+\mu^-\gamma$ events requiring photons to be in the barrel and have $R9 > 0.94$ in Figure 5.26 and for events requiring photons to have $R9 < 0.94$ in Figure 5.27. Figures 5.32 and 5.33 correspond to $\mathrm{Z} \to \mu^+\mu^-\gamma$ events requiring photons to be in the endcaps. Again, these reinforce our previous observation that the relative width of the $\mu\mu\gamma$ mass peak grows nonlinearly with the E^γ resolution. The dependence is weaker for lower values of the resolution and stronger for greater values of the resolution. It seems to approach a linear dependence for large numerical values of the resolution. Again, we also observe that the dependence increases significantly with increasing the photon p_{T}. There is also a visible dependence on the photon R_9 and

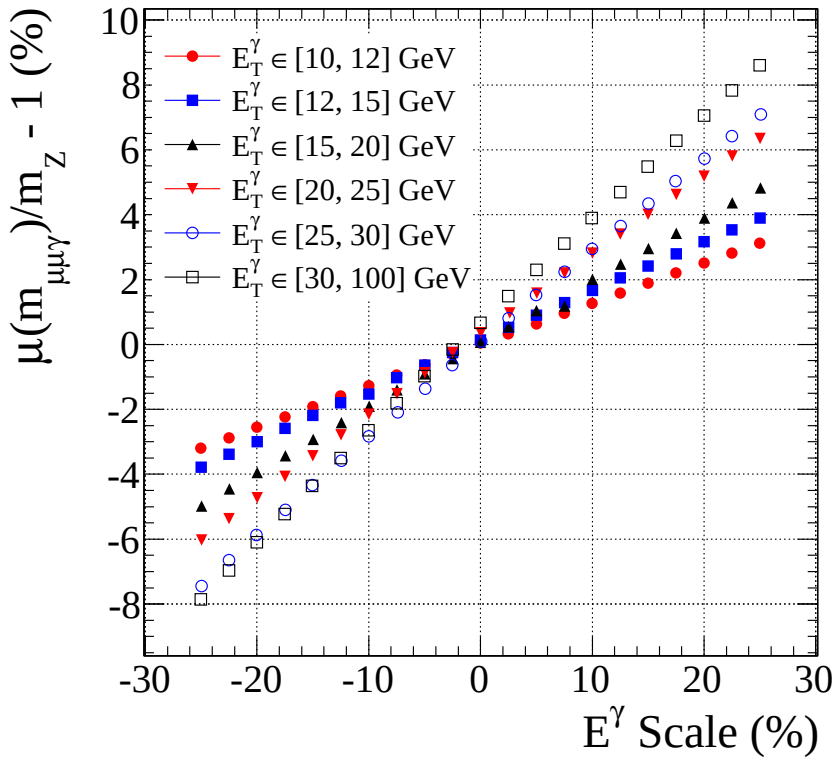

Figure 5.27: Position of the $\mu\mu\gamma$ invariant mass peak as a function of the E^γ scale for $Z \to \mu^+\mu^-\gamma$ events requiring photons to be in the ECAL barrel and have $R_9 < 0.94$.

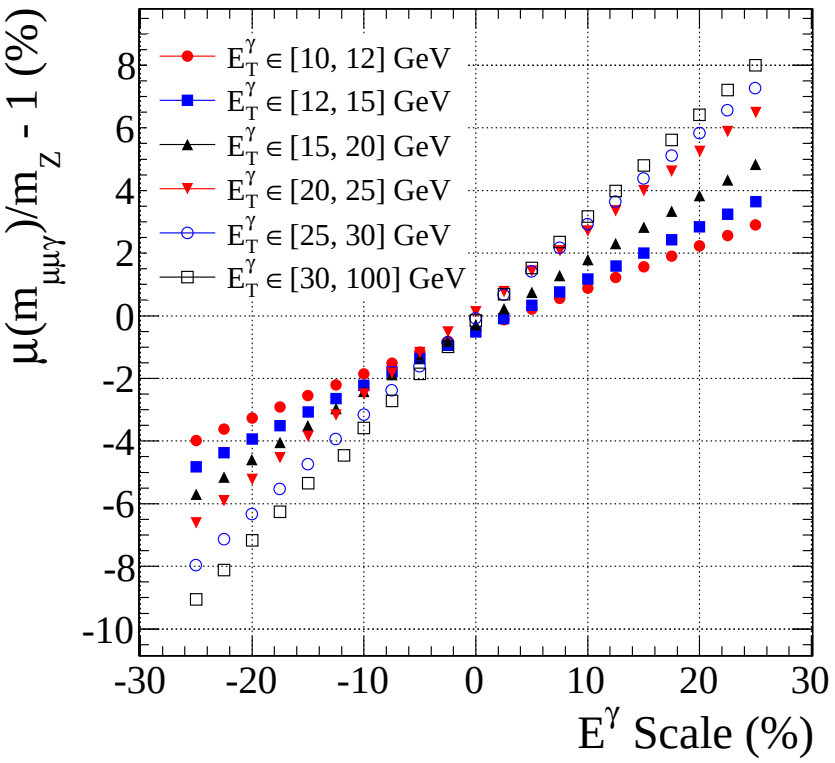

Figure 5.28: Position of the $\mu\mu\gamma$ invariant mass peak as a function of the E^γ scale for $Z \to \mu^+\mu^-\gamma$ events requiring photons to be in the ECAL endcaps and have $R_9 > 0.95$.

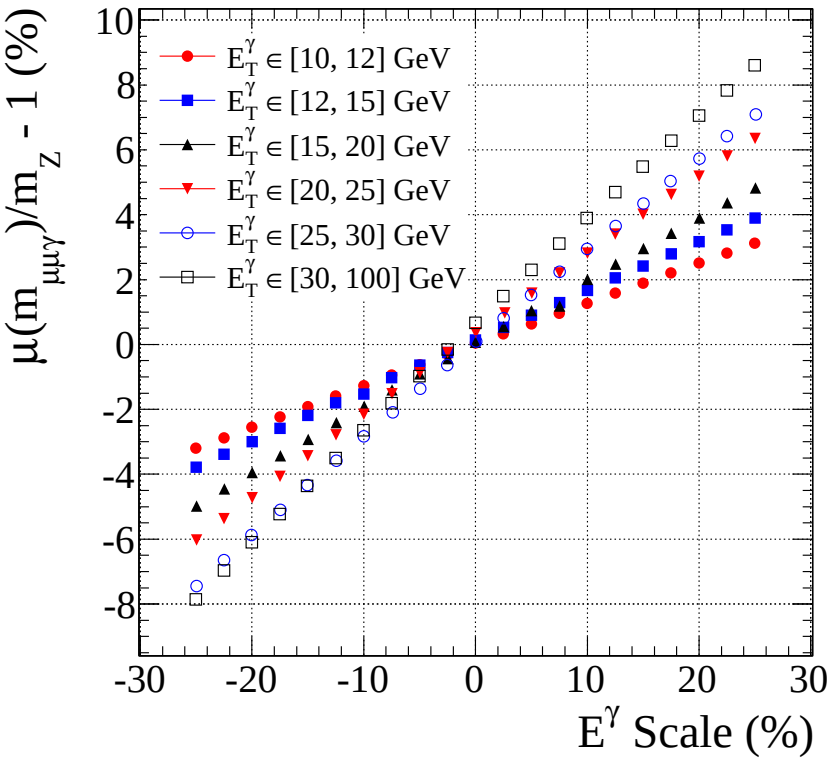

Figure 5.29: Position of the $\mu\mu\gamma$ invariant mass peak as a function of the E^γ scale for $Z \to \mu^+\mu^-\gamma$ events requiring photons to be in the ECAL endcaps and have $R_9 < 0.95$.

η.

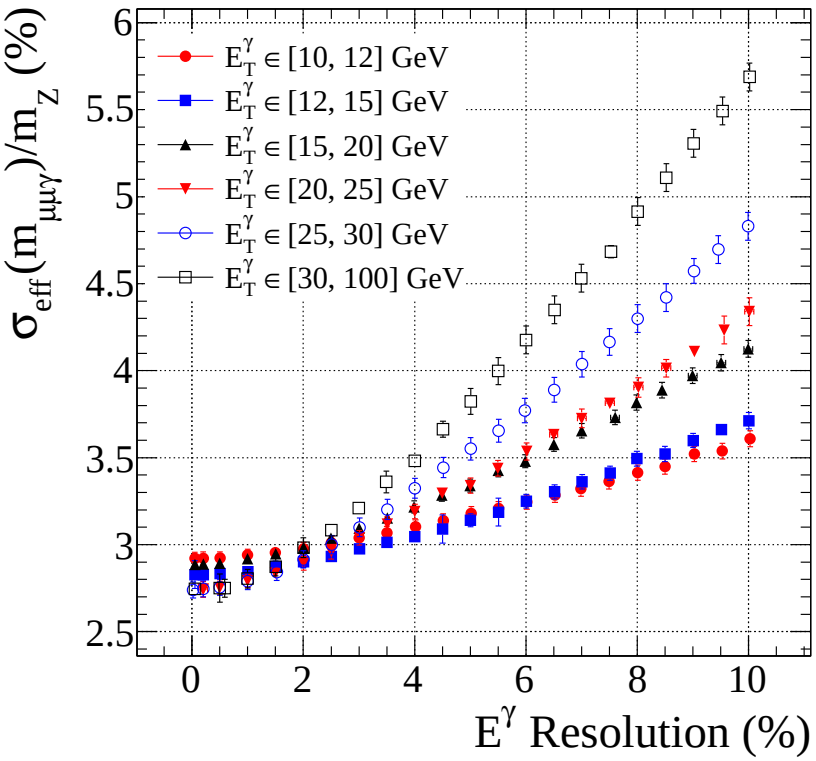

Figure 5.30: Width of the $\mu\mu\gamma$ invariant mass peak as a function of the E^γ resolution for $Z \to \mu^+\mu^-\gamma$ events requiring photons to be in the ECAL barrel and have $R_9 > 0.94$.

These observation are useful to guide us in the construction of model for the $\mu\mu\gamma$ mass probability density that depends on the E^γ scale and resolution.

5.6.5 Model for the $\mu\mu\gamma$ Invariant Mass

To estimate the scale and resolution from the $\mu\mu\gamma$ invariant mass spectrum, we use a similar approach as for the Monte Carlo truth. There are however several important differences:

- We use the $\mu\mu\gamma$ invariant mass spectrum m instead of the photon energy response x.

- We use a different functional form for the observable transform introducing only

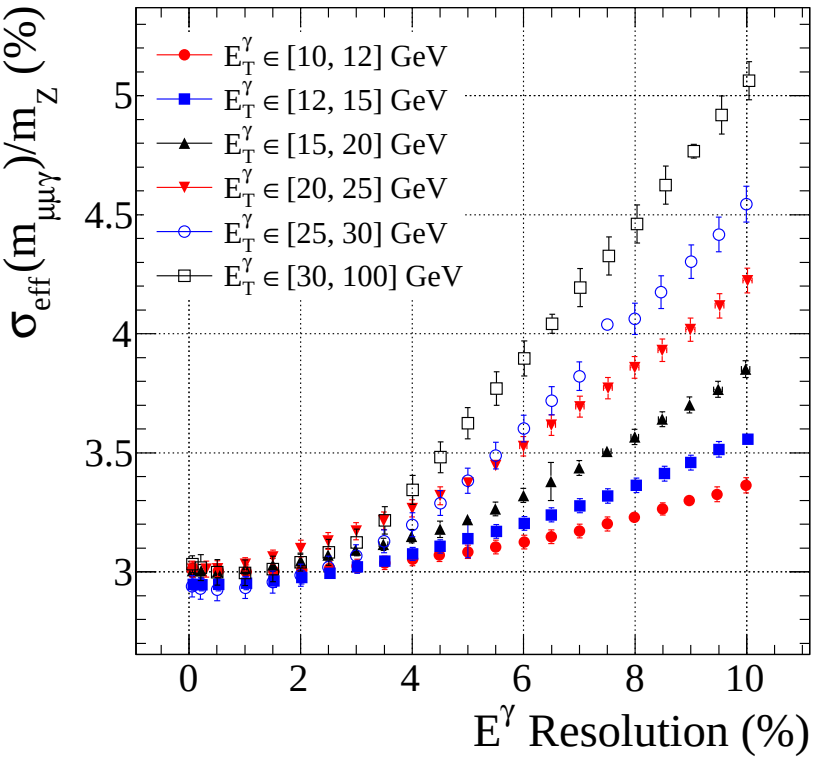

Figure 5.31: Width of the $\mu\mu\gamma$ invariant mass peak as a function of the E^γ resolution for $Z \rightarrow \mu^+\mu^-\gamma$ events requiring photons to be in the ECAL barrel and have $R_9 < 0.94$.

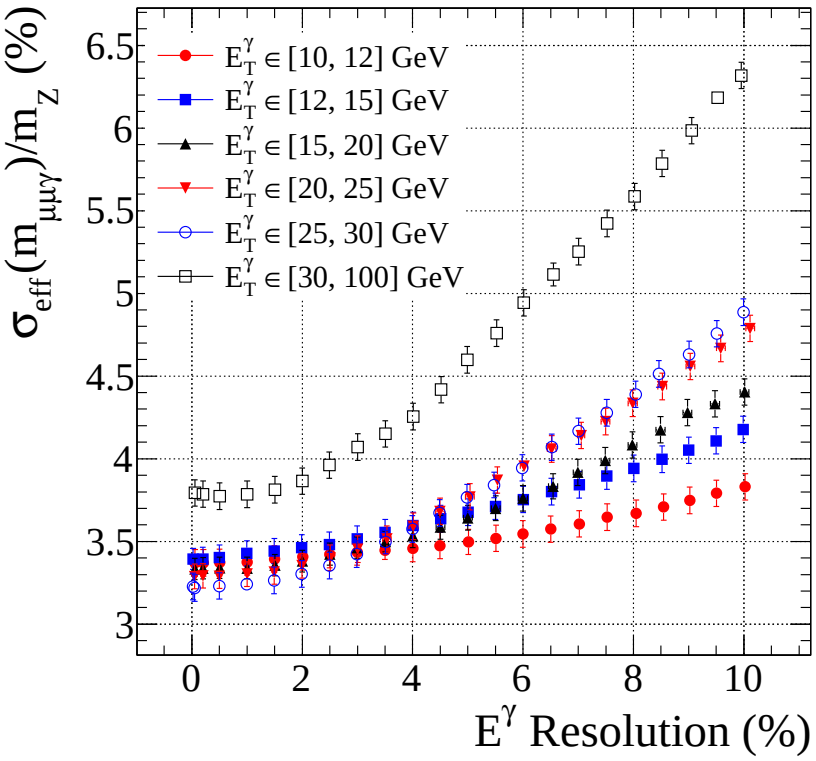

Figure 5.32: Width of the $\mu\mu\gamma$ invariant mass peak as a function of the E^γ resolution for $Z \rightarrow \mu^+\mu^-\gamma$ events requiring photons to be in the ECAL endcaps and have $R_9 > 0.95$.

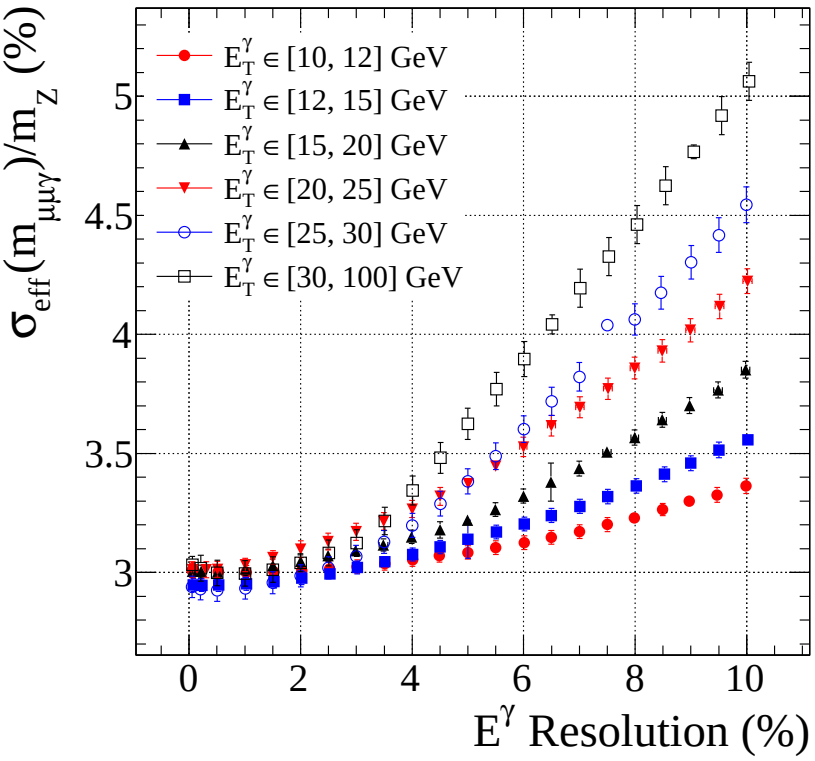

Figure 5.33: Width of the $\mu\mu\gamma$ invariant mass peak as a function of the E^γ resolution for $Z \rightarrow \mu^+\mu^-\gamma$ events requiring photons to be in the ECAL endcaps and have $R_9 < 0.95$.

the dependence on the scale:

$$m \to m' = m + m \left\langle \frac{\partial \ln m}{\partial \ln E} \right\rangle (s' - s).$$

Here the prime (') denotes the transformed quantities) and $< \cdot >$ the mean over the given simulation sample.

- We introduce the dependence on the resolution through *moment morphing*, a technique for interpolating probability density functions, between a number of reference densities. This method is based on a linear interpolation of the linearly transformed reference densities. The linear transform is chosen such that the transformed densities reproduce the linearly interpolated first moment and the linearly interpolated second central moment.

The reference densities are obtained from the simulation. We use (5.34) to smear the photon energies to a desired reference resolution r'. The change in the photon energy is then propagated to the $\mu\mu\gamma$ invariant mass using (5.38).

See Figures 5.37 and 5.38 for the results of the fits to data and MC. We find good agreement between the fitted and true values of the scale and resolution in the MC. Also the corresponding MC smearing to match the measured resolution in data agrees with the results from the $\mathrm{Z} \to \mathrm{e}^+\mathrm{e}^-$ within uncertainties. This gives us more confidence in the application of the $\mathrm{Z} \to \mathrm{e}^+\mathrm{e}^-$ results to photons.

The $\mu\mu\gamma$ invariant mass PDF model is expressed as a sum of the signal and background shapes. The relative proportion of the shapes is given by the signal purity f_{S}.

The background shape is taken from simulation. A KEYS kernel density estimator [124] with no further degrees of freedom is "trained" on the discrete events to obtain a smooth PDF.

The signal shape describes the Z resonance peak. Again, the shape is taken from simulation and smoothed by the KEYS kernel density estimation procedure [124]. The dependence on the E^γ scale is introduced through a linear transformation of the observable, the dependence on the E^γ resolution through moment morphing — an

interpolation technique for PDFs that approximates a PDF dependence on resolution given reference PDF shapes at several reference resolution values.

5.6.6 Dependence on E^γ Scale

Consider a perturbation of the $\mu\mu\gamma$ invariant mass $m_{\mu\mu\gamma}$ induced by a small perturbation of E^γ:

$$E^\gamma \to E^{\gamma\prime} = E^\gamma + \Delta E^\gamma$$
$$m_{\mu\mu\gamma} \to m'_{\mu\mu\gamma} = m_{\mu\mu\gamma} + \Delta m_{\mu\mu\gamma}$$

with

$$\begin{aligned}\Delta m_{\mu\mu\gamma} &\approx \frac{\partial m_{\mu\mu\gamma}}{\partial E^\gamma}\Delta E^\gamma \\ &\approx \frac{\partial m_{\mu\mu\gamma}}{\partial E^\gamma} E^\gamma \Delta x.\end{aligned}$$

We are interested in the situation where the E^γ perturbation is due to a small change in the E^γ scale. The E^γ response change is then identical for all the events in the sample $\Delta x = \Delta s$. Therefore we take the sample average of the second equation factoring Δx out of the average:

$$\begin{aligned}\langle \Delta m_{\mu\mu\gamma} \rangle &\approx \left\langle \frac{\partial m_{\mu\mu\gamma}}{\partial E^\gamma} E^\gamma \Delta x \right\rangle \\ &= \left\langle \frac{\partial m_{\mu\mu\gamma}}{\partial E^\gamma} E^\gamma \right\rangle \Delta x \\ &= \left\langle \frac{\partial m_{\mu\mu\gamma}}{\partial E^\gamma} E^\gamma \right\rangle \Delta s.\end{aligned}$$

The last relation provides a proportionality factor between the $m_{\mu\mu\gamma}$ and s that we use to define the linear transform:

$$m_{\mu\mu\gamma} \to m_{\mu\mu\gamma}(s) = m_{\mu\mu\gamma}(s_0) + \left\langle E^\gamma \frac{\partial m_{\mu\mu\gamma}}{\partial E^\gamma} \right\rangle (s - s_0)$$

where s_0 is the reference E^γ scale at which the reference signal PDF is obtained, i.e. for the nominal simulation.

5.6.7 Dependence on E^γ Resolution

The dependence of the resonance peak on the E^γ resolution is too complex to be described through a simple linear transform like in the case of the scale. Therefore we smear photon energies in the simulation to several reference resolution values and obtain the signal model for each of them. We then interpolate the model shape for all the E^γ resolution values using Moment Morphing.

This technique uses the mean and width, the first moment and the second central moment, hence the name. It calculates them for each reference resolution and linearly interpolates them to other values. It then linearly transforms the observables of the reference densities to match the interpolated width and mean. The morphed density is then an average of the transformed reference densities weighted proportionally to the distance in the morphing parameter. Figure 5.34 shows the resulting dependence of the $\mu\mu\gamma$ mass model on the E^γ resolution.

5.6.8 Mass Model Validation

To test the consistency of the $\mu\mu\gamma$ mass model, we fit it to the $\mu\mu\gamma$ mass distribution of the simulated events and compare the resulting estimates of the E^γ scale and resolution with those obtained directly from the distribution of the E^γ response. For brevity, we refer to the former as the *fit* E^γ scale and resolution, and to the latter as the *true* E^γ scale and resolution.

To account for the fact that the E^γ response in data may be arbitrary, we also smear the response to a range of different scale and resolution values and propagate the smearing to the mass accordingly. For all fits, we use the same $\mu\mu\gamma$ invariant mass model trained on the nominal simulation without any smearing.

Figure 5.35 shows the E^γ scale estimate from the fit to the $\mu\mu\gamma$ mass as a function of the true photon energy scale. The photons in this example are required to be in

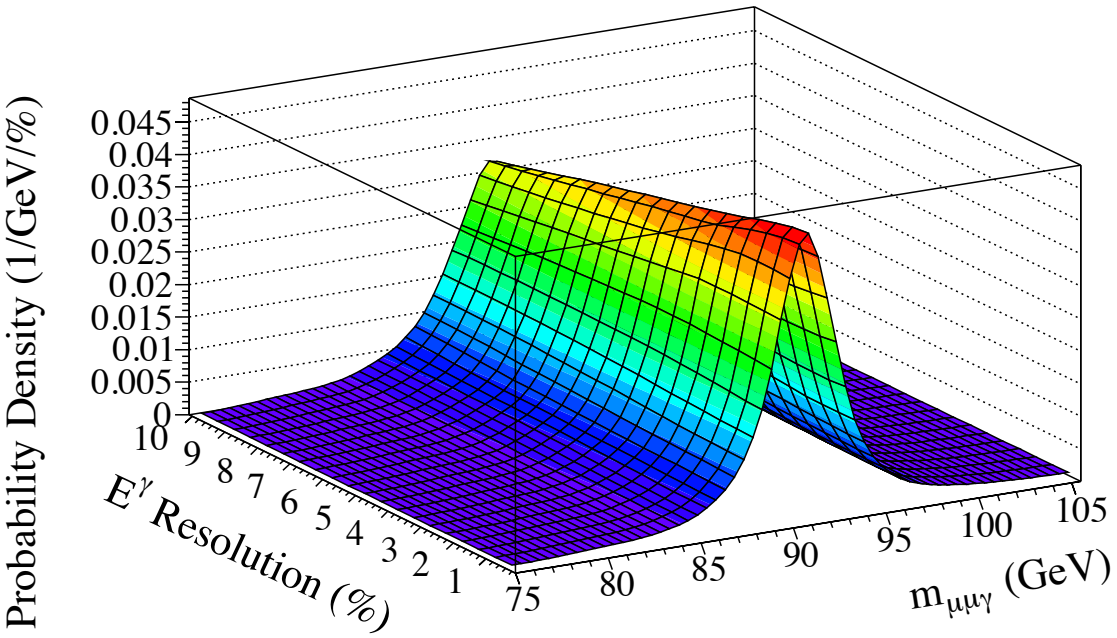

Figure 5.34: The dependence of the $\mu\mu\gamma$ mass model on the E^γ resolution illustrating the result of moment morphing. We plot the probability density $f(m_{\mu\mu\gamma}|s,r)$ as a function of the $\mu\mu\gamma$ invariant mass $m_{\mu\mu\gamma}$ and the E^γ resolution r. We use color coding to represent the density values.

the barrel, have $R_9 > 0.94$ and $p_\mathrm{T} > 25\,\mathrm{GeV}$. Figure 5.36 show the same for the E^γ resolution. We observe an excellent agreement between the fitted and true values for both the scale and the resolution. This indicates that indeed the PHOSPHOR Fit can estimate the E^γ scale and resolution correctly and validates the so-constructed $\mu\mu\gamma$ mass model.

5.6.9 Results and Correction

See Figures 5.37 and 5.38 for example results of the fits to data and MC, and Appendix **??** for all of the results. We find good agreement between the fitted and true values of the scale and resolution in the MC. Also the corresponding MC smearing to match measured resolution in data agrees with the results from the $\mathrm{Z} \to \mathrm{e^+e^-}$ within uncertainties. This gives us more confidence in the application of the $\mathrm{Z} \to \mathrm{e^+e^-}$ results to photons.

See Table 5.4 and 5.5 for the results of the energy scale and resolution measure-

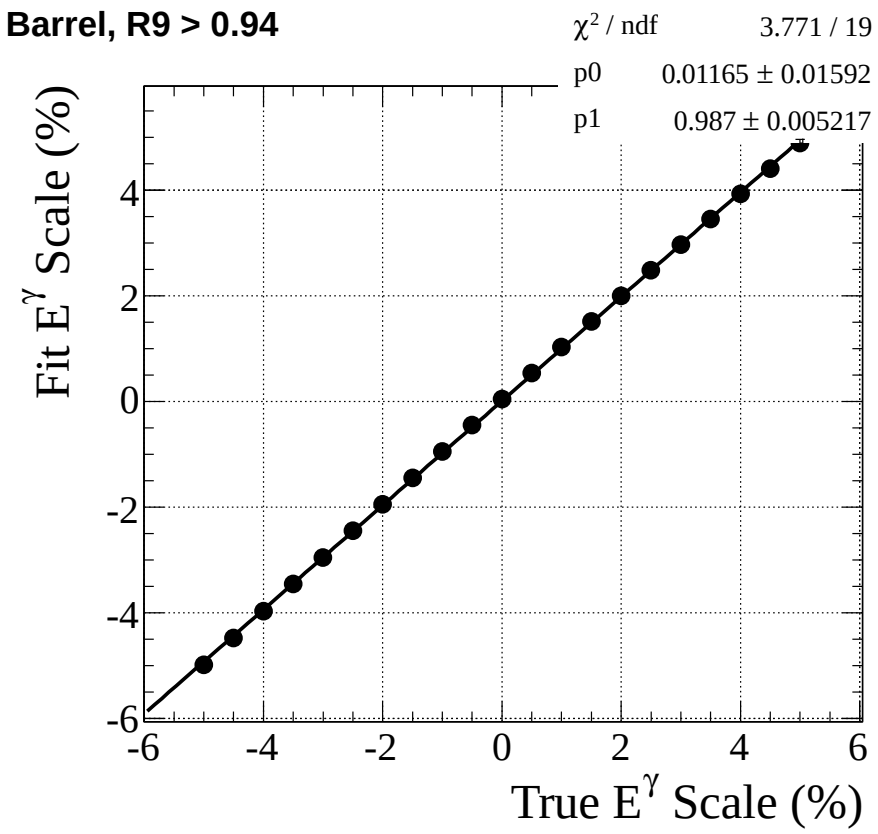

Figure 5.35: Photon energy scale estimate from the fit to the $\mu\mu\gamma$ mass in simulation (black dots with error bars) as a function of the true photon energy scale, overlaid with a linear χ^2 fit to its values (solid black line). The results of the fit are displayed in the top right: χ^2 denotes the χ^2 of the fit, ndf denotes the number of degrees of freedom of the fit, p0 is the offset, and p1 the slope. We observe an excellent agreement between the fitted and true values of the E^γ scale. Here, the photons are required to be in the barrel, have $R_9 > 0.94$ and $p_\mathrm{T} > 25\,\mathrm{GeV}$.

ments.

The relation 5.19 is also used for the final correction of the simulation requiring perfect scale $s' = 0$ and resolution equal to the one in data $r' = r_\mathrm{data}$. Given the scale in data s, we calculate the corrected energy E' as:

$$E' = \frac{E}{1+s}. \tag{5.39}$$

After these corrections, the photon energy scale and resolution (averaged over the

				Photon Energy Scale (%)	
Category	Subdetector	R_9	p_{T} (GeV)	MC True	Data Fit
1	Barrel	> 0.94	10-12	0.30 ± 0.13	-0.79 ± 0.39
2			12-15	0.10 ± 0.10	-1.10 ± 0.30
3			15-20	0.11 ± 0.07	-0.64 ± 0.22
4			> 20	-0.10 ± 0.05	-0.32 ± 0.12
5		< 0.94	10-12	5.15 ± 0.27	3.19 ± 0.39
6			12-15	4.25 ± 0.21	2.34 ± 0.31
7			15-20	3.51 ± 0.17	1.71 ± 0.25
8			> 20	2.51 ± 0.11	0.58 ± 0.15
9	Endcaps	> 0.95	10-15	0.31 ± 0.25	0.68 ± 0.62
10			> 15	0.50 ± 0.13	1.31 ± 0.29
11		< 0.95	10-12	12.27 ± 0.66	11.50 ± 0.66
12			12-15	10.67 ± 0.52	10.16 ± 0.58
13			15-20	8.10 ± 0.42	7.61 ± 0.49
14			> 20	5.89 ± 0.29	6.68 ± 0.33

Table 5.4: A summary of the derived photon energy scale estimates.

				Photon Energy Resolution (%)	
Category	Subdetector	R_9	p_{T} (GeV)	MC True	Data Fit
1	Barrel	> 0.94	10-12	2.49 ± 0.03	4.30 ± 0.81
2			12-15	2.15 ± 0.02	3.71 ± 0.51
3			15-20	1.77 ± 0.02	3.20 ± 0.05
4			> 20	1.37 ± 0.01	2.14 ± 0.22
5		< 0.94	10-12	8.11 ± 0.08	10.96 ± 0.62
6			12-15	6.77 ± 0.06	9.19 ± 0.45
7			15-20	5.39 ± 0.05	6.53 ± 0.49
8			> 20	3.82 ± 0.03	5.21 ± 0.09
9	Endcaps	> 0.95	10-15	3.30 ± 0.06	7.76 ± 0.73
10			> 15	2.49 ± 0.03	4.81 ± 0.33
11		< 0.95	10-12	11.10 ± 0.16	15.79 ± 0.81
12			12-15	9.65 ± 0.13	13.49 ± 1.31
13			15-20	8.03 ± 0.10	12.90 ± 0.86
14			> 20	6.08 ± 0.07	9.16 ± 0.62

Table 5.5: A summary of the derived photon energy resolution estimates.

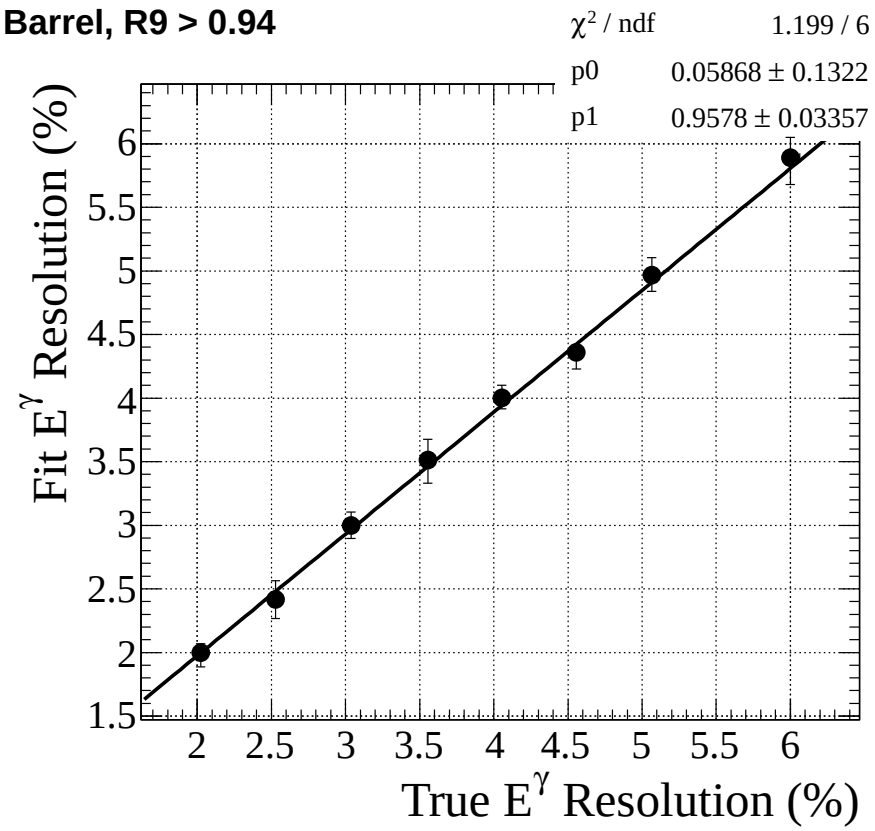

Figure 5.36: Photon energy resolution estimate from the fit to the $\mu\mu\gamma$ mass in simulation (black dots with error bars) as a function of the true photon energy resolution, overlaid with a linear χ^2 fit to its values (solid black line). The results of the fit are displayed in the top right: χ^2 denotes the χ^2 of the fit, ndf denotes the number of degrees of freedom of the fit, p0 is the offset of the fitted line, and p1 its slope. We observe an excellent agreement between the fitted and true values of the E^γ resolution. Here, the photons are required to be in the barrel, have $R_9 > 0.94$ and $p_\mathrm{T} > 25\,\mathrm{GeV}$.

categories used in Tables 5.4 and 5.5) agree between data and simulation. The uncertainties on these corrections are then taken into account as systematic uncertainties as discussed in Section 5.8.

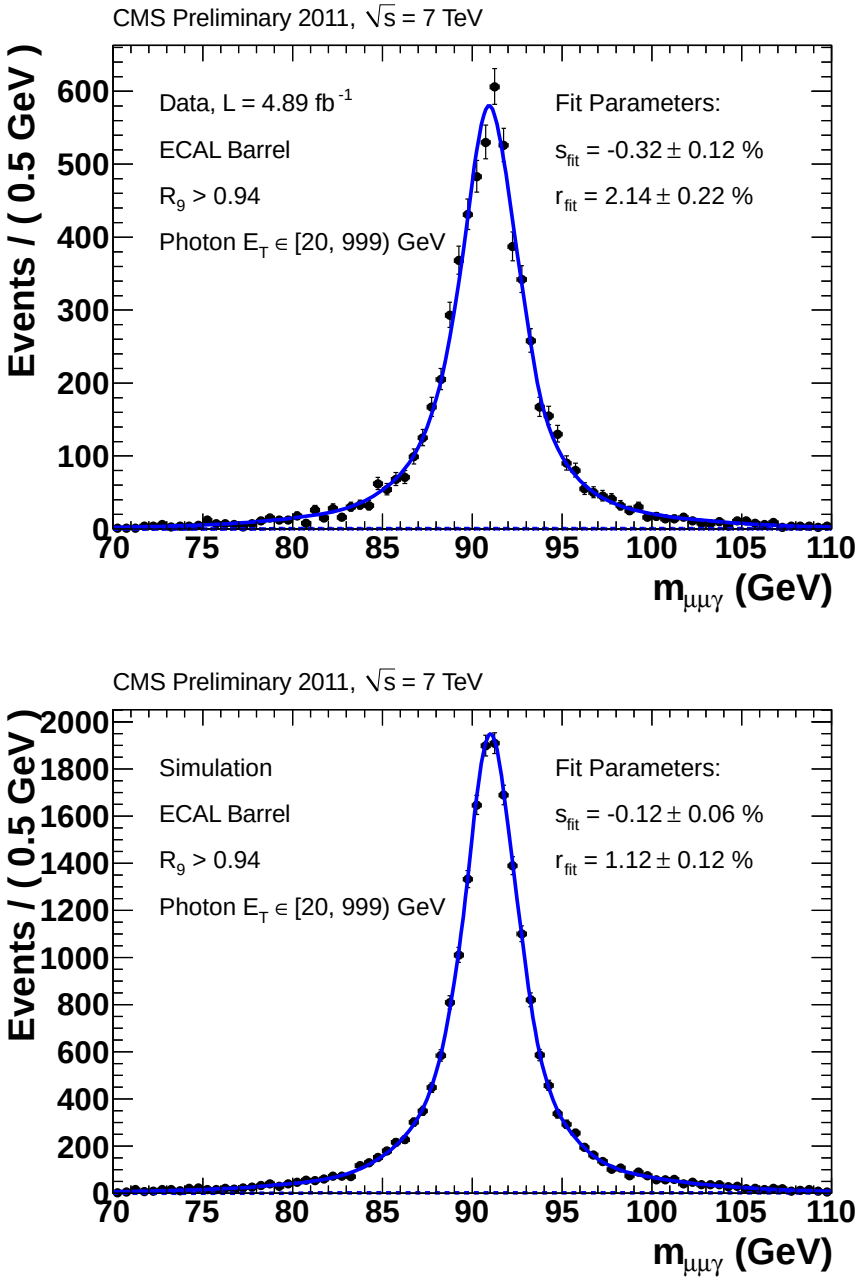

Figure 5.37: The invariant mass of the $\mu\mu\gamma$ system for $Z \to \mu^+\mu^-\gamma$ events selected in data and simulation together with the fitted PHOSPHOR model, top and bottom respectively. The photon is required to be in the ECAL barrel, have $R_9 > 0.94$, and the transverse momentum $p_T > 20\,\text{GeV}$. The photon energy scale and resolution and the fraction of the signal events are floated in the fit. The dashed line corresponds to the fitted background model component.

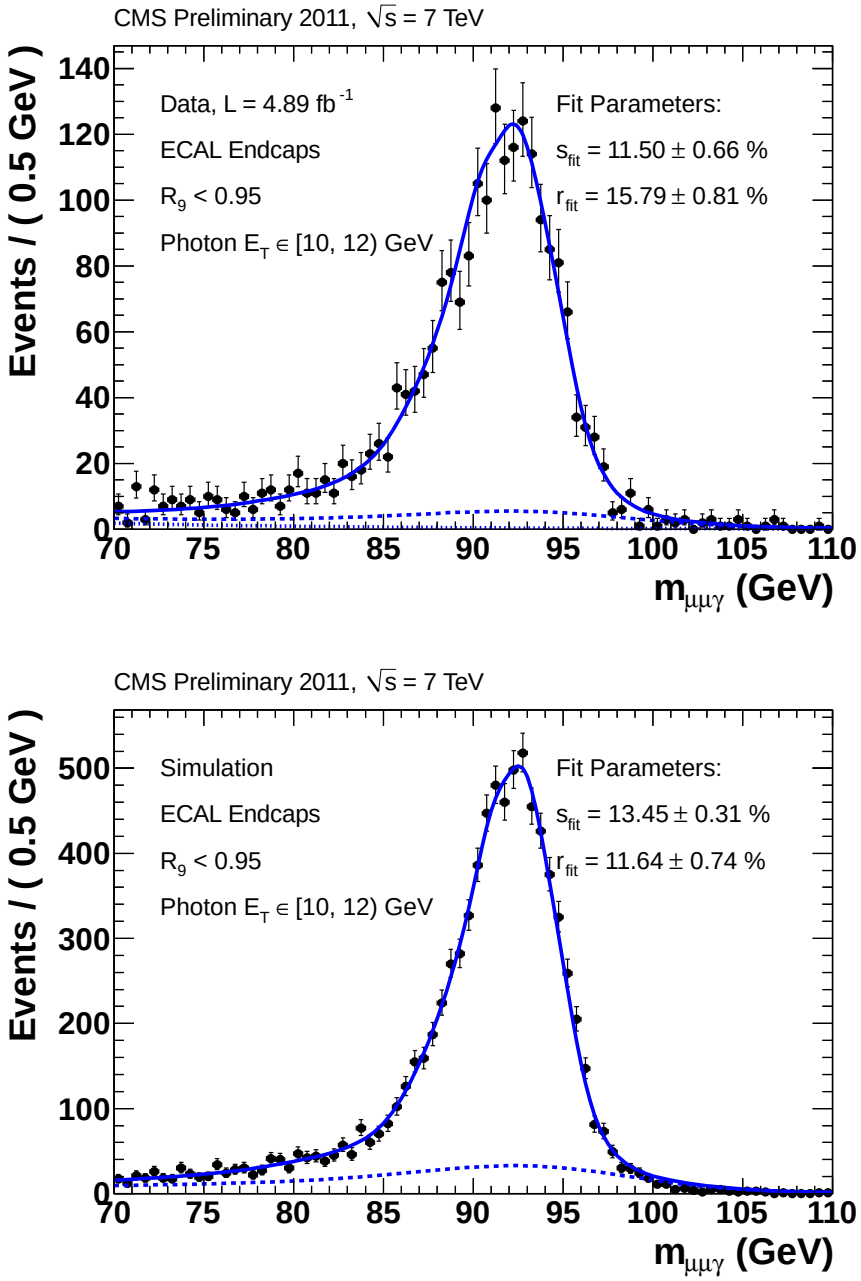

Figure 5.38: Same as Figure 5.37 but for a different category of photons. The invariant mass of the $\mu\mu\gamma$ system for $Z \to \mu^+\mu^-\gamma$ events selected in data and simulation together with the fitted PHOSPHOR model, top and bottom respectively . The photon is required to be in the ECAL endcaps, have $R_9 < 0.95$, and the transverse momentum $p_T = (10 \text{ to } 12)\,\text{GeV}$. The photon energy scale and resolution and the fraction of the signal events are floated in the fit. The dashed blue line corresponds to the sum of the fitted background model components, the dotted blue line corresponds to the fitted exponential background component.

5.7 Pixel Match Veto Efficiency

Here we describe the efficiency measurement of the photon pixel match — a variable used to veto photon candidates due to electrons. Using the full 2011 dataset of proton collisions at $\sqrt{s} = 7\,\text{TeV}$, we select radiative $\text{Z} \to \mu^+\mu^-\gamma$ events and employ the cut-and-count variant of the tag-and-probe method. We tag the events with the muon pair and probe the veto with the photon.

5.7.1 Trigger Requirements

We do not require any specific trigger paths since we do not need to estimate the rate. We use all the available events for both the real data and the Monte Carlo samples. In this sense, the trigger for the real data is defined by the union of all triggers with intended for muon pairs.

5.7.2 Collision Data Cleaning

We apply the standard collision data cleaning filters [126]. The collision data cleaning criteria are as follows:

- remove the beam scraping events by requiring at least 25% of high purity tracks for events with more than 10 tracks, and
- require a good vertex selection:
  - at least 4 degrees of freedom of the vertex fit as defined by (4.4),
  - $|z| < 24$ cm,
  - $d_0 < 2$ cm.

5.7.3 Selection of Muons

The muon selection criteria are as follows:

- the muon must be reconstructed as a global muon,

- the global muon track fit should have a $\chi^2/\text{ndof} < 10$,
- the global muon must have at least one valid muon chamber hit matched to the global fit,
- the muon must be reconstructed also as a tracker muon,
- the tracker muon must match to at least two muon stations,
- the muon inner track must have at least one hit in the silicon pixel detector,
- the muon inner track must have more than 10 hits (pixels + strips),
- $|d_{xy}(\mathbf{o})| < \mathbf{1}$ cm where $d_{xy}(\mathbf{o})$ is the (approximate) inner track impact parameter in the transverse plane calculated with respect to the origin of the CMS coordinate system,
- $|d_{xy}| < 2$ mm where d_{xy} is the (approximate) inner track impact parameter in the transverse plane calculated with respect to the beam spot position, and
- $p_{\mathrm{T}}^{\mu} > 10$ GeV where p_{T}^{μ} is the muon transverse momentum.

Cosmic ray muon contamination is significantly reduced by the requirement of $|d_{xy}|$ to be consistent with prompt muon production. Further cross-checks of timing and cosmic tagger information [127] indicate that there is a negligible contribution from the cosmic background.

These identification criteria are identical to those used in previous analyses studying the $W \to \mu\nu$ and $Z \to \mu\mu$ processes [127]. The muon isolation criterion, however, is looser.

Based on the $\Delta R(\mu^{\pm}, \gamma)$ distance of the muons and the photon in the η-ϕ plane we define the near and far muons μ_{near} and μ_{far}:

$$\Delta R(\mu_{\text{near}}, \gamma) = \min \Delta R(\mu^{\pm}, \gamma),$$
$$\Delta R(\mu_{\text{far}}, \gamma) = \max \Delta R(\mu^{\pm}, \gamma).$$

Requiring the tracker isolation for a muon in the vicinity of a photon probe biases the pixel match veto efficiency upwards. Therefore we apply the tracker isolotion to the "far" muon only.

We list the full details below for the $\mu^+\mu^-\gamma$ candidate selection in Section 5.7.6, since this isolation criterion depends on the topology of the three final state objects.

More details and studies on muon identification can be found elsewhere [128].

5.7.4 Selection of Dimuons

We require at least two muons passing the muon selection in Section 5.7.3. The dimuon selection criteria are as follows:

- the two muons must have opposite charge,
- $m_{\mu^+\mu^-} \in [40, 80]$ GeV, where $m_{\mu^+\mu^-}$ is the dimuon system invariant mass.

5.7.5 Selection of Photons

We reconstruct the photons as superclusters with $E_T > 2$ GeV in the fiducial volume of the ECAL detector: barrel with $|\eta| < 1.4442$ and endcap with $1.566 < |\eta| < 2.5$.

This differs from the standard reconstruction by relaxing the default supercluster requirement of $E_T > 10\,\text{GeV}$. Therefore we rereconstruct the photons ourselves.

The photon selection criteria are as follows:

- the photon must be in the ECAL fiducial volume, $|\eta_{\text{SC}}| < 2.5$, where $|\eta_{\text{SC}}|$ is the photon supercluster pseudorapidity,
- the photon must be outside the barrel-endcap gap, $|\eta_{\text{SC}}| \notin [1.4442, 1.566]$,
- the photon supercluster seed rec hit (as described in 4.4) must not be flagged as "out-of-time" by the reconstruction algorithm,
- the photon supercluster seed rec hit must not be flagged as "weird" or "bad" by the ECAL severity level algorithm (meaning that the readout samples were consistent with scintillation light signals),

- $I_{\rm ECAL} < 4.2 + 0.006 \times p_{\rm T}^{\gamma}$, where $I_{\rm ECAL}$, the so-called *"Jurassic" ECAL isolation*, is the sum of the transverse energy deposited in the ECAL in an annulus $0.06 < R < 0.40$, excluding a rectangular strip of $\Delta\eta \times \Delta\phi = 0.04 \times 0.40$, and $p_{\rm T}^{\gamma}$ is the photon transverse momentum,

- $p_{\rm T}^{\gamma} > 5$ GeV.

We also apply a tracker isolation criterion as defined in Section 4.5. However, special care has to be taken to remove the near muon footprint. Since this criterion depends on the topology of the $\mu\mu\gamma$ system, we discuss it below in Section 5.7.6.

The standard photon identification also involves the H/E and HCAL isolation selections [118]. We do not apply these criteria since they are significantly biased by the near muon footprint, the removal of which is not trivial.

5.7.6 Selection of $\mu\mu\gamma$ Candidates

We require at least one dimuon and one photon passing the selections in Sections 5.7.4 and 5.7.5 respectively.

The $\mu^+\mu^-\gamma$ candidate selection criteria are as follows:

- $I_{\rm HCAL}^{\mu,\rm near} < 1$ GeV, where $I_{\rm HCAL}^{\mu,\rm near}$ is is the near muon HCAL isolation as defined in Section 4.7,

- $I_{\rm TRK}^{\mu,\rm far} < 3$ GeV, where $I_{\rm TRK}^{\mu,\rm far}$ is the far muon tracker isolation as defined in Section 4.7,

- $I_{\rm ECAL}^{\mu,\rm far} < 1$ GeV, where $I_{\rm ECAL}^{\mu,\rm far}$ is the far muon ECAL isolation as defined in Section 4.7,

- $I_{\rm TRK}^{\gamma,\rm corr} - 0.001 \times p_{\rm T}^{\gamma} < 2\,{\rm GeV}$, where $I_{\rm TRK}^{\gamma,\rm corr}$ is the hollow-cone photon tracker isolation $I_{\rm TRK}^{\gamma}$ as defined in Section 4.5, corrected for the presence of the near muon, the $p_{\rm T}$ of which is removed from the sum,

- $\Delta R(\mu_{\rm near}, \gamma) < 1$, where $\Delta R(\mu_{\rm near}, \gamma)$ is distance between the photon and the near muon in the η-ϕ plane,

- $p_{\mathrm{T}}(\mu_{\mathrm{far}}) > 15\,\mathrm{GeV}$, where $p_{\mathrm{T}}(\mu_{\mathrm{far}})$ is the far muon transverse momentum,
- $m_{\mu^+\mu^-\gamma} \in [75, 105]$ GeV, where $m_{\mu^+\mu^-\gamma}$ is the $\mu^+\mu^-\gamma$ system invariant mass.

We reject all events with multiple $\mu^+\mu^-\gamma$ candidates passing this selection. Using Monte Carlo we find that this causes a negligible decrease of the signal selection efficiency.

5.7.7 Monte Carlo Signal and Background

The $Z \to \mu\mu + X$ Monte Carlo sample is used as a source of both the signal and the background for $X = \gamma$ and $X = \mathrm{jet}$. The signal and background are defined by matching to the Monte Carlo truth event topology. We require exactly one reconstructed $\mu^+\mu^-\gamma$ candidate passing the selection in Section 5.7.6.

The signal selection criteria are as follows:

- the photon must be matched to a generator-level photon using the default Monte Carlo matching of the CMS Physics Analysis Tookit (PAT) [129],
- the matched generator-level photon must have a muon mother.

Every $\mu^+\mu^-\gamma$ candidate failing these criteria is considered background.

5.7.8 Summary and Results

We carry out the measurement in four different categories of photons, based on the subdetector region registering them (barrel or endcap), and the supercluster variable R_9 (see Section 4.4 for definition) designed to separate between converted and unconverted photons (see Table **??** for definitions). We choose to categorize this way because the electron efficiency varies significantly with category. We only use four categories to maintain large enough sample per-category. We further split the measurement based on the two run periods 2011A and 2011B introduced in Section 5.3.

We list the resulting electron-rejection efficiencies in Table 5.7.8.

The asymmetric errors on the efficiencies obtained for the data represent the statistical uncertainty defined as the Cloper-Pearson 68.3% confidence intervals. The

Table 5.6: Photon categories used for the electron rejection cut efficiency measurements.

Category	Subdetector	R_9
1	Barrel	$R_9 > 0.94$
2		$R_9 < 0.94$
3	Endcaps	$R_9 > 0.95$
4		$R_9 < 0.95$

symmetric errors on data represent the systematic uncertainty due to the 100% uncertainty on the background yield. The errors on the efficiencies obtained for the Monte Carlo have the same meaning.

We also give the ratio of the data/MC efficiencies. We take the largest statistical uncertainty, add the systematic uncertainty in quadrature and propagate the uncertainties for both data and Monte Carlo to obtain the error on this ratio.

The resulting inclusive barrel photon pixel match veto efficiency is $97.4^{+0.9}_{-1.2}\,(\text{stat.}) \pm 0.5\,(\text{syst.})$ % in data and $97.75 \pm 0.05\,(\text{stat.}) \pm 0.01\,(\text{syst.})$ % in simulation giving the data/simulation efficiency ratio 0.996 ± 0.013.

Similarly, the resulting inclusive endcaps photon pixel match veto efficiency is $86.0^{+4.1}_{-5.0}\,(\text{stat.}) \pm 2.5\,(\text{syst.})$ % in data and $89.72 \pm 0.19\,(\text{stat.}) \pm 0.01\,(\text{syst.})$ % in simulation giving the data/simulation efficiency ratio 0.959 ± 0.062.

In general, we find good agreement between data and Monte Carlo within the estimated errors.

The efficiency results in the four categories are used, together with the identification efficiencies of the remaining photon selection requirements, estimated from $Z \to e^+e^-$ events, to obtain an overall efficiency of the photon identification ϵ_γ in (5.5). The related uncertainties are taken into acount as systematic uncertainties, as discussed in Section 5.8.

Table 5.7: Pixel match veto efficiency for photons in four different subdetector $\times$ R_9 categories defined in Table 5.7.8.

	2011 - all		
Category	ϵ_{data} (%)	ϵ_{MC} (%)	$\epsilon_{data}/\epsilon_{MC}$
1	$98.81^{+0.15}_{-0.17}$	$99.38^{+0.05}_{-0.06}$	$0.9943^{+0.0016}_{-0.0018}$
2	$93.79^{+0.62}_{-0.62}$	$95.10^{+0.14}_{-0.14}$	$0.9862^{+0.0063}_{-0.0064}$
3	$94.46^{+0.70}_{-0.79}$	$97.25^{+0.29}_{-0.32}$	$0.9713^{+0.0076}_{-0.0085}$
4	$81.90^{+1.23}_{-1.25}$	$82.66^{+0.43}_{-0.44}$	$0.9907^{+0.0130}_{-0.0132}$
	2011A		
1	$99.15^{+0.17}_{-0.20}$	$99.57^{+0.05}_{-0.05}$	$0.9958^{+0.0017}_{-0.0020}$
2	$94.07^{+0.63}_{-0.65}$	$95.29^{+0.14}_{-0.14}$	$0.9872^{+0.0065}_{-0.0067}$
3	$95.61^{+0.86}_{-1.04}$	$97.31^{+0.28}_{-0.31}$	$0.9824^{+0.0091}_{-0.0108}$
4	$83.33^{+1.36}_{-1.41}$	$82.89^{+0.43}_{-0.44}$	$1.0053^{+0.0143}_{-0.0148}$
	2011B		
1	$98.46^{+0.24}_{-0.28}$	$99.17^{+0.06}_{-0.07}$	$0.9929^{+0.0025}_{-0.0029}$
2	$93.51^{+0.74}_{-0.76}$	$94.92^{+0.14}_{-0.15}$	$0.9851^{+0.0076}_{-0.0077}$
3	$93.35^{+1.13}_{-1.32}$	$97.16^{+0.29}_{-0.32}$	$0.9607^{+0.0116}_{-0.0135}$
4	$80.35^{+1.65}_{-1.70}$	$82.45^{+0.43}_{-0.44}$	$0.9746^{+0.0170}_{-0.0175}$

5.8 Systematic Uncertainties

In this section we discuss the systematic uncertainties in the cross section measurement. These uncertainties come from various sources. They may also be of statistical origin but, in contrast to the statistical uncertainty, they are due to a limited size of some event sample other than the sample of the selected Zγ events from pp collisions. These other samples include simulation samples and independent control samples of the collision data.

We categorize the systematic uncertainties by the input of the cross section extraction formula (5.4) they affect: the estimated yield of the Z + jets background events $B_{\mathrm{Z+jets}}$, the estimated yield of the selected signal events S, the product of acceptance and efficiency $A \times \epsilon = \mathcal{F}$, the data/simulation efficiency scale factor ρ_{eff}, and the uncertainty on the total integrated luminosity L.

Below we describe the sources of the various uncertainties for each of these factors, explain how their impact is estimated, and give the size of these estimates. In the end, we summarize all the effects and combine them to a total systematic uncertainty.

5.8.1 Uncertainties on the Z + jets Background $B_{\mathrm{Z+jets}}$

The estimated number of background events $B_{\mathrm{Z+jets}}$ is subject to the uncertainties of the fits in the various bins of p_{T}^{γ} as discussed in Section 5.5 above. We add these per-bin uncertainties in quadrature as they are mutually statistically independent. The total combined uncertainty on $B_{\mathrm{Z+jets}}$ is 4.2 % and 5.5 % in the eeγ and $\mu\mu\gamma$ channels, respectively.

Note that the relative effect of this uncertainty on the final cross section estimate is smaller because it enters through the difference $S = N - \sum_i B_i$ where i runs over the various background components including Z + jets.

5.8.2 Uncertainties on the Signal S

The total estimated number of the selected signal events S is affected by the uncertainties on the energy scale of photons and electrons, and by the uncertainty on the

transverse-momentum scale of muons. It is estimated as the relative change in S due to variations of these scales, independently up and down, by their uncertainty. We propagate such scale perturbations as small changes in the energies of the selected photons and leptons. These result in rejection of some events that would otherwise pass the nominal selection due to the requirements on the minimal values of the transverse momenta of the photons and leptons, and on the minimal value of the invariant mass of the lepton pair. We estimate the scale uncertainties from control samples of inclusive Z^0 decays, $Z \to e^+e^-$ for electrons as 0.5 %, $Z \to \mu^+\mu^-$ for muons as 0.2 %, and radiative Z^0 decays $Z \to \mu^+\mu^-\gamma$ for photons as 1.0 % in the ECAL barrel (EB) and 3.0 % in the ECAL endcaps (EE). The resulting combined uncertainty on S is 3.0 % and 4.2 % in the eeγ and $\mu\mu\gamma$ channels, respectively.

5.8.3 Uncertainties on the Acceptance-Efficiency Product $\mathcal{F}$

Of all the various factors in the cross section extraction formula (5.4), the acceptance-times-efficiency product $\mathcal{F}$ has the longest list of systematic uncertainties associated with it. We evaluate their effects on $\mathcal{F}$ by propagating changes of the individual sources up and down by one σ. They are:

E^γ resolution

The photon energy resolution. Similarly to the photon energy scale, this comes from the measurements with the radiative Z^0 decays to muons $Z \to \mu^+\mu^-\gamma$. The uncertainties on the measured in-situ photon energy resolution are 1.0 % in EB and 3.0 % in EE. Their effect on $\mathcal{F}$ in the eeγ channel — combined together with the effect of the uncertainties on the electron energy resolution discussed below — is 0.2 %. In the $\mu\mu\gamma$ channel, it is 0.1 %.

E^e resolution

The electron (and positron) energy resolution. Similarly to the electron energy scale, this comes from the measurements of inclusive Z^0 decays to electrons $Z \to e^+e^-$. The uncertainties on the measured in-situ electron energy resolution are 1.0 % in EB and 3.0 % in EE. We evaluate their effect on $\mathcal{F}$ in the eeγ

channel together with the photon energy resolution. The combined effect in the eeγ channel is 0.2 % as discussed above.

p_{T}^{μ} resolution

The muon transverse-momentum resolution. Again, similarly to the muon transverse-momentum scale, this comes from the measurements of inclusive Z^0 decays to muons $\mathrm{Z} \to \mu^+\mu^-$. The uncertainty on the measured in-situ muon transverse-momentum resolution is 0.6 %. Its effect on $\mathcal{F}$ in the $\mu\mu\gamma$ channel is 0.1 %.

Pileup

The uncertainty on the simultaneous inelastic pp collision multiplicity. We infer the distribution of pileup events $\langle N_{\mathrm{evt}} \rangle$ in data by integrating the relation (3.4) over time, where the distributions of the instantaneous luminosity $\mathscr{L}$ and number of bunches n_{b} in the LHC are known, and we use the central value of the measured inelastic cross section $\sigma_{\mathrm{inel}} = 68.0 \pm 3.4\,\mathrm{mb}$ [65]. We reweight the simulated events to match the inferred pileup distribution in data. To account for uncertainties in the estimate of this distribution, we scale it up and down by 5 %. This covers the uncertainties on $L = \int \mathscr{L}\,\mathrm{d}t$, n_{b}, and further effects due to the imperfect pileup simulation, that is the differences with respect to the data in the multiplicity, momentum and energy spectra, angular distributions, beamsize along the z axis, etc. [130]. The total effect on $\mathcal{F}$ is 0.6 % and 0.4 % in the eeγ and $\mu\mu\gamma$ channels, respectively.

PDF

The uncertainty on the modeling of the *parton distribution functions* (PDFs) of the proton. We follow [131] to estimate these uncertainties for the CTEQ6L [132] PDF set. The software package *Les Houches Accord PDF Interface* (LHAPDF) [133–135] is used to calculate per-event weights $w_{i,j}^{\pm}$ due to variations along the 21 eigenvectors of the PDF set parametrisation. Here, $i = 0, \ldots, 20$ labels the eigenvectors, $j = 1, \ldots, S_{\mathrm{gen}}$ labels the simulated events, and the superscript $\pm$ denotes the variation by $\pm 1\,\sigma$ (68 % confidence level). A weight $w_{i,j}^{\pm}$ expresses

the ratio of the probabilities for an event j to be generated using the $\pm 1\,\sigma$ variation along the i-th eigenvector of the PDF set over the central value of the PDF. Following the *modified tolerance method* [136, 137] as described in [134], we define the total uncertainty as the greater value of the asymmetric uncertainties $\Delta\mathcal{F}^+$ and $\Delta\mathcal{F}^-$. Here, the asymmetric uncertainties read:

$$\Delta\mathcal{F}^{\pm} = \bigoplus_{i=1}^{20} \max\{\pm\Delta\mathcal{F}_i^+,\, \pm\Delta\mathcal{F}_i^-,\, 0\}\,,$$

where $\bigoplus$ denotes *serial summation in quadrature*, $\bigoplus_i x_i = \sqrt{\sum_i x_i^2}$, and $\Delta\mathcal{F}_i^{\pm}$ denotes the differences $\Delta\mathcal{F}_i^{\pm} = \mathcal{F}_i^{\pm} - \mathcal{F}_0$. Here, $\mathcal{F}_0$ corresponds to the central value of $\mathcal{F}$ using the eigenvector $i = 0$ of the PDF set without variations, and $\mathcal{F}_i^{\pm}$ to the variation of the eigenvector $i = 1, \ldots, 20$ by $\pm 1\,\sigma$. To calculate $\mathcal{F}_i^{\pm}$, we generalize (5.2) to take into account the event weights $w_{i,j}^{\pm}$. Instead of counting the events, we sum their weights:

$$\begin{aligned} N \quad &\rightarrow \quad \sum_{j=1}^{N} w_j \\ \mathcal{F} = \frac{S_{\text{sel}}}{S_{\text{gen}}} \quad &\rightarrow \quad \mathcal{F}_i^{\pm} = \frac{\sum_{j=1}^{S_{\text{sel}}} w_{i,j}^{\pm}}{\sum_{k=1}^{S_{\text{gen}}} w_{i,k}^{\pm}}\,, \end{aligned}$$

where $j = 1, \ldots, S_{\text{sel}}$ runs over the selected signal events, and $k = 1, \ldots, S_{\text{gen}}$ runs over all the generated signal events within the kinematic acceptance. For the estimate of the central value, both of these yield the same, $N = \sum_{j=1}^{N} w_{0,j}$, as the weights are equal to unity for the PDF central value, $w_{0,j} = 1$ with $j = 1, \ldots, N$. We find the total PDF uncertainty value of $\max\{\Delta\mathcal{F}^+,\, \Delta\mathcal{F}^-\}/\mathcal{F}_0 = 1.1\,\%$ for both the eeγ and $\mu\mu\gamma$ decay channels.

Signal modeling

Futher uncertainties due to signal modeling in the simulation including NLO effects, the parton-shower matrix-element merging, hadronization, and other systematic uncertainties. We estimate these as the difference between the results obtained from the Monte Carlo integrator MCFM [138], and the Monte Carlo

generator Madgraph [139]. The effect on $\mathcal{F}$ from these sources is 0.6 % in the eeγ channel and 1.1 % in the $\mu\mu\gamma$ channel.

Combining all the above effects, we find that the total systematic uncertainties on $\mathcal{F}$ in the eeγ and $\mu\mu\gamma$ channels are 1.4 % and 1.6 %, respectively.

5.8.4 Uncertainties on Efficiency Scale Factors ρ_{eff}

The data/MC efficiency scale factors ρ_{eff} are affected by uncertainties from several sources. Some of them are of statistical origin due to the limited size of the control samples used for the tag-and-probe measurements, both for the data and the simulation. These uncertainties are returned by the maximum likelihood fit together with the tag-and-probe efficiencies. Other uncertainties are due to the ambiguities in the signal and background modeling in the tag-and-probe fit. These arise in situations when multiple models are consistent with the data, while yielding slightly different results. These uncertainties are estimated from differences in ρ_{eff} between the various assumed models. Further unknown systematic uncertainties are estimated as the difference in efficiencies from the fit to simulation, and from direct counting of the passing and failing events using the Monte Carlo truth information for the signal and background that is not available in data.

We sum in quadrature all of the various uncertainties mentioned above, to obtain the total systematic uncertainty. We estimate them separately for the different final state objects: photons, electrons and muons. In the cases of electrons and muons, we take into account the efficiencies of triggering, reconstruction, and identification and isolation. In the case of photons, we only account for the efficiencies of identification and isolation. We do not include the triggering and reconstruction efficiency uncertainties for photons because we do not make use of the photon triggers and because the photon identification efficiency is so high that its difference from unity is negligible, and so is the related uncertainty.

The systematic uncertainties on the data/simulation efficiency ratios ρ_{eff} in the various categories are:

Lepton Trigger

1.0 % and 0.8 % for the electron and muon triggers, respectively.

Lepton Reconstruction

0.1 % and 1.0 % for the electron and muon reconstruction, respectively.

Lepton ID & isolation

5.0 % and 2.3 % for the identification and isolation of electrons and muons, respectively.

Photon ID & isolation

0.5 % and 1.0 % for the identification and isolation of photons in the ECAL barrel and ECAL endcaps, respectively. These lead to combined uncertainties of 0.5 % and 1.0 % in the eeγ and $\mu\mu\gamma$ channels, respectively.

Summing in quadrature all the above uncertainties, we find the total systematic uncertainties on the data/simulation efficiency scale factors ρ_{eff} in the eeγ and $\mu\mu\gamma$ channels of 5.1 % and 2.9 %, respectively.

5.8.5 Uncertainty on Luminosity L

Finally, we include an uncertainty on the total integrated luminosity. It is based on the calibration of the effective cross section of pixel clusters using Van der Meer scans [140]. The value of this uncertainty is 2.2 %.

This uncertainty is the same for both the eeγ and $\mu\mu\gamma$ channels and is fully correlated. Also, it is common to a large number of other CMS analyses, unlike the other systematic uncertainties that are specific to the measurement discussed in this work. Therefore, we choose to quote the resulting uncertainty on the final result due to this uncertainty on luminosity, separately from all the other systematic uncertainties.

5.8.6 Summary of Systematic Uncertainties

Table 5.8 summarizes the systematic uncertainties due to the various sources, and their impact as discussed above. We propagate these to the estimated cross section individually. Except for the uncertainty due to luminosity, we add up in quadrature all the contributions to obtain the total systematic uncertainty.

			Effect (%)			
			Individual		Combined	
Affects	Source	Size (%)	eeγ	$\mu\mu\gamma$	eeγ	$\mu\mu\gamma$
$B_{\mathrm{Z+jets}}$	Template method	—	4.2	5.5	4.2	5.5
S	E^{γ} scale in EB, EE	1.0, 3.0	3.0	4.2		
	E^{e} scale, p_{T}^{μ} scale	0.5, 0.2		0.6	3.0	4.2
$\mathcal{F}$	E^{γ} resolution in EB, EE	1.0, 3.0	0.2	0.1		
	E^{e} resolution in EB, EE	1.0, 3.0		—		
	p_{T}^{μ} resolution	0.6	—	0.1		
	Pileup	5.0	0.6	0.4		
	PDF	—	1.1	1.1		
	Signal modeling	—	0.6	1.1	1.4	1.6
ρ_{eff}	Lepton trigger	—	0.8	1.0		
	Lepton reconsturction	—	0.1	1.0		
	Lepton ID & iso.	—	5.0	2.3		
	Photon ID & iso. in EB, EE	0.5, 1.0	0.5	1.0	5.1	2.9
L	Luminosity	2.2	2.2	2.2	2.2	2.2

Table 5.8: Summary of systematic uncertainties for the measurement of the Zγ cross section.

Chapter 6

Results

6.1 Cross Section Measurement

In Tables 6.1 and 6.2 we give the summary of the input parameters used to extract the measured value of the cross section in the eeγ and $\mu\mu\gamma$ channels using eq. (5.1). We present a summary of the systematic uncertainties in Table 5.8.

Parameter	Value
N	$4108 \pm 64.1\,(\text{stat})$
$B_{\text{Z+jets}}$	$905.9 \pm 49.8\,(\text{stat}) \pm 38.4\,(\text{syst})$
B_{other}	$38.3 \pm 2.8\,(\text{stat})$
S	$3163.8 \pm 81.0\,(\text{stat}) \pm 95.1\,(\text{syst})$
$\mathcal{F}$	$0.132 \pm 0.0018\,(\text{syst})$
ρ_{eff}	$0.929 \pm 0.0466\,(\text{syst})$
$\int \mathscr{L}\,\mathrm{d}t$ (fb^{-1})	$4.96 \pm 0.11\,(\text{syst})$

Table 6.1: Summary of input parameters for the extraction of the Zγ cross section in the eeγ channel.

The measured cross sections are:

$$\sigma(\text{pp} \to \text{Z}\gamma \to \text{ee}\gamma) = 5.20 \pm 0.13\,(\text{stat}) \pm 0.30\,(\text{syst}) \pm 0.11\,(\text{lumi})\,\text{pb}, \tag{6.1}$$

$$\sigma(\text{pp} \to \text{Z}\gamma \to \mu\mu\gamma) = 5.43 \pm 0.10\,(\text{stat}) \pm 0.29\,(\text{syst}) \pm 0.12\,(\text{lumi})\,\text{pb}. \tag{6.2}$$

These measurements are compatible with each other within their uncertainties. We

Parameter	Value
N	$6463 \pm 80.4\,(\text{stat})$
$B_{\text{Z+jets}}$	$1404.3 \pm 56.4\,(\text{stat}) \pm 77.0\,(\text{syst})$
B_{other}	$23.7 \pm 2.2\,(\text{stat})$
S	$5034.9 \pm 98.2\,(\text{stat}) \pm 213.2\,(\text{syst})$
$\mathcal{F}$	$0.196 \pm 0.001\,(\text{stat})$
ρ_{eff}	$0.945 \pm 0.016\,(\text{syst})$
$\int \mathscr{L}\,\mathrm{d}t$ (fb^{-1})	$5.00 \pm 0.11\,(\text{syst})$

Table 6.2: Summary of input parameters for the extraction of the Zγ cross section in the $\mu\mu\gamma$ channel.

use the *Best Linear Unbiased Estimator* [141] to combine them to:

$$\sigma(\text{pp} \to \text{Z}\gamma \to \ell\ell\gamma) = 5.33 \pm 0.08\,(\text{stat}) \pm 0.25\,(\text{syst}) \pm 0.12\,(\text{lumi})\,\text{pb}. \tag{6.3}$$

Both the per-channel results as well the combined one are compatible with the theoretical prediction calculated at the next-to-leading order in α_{S} as computed by MCFM:

$$\sigma_{\text{NLO}}(\text{pp} \to \text{Z}\gamma \to \ell\ell\gamma) = 5.45 \pm 0.27\,(\text{theory})\,\text{pb}. \tag{6.4}$$

In addition to these results, corresponding to the lower bound on the photon transverse momentum of $p_{\text{T}}^{\gamma} > 15\,\text{GeV}$, we measure the Z$\gamma$ cross section also for greater values of this bound, $p_{\text{T}}^{\gamma} > 60\,\text{GeV}$ and $p_{\text{T}}^{\gamma} > 90\,\text{GeV}$. We give these results together with their predictions in Table 6.3. Again, we find no significant disagreement between the measurement and the theory. We summarize all of the cross section results in Figure 6.1.

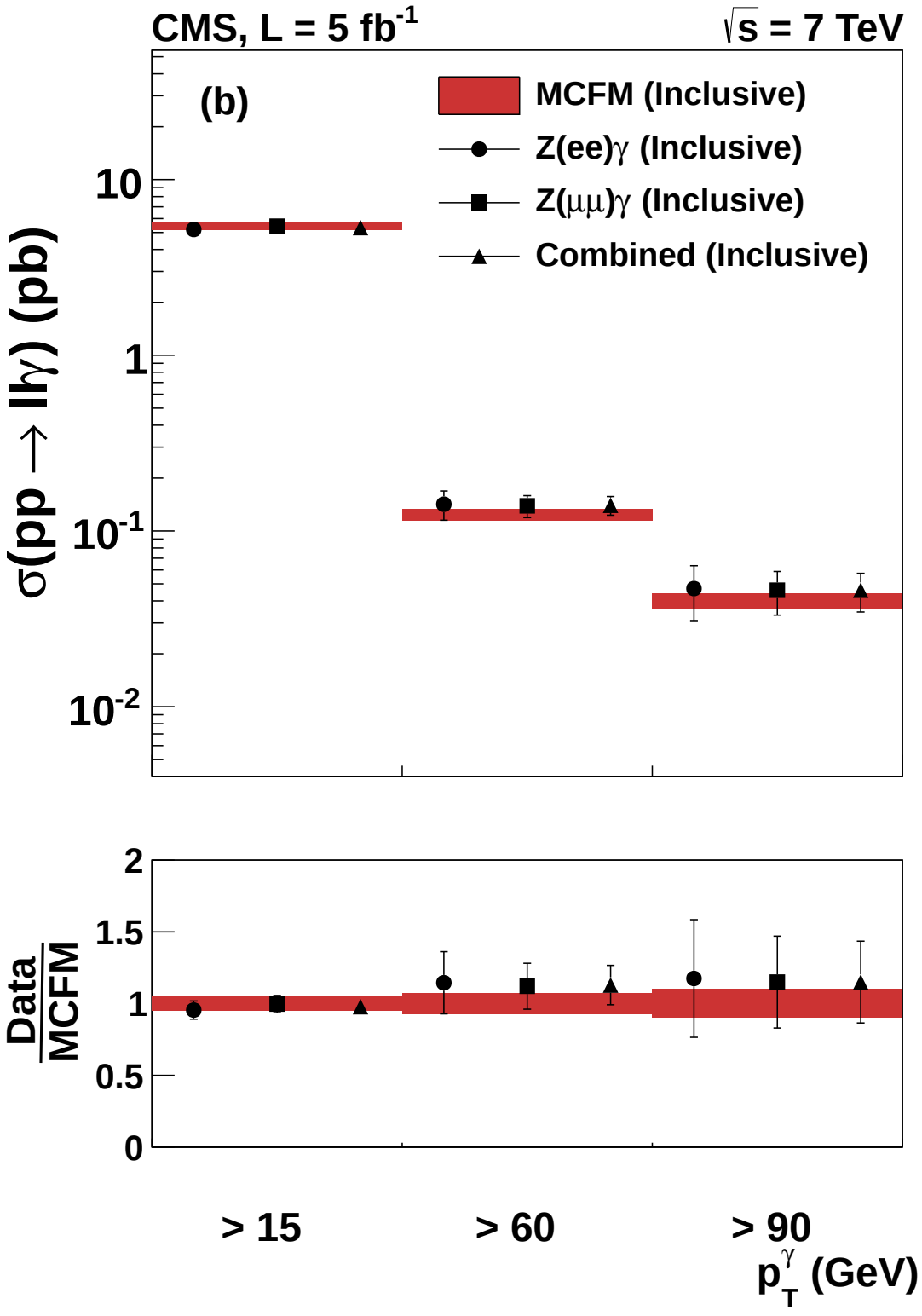

Figure 6.1: A summary of the measured Zγ cross section values compared to their theoretical predictions.

p_{T}^{γ} requirement	Result	Cross section (pb)
$p_{\mathrm{T}}^{\gamma} > 15\,\mathrm{GeV}$	eeγ channel	$5.20 \pm 0.13\,(\mathrm{stat}) \pm 0.30\,(\mathrm{syst}) \pm 0.11\,(\mathrm{lumi})$
	$\mu\mu\gamma$ channel	$5.43 \pm 0.10\,(\mathrm{stat}) \pm 0.29\,(\mathrm{syst}) \pm 0.12\,(\mathrm{lumi})$
	Mean	$5.33 \pm 0.08\,(\mathrm{stat}) \pm 0.25\,(\mathrm{syst}) \pm 0.12\,(\mathrm{lumi})$
	Prediction	$5.45 \pm 0.27\,(\mathrm{theory})$
$p_{\mathrm{T}}^{\gamma} > 60\,\mathrm{GeV}$	eeγ channel	$0.77 \pm 0.07\,(\mathrm{stat}) \pm 0.13\,(\mathrm{syst}) \pm 0.02\,(\mathrm{lumi})$
	$\mu\mu\gamma$ channel	$0.76 \pm 0.06\,(\mathrm{stat}) \pm 0.08\,(\mathrm{syst}) \pm 0.02\,(\mathrm{lumi})$
	Mean	$0.76 \pm 0.05\,(\mathrm{stat}) \pm 0.08\,(\mathrm{syst}) \pm 0.02\,(\mathrm{lumi})$
	Prediction	$0.58 \pm 0.08\,(\mathrm{theory})$
$p_{\mathrm{T}}^{\gamma} > 90\,\mathrm{GeV}$	eeγ channel	$0.047 \pm 0.013\,(\mathrm{stat}) \pm 0.010\,(\mathrm{syst}) \pm 0.001\,(\mathrm{lumi})$
	$\mu\mu\gamma$ channel	$0.046 \pm 0.008\,(\mathrm{stat}) \pm 0.010\,(\mathrm{syst}) \pm 0.001\,(\mathrm{lumi})$
	Mean	$0.046 \pm 0.007\,(\mathrm{stat}) \pm 0.009\,(\mathrm{syst}) \pm 0.001\,(\mathrm{lumi})$
	Prediction	$0.040 \pm 0.004\,(\mathrm{theory})$

Table 6.3: A summary of the Zγ cross section measurements together with their theoretical predictions using NLO QCD calculations using MCFM.

6.2 Anomalous Triple Gauge Coupling (ATGC) Limits

We use the SHERPA Monte Carlo generator [142] to produce simulations of the expected ATGC signals for Zγ with up to 1 additional jet. We set the limits on the values of the h_3^V and h_4^V coupling constants with V = Z, γ. We estimate the one-dimensional limits for all of these couplings together with two-dimensional limits on both the Z-type and γ-type couplings. In all of these cases, we assume SM values for all the other couplings whose limits are not considered.

As discussed in Section 2.10, we calculate the limits without a dipole form-factor scaling (2.78). Such a form-factor is often used to prevent violation of unitarity at hight $\hat{s}$ [38]. Our approach has the advantage that it is free of ad-hoc assumptions about the energy dependence of such a scaling, and that it is correct when the scale of new physics Λ is significantly greater than $\sqrt{\hat{s}}$. The absence of observation of novel interactions and particles at the energy scale $\sqrt{\hat{s}}$, that we probe, supports the correctness of the assumption $\Lambda^2 \gg \hat{s}$.

We give the one-dimensional ATGC limits in Table 6.2. Figures 6.2 and 6.3 show the two-dimensional limits.

Channel	$\lvert h_3^\gamma\rvert \times 10^3$	$\lvert h_4^\gamma\rvert \times 10^5$	$\lvert h_3^{\mathrm{Z}}\rvert \times 10^3$	$\lvert h_4^{\mathrm{Z}}\rvert \times 10^5$
eeγ	< 13	< 11	< 11	< 9.9
$\mu\mu\gamma$	< 13	< 12	< 11	< 11
Combined	< 10	< 8.8	< 8.6	< 8.0

Table 6.4: One-dimensional limits on the Z$\gamma\gamma$ and ZZγ ATGC couplings h_3^V and h_4^V with $V = \gamma$, Z.

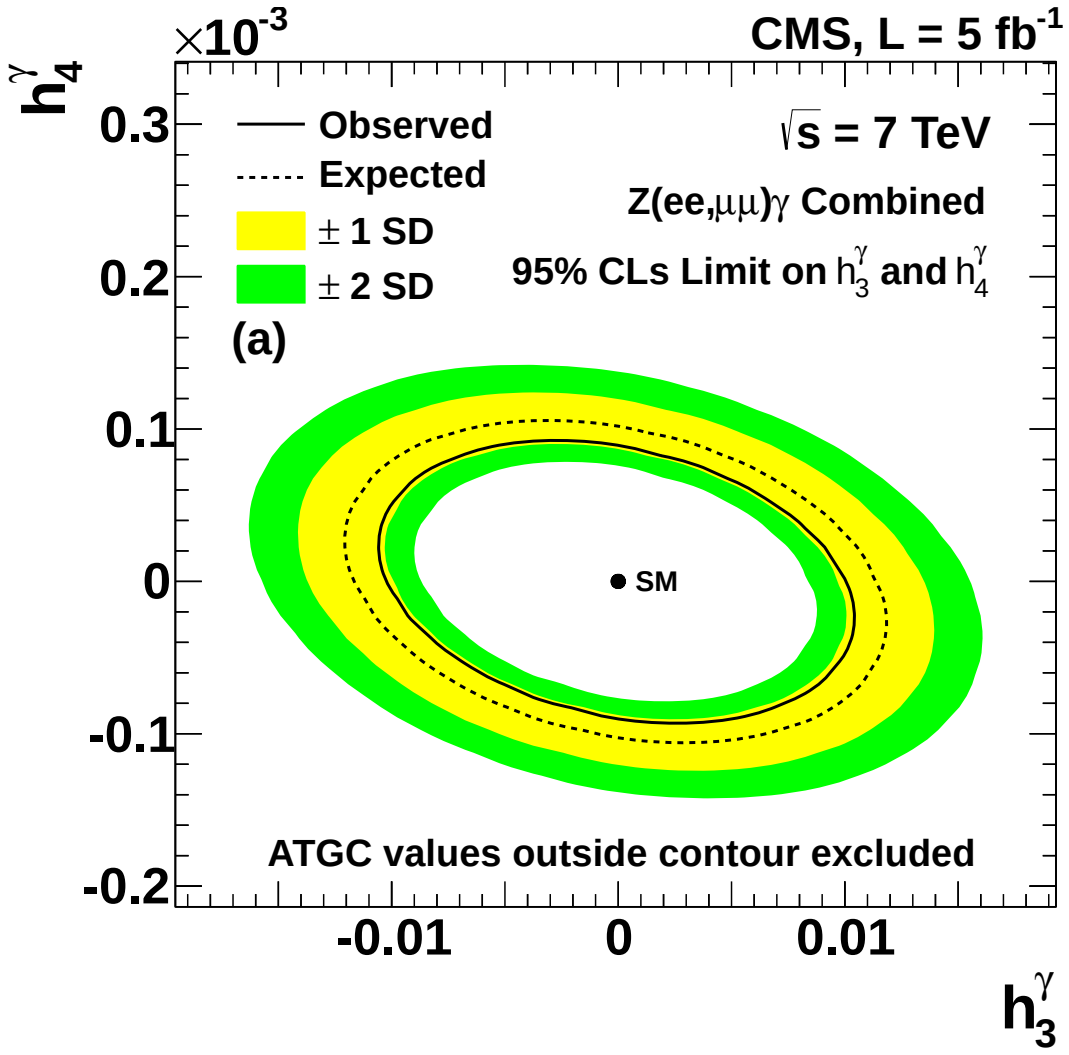

Figure 6.2: Two-dimensional limits on the Z$\gamma\gamma$ ATGCs h_3^γ vs. h_4^γ. The observed (solid black contour) and expected (dashed black contour) 95 % CL exclusion limits are shown together with bands indicating ± 1 (light yellow) and ± 2 (light green) standard deviation expectations on the expected limit. The SM expected value is denoted by the solid black dot in the center.

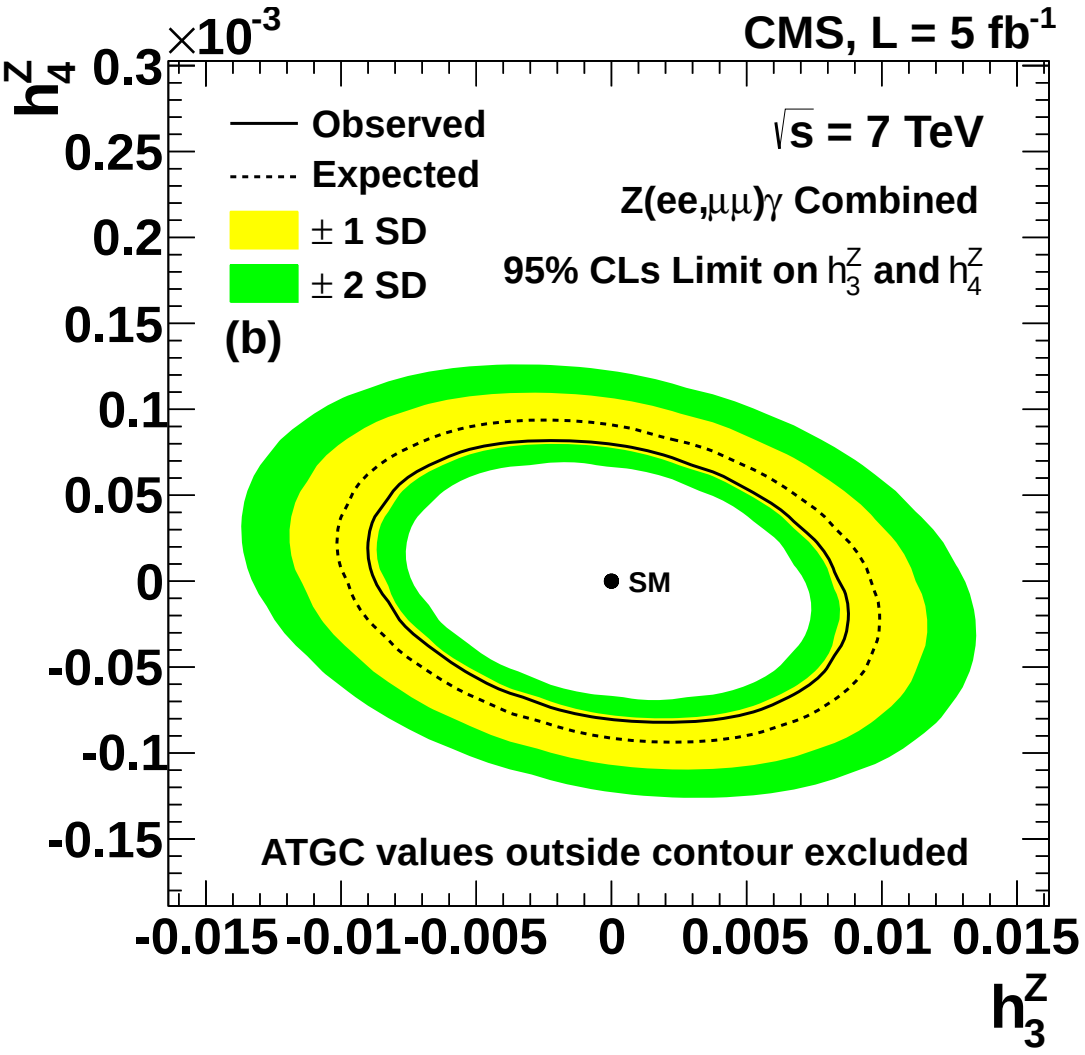

Figure 6.3: Two-dimensional limits on ZZγ ATGCs h_3^Z vs. h_4^Z. The observed (solid black contour) and expected (dashed black contour) 95 % CL exclusion limits are shown together with bands indicating ± 1 (light yellow) and ± 2 (light green) standard deviation expectations on the expected limit. The SM expected value is denoted by the solid black dot in the center.

6.3 Comparison with Other Experiments

Electroweak measurements at LEP [143–149], the Tevatron [150–152], and initial data from the LHC [153, 154] have previously constrained the values of the Zγ ATGCs. All of these results are compatible with the SM and are superseded by the following LHC measurements preceding this work that we discuss next.

CMS has previously measured the Zγ cross section and ATGC limits using $36\,\mathrm{pb}^{-1}$ of data collected in 2010 at $\sqrt{s} = 7\,\mathrm{TeV}$ [155]. The ATLAS collaboration also published the cross section measurements at $\sqrt{s} = 7\,\mathrm{TeV}$ for the 2010 data [156] as well as an update for $1\,\mathrm{fb}^{-1}$ of the 2011 data including ATGC limits [157].

In the analysis of the 2010 data, CMS used a looser requirement on the photon transverse momentum, $p_{\mathrm{T}} > 10\,\mathrm{GeV}$. Therefore, the 2010 cross section measurement is not directly comparable with the results presented in section 6.1. Table 6.3 shows the corresponding previous ATGC results.

Source	$\lvert h_3^\gamma\rvert \times 10^3$	$\lvert h_4^\gamma\rvert \times 10^5$	$\lvert h_3^{\mathrm{Z}}\rvert \times 10^3$	$\lvert h_4^{\mathrm{Z}}\rvert \times 10^5$
CMS, $36\,\mathrm{pb}^{-1}$ [119]	< 70	< 60	< 50	< 50
ATLAS, $1\,\mathrm{fb}^{-1}$ [157]	< 28	< 21	< 26	< 22

Table 6.5: Previous ATGC limit results using LHC data

.

6.4 Current Status and Outlook

In 2012, the Zγ analysis of the CMS collaboration has focused on a search for a SM Higgs boson in this decay channel using $5.0\,\mathrm{fb}^{-1}$ of the 2011 proton-proton collision data collected at $\sqrt{s} = 7\,\mathrm{TeV}$ and $19.6\,\mathrm{fb}^{-1}$ of the 2012 proton-proton collision data collected at $\sqrt{s} = 8\,\mathrm{TeV}$. The results have recently been published in [158]. The sensitivity is too low to observe a Standard Model Higgs boson but it is interesting for its power to exclude some exotic non-Standard-Model scenarios predicting greater Higgs cross section times $\mathrm{H} \to \mathrm{Z}\gamma$ branching fraction being first such analysis at the LHC.

The search is performed by looking for a narrow peak above a smooth background in the spectrum of the Zγ invariant mass with the Z decaying to electrons and muons, ℓ = e, μ, in the range of $m_{\ell\ell\gamma}$ between 120 GeV and 150 GeV. The main sources of background coming from Zγ and Z + jets production are estimated from the data through a fit to the $m_{\ell\ell\gamma}$ spectrum in the range of 100 GeV to 180 GeV, cf. Figure 6.4.

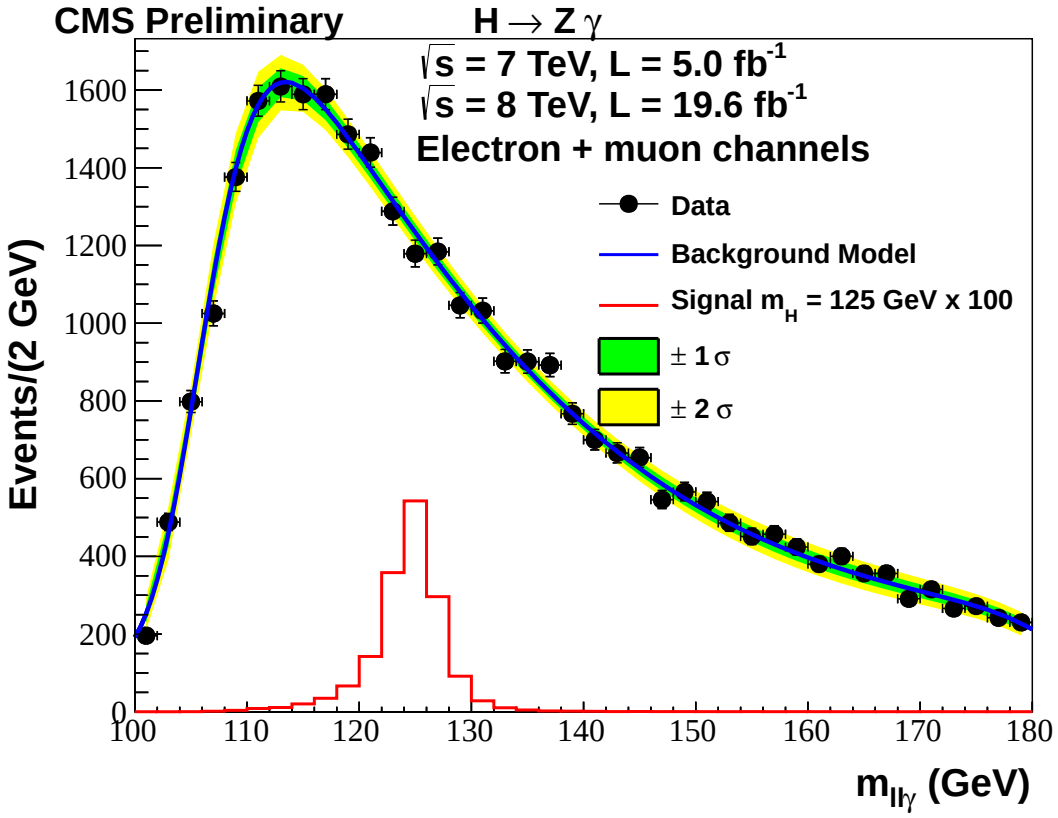

Figure 6.4: The spectrum of $m_{\ell\ell\gamma}$ for events selected in the H $\to$ Zγ $\to$ $\ell\ell\gamma$ search with data collected at 7 and 8 TeV [158].

To model the expected signal distribution, the CMS analysis employs the PHOSPHOR Fit photon energy measurements and corrections discussed in Section 5.6 and developed for the analysis described in this work. The currently low sensitivity is dominated by the low signal-to-background ratio. To increase the sensitivity, events are classified in four categories based on the $m_{\ell\ell\gamma}$ resolution for both the eeγ and $\mu\mu\gamma$ channels. Figure 6.4 shows the $m_{\ell\ell\gamma}$ spectrum and background model fit combined

over all the categories of both eeγ and $\mu\mu\gamma$ channels.

The expected 95 % confidence level limits on the Higgs production cross section times the H $\rightarrow$ Zγ branching fraction are between 6 and 19 times the Standard Model cross section in the range of 120 GeV to 150 GeV. No significant excess is observed. The observed 95 % confidence level upper cross section limits on the Higgs production times the H $\rightarrow$ Zγ branching fraction are between about 3 and 31 times the Standard Model cross section across the considered mass range, and about 10 times the Standard Model cross section at $m_{\mathrm{H}} = 125\,\mathrm{GeV}$, cf. Figure 6.5

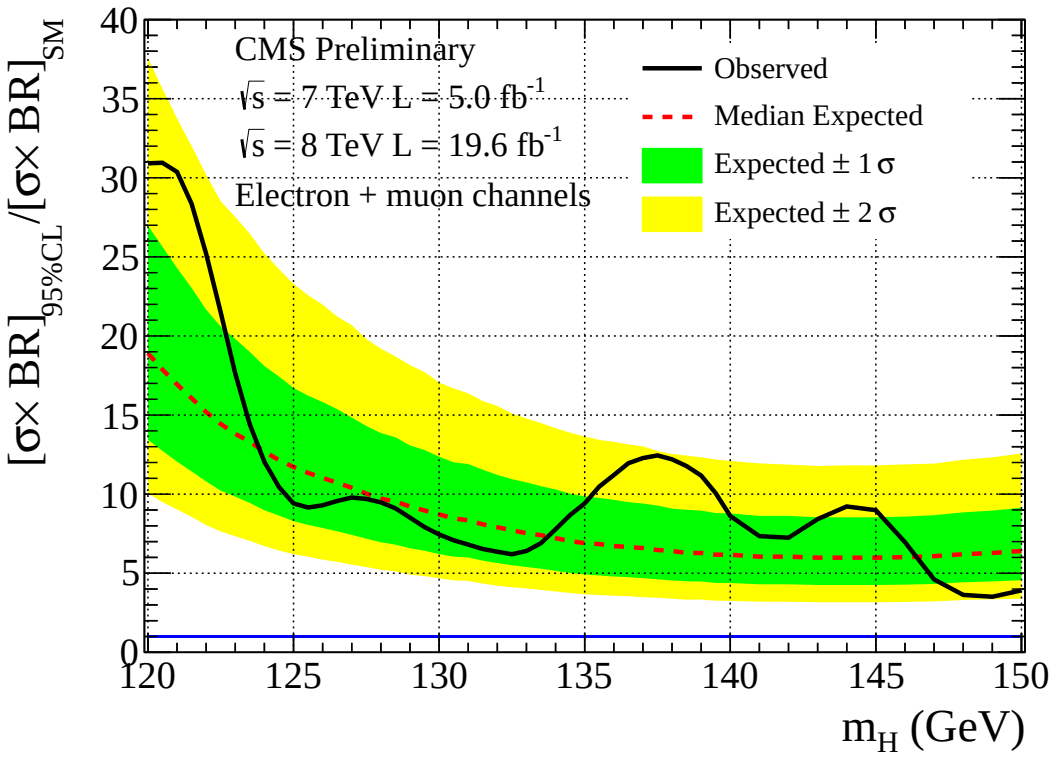

Figure 6.5: The observed and expected limit on the cross section times branching fraction of the H $\rightarrow$ Zγ process [158].

In addition to the Higgs search, the CMS collaboration intends to produce the Zγ production cross section measurement and Zγ ATGC limits using the proton-proton collision data collected in 2012. As of this writing, these analyses are about to commence. These are interesting since they will provide the first measurements at $\sqrt{s} = 8\,\mathrm{TeV}$ of this kind. Compared to the analyses at $\sqrt{s} = 7\,\mathrm{TeV}$, they will benefit

from the increased energy and data sample size.

The increase of the center of mass energy is the leading effect here. It leads to an increase of the production cross section of events with high p_{T} photons. This increase is especially significant for scenarios with nonzero ATGCs. The ATGC sensitivity scales with a square root of such a cross section increase because of the quadratic dependence of the cross section on h_3 and h_4 (2.80).

The accuracy of the cross section measurements scales approximately with a square root of the luminosity because the systematic uncertainties are largely of statistical origin due to limited sizes of control samples. Similarly to the $\sqrt{s}$ dependence, The ATGC sensitivity then scales with a square root of the cross section accuracy also because of the quadratic dependence of the cross section on the couplings. This results in a scaling of the ATGC sensitivity with approximately the fourth root of the luminosity. Accounting for both of these effects, Monte Carlo studies show that we may expect the analysis of the 2012 data to improve the sensitivity of the limits on h_3 and h_4 by factors of approximately 2 and 3, respectively.

A natural longer-term outlook is to perform all of the above $\mathrm{Z}\gamma$ analyses—the $\mathrm{Z}\gamma$ production cross section measurement, the $\mathrm{Z}\gamma$ ATGC limits, and the search for a Higgs boson in the $\mathrm{H} \to \mathrm{Z}\gamma$ decay channel—with the upcoming proton-proton collision data $\sqrt{s} \approx 13\,\mathrm{TeV}$ when the LHC commences operation in 2015.

The increase in the center of mass energy is of major importance as it will enable potentially discoveries of new heavy TeV-scale resonances at 13 TeV that are simple inaccessible at 7-8 TeV. Furthermore, the increased center of mass energy would lead to a significant increase of the ATGC hard-photon $\mathrm{Z}\gamma$ production, especially due to the *sqrts* scaling of the h_4 terms. In addition, the increased production cross section and luminosity will lead to larger data samples. That will further decrease the statistical uncertainties and also other systematic uncertainties that are of statistical origin due to the sizes of control samples, such as the measurements of the energy scale and resolution of photons and electrons, and measurements of the momentum scale and resolution of the muons. Again, Monte Carlo studies show, that an analysis of $20\,\mathrm{fb}^{-1}$ data may lead to an improvement of the h_3 and h_4 limit sensitivity by

factors of approximately 5 and 20, respectively.

Finally, a new method has been developed to estimate the dominant Z + jets background based on the isolation variables. This method performs better in terms of the uncertainties thus mitigating the leading systematic uncertainty.

These Zγ studies can be extended by measurements of the Zγ polarization, differential cross section in the transverse momentum of the photon, Zγ+n jets cross section with $n = 0, 1, 2, \ldots$, and searches for heavy resonances beyond $m_{\ell\ell\gamma} = 150\,\text{GeV}$. The Z$\gamma$ final state promises a rich and exciting field of future studies.

Appendix A

PHOSPHOR Fit

Figures A.1 through A.42 show the fits of photon energy scale and resolution in data and simulation as described in Section 5.6 about the PHOSPHOR Fit. We include all the fits for 14 photon categories based on the photon transverse momentum p_{T} (2 to 4 bins with edges at 10 GeV, 12 GeV, 15 GeV and 20 GeV), pseudorapidity (2 bins; photons registered in the ECAL barrel and the ECAL endcaps), and R_9 (2 bins with an edge at 0.94 in the barrel and 0.95 in the endcaps), see Table A.1.

For each category, we extract the photon energy scale and resolution in three different ways:

Monte Carlo Truth (MC Truth)

A fit to the photon energy response in simulation.

Monte Carlo Fit (MC Fit)

A fit to the $\mu\mu\gamma$ invariant mass in simulation.

Data Fit

A fit to the $\mu\mu\gamma$ invariant mass in data.

The MC truth represents the benchmark estimate of the photon energy scale and resolution in the simulation. The comparison of the MC truth and the MC fit represents a closure test of the PHOSPHOR Fit method. The data fit represents the estimate of the photon energy scale and resolution in the data.

For each fit, we plot the data (black points with error bars) overlaid with the fitted model (blue solid line) twice. Once in the full fit range on a logarithmic y-axis scale

				Figure		
Category	Subdetector	R_9	p_{T} (GeV)	MC Truth	MC Fit	Data Fit
1	Barrel	> 0.94	10-12	A.1	A.15	A.29
2			12-15	A.2	A.16	A.30
3			15-20	A.3	A.17	A.31
4			> 20	A.4	A.18	A.32
5		< 0.94	10-12	A.5	A.19	A.33
6			12-15	A.6	A.20	A.34
7			15-20	A.7	A.21	A.35
8			> 20	A.8	A.22	A.36
9	Endcaps	> 0.95	10-15	A.9	A.23	A.37
10			> 15	A.10	A.24	A.38
11		< 0.95	10-12	A.11	A.25	A.39
12			12-15	A.12	A.26	A.40
13			15-20	A.13	A.27	A.41
14			> 20	A.14	A.28	A.42

Table A.1: Photon categories used in the PHOSPHOR Fit. The (endcaps, $R_9 > 0.95$) category contains the fewest events. This is the reason for the lower number of p_{T} bins: only 2 instead of 4.

(top left), and once in a shorter range, which covers the peak area in more detail, on a linear y-axis scale (top middle).

We also evaluate the goodness of each fit as described in Section 5.6.2. We plot the χ^2 pulls (bottom left), the χ^2 residuals (bottom middle), and the χ^2 pull distribution (black points with error bars; top right) overlaid with a properly normalized unit Gaussian (solid blue line). We evaluate the χ^2 statistic, together with the related number of degrees of freedom N_{DOF} and the p-value of the χ^2 statistic assuming it follows the known χ^2 PDF (bottom right).

In addition to the goodness-of-fit quantities, we also list the parameters of the fitted model in the bottom right. These vary depending on the kind of the fit: Monte Carlo (MC) truth, MC fit or data fit. For the parameters, that are floated in the fit, we also list the resulting uncertainties. For the parameters, that are fixed in the fit, we only give the central values.

A.1 Monte Carlo Truth

Figures A.1 to A.14 show fits to the photon energy response in simulation for the 14 different photon categories as detailed in Table A.1. The model parameters shown in the bottom right are:

$s_{\mathbf{true}}$

: The fitted photon energy scale.

$r_{\mathbf{true}}$

: The fitted photon energy resolution.

We float both of these parameters in all the fits.

All fits show a good agreement between the data and the model with p-values ranging from 0.18 % (Figure A.8) to 93 % (Figure A.10). Also of note are the strongly non-Gaussian forms of the response spectra in all categories.

A.1.1 Barrel, $R_9 > 0.94$

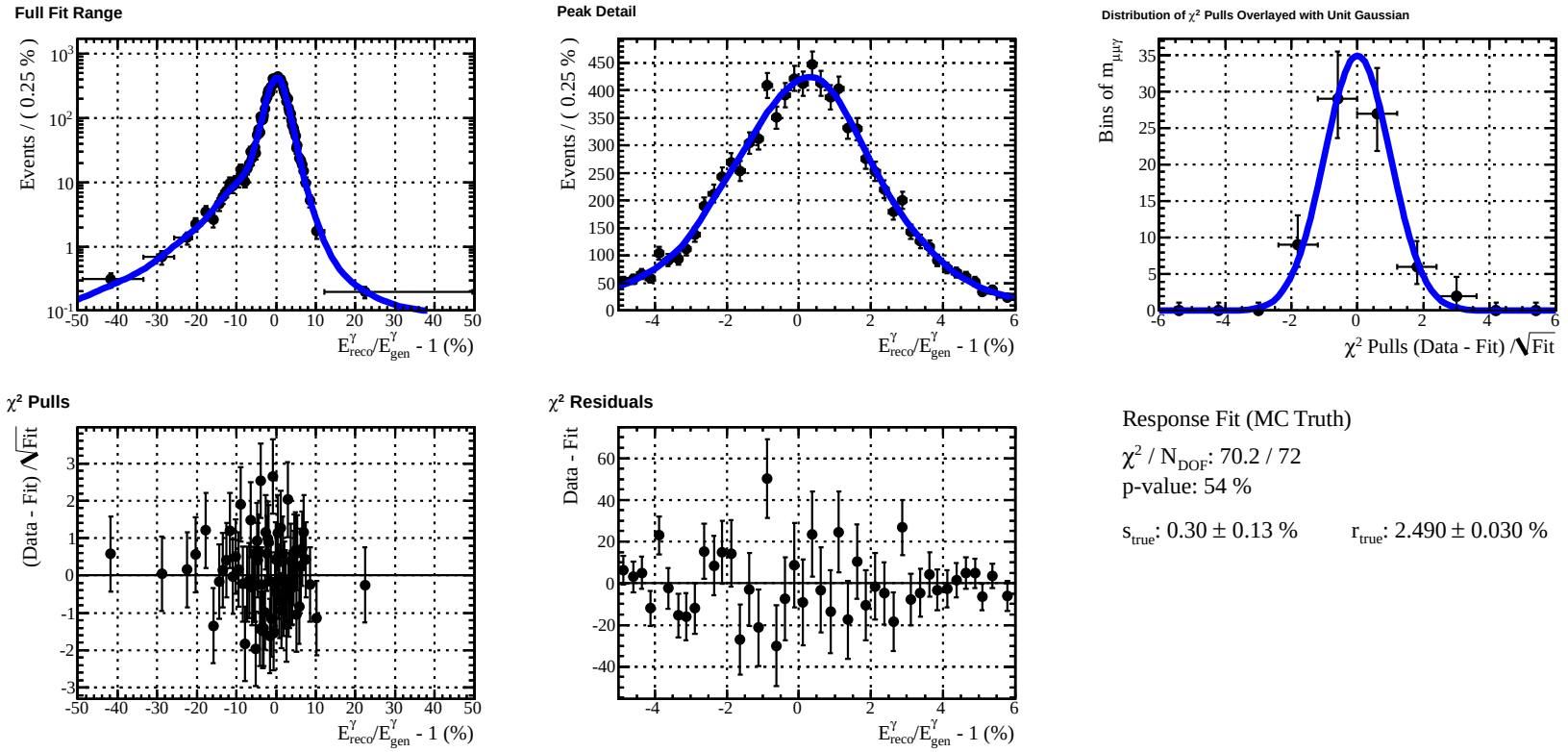

Figure A.1: Fit to photon energy response for photons in the barrel, with $R_9 > 0.94$, and p_{T} of (10 to 12) GeV.

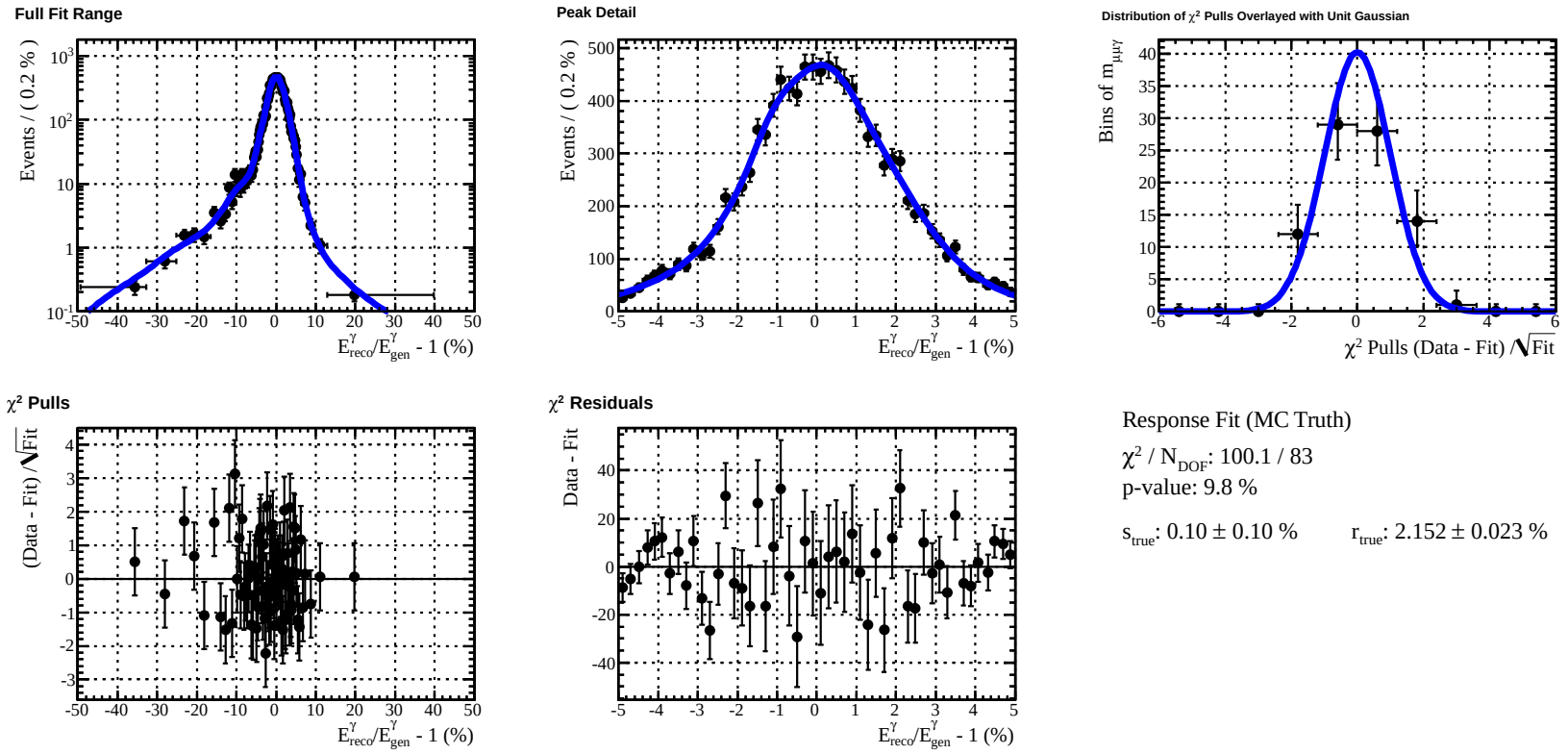

Figure A.2: Fit to photon energy response for photons in the barrel, with $R_9 > 0.94$, and p_{T} of (12 to 15) GeV.

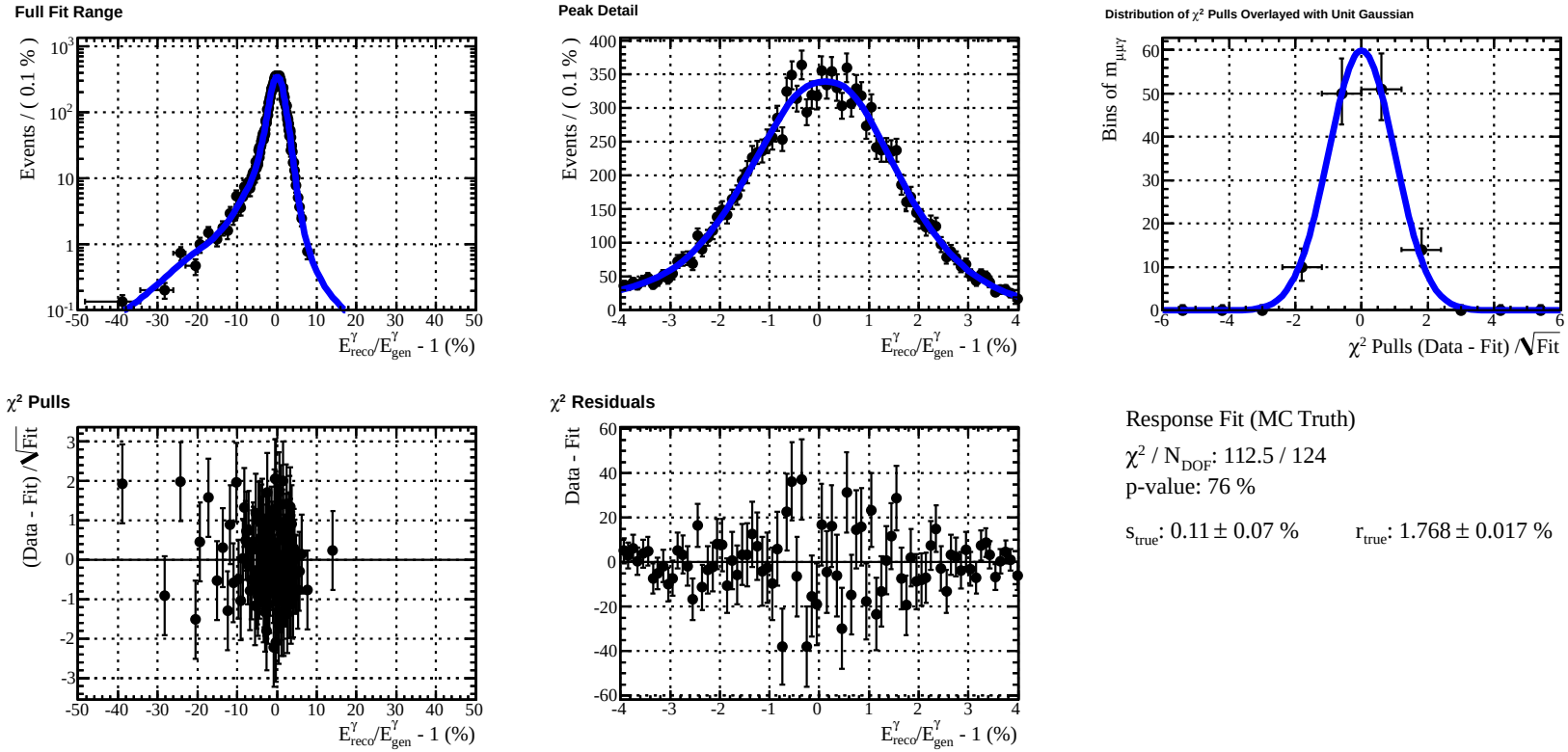

Figure A.3: Fit to photon energy response for photons in the barrel, with $R_9 > 0.94$, and p_{T} of (15 to 20) GeV.

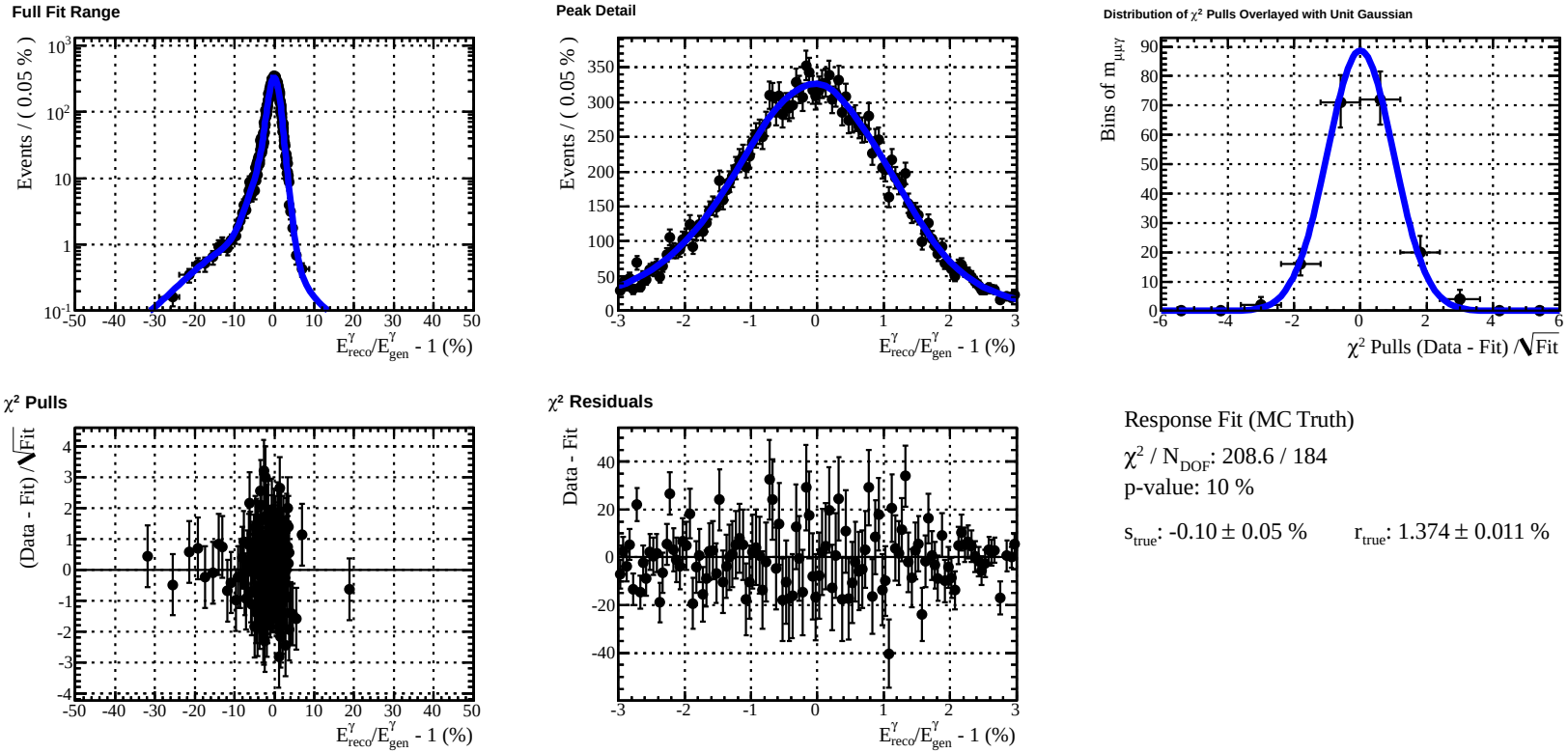

Figure A.4: Fit to photon energy response for photons in the barrel, with $R_9 > 0.94$, and $p_{\mathrm{T}} > 20\,\mathrm{GeV}$.

A.1.2 Barrel, $R_9 < 0.94$

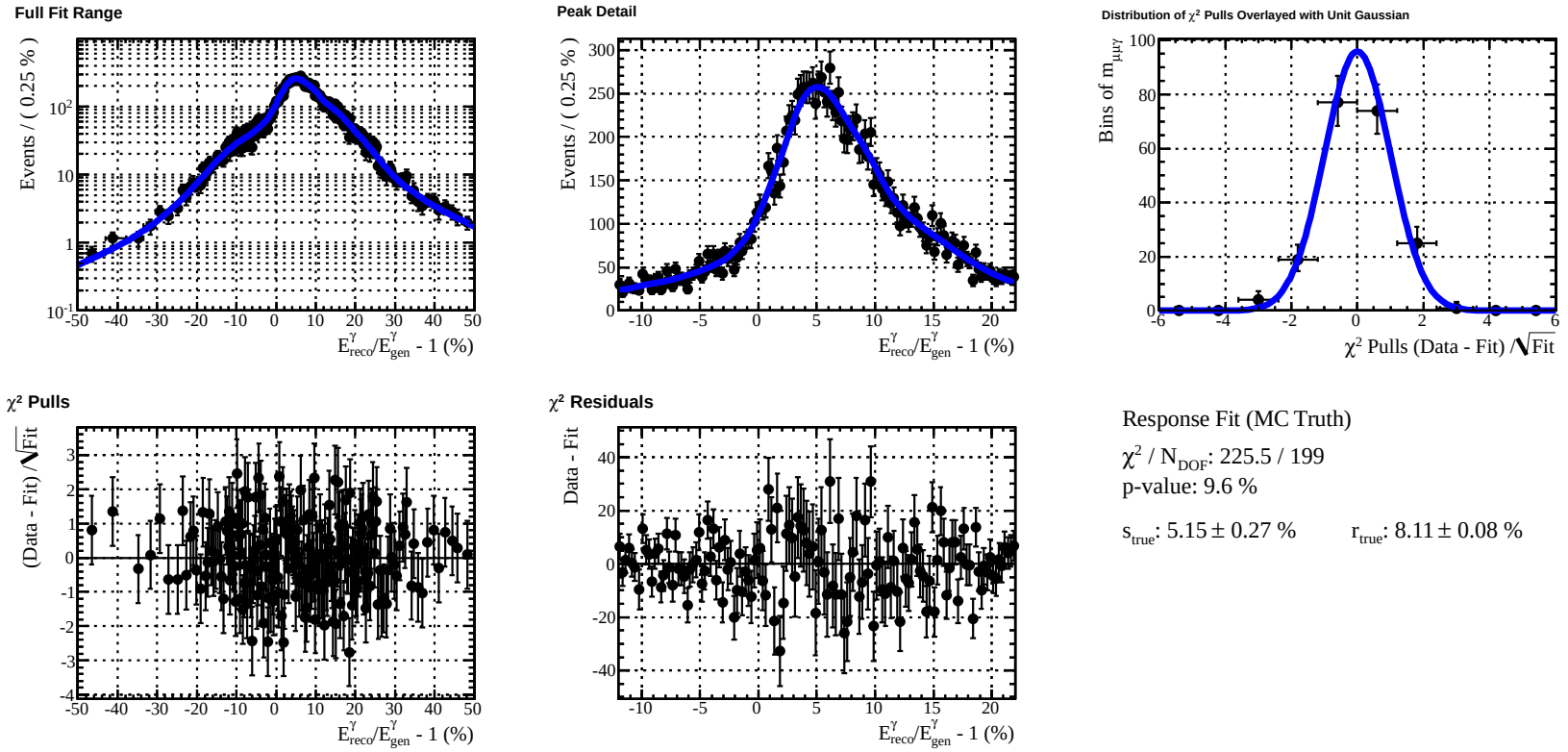

Figure A.5: Fit to photon energy response for photons in the barrel, with $R_9 < 0.94$, and p_{T} of (10 to 12) GeV.

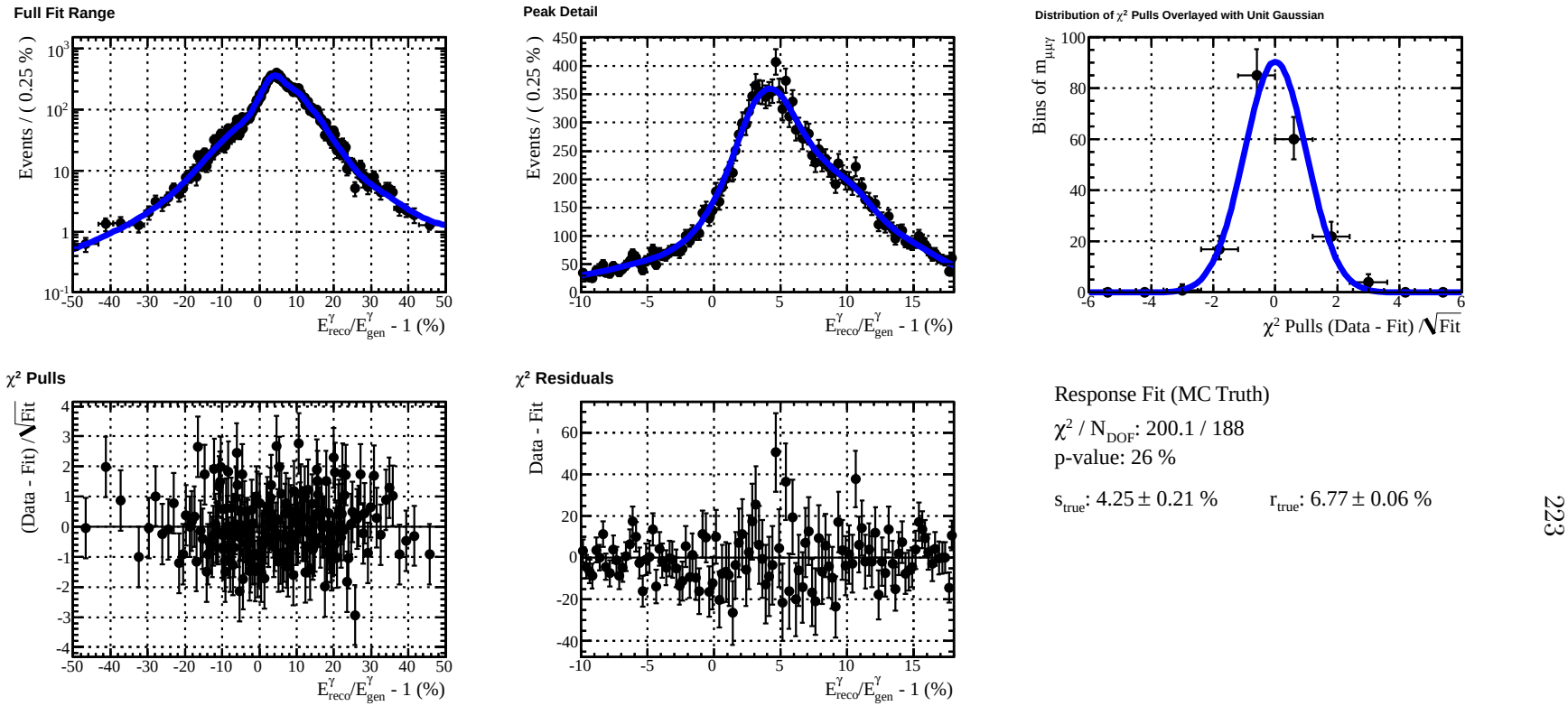

Figure A.6: Fit to photon energy response for photons in the barrel, with $R_9 < 0.94$, and p_{T} of (12 to 15) GeV.

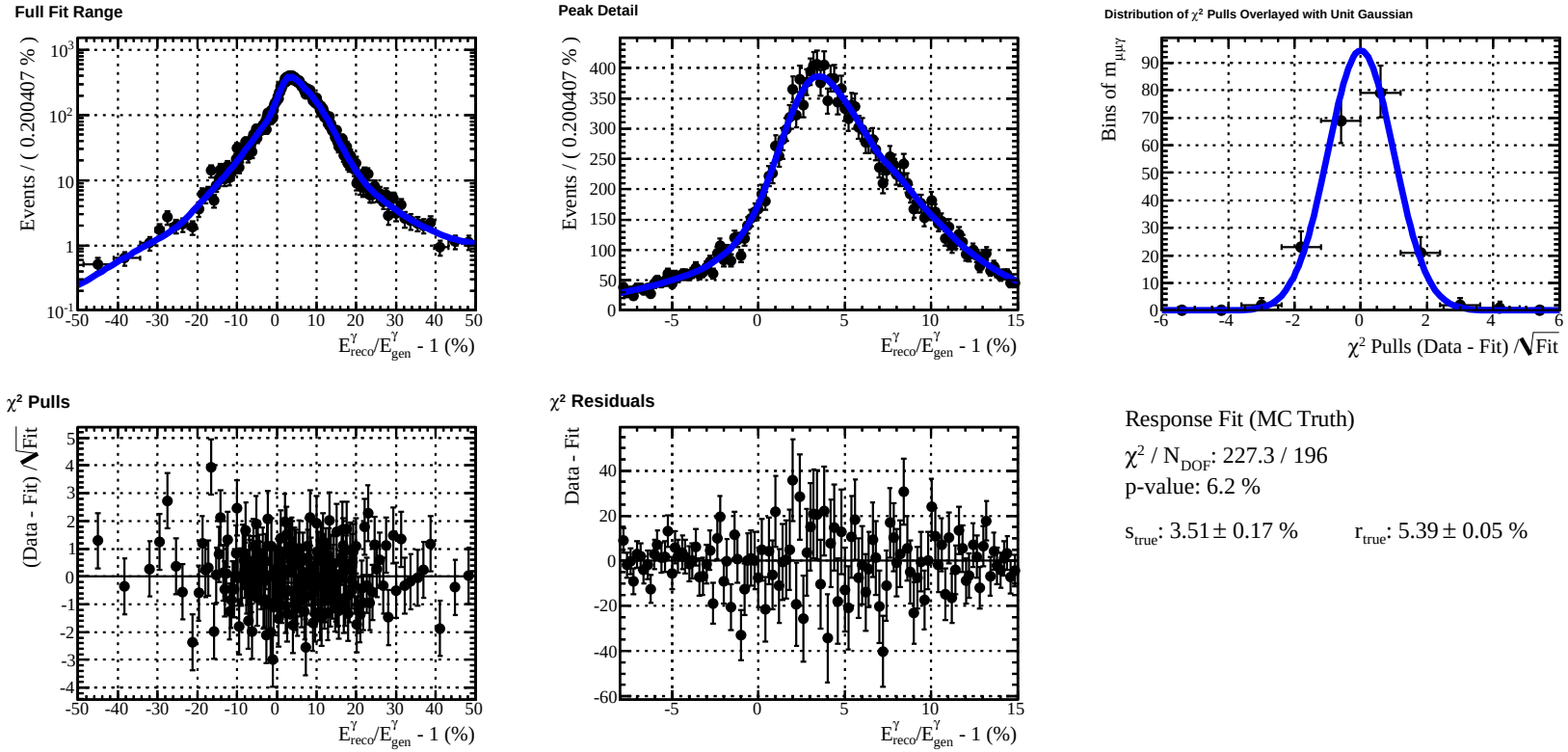

Figure A.7: Fit to photon energy response for photons in the barrel, with $R_9 < 0.94$, and p_{T} of (15 to 20) GeV.

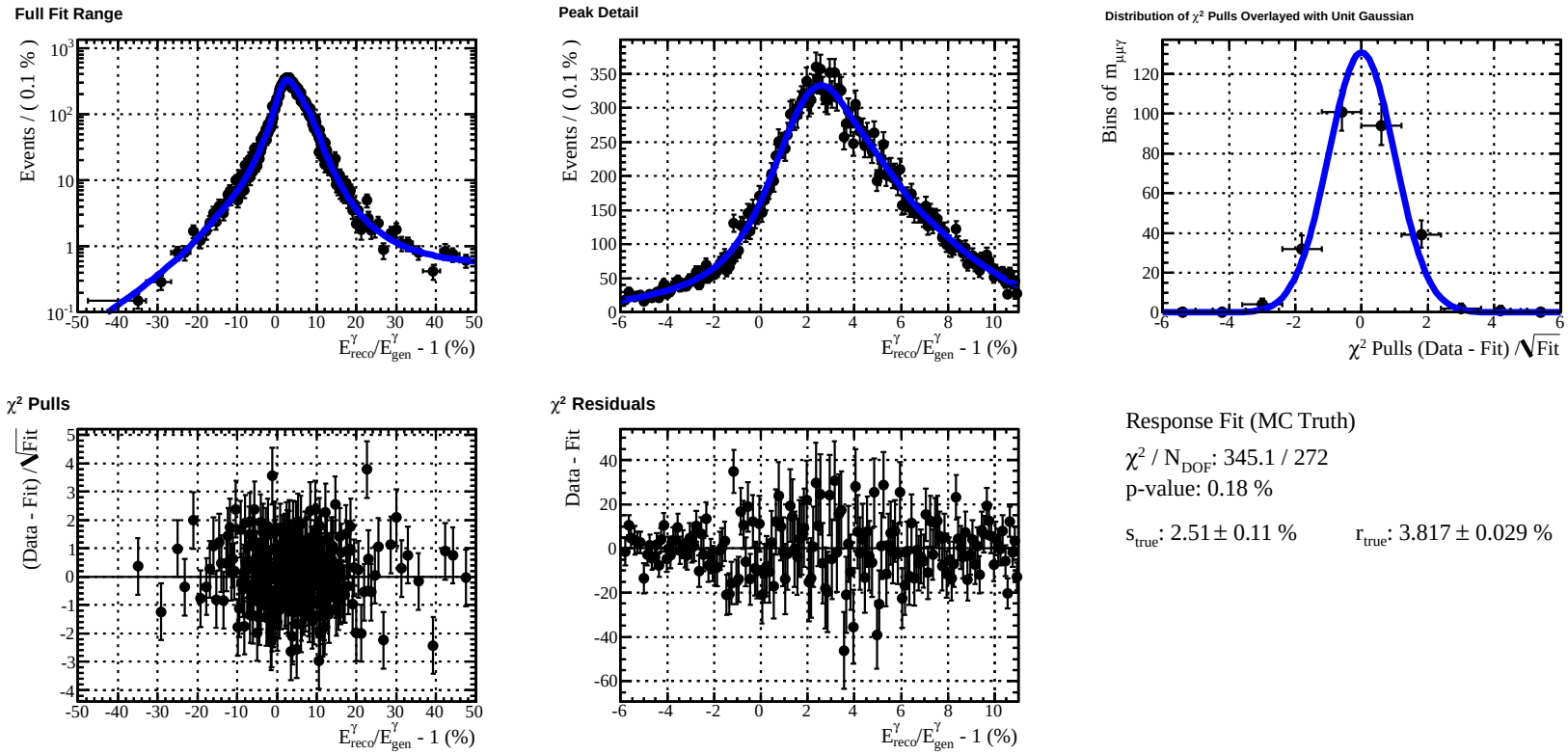

Figure A.8: Fit to photon energy response for photons in the barrel, with $R_9 < 0.94$, and $p_{\mathrm{T}} > 20\,\mathrm{GeV}$.

A.1.3 Endcaps, $R_9 > 0.95$

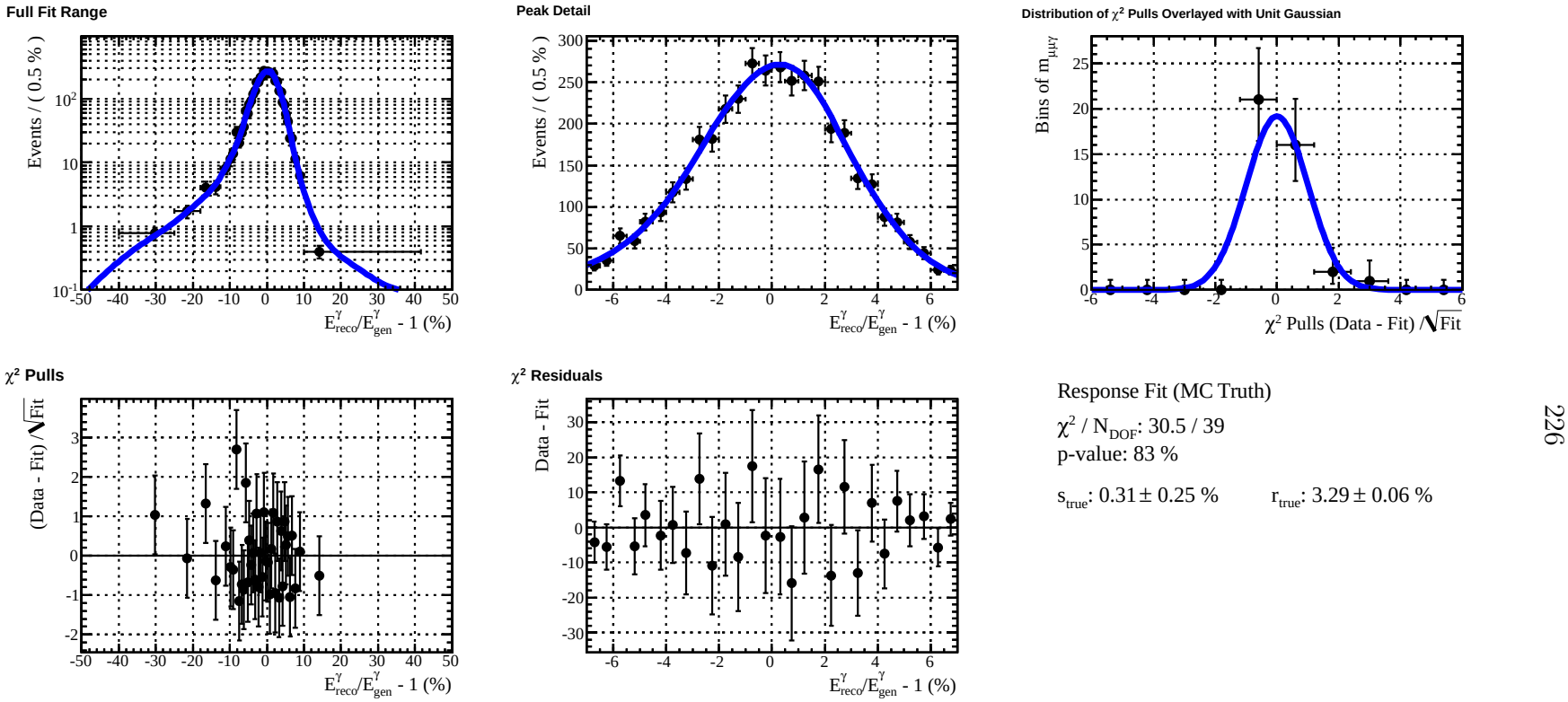

Figure A.9: Fit to photon energy response for photons in the endcaps, with $R_9 > 0.95$, and p_{T} of (10 to 15) GeV.

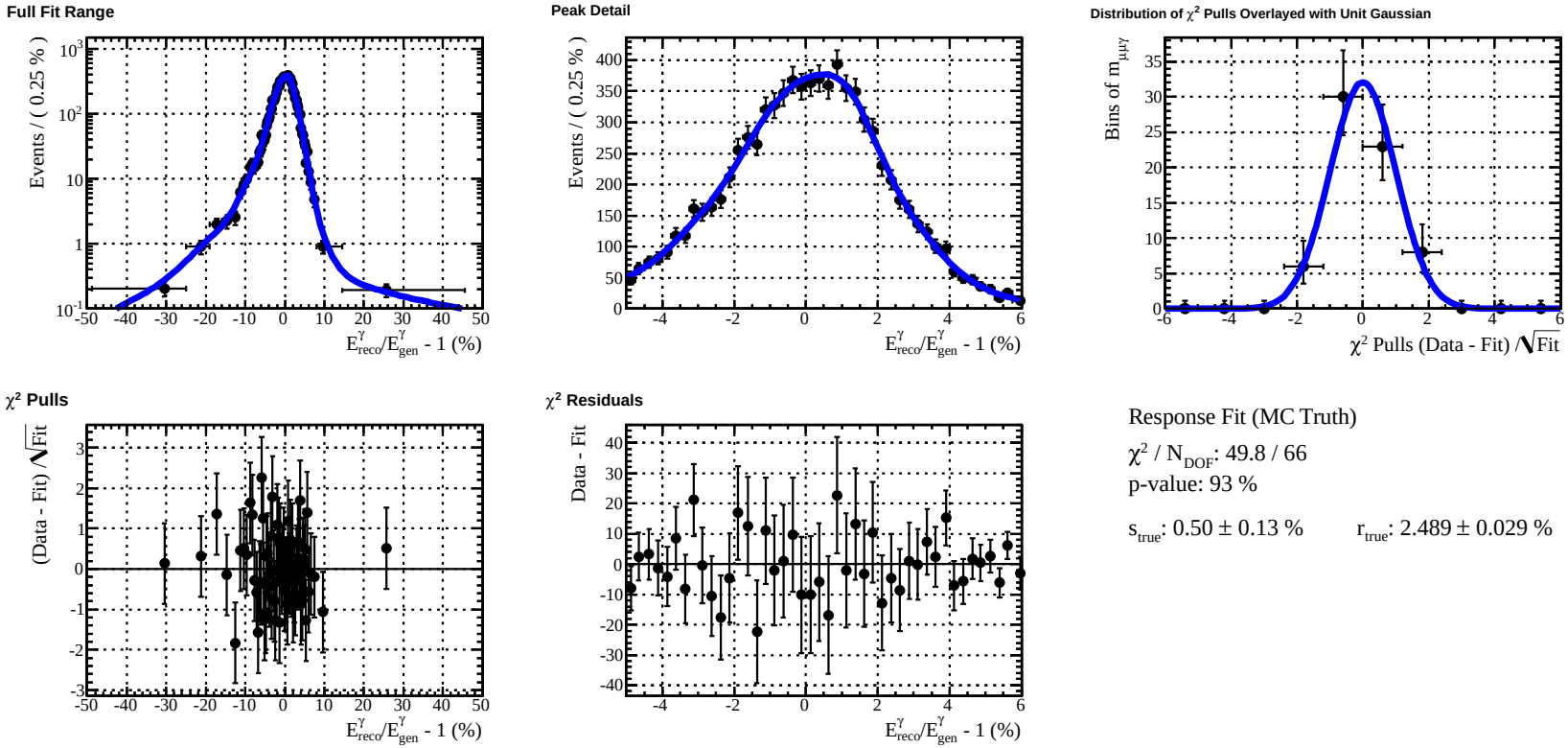

Figure A.10: Fit to photon energy response for photons in the endcaps, with $R_9 > 0.95$, and $p_{\mathrm{T}} > 15\,\mathrm{GeV}$.

A.1.4 Endcaps, $R_9 < 0.95$

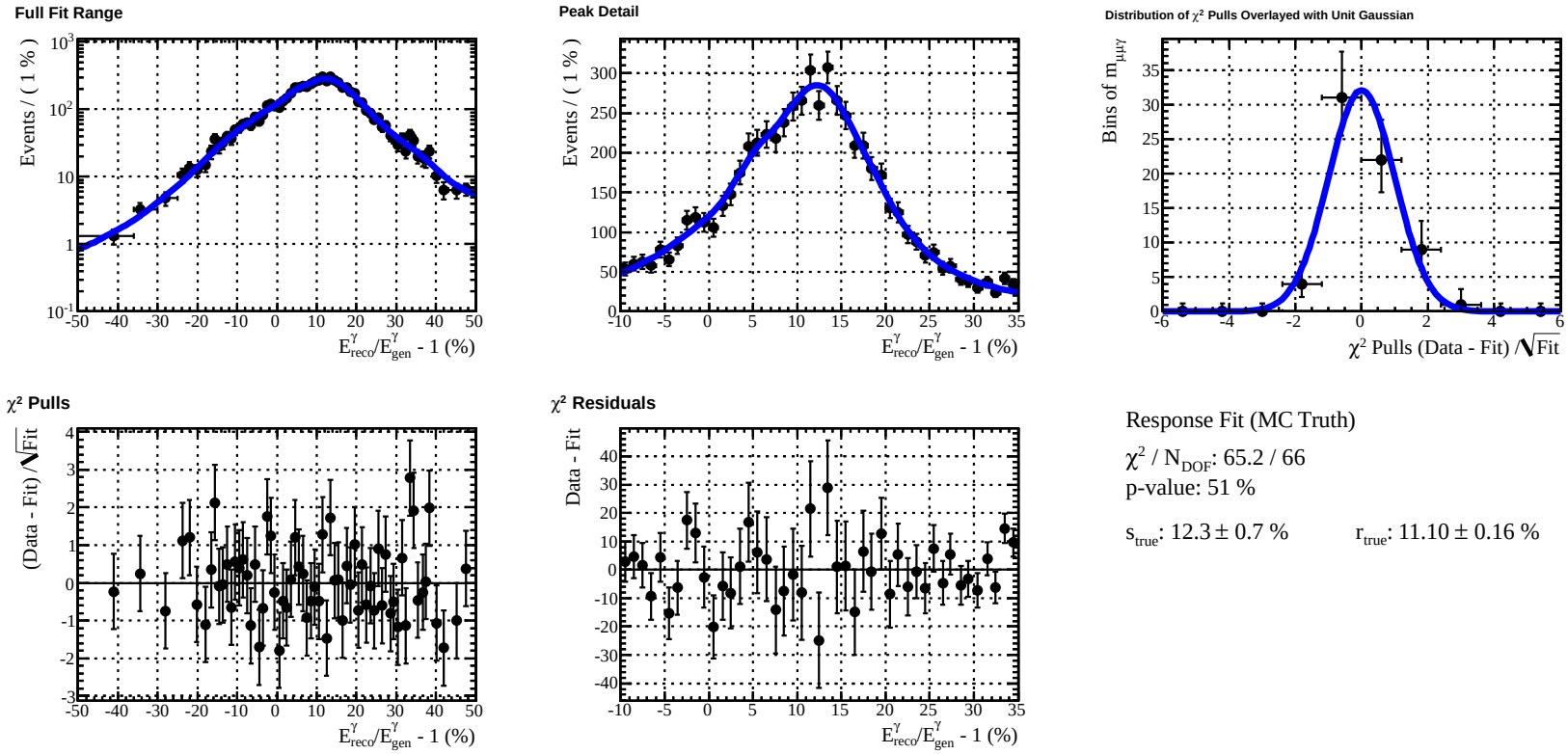

Figure A.11: Fit to photon energy response for photons in the endcaps, with $R_9 < 0.95$, and p_{T} of (10 to 12) GeV.

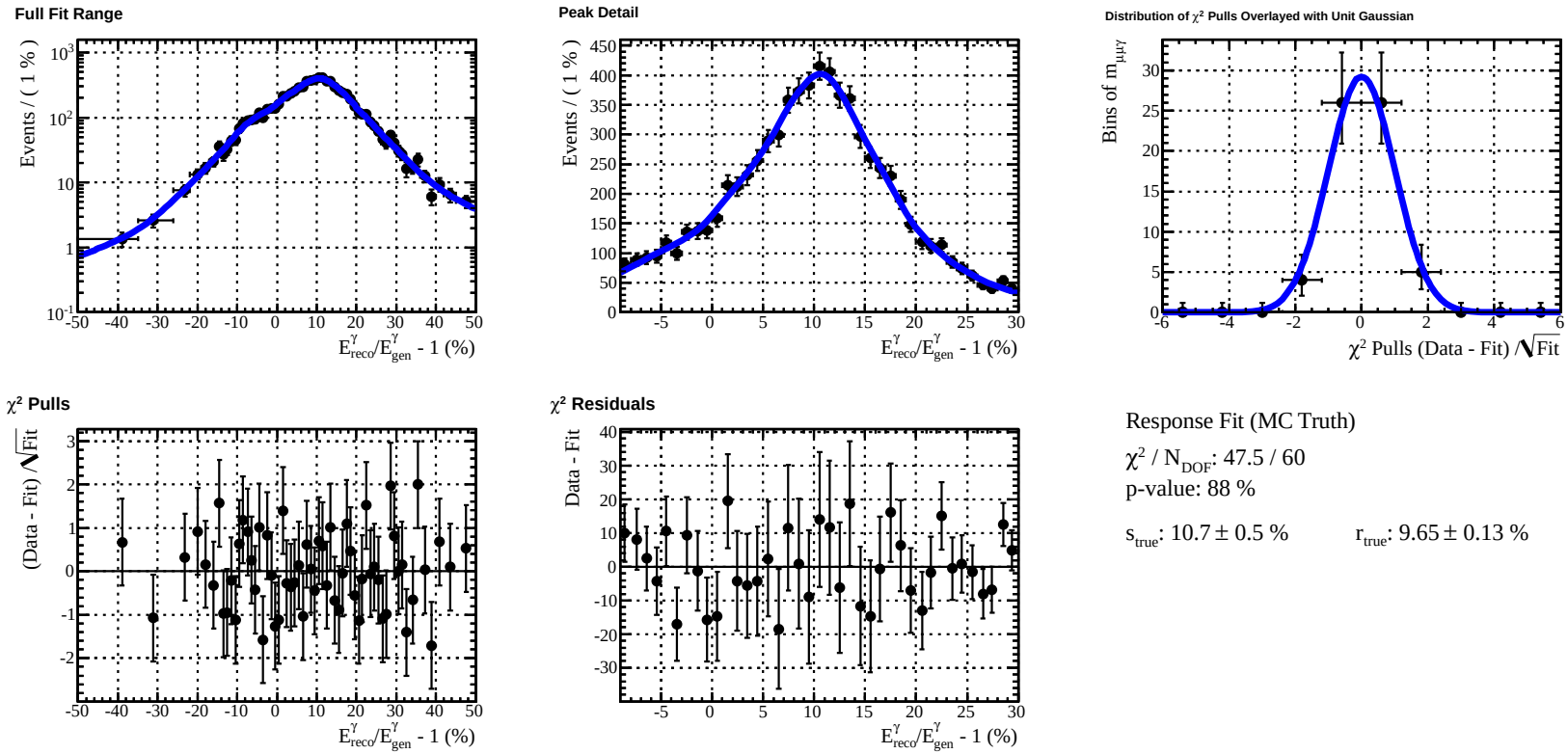

Figure A.12: Fit to photon energy response for photons in the endcaps, with $R_9 < 0.95$, and p_T of (12 to 15) GeV.

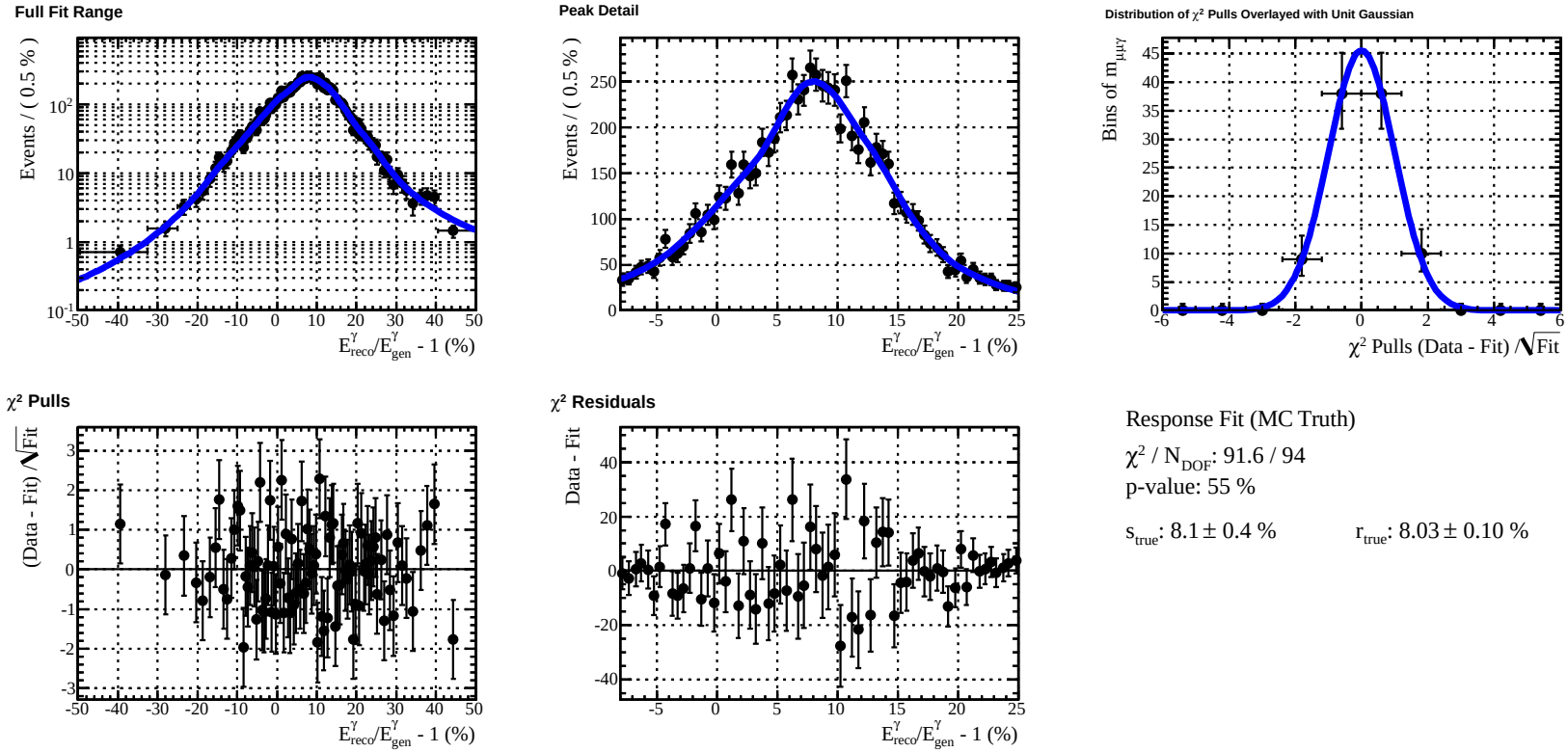

Figure A.13: Fit to photon energy response for photons in the endcaps, with $R_9 < 0.95$, and p_{T} of (15 to 20) GeV.

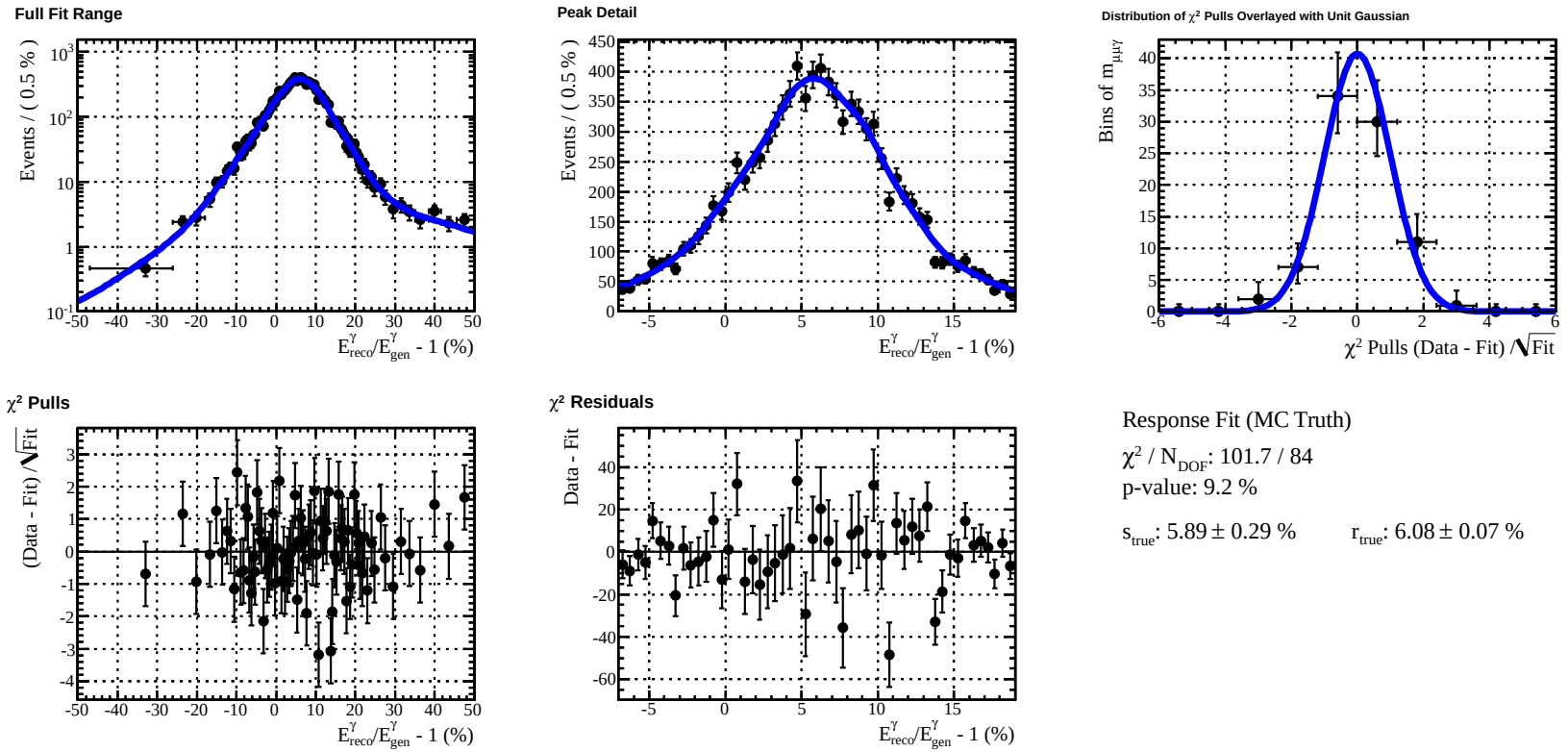

Figure A.14: Fit to photon energy response for photons in the endcaps, with $R_9 < 0.95$, and $p_T > 20\,\text{GeV}$.

A.2 Monte Carlo Fits

Figures A.15 to A.28 show fits to the $\mu\mu\gamma$ invariant mass in simulation for the 14 different photon categories as detailed in Table A.1. The occasional dashed blue line denotes the Z+jets background component (top left and top middle). The parameters shown in the bottom right of each fit are:

$s_{\mathbf{true}}$

The MC true photon energy scale from Section A.1. (Not a parameter of the model; shown only for comparison with s_{fit}.)

$r_{\mathbf{true}}$

The MC true photon energy resolution from Section A.1. (Not a parameter of the model; shown only for comparison with r_{fit}.)

$s_{\mathbf{fit}}$

The fitted photon energy scale.

$r_{\mathbf{fit}}$

The fitted photon energy resolution.

$N_{\mathbf{S}}$

The fitted number of signal events.

$N_{\mathbf{Z+jets}}$

The fitted number of Z + jets background events.

$N_{\mathbf{exp}}$

The number of other background events with an exponentially falling invariant mass spectrum.

$\lambda_{\mathbf{exp}}$

A parameter of the exponential density describing the other backgrounds.

We fix $N_{\mathrm{exp}} = 0$ and λ_{exp}, and float s_{fit}, r_{fit}, N_{S}, and $N_{\mathrm{Z+jets}}$ in all the fits.

A.2.1 Barrel, $R_9 > 0.94$

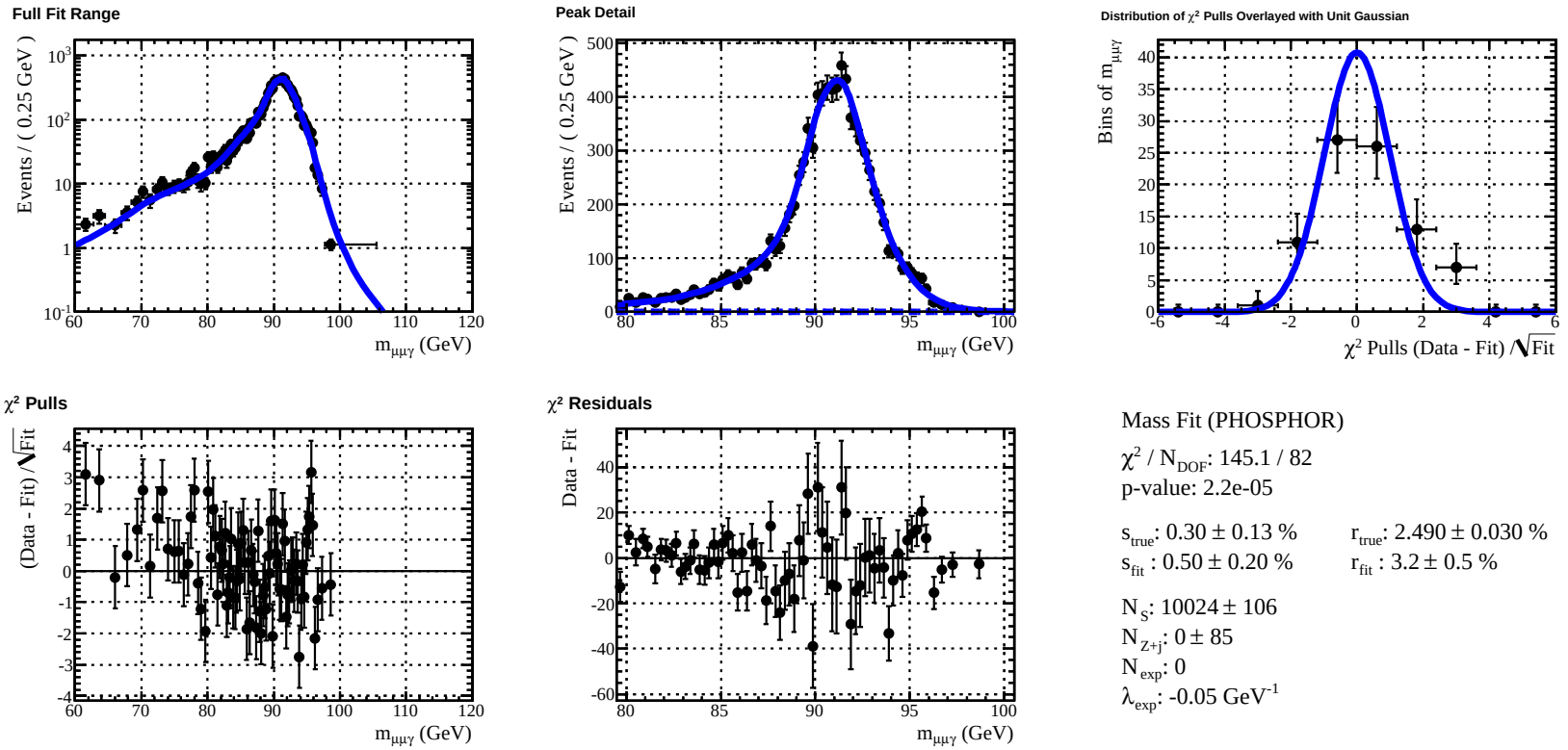

Figure A.15: Fit to $\mu\mu\gamma$ invariant mass in simulation for photons in the barrel, with $R_9 > 0.94$, and p_T of (10 to 12) GeV.

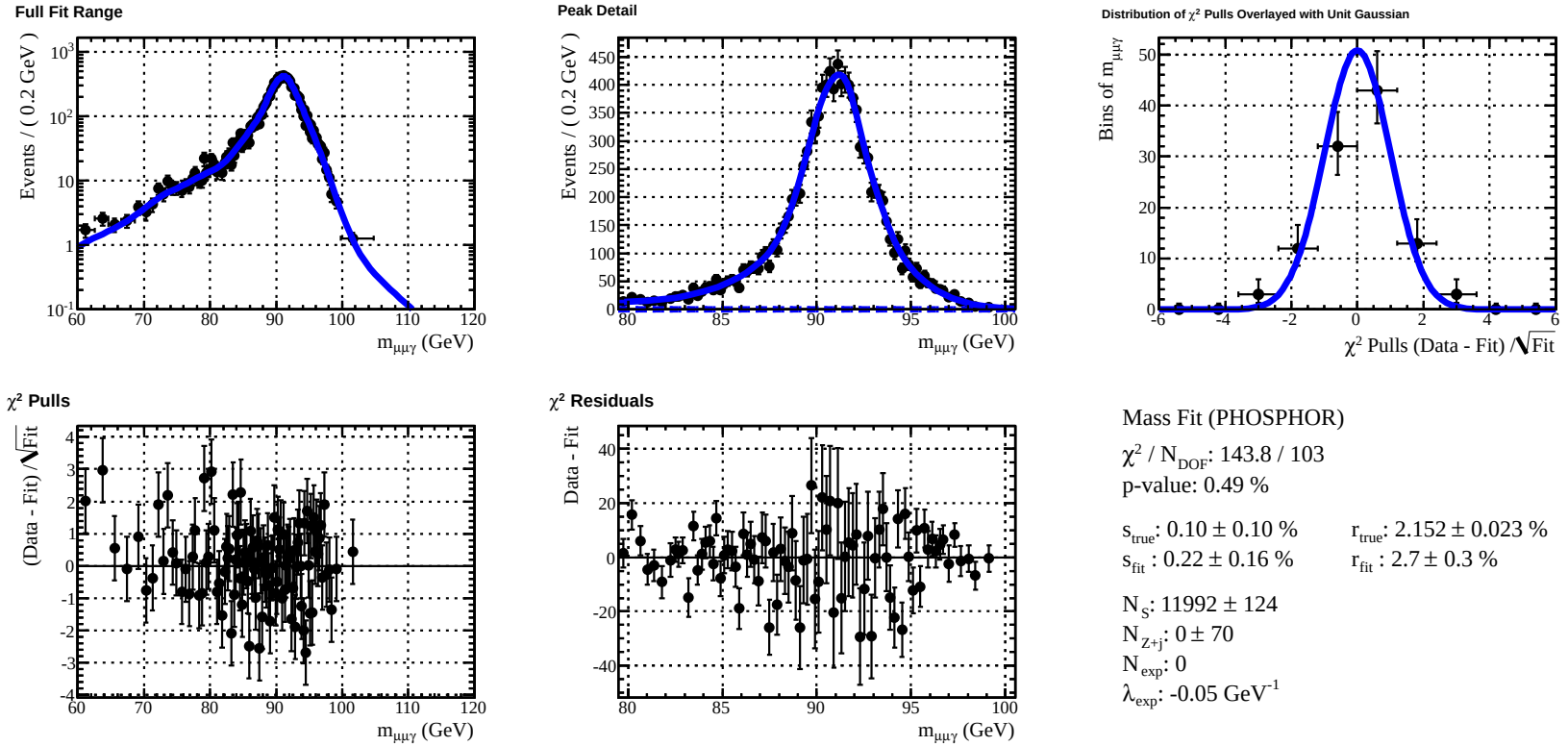

Figure A.16: Fit to $\mu\mu\gamma$ invariant mass in simulation for photons in the barrel, with $R_9 > 0.94$, and p_{T} of (12 to 15) GeV.

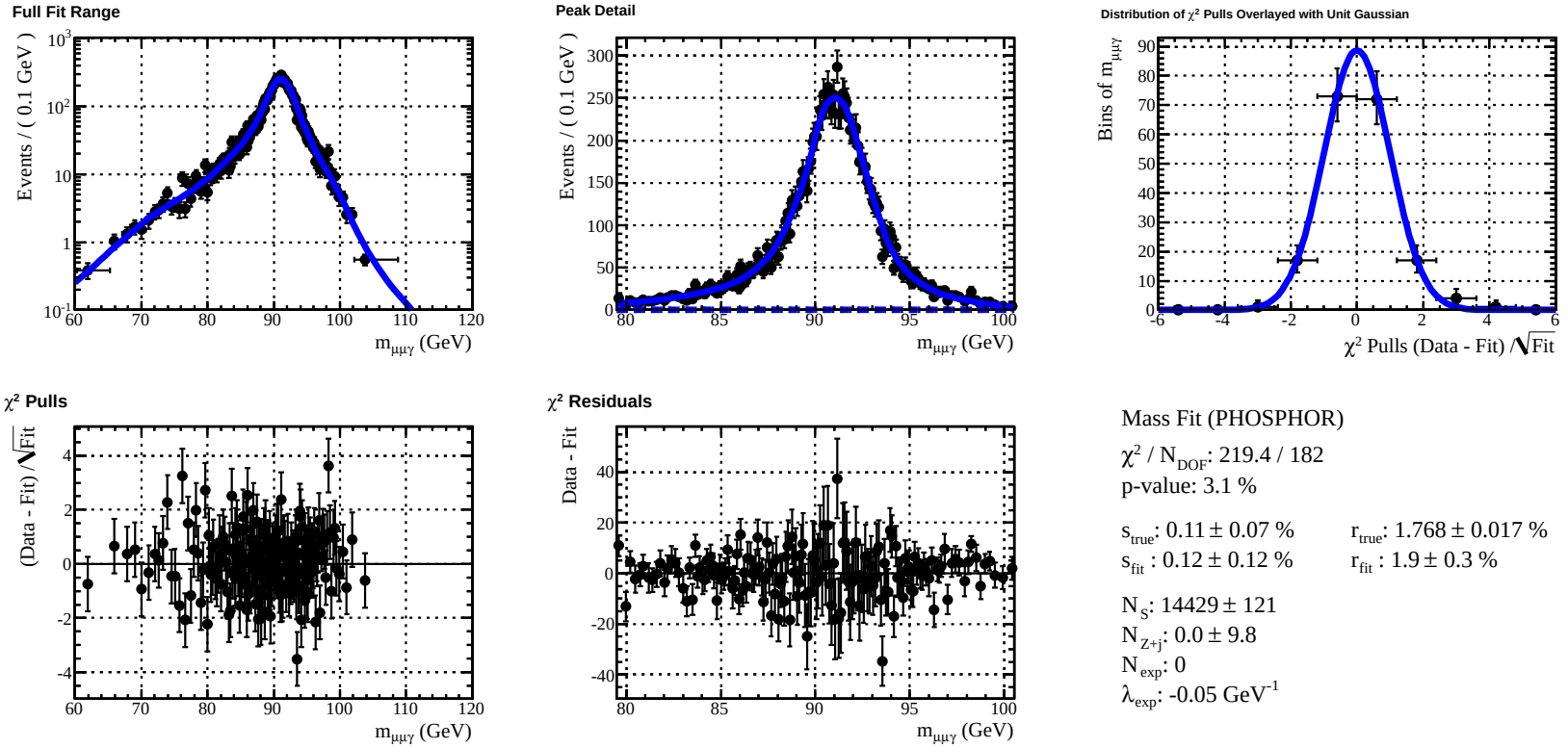

Figure A.17: Fit to $\mu\mu\gamma$ invariant mass in simulation for photons in the barrel, with $R_9 > 0.94$, and p_{T} of (15 to 20) GeV.

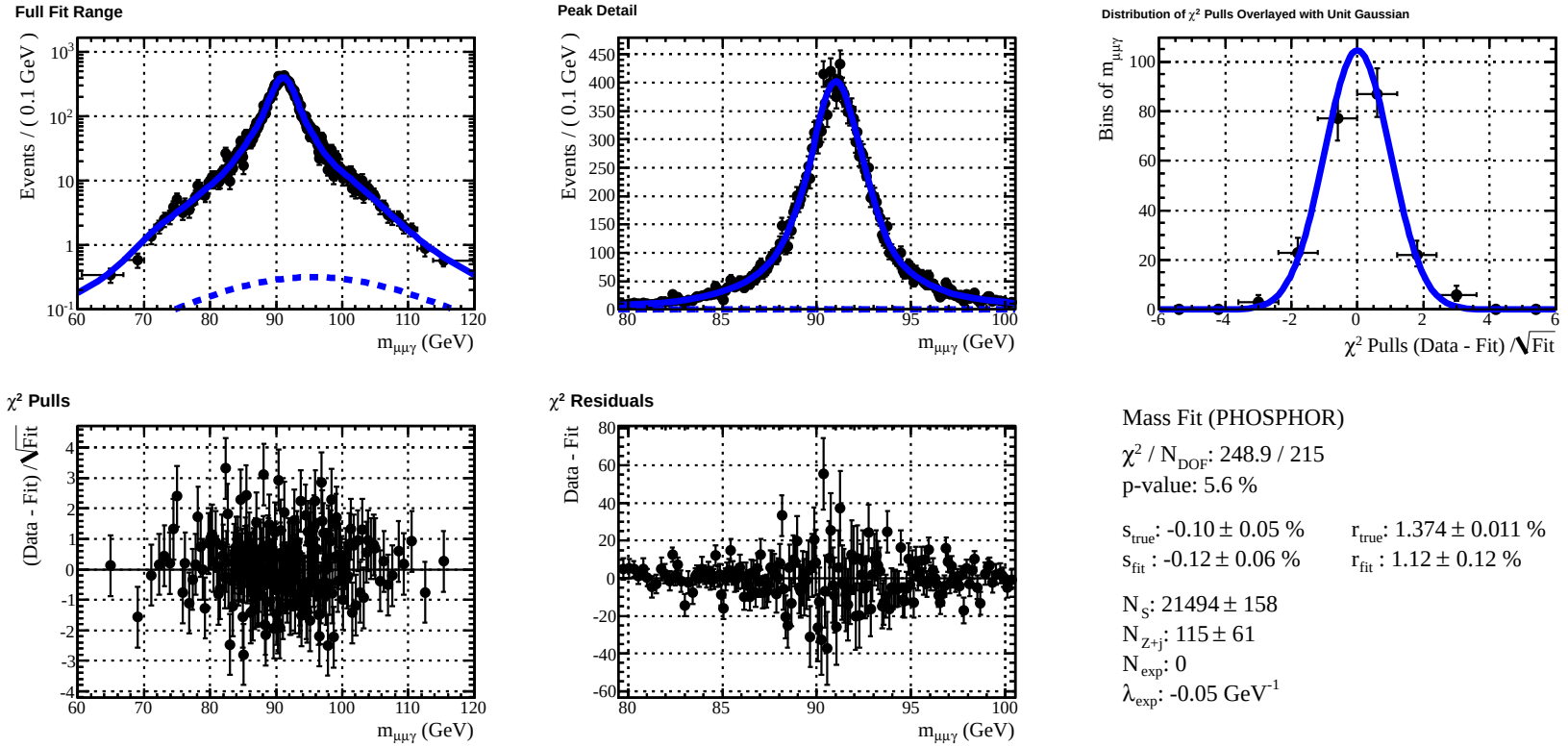

Figure A.18: Fit to $\mu\mu\gamma$ invariant mass in simulation for photons in the barrel, with $R_9 > 0.94$, and $p_T > 20\,\text{GeV}$.

A.2.2 Barrel, $R_9 < 0.94$

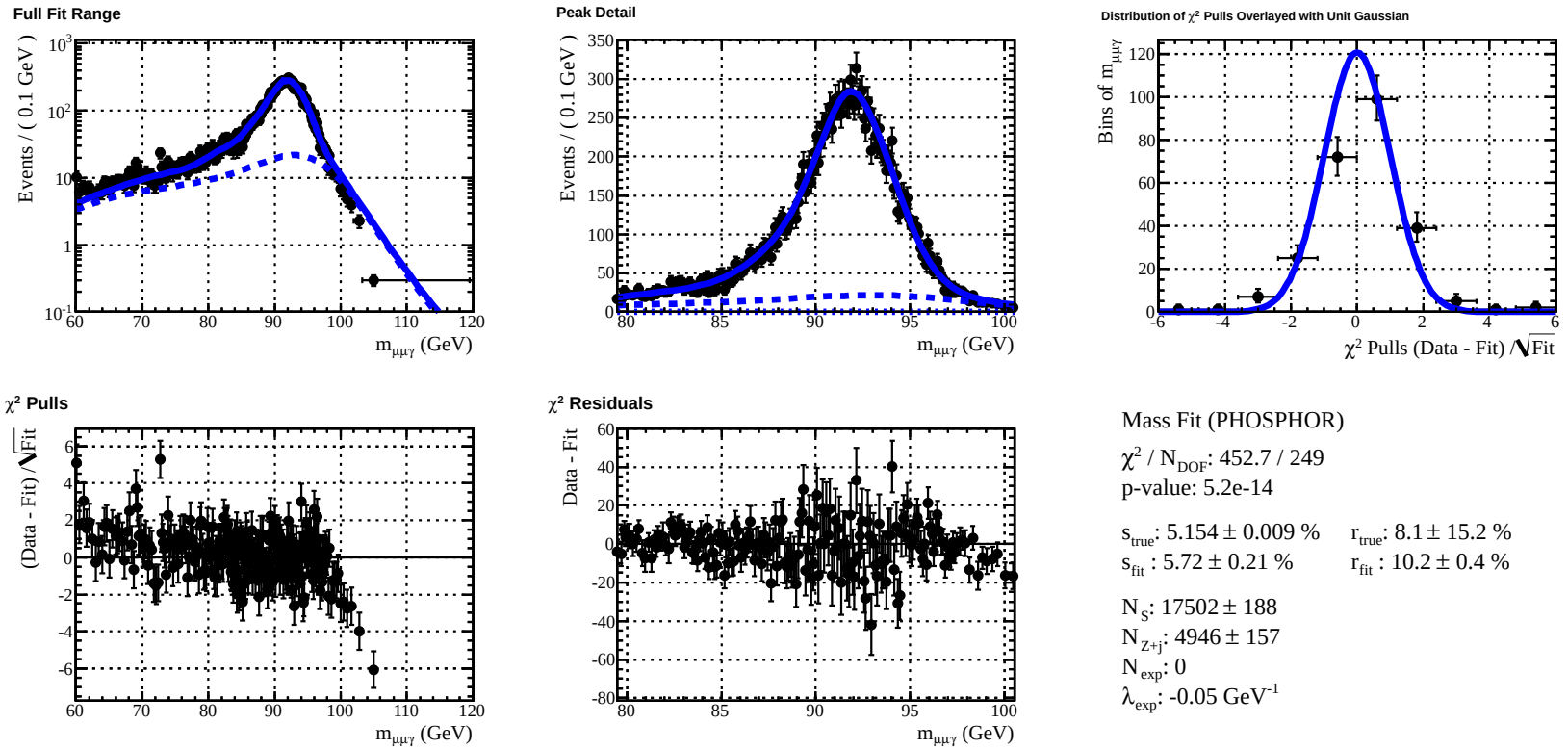

Figure A.19: Fit to $\mu\mu\gamma$ invariant mass in simulation for photons in the barrel, with $R_9 < 0.94$, and p_T of (10 to 12) GeV.

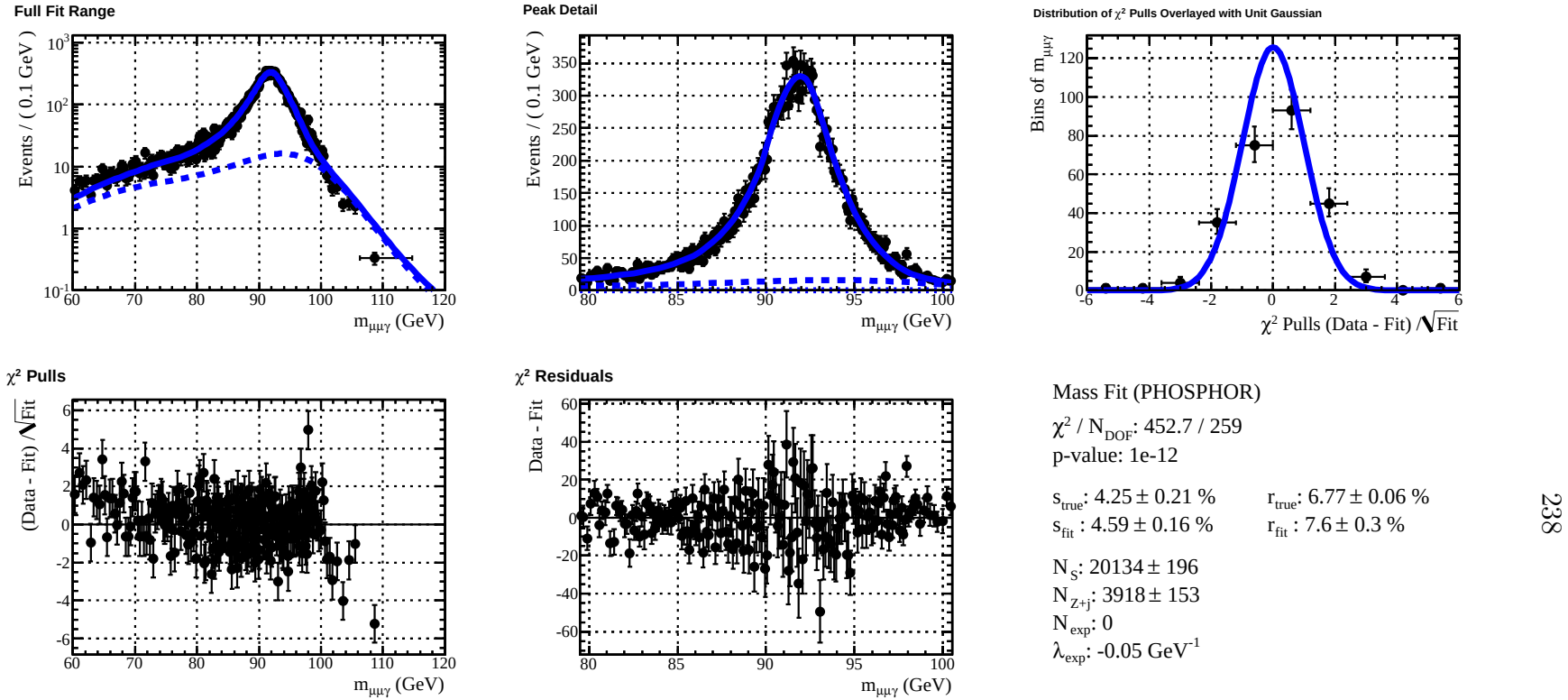

Figure A.20: Fit to $\mu\mu\gamma$ invariant mass in simulation for photons in the barrel, with $R_9 < 0.94$, and p_{T} of (12 to 15) GeV.

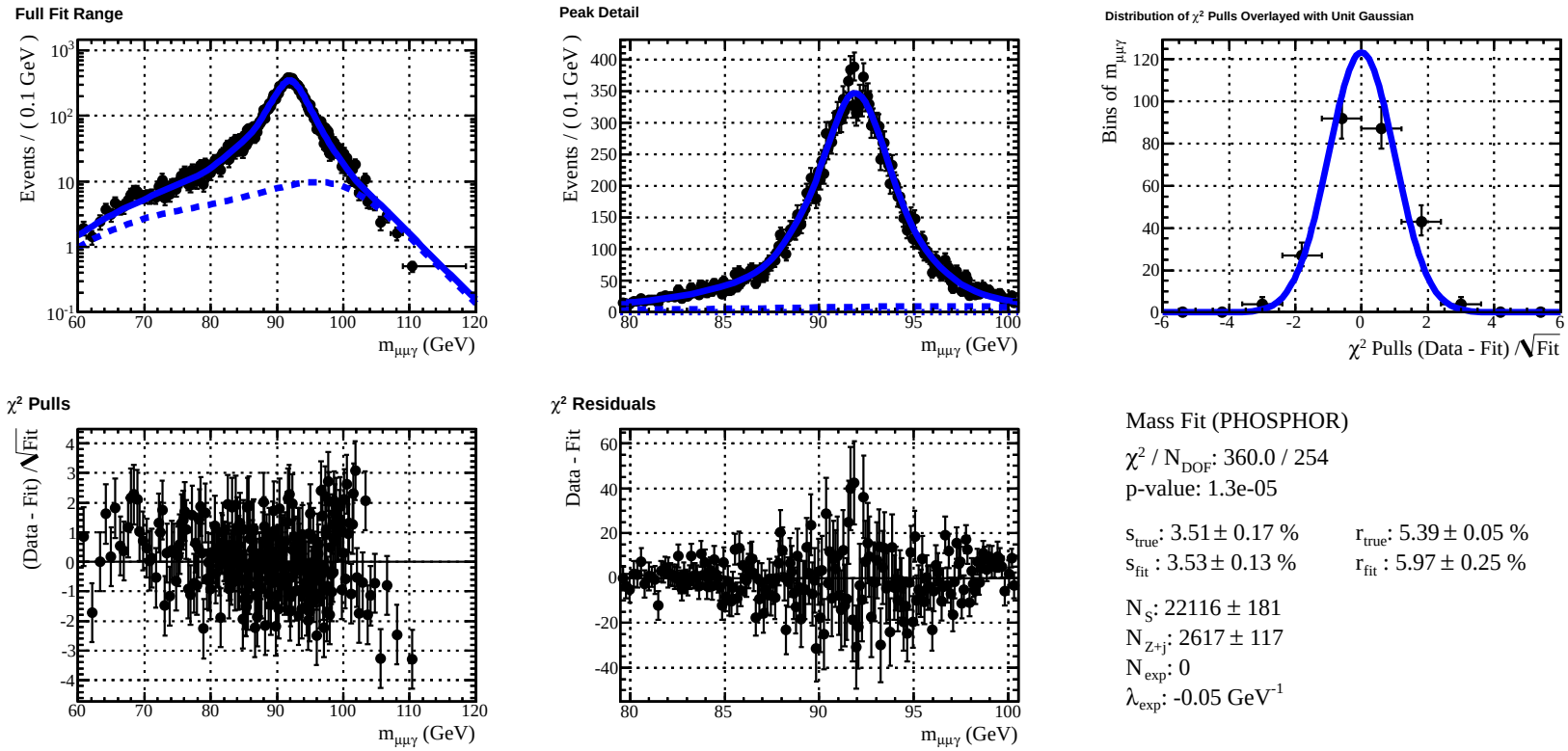

Figure A.21: Fit to $\mu\mu\gamma$ invariant mass in simulation for photons in the barrel, with $R_9 < 0.94$, and p_{T} of (15 to 20) GeV.

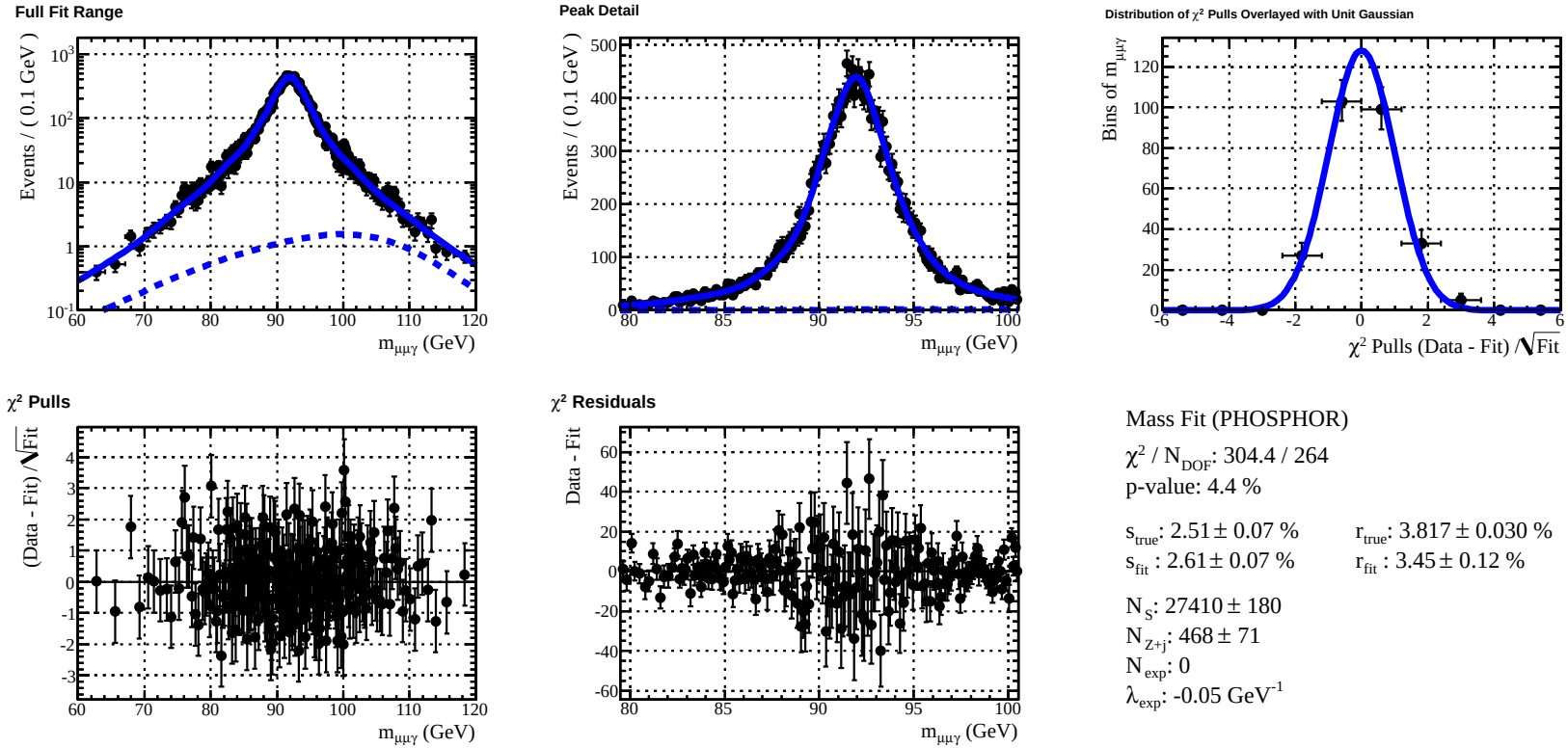

Figure A.22: Fit to $\mu\mu\gamma$ invariant mass in simulation for photons in the barrel, with $R_9 < 0.94$, and $p_T > 20\,\text{GeV}$.

A.2.3 Endcaps, $R_9 > 0.94$

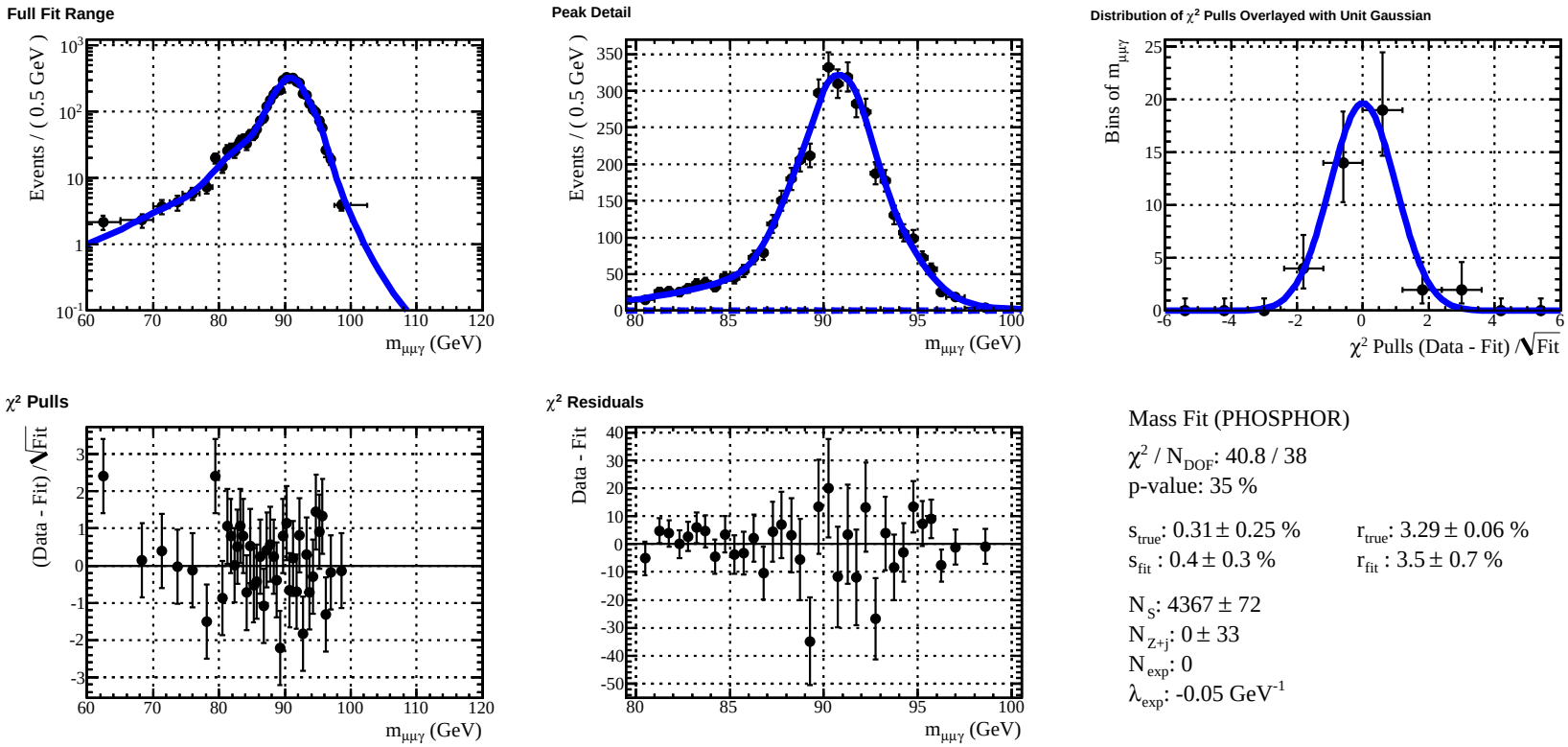

Figure A.23: Fit to $\mu\mu\gamma$ invariant mass in simulation for photons in the endcaps, with $R_9 > 0.94$, and p_T of (10 to 15) GeV.

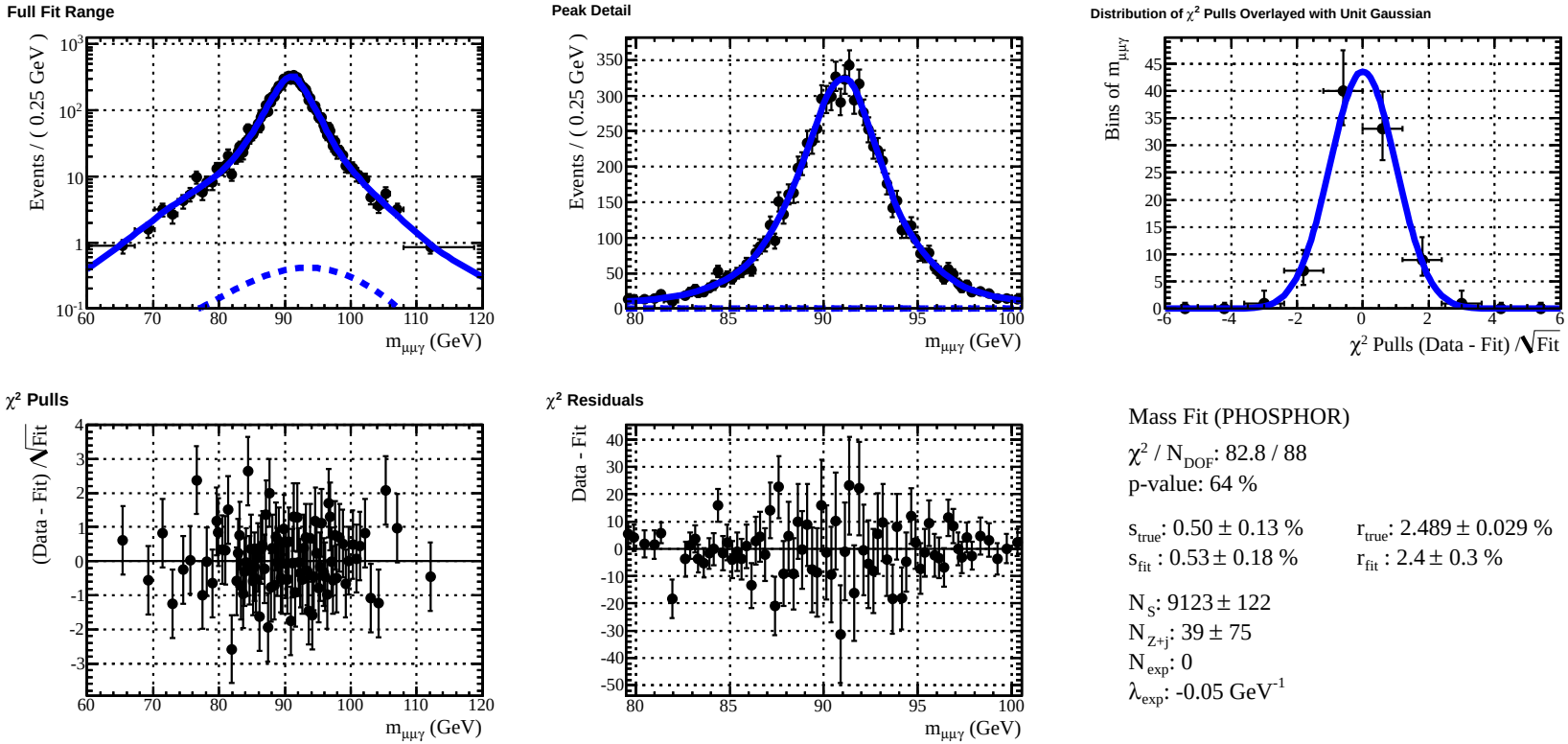

Figure A.24: Fit to $\mu\mu\gamma$ invariant mass in simulation for photons in the endcaps, with $R_9 > 0.94$, and $p_T > 15\,\text{GeV}$.

A.2.4 Endcaps, $R_9 < 0.94$

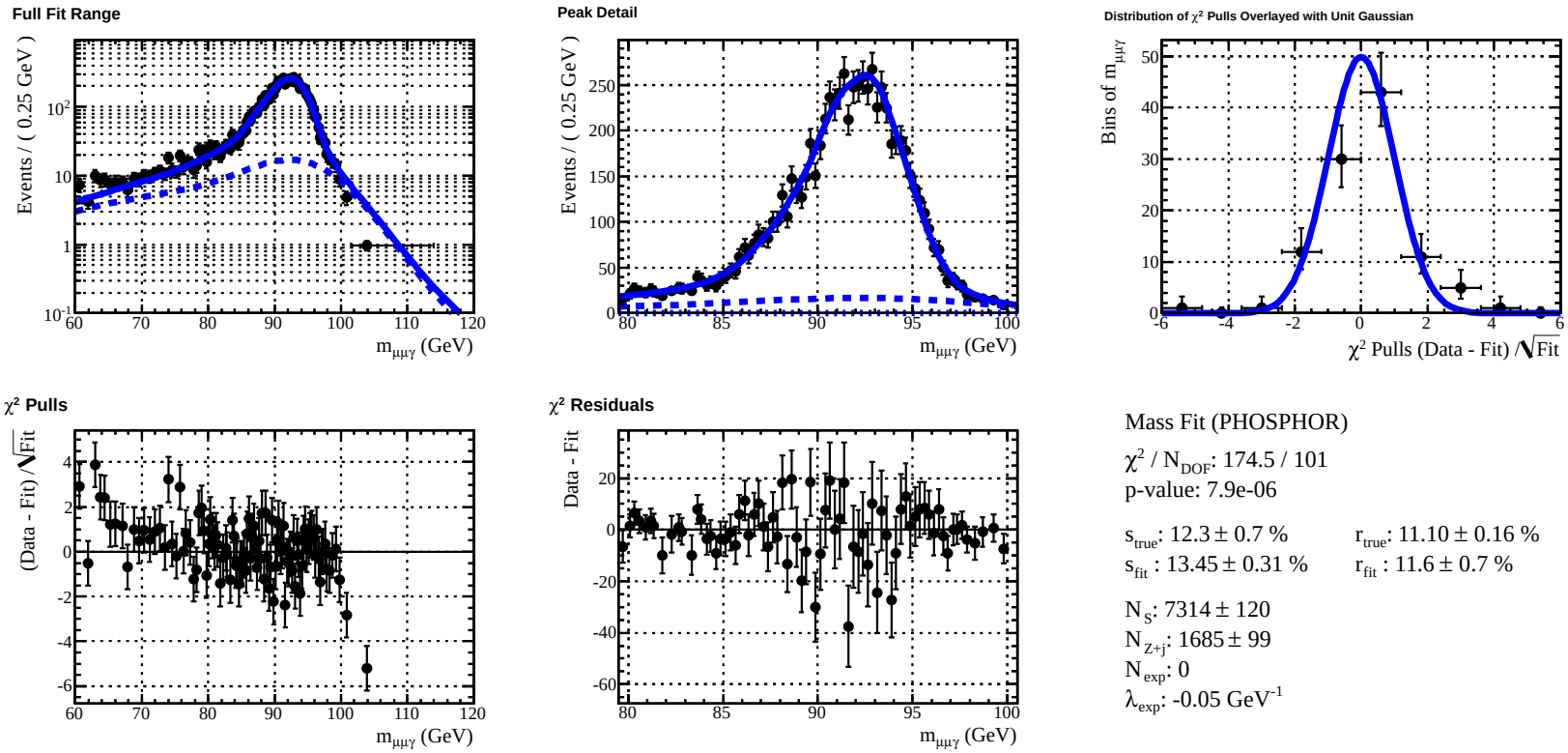

Figure A.25: Fit to $\mu\mu\gamma$ invariant mass in simulation for photons in the endcaps, with $R_9 < 0.94$, and p_T of (10 to 12) GeV.

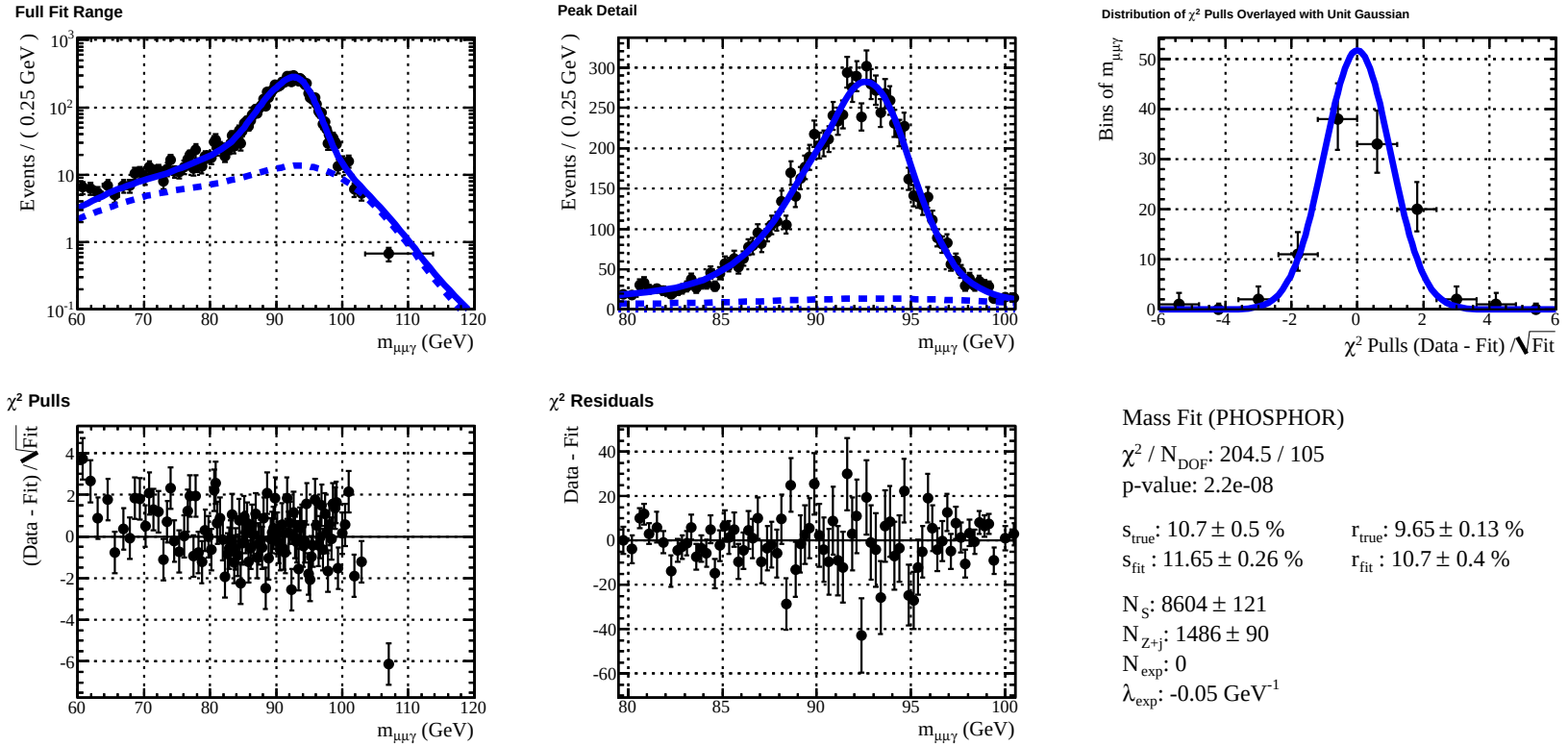

Figure A.26: Fit to $\mu\mu\gamma$ invariant mass in simulation for photons in the endcaps, with $R_9 < 0.94$, and p_T of (12 to 15) GeV.

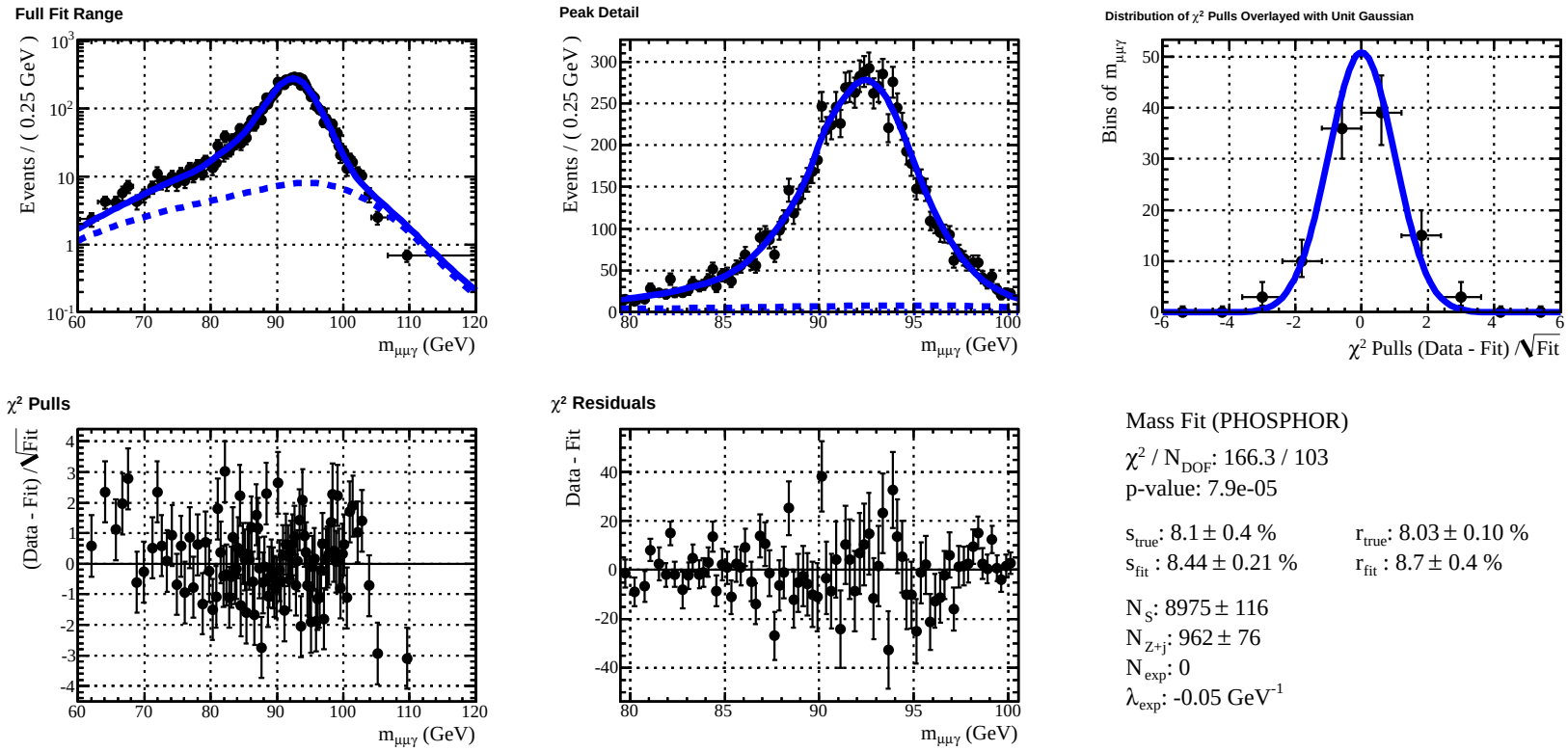

Figure A.27: Fit to $\mu\mu\gamma$ invariant mass in simulation for photons in the endcaps, with $R_9 < 0.94$, and p_T of (15 to 20) GeV.

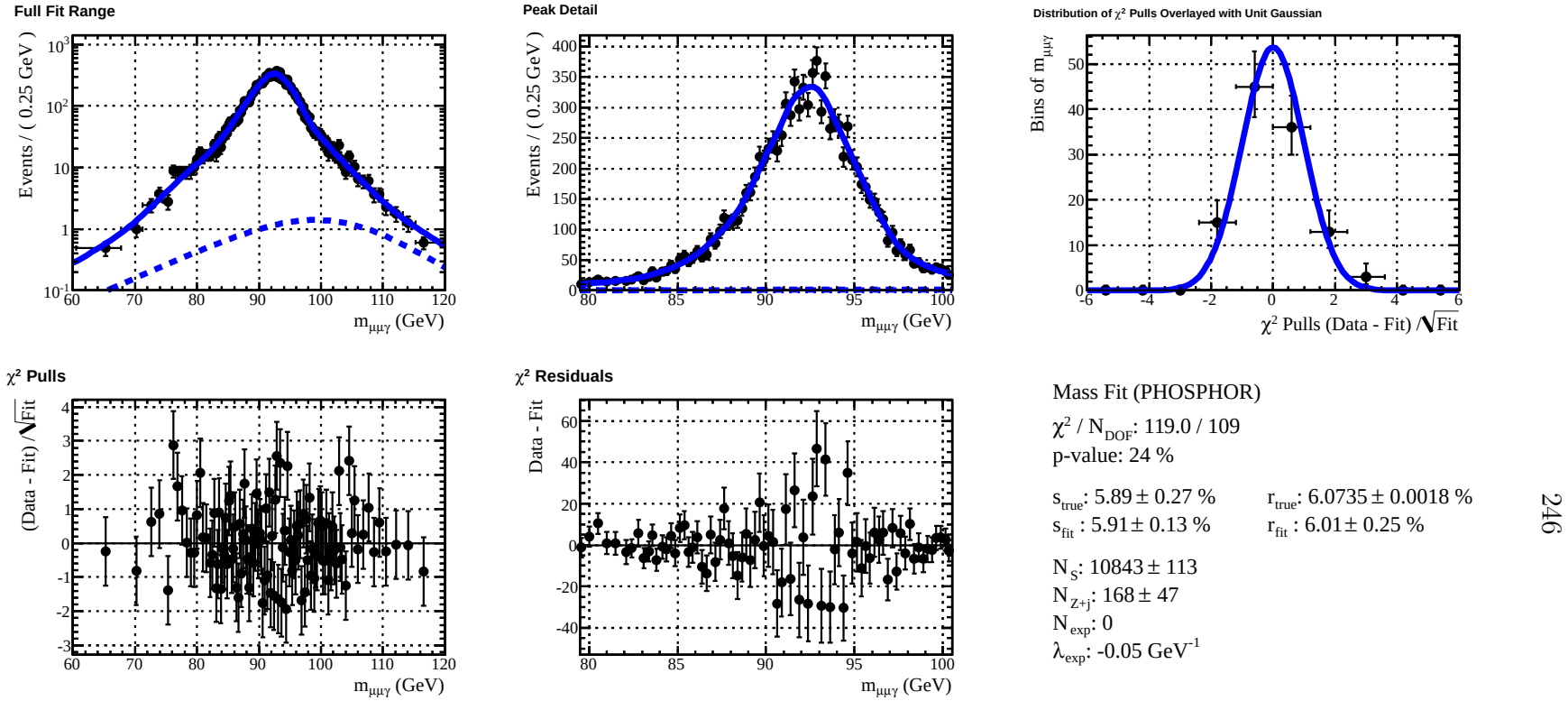

Figure A.28: Fit to $\mu\mu\gamma$ invariant mass in simulation for photons in the endcaps, with $R_9 < 0.94$, and $p_T > 20\,\text{GeV}$.

A.3 Data Fits

Figures A.29 to A.42 show fits to the $\mu\mu\gamma$ invariant mass in data for the 14 different photon categories as detailed in Table A.1. The occasional dashed blue line denotes the sum of the background components (top left and top middle). The occasional dotted blue line denotes the exponential background component (also top left and top middle). The model parameters shown in the bottom right of each fit are the same as for the MC fits. We float $s_{\rm fit}$, $r_{\rm fit}$, $N_{\rm S}$, and $N_{\rm Z+jets}$ in all the fits. We fix $N_{\rm exp} = 0$, and $\lambda_{\rm exp}$ for the (barrel, $R_9 > 0.94$) categories since the exponential backgrounds do not contribute here. We float $N_{\rm exp}$ and $\lambda_{\rm exp}$ in all the other categories.

A.3.1 Barrel, $R_9 > 0.94$

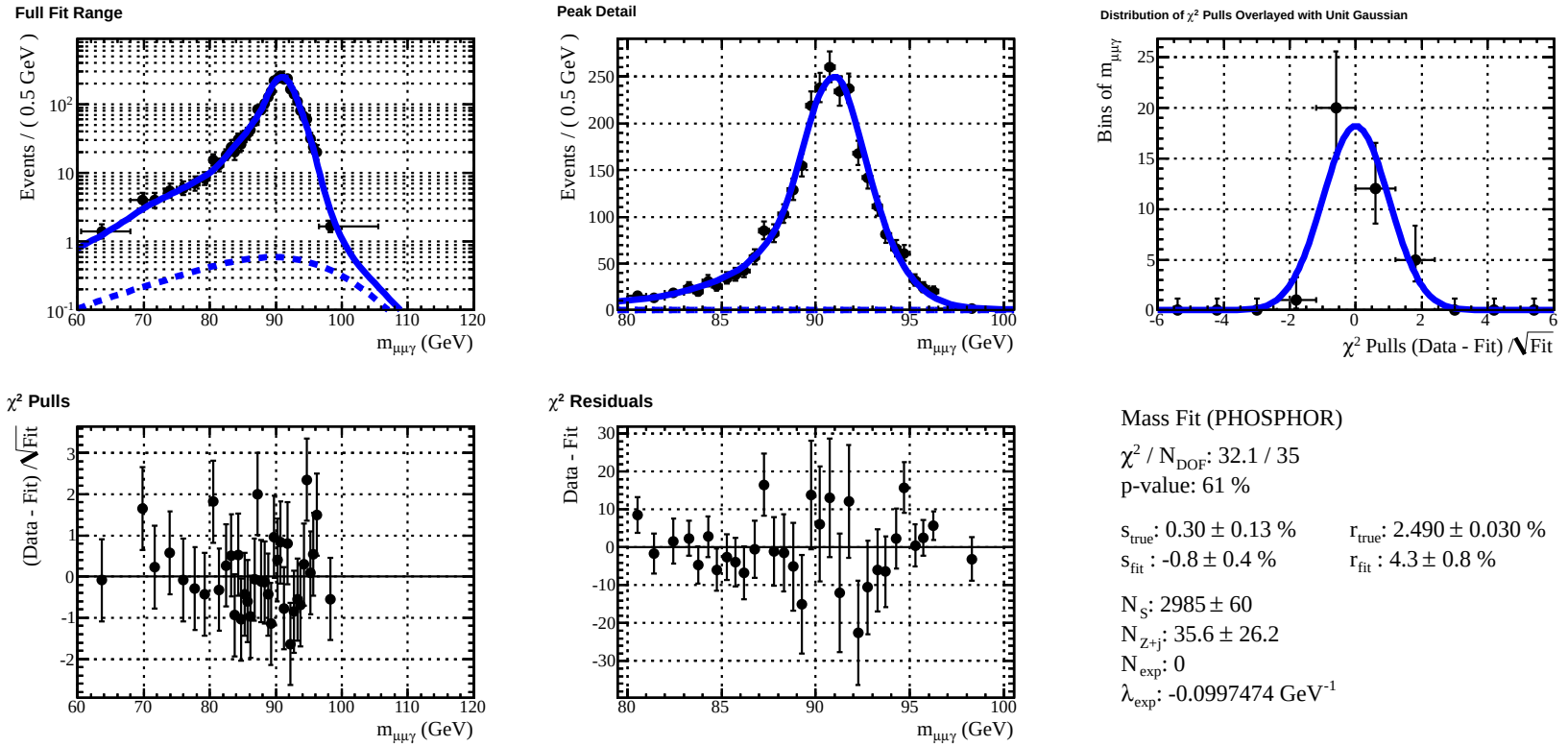

Figure A.29: Fit to $\mu\mu\gamma$ invariant mass in data for photons in the barrel, with $R_9 > 0.94$, and p_{T} of (10 to 12) GeV.

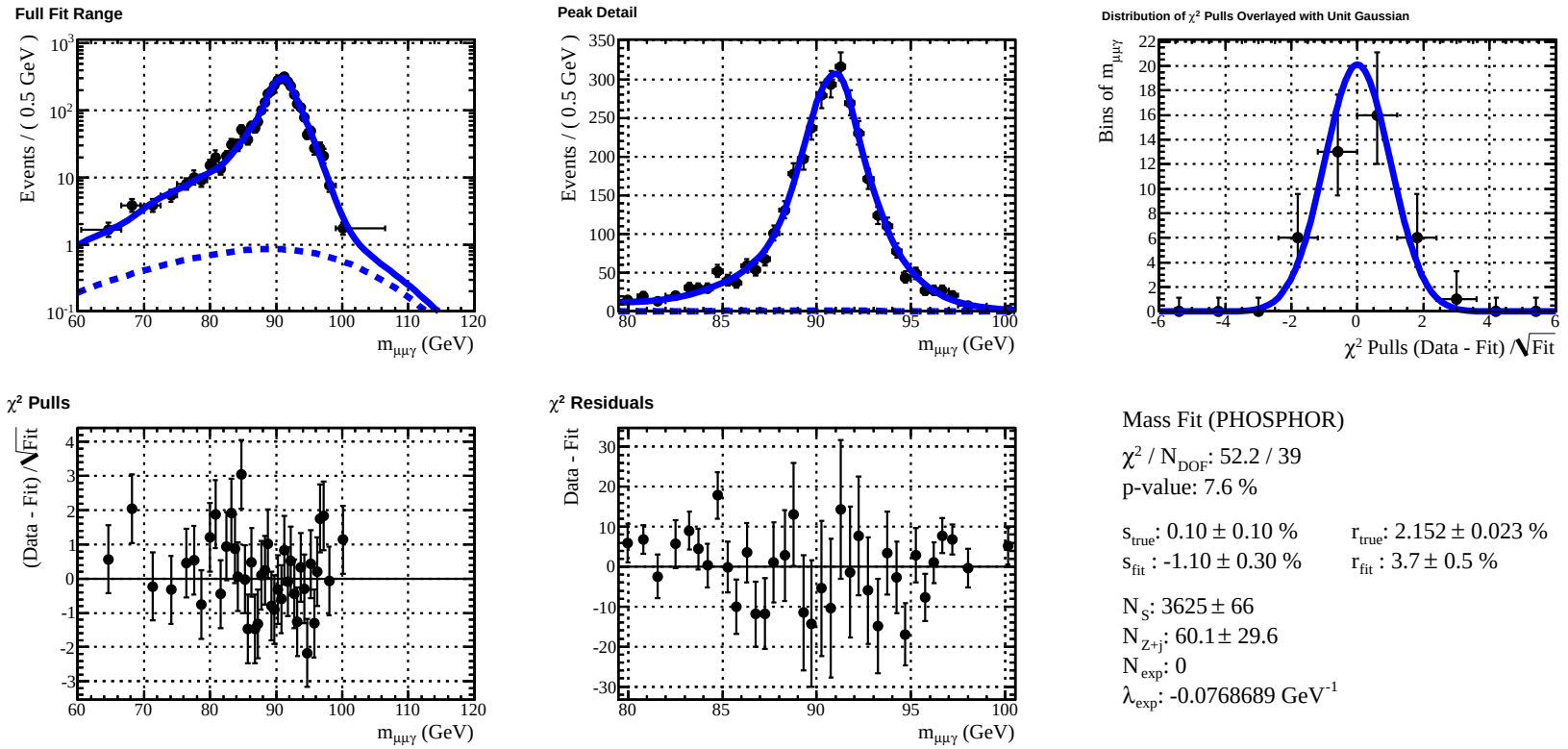

Figure A.30: Fit to $\mu\mu\gamma$ invariant mass in data for photons in the barrel, with $R_9 > 0.94$, and p_{T} of (12 to 15) GeV.

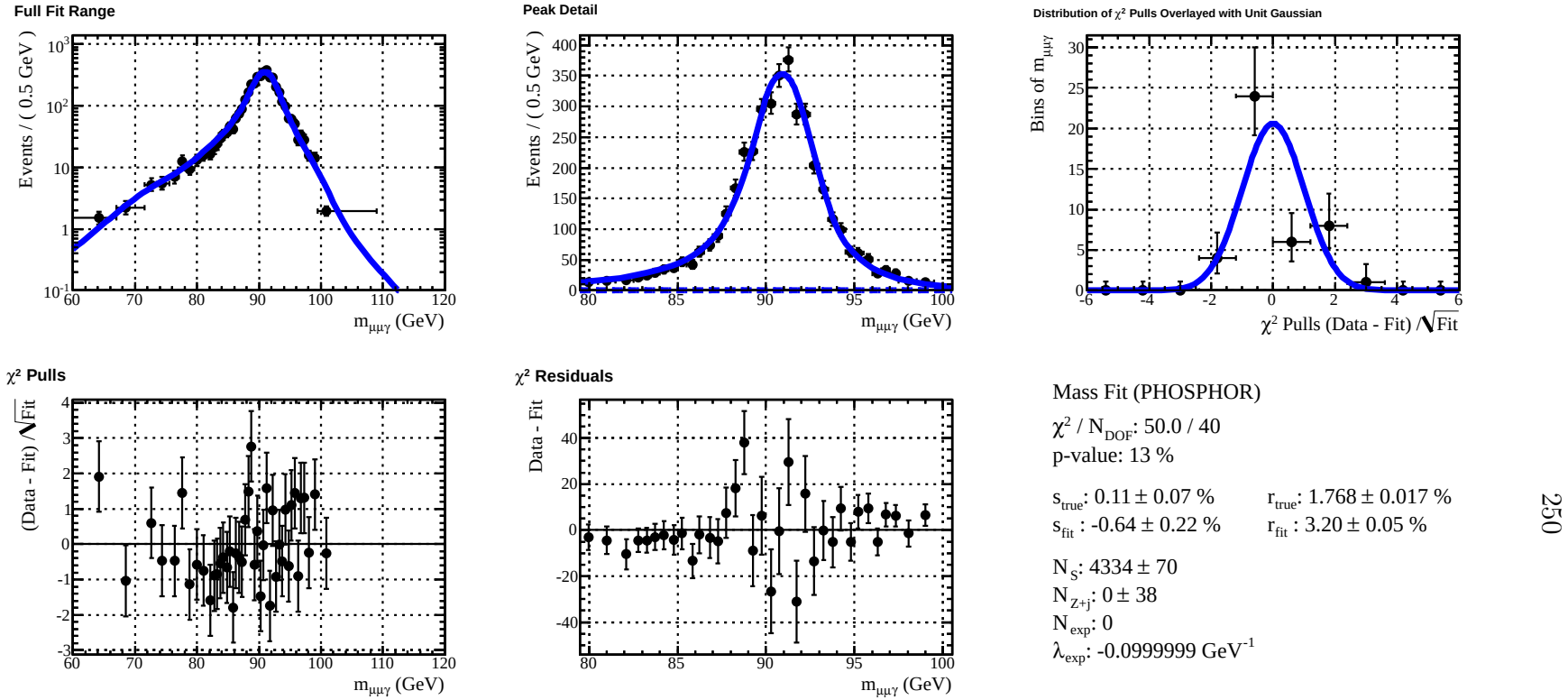

Figure A.31: Fit to $\mu\mu\gamma$ invariant mass in data for photons in the barrel, with $R_9 > 0.94$, and p_{T} of (15 to 20) GeV.

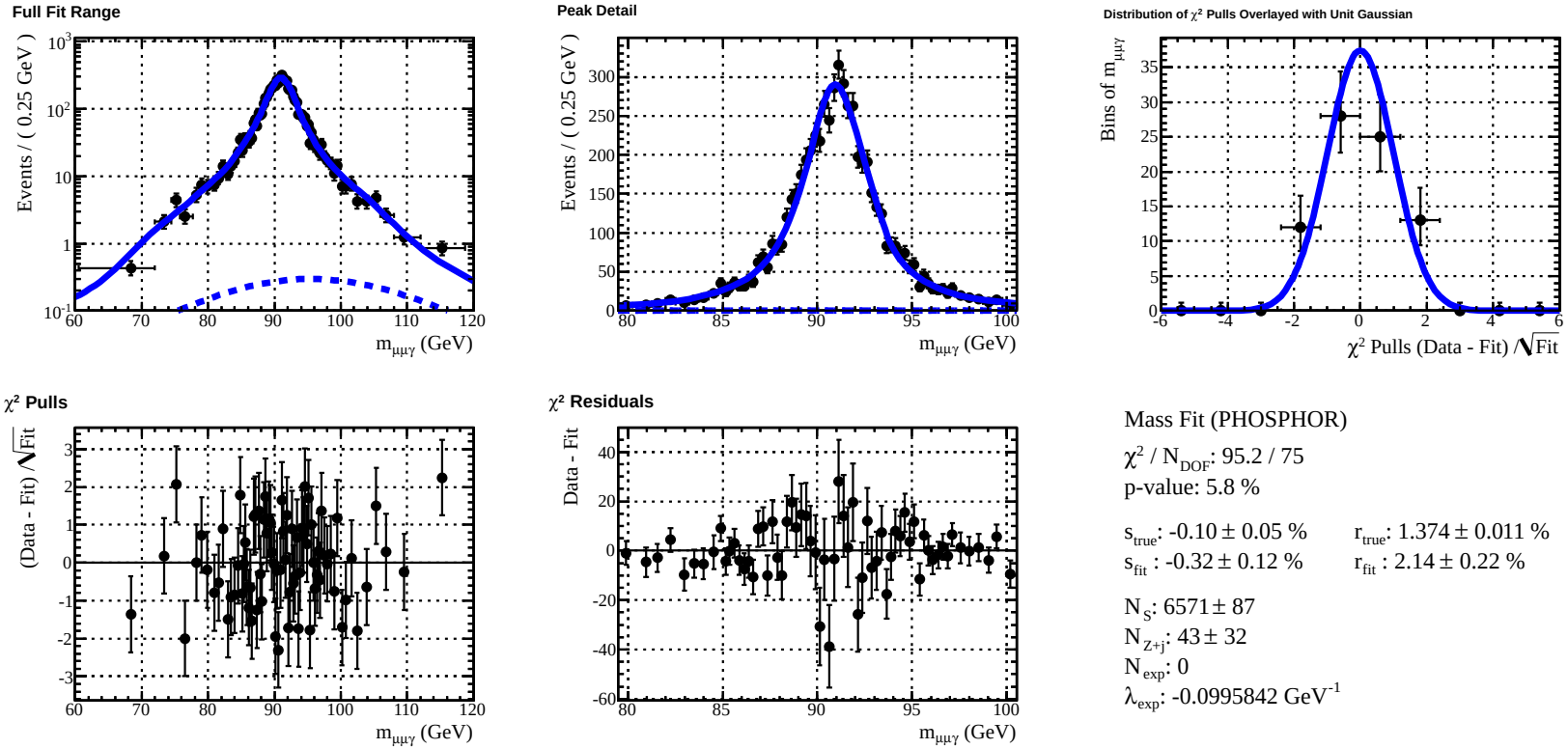

Figure A.32: Fit to $\mu\mu\gamma$ invariant mass in data for photons in the barrel, with $R_9 > 0.94$, and $p_T > 20\,\text{GeV}$.

A.3.2 Barrel, $R_9 < 0.94$

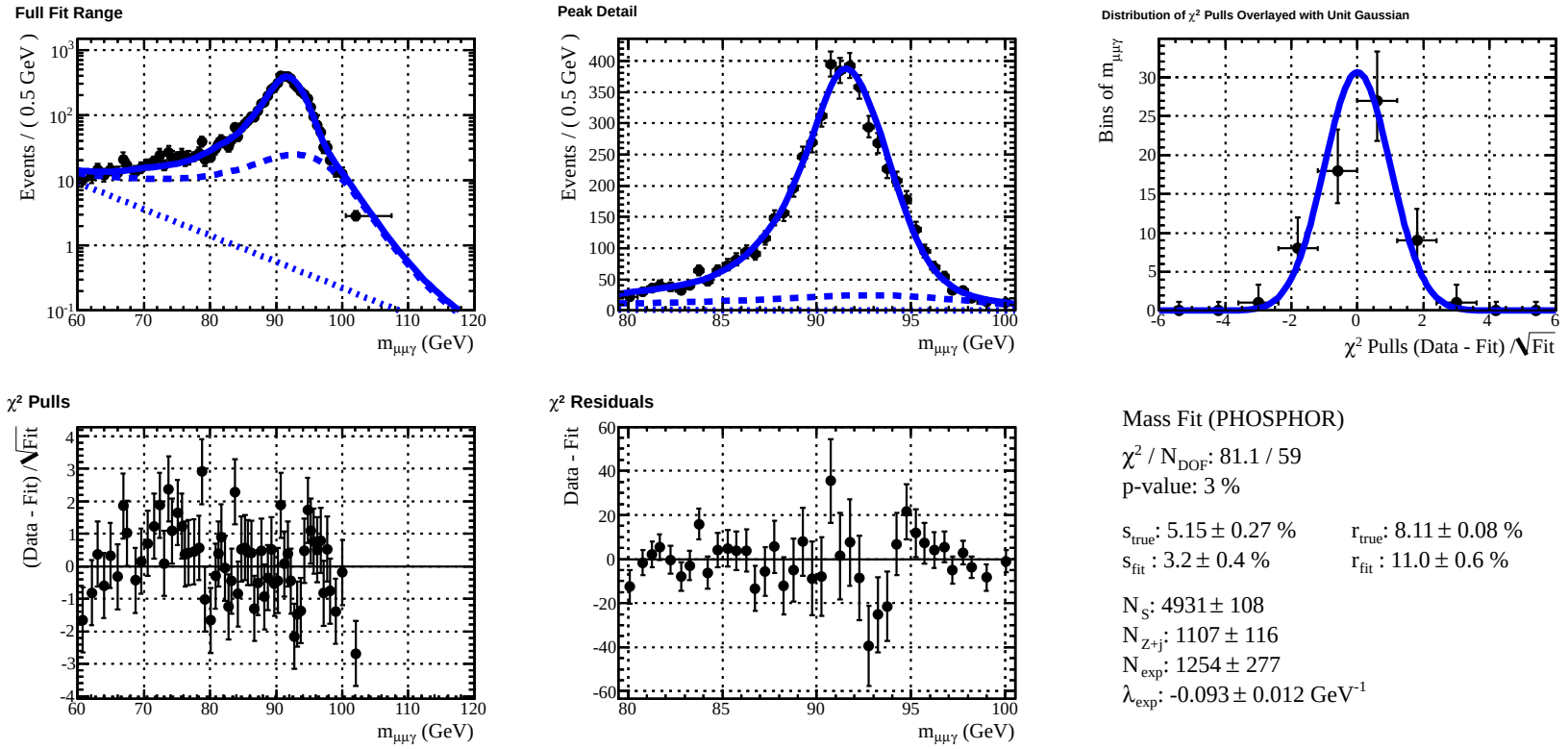

Figure A.33: Fit to $\mu\mu\gamma$ invariant mass in data for photons in the barrel, with $R_9 < 0.94$, and p_T of (10 to 12) GeV.

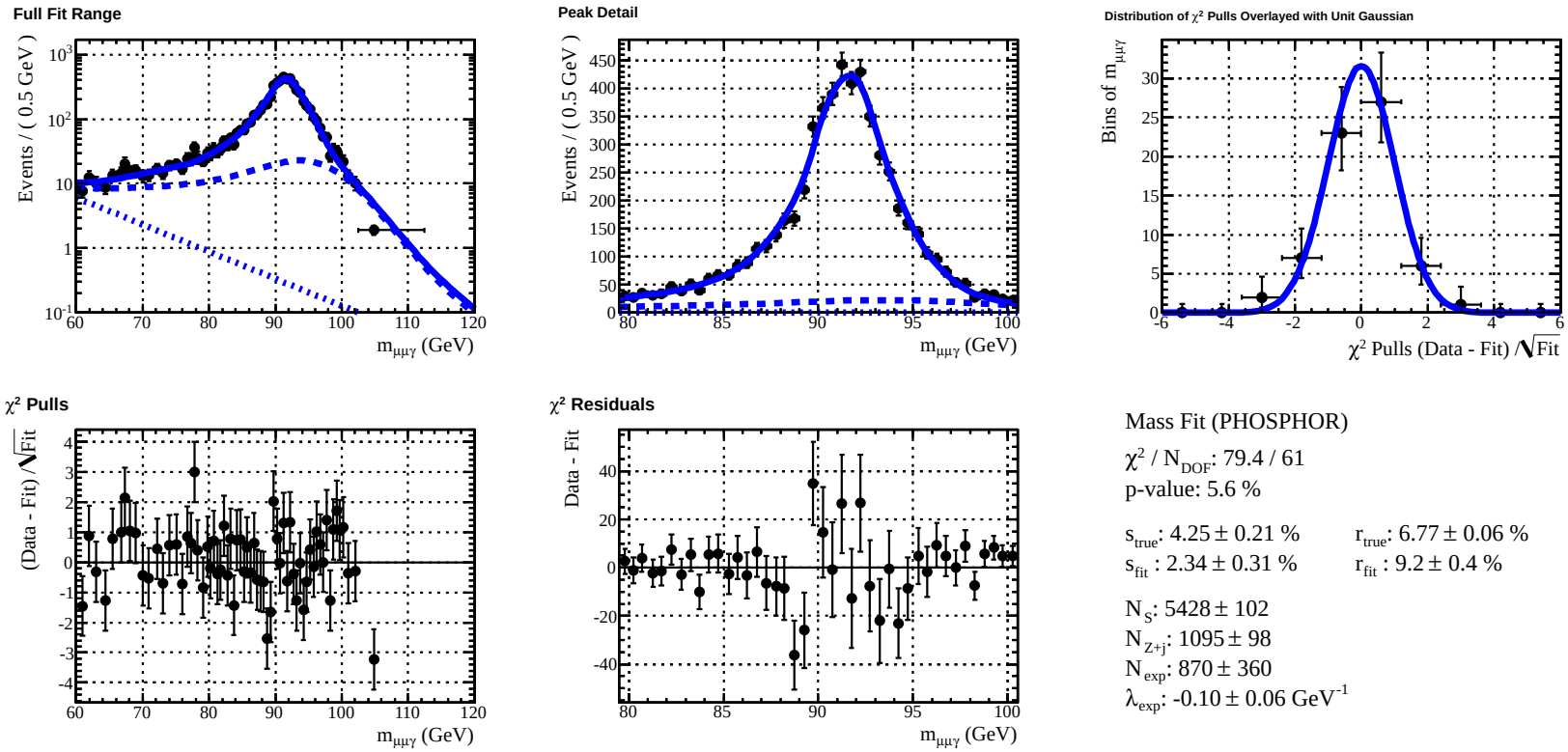

Figure A.34: Fit to $\mu\mu\gamma$ invariant mass in data for photons in the barrel, with $R_9 < 0.94$, and p_{T} of (12 to 15) GeV.

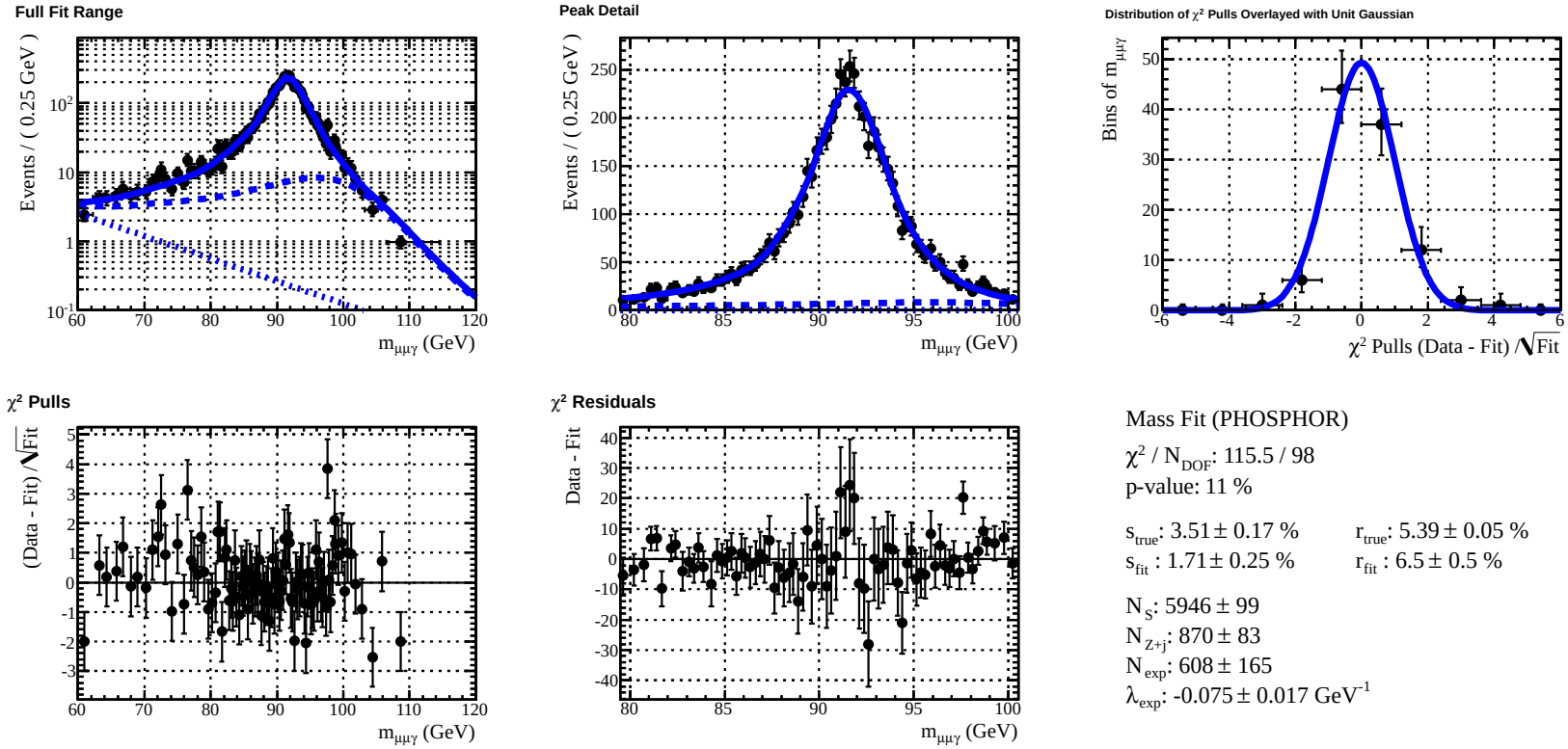

Figure A.35: Fit to $\mu\mu\gamma$ invariant mass in data for photons in the barrel, with $R_9 < 0.94$, and p_T of (15 to 20) GeV.

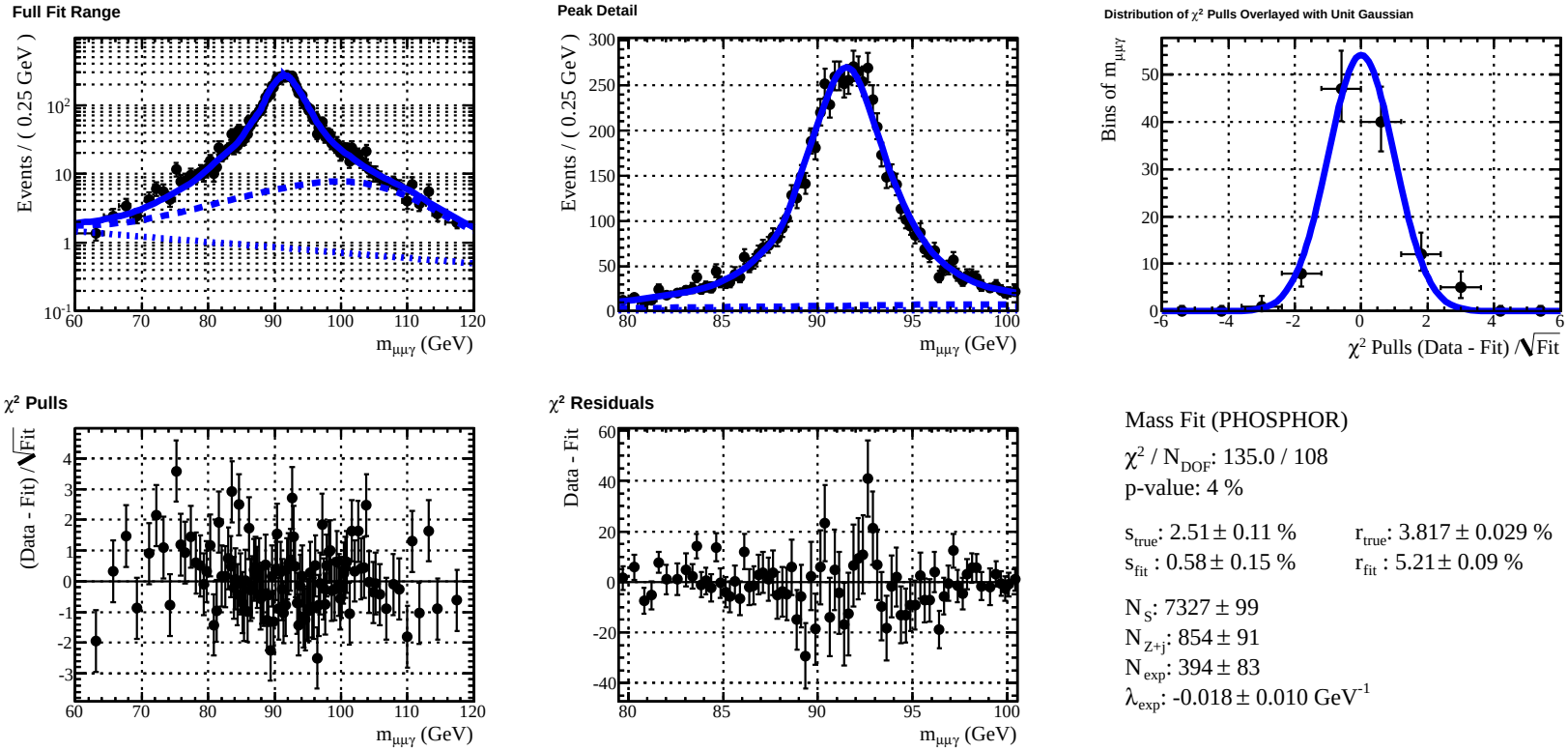

Figure A.36: Fit to $\mu\mu\gamma$ invariant mass in data for photons in the barrel, with $R_9 < 0.94$, and $p_T > 20\,\text{GeV}$.

A.3.3 Endcaps, $R_9 > 0.94$

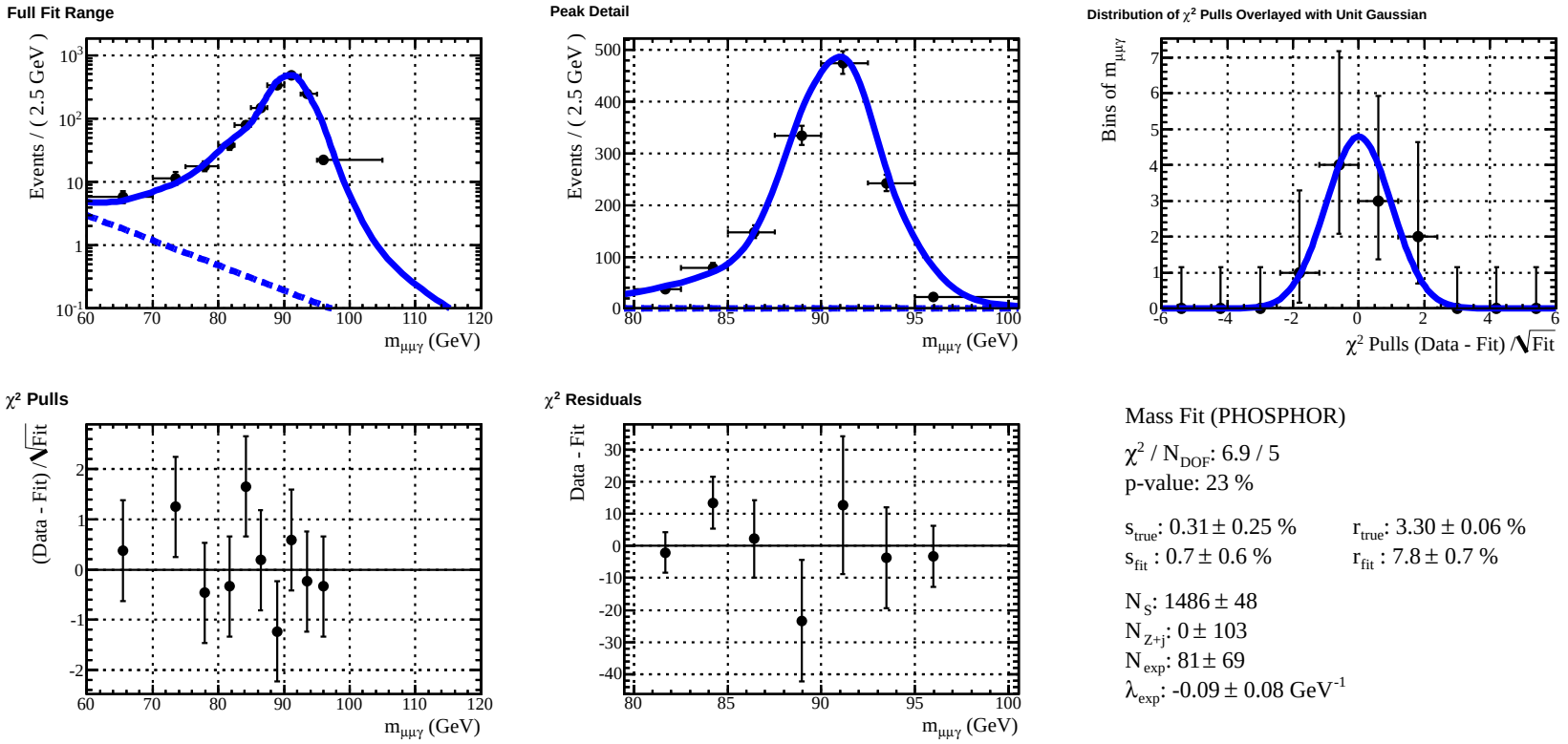

Figure A.37: Fit to $\mu\mu\gamma$ invariant mass in data for photons in the endcaps, with $R_9 > 0.94$, and p_T of (10 to 15) GeV.

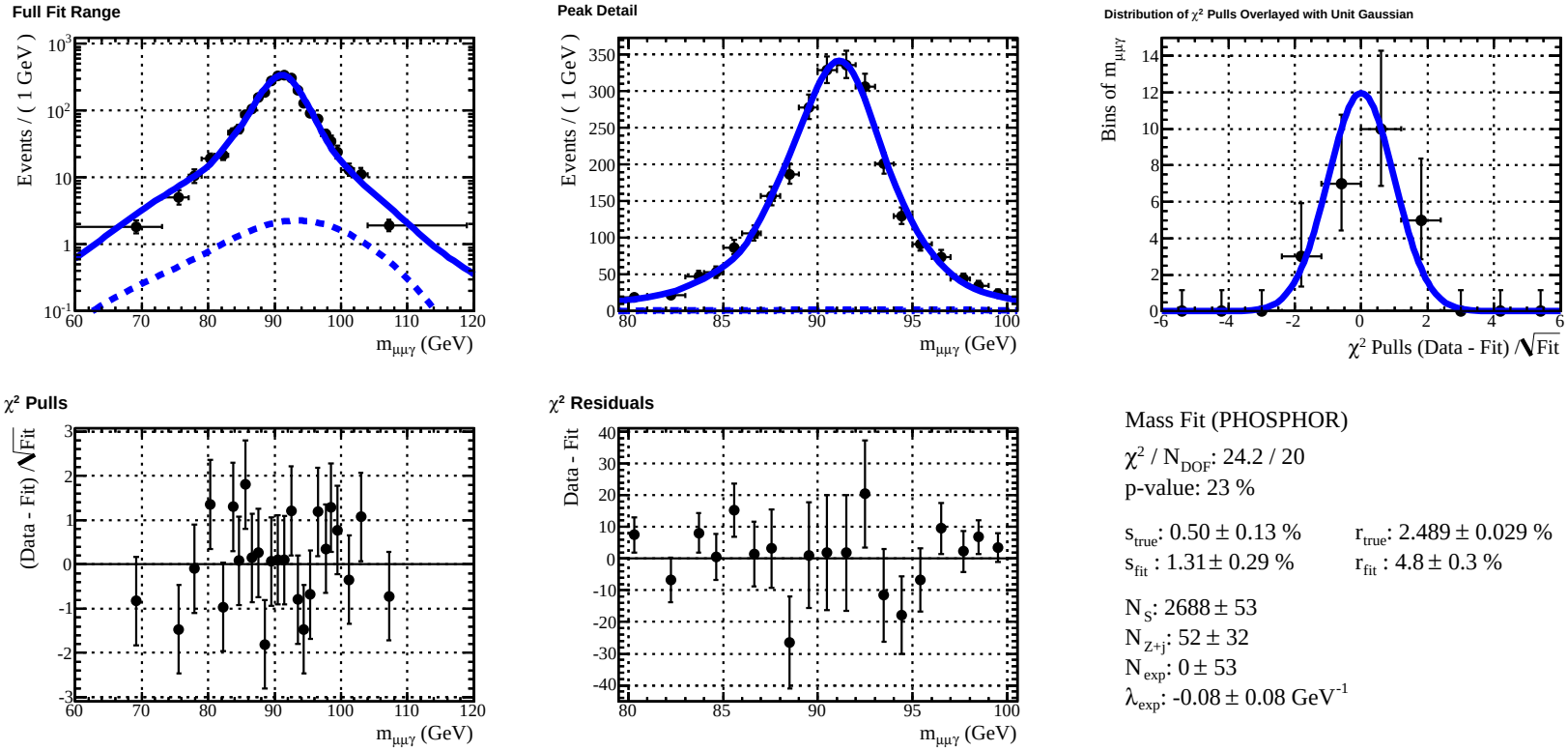

Figure A.38: Fit to $\mu\mu\gamma$ invariant mass in data for photons in the endcaps, with $R_9 > 0.94$, and $p_T > 15\,\text{GeV}$.

A.3.4 Endcaps, $R_9 < 0.94$

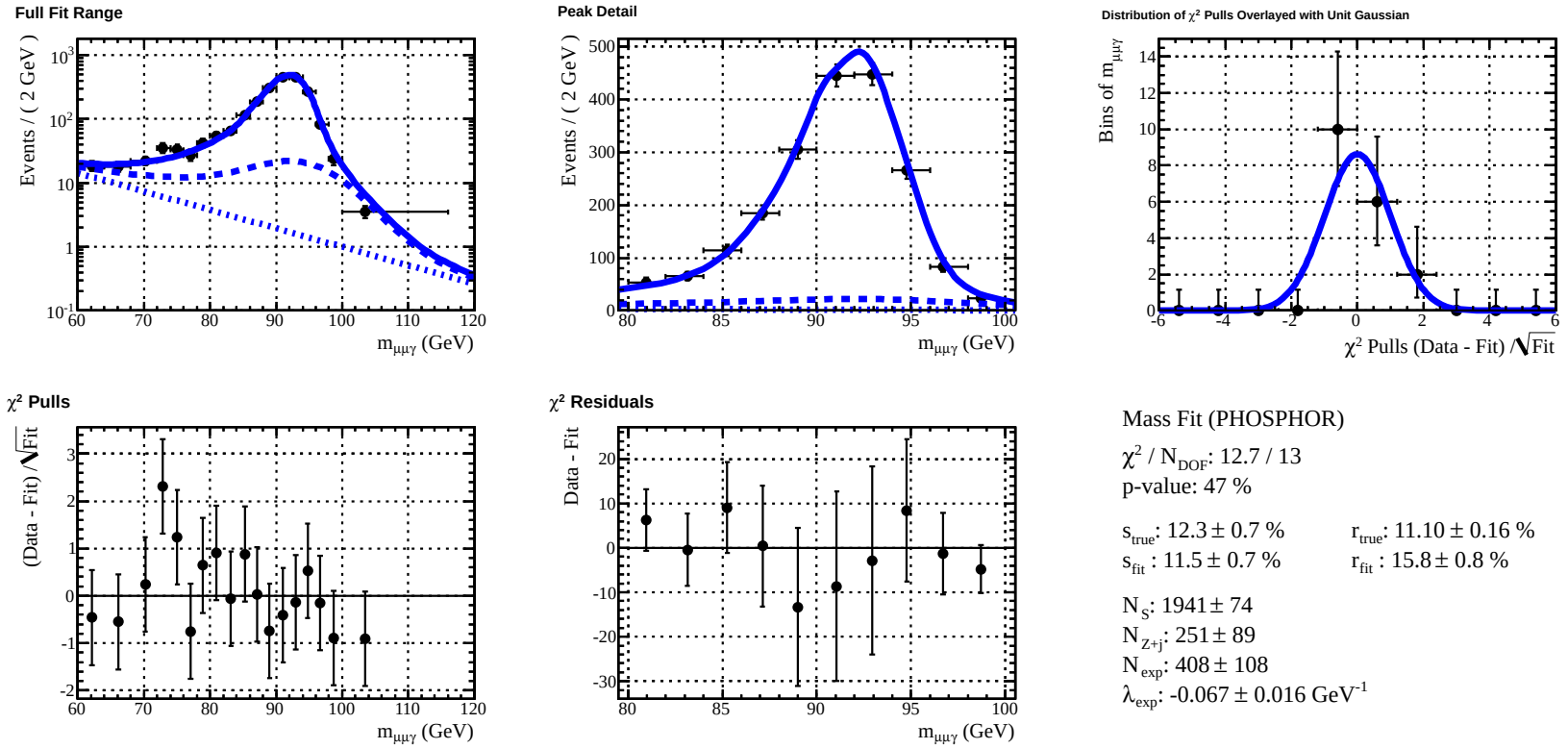

Figure A.39: Fit to $\mu\mu\gamma$ invariant mass in data for photons in the endcaps, with $R_9 < 0.94$, and p_T of (10 to 12) GeV.

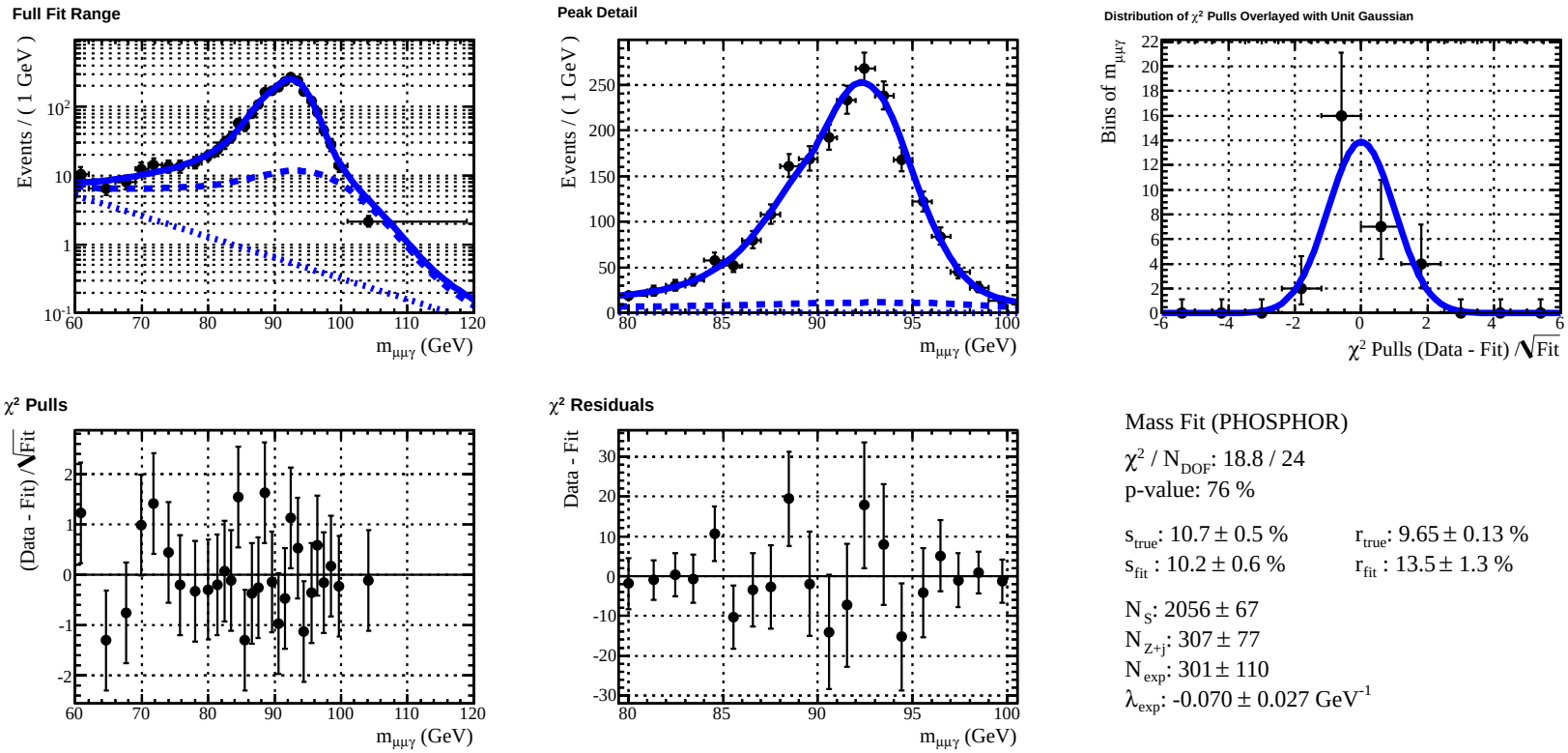

Figure A.40: Fit to $\mu\mu\gamma$ invariant mass in data for photons in the endcaps, with $R_9 < 0.94$, and p_{T} of (12 to 15) GeV.

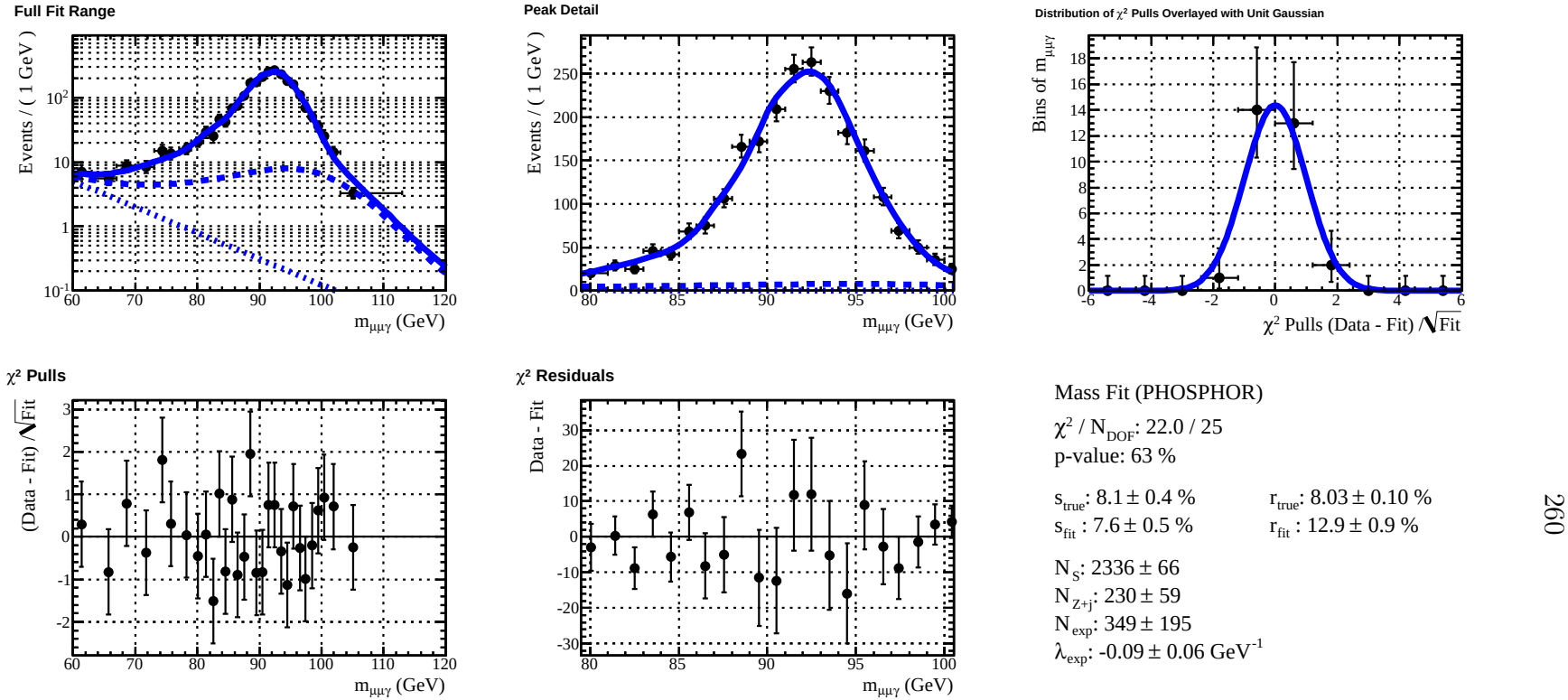

Figure A.41: Fit to $\mu\mu\gamma$ invariant mass in data for photons in the endcaps, with $R_9 < 0.94$, and p_T of (15 to 20) GeV.

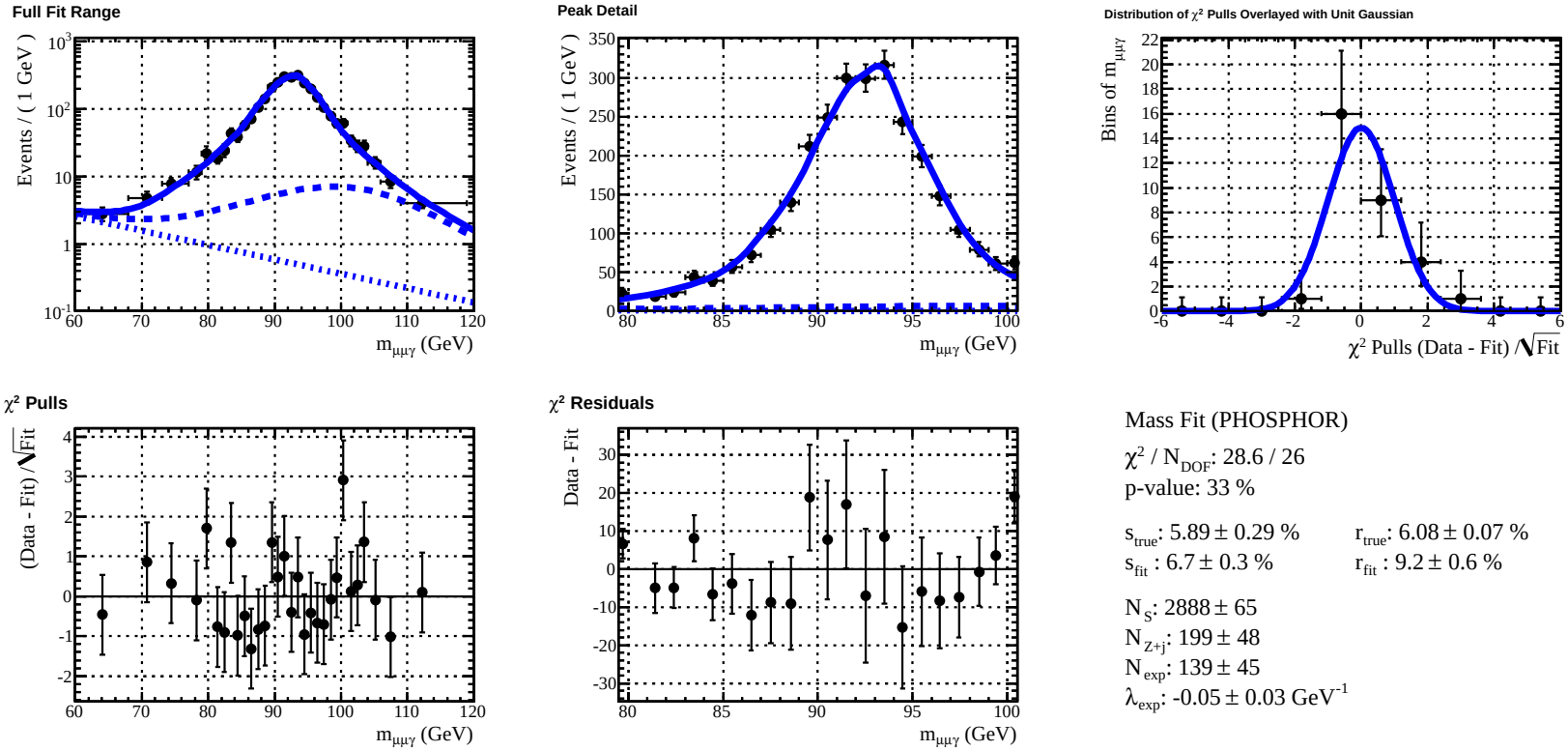

Figure A.42: Fit to $\mu\mu\gamma$ invariant mass in data for photons in the endcaps, with $R_9 < 0.94$, and $p_T > 20\,\text{GeV}$.

Bibliography

[1] M. Baak, M. Goebel, J. Haller, A. Hoecker, D. Kennedy, et al. The Electroweak Fit of the Standard Model after the Discovery of a New Boson at the LHC. 2012. arXiv:1209.2716.

[2] Michael E. Peskin and Dan V. Schroeder. *An Introduction To Quantum Field Theory (Frontiers in Physics)*. Westview Press, 1995. URL: http://www.westviewpress.com/book.php?isbn=9780201503975.

[3] J. Beringer *et al.* (Particle Data Group). Review of particle physics. *Phys. Rev. D*, 86:010001, Jul 2012. URL: http://link.aps.org/doi/10.1103/PhysRevD.86.010001, doi:10.1103/PhysRevD.86.010001.

[4] M. Gell-Mann and Y. Ne'eman. *The Eightfold Way: A Review - With Collection of Reprints*. Frontiers in Physics. W. A. Benjamin, Inc., New York - Amsterdam, 1964.

[5] B. Pontecorvo. Mesonium and anti-mesonium. *Sov.Phys.JETP*, 6:429, 1957.

[6] Z. Maki, M. Nakagawa, and S. Sakata. Remarks on the Unified Model of Elementary Particles. *Progress of Theoretical Physics*, 28:870–880, November 1962. doi:10.1143/PTP.28.870.

[7] B. Pontecorvo. Neutrino Experiments and the Problem of Conservation of Leptonic Charge. *Sov. Phys. JETP*, 26:984–988, 1968.

[8] Nicola Cabibbo. Unitary symmetry and leptonic decays. *Phys. Rev. Lett.*, 10:531–533, Jun 1963. URL:

http://link.aps.org/doi/10.1103/PhysRevLett.10.531, doi:10.1103/PhysRevLett.10.531.

[9] M. Kobayashi and T. Maskawa. CP-Violation in the Renormalizable Theory of Weak Interaction. *Progress of Theoretical Physics*, 49:652–657, February 1973. doi:10.1143/PTP.49.652.

[10] Ettore Majorana. Teoria simmetrica dell'elettrone e del positrone. *Il Nuovo Cimento*, 14(4):171–184, 1937. doi:10.1007/BF02961314.

[11] Luciano Maiani. A symmetric Theory of Electrons and Positrons, April 1981. English translation of a Note by Ettore Majorana published in *Il Nuovo Cimento* 14 (1937) 171-184, Accessed on-line: 7 April 2013. URL: http://www2.phys.canterbury.ac.nz/editorial/Majorana1937-Maiani2.pdf.

[12] Peter Minkowski. $\mu \to e\gamma$ at a rate of one out of 10^9 muon decays? *Physics Letters B*, 67(4):421 – 428, 1977. URL: http://www.sciencedirect.com/science/article/pii/037026937790435X, doi:10.1016/0370-2693(77)90435-X.

[13] M. Gell-Mann, P. Ramond, and R. Slansky. Supergravity: proceedings of the Supergravity Workshop at Stony Brook, 27-29 September 1979. volume 68 of *Physics reports*, pages 315–321. North-Holland Pub. Co., 1979. URL: http://books.google.ch/books?id=Dg-CAAAAIAAJ.

[14] Tsutomu Yanagida. Horizontal Symmetry and Masses of Neutrinos. *Progress of Theoretical Physics*, 64(3):1103–1105, 1980. URL: http://ptp.ipap.jp/link?PTP/64/1103/, doi:10.1143/PTP.64.1103.

[15] Rabindra N. Mohapatra and Goran Senjanović. Neutrino Mass and Spontaneous Parity Nonconservation. *Phys. Rev. Lett.*, 44:912–915, Apr 1980. URL: http://link.aps.org/doi/10.1103/PhysRevLett.44.912, doi:10.1103/PhysRevLett.44.912.

[16] J. Schechter and J. W. F. Valle. Neutrino masses in SU(2) $\bigotimes$ U(1) theories. *Phys. Rev. D*, 22:2227–2235, Nov 1980. URL: http://link.aps.org/doi/10.1103/PhysRevD.22.2227, doi:10.1103/PhysRevD.22.2227.

[17] R. Jackiw and C. Rebbi. Vacuum Periodicity in a Yang-Mills Quantum Theory. *Phys. Rev. Lett.*, 37:172–175, Jul 1976. URL: http://link.aps.org/doi/10.1103/PhysRevLett.37.172, doi:10.1103/PhysRevLett.37.172.

[18] C.G. Callan Jr., R.F. Dashen, and D.J. Gross. The structure of the gauge theory vacuum. *Physics Letters B*, 63(3):334 – 340, August 1976. URL: http://www.sciencedirect.com/science/article/pii/037026937690277X, doi:10.1016/0370-2693(76)90277-X.

[19] R. D. Reccei. *CP Violation*, volume 3 of *Advanced Series on Directions in High Energy Physics*, chapter The Strong CP Problem. World Scientific Publishing Co., 1989. URL: http://www.worldscientific.com/worldscibooks/10.1142/0496.

[20] G. Gabrielse, D. Hanneke, T. Kinoshita, M. Nio, and B. Odom. New determination of the fine structure constant from the electron g value and qed. *Phys. Rev. Lett.*, 97:030802, Jul 2006. URL: http://link.aps.org/doi/10.1103/PhysRevLett.97.030802, doi:10.1103/PhysRevLett.97.030802.

[21] G. Gabrielse, D. Hanneke, T. Kinoshita, M. Nio, and B. Odom. Erratum: New Determination of the Fine Structure Constant from the Electron g Value and QED [Phys. Rev. Lett. 97, 030802 (2006)]. *Phys. Rev. Lett.*, 99:039902, Jul 2007. URL: http://link.aps.org/doi/10.1103/PhysRevLett.99.039902, doi:10.1103/PhysRevLett.99.039902.

[22] D. Hanneke, S. Fogwell, and G. Gabrielse. New Measurement of the Electron Magnetic Moment and the Fine Structure Constant. *Phys. Rev. Lett.*,

100:120801, Mar 2008. URL:
http://link.aps.org/doi/10.1103/PhysRevLett.100.120801,
doi:10.1103/PhysRevLett.100.120801.

[23] Tatsumi Aoyama, Masashi Hayakawa, Toichiro Kinoshita, and Makiko Nio. Tenth-order qed contribution to the electron $g-2$ and an improved value of the fine structure constant. *Phys. Rev. Lett.*, 109:111807, Sep 2012. URL: http://link.aps.org/doi/10.1103/PhysRevLett.109.111807, doi:10.1103/PhysRevLett.109.111807.

[24] E. Fermi. Versuch einer Theorie der ß-Strahlen. I. *Zeitschrift für Physik*, 88(3-4):161–177, 1934. doi:10.1007/BF01351864.

[25] Fred L. Wilson. Fermi's Theory of Beta Decay. *American Journal of Physics*, 36(12):1150–1160, 1968. A complete English translation of the classic Enrico Fermi paper on beta decay published in *Zeitschrift für Physik* in 1934. URL: http://link.aip.org/link/?AJP/36/1150/1, doi:10.1119/1.1974382.

[26] David Griffiths. *Introduction to Elementary Particles*, pages 314–315. WILLEY-VCH Verlag GmbH & Co., Berlin, 2nd edition, October 2008. URL: http://www.wiley-vch.de/publish/en/books/ISBN3-527-40601-8/.

[27] The MuLan Collaboration, D. M. Webber, V. Tishchenko, Q. Peng, S. Battu, R. M. Carey, D. B. Chitwood, J. Crnkovic, P. T. Debevec, S. Dhamija, W. Earle, A. Gafarov, K. Giovanetti, T. P. Gorringe, F. E. Gray, Z. Hartwig, D. W. Hertzog, B. Johnson, P. Kammel, B. Kiburg, S. Kizilgul, J. Kunkle, B. Lauss, I. Logashenko, K. R. Lynch, R. McNabb, J. P. Miller, F. Mulhauser, C. J. G. Onderwater, J. Phillips, S. Rath, B. L. Roberts, P. Winter, and B. Wolfe. Measurement of the Positive Muon Lifetime and Determination of the Fermi Constant to Part-per-Million Precision. *Phys. Rev. Lett.*, 106:041803, Jan 2011. URL: http://link.aps.org/doi/10.1103/PhysRevLett.106.041803, doi:10.1103/PhysRevLett.106.041803.

[28] R. The ALEPH CollaborationBarate et al. Measurement of the Z resonance parameters at LEP. *The European Physical Journal C - Particles and Fields*, 14(1):1–50, 2000. URL: http://dx.doi.org/10.1007/s100520000319, doi:10.1007/s100520000319.

[29] M. The L3 Collaboration Acciarri et al. Measurements of cross sections and forward-backward asymmetries at the Z resonance and determination of electroweak parameters. *The European Physical Journal C - Particles and Fields*, 16(1):1–40, 2000. URL: http://dx.doi.org/10.1007/s100520050001, doi:10.1007/s100520050001.

[30] The DELPHI Collaboration, P. Abreu, et al. Cross-sections and leptonic forward backward asymmetries from the Z^0 running of LEP. *The European Physical Journal C - Particles and Fields*, 16(3):371–405, 2000. URL: http://dx.doi.org/10.1007/s100520000392, doi:10.1007/s100520000392.

[31] The OPAL Collaboration, G. Abbiendi, et al. Precise determination of the Z resonance parameters at LEP: 'Zedometry'. *The European Physical Journal C - Particles and Fields*, 19(4):587–651, 2001. URL: http://dx.doi.org/10.1007/s100520100627, arXiv:hep-ex/0012018, doi:10.1007/s100520100627.

[32] ALEPH Collaboration, CDF Collaboration, D0 Collaboration, DELPHI Collaboration, L3 Collaboration, OPAL Collaboration, SLD Collaboration, LEP Electroweak Working Group, Tevatron Electroweak Working Group, SLD Electroweak, and Heavy Flavour Groups. Precision Electroweak Measurements and Constraints on the Standard Model. 2010. URL: https://cds.cern.ch/record/1313716, arXiv:1012.2367.

[33] The Atlas Collaboration. Combined measurements of the mass and signal strength of the Higgs-like boson with the ATLAS detector using up to 25 fb^{-1}

of proton-proton collision data. Technical Report ATLAS-CONF-2013-014, CERN, Geneva, Mar 2013. URL: http://cds.cern.ch/record/1523727.

[34] The CMS Collaboration. Combination of standard model Higgs boson searches and measurements of the properties of the new boson with a mass near 125 GeV. Technical Report CMS-PAS-HIG-12-045, CERN, Geneva, November 2012. URL: http://cds.cern.ch/record/1494149.

[35] Workshop on Z Physics at LEP1 : General Meetings, vol. 1 : Standard Physics. In M. Consoli, W. Hollik, and F. Jegerlehner, editors, *Z Physics at LEP1: Standard Physics*, volume 1: Standard Physics, pages 7–52, Geneva, 1989. CERN, CERN. Coordinated and supervised by G. Altarelli. URL: http://cds.cern.ch/record/116932, doi:10.5170/CERN-1989-008-V-1.

[36] W.F.L. Hollik. Radiative Corrections in the Standard Model and their Role for Precision Tests of the Electroweak Theory. *Fortsch.Phys.*, 38:165–260, 1990. doi:10.1002/prop.2190380302.

[37] K. Hagiwara, R. D. Peccei, D. Zeppenfeld, and K. Hikasa. Probing the Weak Boson Sector in $e^-e^+ \to W^+W^-$. *Nuclear Physics B*, 282(0):253 – 307, 1987. URL: http://www.sciencedirect.com/science/article/pii/0550321387906857, doi:10.1016/0550-3213(87)90685-7.

[38] U. Baur and E. L. Berger. Probing the weak-boson sector in $Z\gamma$ production at hadron colliders. *Phys. Rev. D*, 47:4889–4904, Jun 1993. URL: http://link.aps.org/doi/10.1103/PhysRevD.47.4889, doi:10.1103/PhysRevD.47.4889.

[39] U. Baur, T. Han, and J. Ohnemus. QCD corrections and anomalous couplings in $Z\gamma$ production at hadron colliders. *Phys. Rev. D*, 57:2823–2836, Mar 1998. URL: http://link.aps.org/doi/10.1103/PhysRevD.57.2823, doi:10.1103/PhysRevD.57.2823.

[40] L. D. Landau. The moment of a 2-photon system. *Doklady Akademii Nauk SSSR*, 60:207, 1948.

[41] C. N. Yang. Selection Rules for the Dematerialization of a Particle into Two Photons. *Phys. Rev.*, 77:242–245, Jan 1950. doi:10.1103/PhysRev.77.242.

[42] G. Bélanger and F. Boudjema. Probing quartic couplings of weak bosons through three vector production at a 500 GeV NLC. *Physics Letters B*, 288(1–2):201 – 209, 1992. URL: http://www.sciencedirect.com/science/article/pii/037026939291978I, doi:10.1016/0370-2693(92)91978-I.

[43] G. A. Leil and W. J. Stirling. Anomalous quartic couplings in W+ W- gamma production at e+ e- colliders. *Journal of Physics G: Nuclear and Particle Physics*, 21(4):517, 1995. URL: http://stacks.iop.org/0954-3899/21/i=4/a=003, doi:10.1088/0954-3899/21/4/003.

[44] F. Gangemi, G. Montagna, M. Moretti, O. Nicrosini, and F. Piccinini. Electroweak physics in six fermion final states at future e+ e- colliders. In G. Jarlskog, U. Mjornmark, and T. Sjostrand, editors, *The development of future linear electron positron colliders: For particle physics and for research using free electron lasers. Proceedings, Workshop, Lund, Sweden, September 23-25, 1999*, pages 296–303, 1999. URL: http://www.hep.lu.se/workshop/lincol/, arXiv:hep-ph/0001065.

[45] W. James Stirling and Anja Werthenbach. Anomalous quartic couplings in $\nu\overline{\nu}\gamma\gamma$ production via WW-fusion at LEP2. *Physics Letters B*, 466(2–4):369 – 374, 1999. URL: http://www.sciencedirect.com/science/article/pii/S037026939901165X, doi:10.1016/S0370-2693(99)01165-X.

[46] G. Bélanger, F. Boudjema, Y. Kurihara, D. Perret-Gallix, and A. Semenov. Bosonic quartic couplings at LEP2. *The European Physical Journal C -*

Particles and Fields, 13(2):283–293, 2000. URL: http://dx.doi.org/10.1007/s100520000305, doi:10.1007/s100520000305.

[47] W.J. Stirling and A. Werthenbach. Anomalous quartic couplings in $W^+W^-\gamma$, $Z^0Z^0\gamma$ and $Z^0\gamma\gamma$ production at present and future e^+e^- colliders. *The European Physical Journal C - Particles and Fields*, 14(1):103–110, 2000. URL: http://dx.doi.org/10.1007/s100520000399, doi:10.1007/s100520000399.

[48] A. Denner, S. Dittmaier, M. Roth, and D. Wackeroth. Probing anomalous quartic gauge-boson couplings via $e^+e^- \to 4$ fermions $+ \gamma$. *The European Physical Journal C - Particles and Fields*, 20(2):201–215, 2001. URL: http://dx.doi.org/10.1007/s100520100678, doi:10.1007/s100520100678.

[49] G. Montagna, M. Moretti, O. Nicrosini, M. Osmo, and F. Piccinini. Quartic anomalous couplings at LEP. *Physics Letters B*, 515(1–2):197 – 205, 2001. URL: http://www.sciencedirect.com/science/article/pii/S0370269301008346, doi:10.1016/S0370-2693(01)00834-6.

[50] John M. Cornwall, David N. Levin, and George Tiktopoulos. Uniqueness of Spontaneously Broken Gauge Theories. *Phys. Rev. Lett.*, 30:1268–1270, Jun 1973. URL: http://link.aps.org/doi/10.1103/PhysRevLett.30.1268, doi:10.1103/PhysRevLett.30.1268.

[51] John M. Cornwall, David N. Levin, and George Tiktopoulos. Derivation of gauge invariance from high-energy unitarity bounds on the S matrix. *Phys. Rev. D*, 10:1145–1167, Aug 1974. URL: http://link.aps.org/doi/10.1103/PhysRevD.10.1145, doi:10.1103/PhysRevD.10.1145.

[52] John M. Cornwall, David N. Levin, and George Tiktopoulos. Erratum: Derivation of gauge invariance from high-energy unitarity bounds on the S matrix. *Phys. Rev. D*, 11:972–972, Feb 1975. URL: http://link.aps.org/doi/10.1103/PhysRevD.11.972, doi:10.1103/PhysRevD.11.972.

[53] C.H. Llewellyn Smith. High energy behaviour and gauge symmetry. *Physics Letters B*, 46(2):233 – 236, 1973. URL: http://www.sciencedirect.com/science/article/pii/0370269373906928, doi:10.1016/0370-2693(73)90692-8.

[54] Satish D Joglekar. S-matrix derivation of the Weinberg Model. *Annals of Physics*, 83(2):427 – 448, 1974. URL: http://www.sciencedirect.com/science/article/pii/000349167490205X, doi:10.1016/0003-4916(74)90205-X.

[55] Robert Hofstadter. Electron Scattering and Nuclear Structure. *Rev. Mod. Phys.*, 28:214–254, Jul 1956. URL: http://link.aps.org/doi/10.1103/RevModPhys.28.214, doi:10.1103/RevModPhys.28.214.

[56] Oliver Sim Brüning, Paul Collier, P Lebrun, Stephen Myers, Ranko Ostojic, John Poole, and Paul Proudlock. *LHC Design Report*, volume v.1: the LHC Main Ring. CERN, Geneva, 2004. URL: http://cdsweb.cern.ch/record/782076.

[57] Oliver Sim Brüning, Paul Collier, P Lebrun, Stephen Myers, Ranko Ostojic, John Poole, and Paul Proudlock. *LHC Design Report*, volume v.2 : the LHC Infrastructure and General Services. CERN, Geneva, 2004. CERN-2004-003-V-2. URL: http://cdsweb.cern.ch/record/815187.

[58] Michael Benedikt, Paul Collier, V Mertens, John Poole, and Karlheinz Schindl. *LHC Design Report*, volume v.3 : the LHC Injector Chain. CERN,

Geneva, 2004. CERN-2004-003-V-3. URL: http://cdsweb.cern.ch/record/823808.

[59] The LEP Injector Study Group. *LEP Design Report*, volume v.1 : The LEP Injector Chain. CERN, Geneva, 1983. CERN-LEP/TH/83-29, CERN/PS/DL/83-31, CERN/SPS/83-26, LAL/RT/83-09. URL: https://cdsweb.cern.ch/record/98881.

[60] *LEP Design Report*, volume v.2 : The LEP Main Ring. CERN, Geneva, 1984. CERN-LEP-84-01. URL: https://cdsweb.cern.ch/record/102083.

[61] AC Team. The scale of the LHC. Vue aérienne du CERN avec le tracé du tunnel LHC. January 2001. URL: https://cdsweb.cern.ch/record/42370.

[62] Christiane Lefèvre. The CERN accelerator complex. Complexe des accélérateurs du CERN. Dec 2008. URL: https://cdsweb.cern.ch/record/1260465.

[63] (ed.) Evans, Lyndon and (ed.) Bryant, Philip. LHC Machine. *JINST*, 3:S08001, 2008. doi:10.1088/1748-0221/3/08/S08001.

[64] The CMS Collaboration. CMS Luminosity - Public Results, February 2013. CMS authentication required. Accessed: 5 April 2013. URL: https://twiki.cern.ch/twiki/bin/view/CMSPublic/LumiPublicResults.

[65] The CMS Collaboration, S Chatrchyan, et al. Measurement of the inelastic pp cross section at $sqrts = 7$ TeV with the CMS detector. 2012. arXiv:1210.6718.

[66] G. L. Bayatian et al. *CMS Physics Technical Design Report, Volume I: Detector Performance and Software*, volume 8.1 of *Technical Design Report CMS*. CERN, Geneva, February 2006. CERN-LHCC-2006-001; CMS-TDR-008-1. URL: http://cdsweb.cern.ch/record/922757.

[67] S. Chatrchyan et al. The CMS experiment at the CERN LHC. *JINST*, 3:S08004, 2008. doi:10.1088/1748-0221/3/08/S08004.

[68] The ATLAS Collaboration. *ATLAS Detector and Physics Performance: Technical Design Report, 1*, volume 14 of *Technical Design Report ATLAS*. CERN, Geneva, May 1999. ATLAS-TDR-014; CERN-LHCC-99-014. URL: https://cdsweb.cern.ch/record/391176.

[69] The ATLAS Collaboration et al. The atlas experiment at the cern large hadron collider. *Journal of Instrumentation*, 3(08):S08003, 2008. doi:doi:10.1088/1748-0221/3/08/S08003.

[70] Lucas Taylor. CMS People Statistics, April 2012. Accessed: 26 April 2013. URL: http://cms.web.cern.ch/content/people-statistics.

[71] Michael Hoch. CMS collaboration Summer 2012. CMS Collection., Jun 2012. URL: http://cdsweb.cern.ch/record/1458569.

[72] The CMS Collaboration, Manfred Markytan, et al. Letter of Intent: by the CMS Collaboration for a General Purpose Detector at LHC. Technical report, CERN, Geneva, October 1992. CERN-LHCC-92-003; LHCC-I-1. URL: https://cdsweb.cern.ch/record/290808.

[73] G. L. Bayatian et al. CMS Physics Technical Design Report, Volume II: Physics Performance. *J. Phys. G*, G34:995–1579, 2007. CERN-LHCC-2006-021; CMS-TDR-008-2. URL: http://cdsweb.cern.ch/record/942733, doi:10.1088/0954-3899/34/6/S01.

[74] David Barney. CMS slice raw illustrator files. CMS Document 5581-v1, Sep 2011. URL: https://cms-docdb.cern.ch/cgi-bin/PublicDocDB/ShowDocument?docid=5581.

[75] The CMS Collaboration. *The CMS Magnet Project: Technical Design Report*, volume 1 of *Technical Design Report CMS*. CERN, Geneva, May 1997.

CERN-LHCC-97-010; CMS-TDR-001. URL: http://cdsweb.cern.ch/record/331056.

[76] The CMS Collaboration. *The CMS Tracker System Project: Technical Design Report*, volume 5 of *Technical Design Report CMS*. CERN, Geneva, April 1998. CERN-LHCC-98-006; CMS-TDR-005. URL: http://cdsweb.cern.ch/record/368412.

[77] The CMS Collaboration. *The CMS Tracker: Addendum to the Technical Design Report*, volume 5.1 of *Technical Design Report CMS*. CERN, Geneva, February 2000. CERN-LHCC-2000-016; CMS-TDR-005-add-1. URL: http://cdsweb.cern.ch/record/490194.

[78] The CMS Collaboration. Description and performance of the CMS track and primary vertex reconstruction. (CMS-TRK-11-001), 2012. To be published. In the internal collaboration review as of this writing. Access requires CMS authentication. URL: http://cms.cern.ch/iCMS/analysisadmin/cadi?ancode=TRK-11-001.

[79] The CMS Collaboration. *The CMS Electromagnetic Calorimeter Project: Technical Design Report*, volume 4 of *Technical Design Report CMS*. CERN, Geneva, December 1997. CERN-LHCC-97-033; CMS-TDR-004. URL: http://cdsweb.cern.ch/record/349375.

[80] Philippe Bloch, Robert Brown, Paul Lecoq, and Hans Rykaczewski. *Changes to CMS ECAL electronics: Addendum to the Technical Design Report*, volume 4.1 of *Technical Design Report CMS*. CERN, Geneva, September 2002. CERN-LHCC-2002-027; CMS-TDR-004-add-1. URL: http://cdsweb.cern.ch/record/581342.

[81] Ren-Yuan Zhu. Radiation damage in scintillating crystals. *Nuclear Instruments and Methods in Physics Research Section A: Accelerators, Spectrometers, Detectors and Associated Equipment*, 413(2–3):297–311, 1998. doi:10.1016/S0168-9002(98)00498-7.

[82] CMS Collaboration. 2012 ECAL detector performance plots. (CMS-DP-2013-007), Mar 2013. URL: http://cdsweb.cern.ch/record/1528235.

[83] P. Adzic et al. Energy resolution of the barrel of the CMS Electromagnetic Calorimeter. *Journal of Instrumentation*, 2(04):P04004, 2007. doi:10.1088/1748-0221/2/04/P04004.

[84] S. Agostinelli et al. GEANT4 – a simulation toolkit. *Nucl. Instr. and Methods*, A506:250, 2003. doi:10.1016/S0168-9002(03)01368-8.

[85] CMS Collaboration. ECAL Detector Performance, 2011 Data. (CMS-DP-2012-007), May 2012. URL: http://cdsweb.cern.ch/record/1457922.

[86] The CMS Collaboration. *The CMS Hadron Calorimeter Project: Technical Design Report*, volume 2 of *Technical Design Report CMS*. CERN, Geneva, June 1997. CERN-LHCC-97-031; CMS-TDR-002. URL: http://cdsweb.cern.ch/record/357153.

[87] The CMS HCAL Collaboration, S. Abdullin, et al. Design, performance, and calibration of CMS forward calorimeter wedges. *The European Physical Journal C - Particles and Fields*, 53:139–166, 2008. doi:10.1140/epjc/s10052-007-0459-4.

[88] The CMS ECAL/HCAL Collaborations, Efe Yazgan, et al. The CMS barrel calorimeter response to particle beams from 2 to 350 GeV/c. *Journal of Physics: Conference Series*, 160(1):012056, 2009. doi:10.1088/1742-6596/160/1/012056.

[89] The CMS collaboration, Serguei Chatrchyan, et al. Determination of jet energy calibration and transverse momentum resolution in CMS. *Journal of Instrumentation*, 6(11):P11002, 2011. URL:

http://stacks.iop.org/1748-0221/6/i=11/a=P11002, arXiv:1107.4277, doi:10.1088/1748-0221/6/11/P11002.

[90] The CMS Collaboration. *The CMS muon project: Technical Design Report*, volume 3 of *Technical Design Report CMS*. CERN, Geneva, December 1997. CERN-LHCC-97-032; CMS-TDR-003. URL: http://cdsweb.cern.ch/record/343814.

[91] Serguei Chatrchyan et al. Performance of CMS Muon Reconstruction in pp Collision Events at sqrt(s) = 7 TeV. 2012. arXiv:1206.4071.

[92] The CMS Collaboration. Tracking and Vertexing Results from First Collisions. (CMS-PAS-TRK-10-001), 2010. URL: http://cdsweb.cern.ch/record/1258204.

[93] Wolfgang Adam, Boris Mangano, Thomas Speer, and Teddy Todorov. Track Reconstruction in the CMS tracker. Technical Report CMS-NOTE-2006-041, CERN, Geneva, Dec 2006. URL: http://cdsweb.cern.ch/record/934067.

[94] Susanna Cucciarelli, Marcin Konecki, Danek Kotlinski, and Teddy Todorov. Track reconstruction, primary vertex finding and seed generation with the Pixel Detector. Technical Report CMS-NOTE-2006-026, CERN, Geneva, Jan 2006. URL: http://cdsweb.cern.ch/record/927384.

[95] R. E. Kalman. A New Approach to Linear Filtering and Prediction Problems. *Journal of Basic Engineering*, 82(1):35–45, 1960. URL: http://www.cs.unc.edu/~welch/kalman/media/pdf/Kalman1960.pdf, doi:10.1115/1.3662552.

[96] R. E. Kalman and R. S. Bucy. New Results in Linear Filtering and Prediction Theory. *Journal of Basic Engineering*, 83(1):95–108, 1961. URL: http://www.eecs.tufts.edu/~khan/Courses/Spring2012/EE194/Lecs/KalmanBucy1961.pdf, doi:10.1115/1.3658902.

[97] R. Frühwirth. Application of Kalman filtering to track and vertex fitting. *Nuclear Instruments and Methods in Physics Research Section A: Accelerators, Spectrometers, Detectors and Associated Equipment*, 262(2–3):444 – 450, 1987. doi:10.1016/0168-9002(87)90887-4.

[98] Lars Bugge and Jan Myrheim. Tracking and track fitting. *Nuclear Instruments and Methods*, 179(2):365 – 381, 1981. doi:10.1016/0029-554X(81)90063-X.

[99] The CMS Collaboration. Tracking and primary vertex results in first 7 tev collisions. (CMS-PAS-TRK-10-005), 2010. URL: http://cdsweb.cern.ch/record/1279383.

[100] K. Rose. Deterministic annealing for clustering, compression, classification, regression, and related optimization problems. *Proceedings of the IEEE*, 86(11):2210 –2239, nov 1998. doi:10.1109/5.726788.

[101] R Frühwirth, Wolfgang Waltenberger, and Pascal Vanlaer. Adaptive Vertex Fitting. CMS Note CMS-NOTE-2007-008, CERN, Geneva, Mar 2007. URL: http://cds.cern.ch/record/1027031.

[102] Ting Miao, N Leioatts, Hans Wenzel, and Francisco Yumiceva. Beam Position Determination using Tracks. Technical Report CMS-NOTE-2007-021, CERN, Geneva, Aug 2007. URL: https://cdsweb.cern.ch/record/1061285.

[103] P. Adzic et al. Reconstruction of the signal amplitude of the CMS electromagnetic calorimeter. *The European Physical Journal C - Particles and Fields*, 46:23–35, 2006. doi:10.1140/epjcd/s2006-02-002-x.

[104] CMS ECAL Group. Studies of the CMS Electromagnetic Calorimeter performance in the electron test beam. *J. Phys. Conf. Ser.*, 160:012048, 2010. doi:10.1088/1742-6596/160/1/012048.

[105] Emilio Meschi, T Monteiro, Christopher Seez, and Pratibha Vikas. Electron Reconstruction in the CMS Electromagnetic Calorimeter. Technical Report

CMS-NOTE-2001-034, CERN, Geneva, Jun 2001. URL: http://cds.cern.ch/record/687345.

[106] Guenter Grindhammer and S. Peters. The Parameterized Simulation of Electromagnetic Showers in Homogeneous and Sampling Calorimeters. 1993. arXiv:hep-ex/0001020.

[107] A. Askew, et. al. Study of $W\gamma$ and $Z\gamma$ production at CMS with $\sqrt{s} = 7TeV$. *CMS Analysis Note*, AN-2011/251, 2012. CMS internal publication (CMS authentication required for on-line access). URL: http://cms.cern.ch/iCMS/jsp/db_notes/showNoteDetails.jsp?noteID=CMS%20AN-2011/251.

[108] H. Bethe and W. Heitler. On the Stopping of Fast Particles and on the Creation of Positive Electrons. *Royal Society of London Proceedings Series A*, 146:83–112, August 1934. doi:10.1098/rspa.1934.0140.

[109] W Adam, R Frhwirth, A Strandlie, and T Todorov. Reconstruction of electrons with the Gaussian-sum filter in the CMS tracker at the LHC. *Journal of Physics G: Nuclear and Particle Physics*, 31(9):N9, 2005. doi:doi:10.1088/0954-3899/31/9/N01.

[110] S. Baffioni, C. Charlot, F. Ferri, D. Futyan, P. Meridiani, I. Puljak, C. Rovelli, R. Salerno, and Y. Sirois. Electron reconstruction in CMS. *The European Physical Journal C*, 49:1099–1116, 2007. doi:10.1140/epjc/s10052-006-0175-5.

[111] CMS Collaboration. Electron reconstruction and identification at $\sqrt{s} = 7$ TeV. CMS Physics Analysis Summary CMS-PAS-EGM-10-004, 2010. URL: http://cdsweb.cern.ch/record/1299116.

[112] CMS Collaboration. Electron tracker isolation producer source code, 2012. Accessed: 28 January 2013. URL: http://cmssw.cvs.cern.ch/cgi-bin/cmssw.cgi/CMSSW/RecoEgamma/EgammaIsolationAlgos/src/ElectronTkIsolation.cc?revision=1.9&view=markup.

[113] CMS Collaboration. Electron tracker isolation producer configuration, 2012. Accessed: 28 January 2013. URL: http://cmssw.cvs.cern.ch/cgi-bin/cmssw.cgi/CMSSW/RecoEgamma/EgammaIsolationAlgos/python/electronTrackIsolationScone_cfi.py?revision=1.4&view=markup.

[114] CMS Collaboration. Electron ECAL isolation producer source code, 2012. Accessed: 28 January 2013. URL: http://cmssw.cvs.cern.ch/cgi-bin/cmssw.cgi/CMSSW/RecoEgamma/EgammaIsolationAlgos/src/EgammaRecHitIsolation.cc?revision=1.14&view=markup.

[115] CMS Collaboration. Electron ECAL isolation producer configuration, 2012. Accessed: 28 January 2013. URL: http://cmssw.cvs.cern.ch/cgi-bin/cmssw.cgi/CMSSW/RecoEgamma/EgammaIsolationAlgos/python/electronEcalRecHitIsolationScone_cfi.py?revision=1.4&view=markup.

[116] Glen Cowan, Kyle Cranmer, Eilam Gross, and Ofer Vitells. Asymptotic formulae for likelihood-based tests of new physics. *The European Physical Journal C*, 71:1–19, 2011. doi:10.1140/epjc/s10052-011-1554-0.

[117] Bob Cousins for the CMS Statistics Committee. Probability Density Functions for Positive Nuisance Parameters, May 2010. Accessed: 6 April 2013. URL: http://www.physics.ucla.edu/~cousins/stats/cousins_lognormal_prior.pdf.

[118] The CMS Collaboration. Photon identification subtask, Oct 2010. CMS authentication required. URL: http://twiki.cern.ch/twiki/bin/view/CMS/PhotonID.

[119] The CMS Collaboration, S. Chatrchyan, et al. Measurement of the Drell-Yan cross section in pp collisions at $\sqrt{s} = 7$ TeV. *Journal of High Energy Physics*, 2011(10):1–41, 2011. URL: http://dx.doi.org/10.1007/JHEP10%282011%29007, doi:10.1007/JHEP10(2011)007.

[120] Murray Rosenblatt. Remarks on Some Nonparametric Estimates of a Density Function. *The Annals of Mathematical Statistics*, 27(3):pp. 832–837, 1956. URL: http://www.jstor.org/stable/2237390, doi:10.1214/aoms/1177728190.

[121] Emanuel Parzen. On Estimation of a Probability Density Function and Mode. *The Annals of Mathematical Statistics*, 33(3):pp. 1065–1076, 1962. URL: http://www.jstor.org/stable/2237880, doi:10.1214/aoms/1177704472.

[122] Mark Joseph Oreglia. *A Study of the Reactions* $\psi' \to \gamma\gamma\psi$, chapter D. Calibration, page 184. 1980. PhD dissertation, Standford University. URL: http://www.slac.stanford.edu/pubs/slacreports/slac-r-236.html.

[123] K. Nakamura et al. The review of particle physics. *J. Phys. G*, 37:075021, 2010. doi:10.1088/0954-3899/37/7A/075021.

[124] Kyle S. Cranmer. Kernel estimation in high-energy physics. *Computer Physics Communications*, 136(3):198 – 207, 2001. URL: http://www.sciencedirect.com/science/article/pii/S0010465500002435, arXiv:hep-ex/0011057, doi:10.1016/S0010-4655(00)00243-5.

[125] Fred James. MINUIT — Function Minimization and Error Analysis, May 2000. Accessed: 05 May 2013. URL: http://wwwasdoc.web.cern.ch/wwwasdoc/minuit/minmain.html.

[126] The CMS Collaboration. Collisions 2010 Recipes TWiki. URL: https://twiki.cern.ch/twiki/bin/viewauth/CMS/Collisions2010Recipes.

[127] J. Alcaraz Maestre *et al.* Updated measurements of inclusive w and z cross sections in pp collisions at $\sqrt{s} = 7$ tev. *CMS Note*, 264, 2010.

[128] Performance of cms muon identification in pp collisions at $\sqrt{s} = 7$ tev. *CMS PAS*, MUO-2010-002, 2010.

[129] The CMS Collaboration. PAT MC Matching TWiki. URL: https://twiki.cern.ch/twiki/bin/view/CMSPublic/SWGuidePATMCMatchingExercise.

[130] The CMS Collaboration. Estimating Systematic Errors Due to Pileup Modeling (PRELIMINARY Update for new 2011 and 2012 Luminosity Values), Mar 2013. CMS authentication required. Accessed: 14 April 2013. URL: https://twiki.cern.ch/twiki/bin/view/CMS/PileupSystematicErrors.

[131] Michiel Botje, Jon Butterworth, Amanda Cooper-Sarkar, Albert de Roeck, Joel Feltesse, et al. The PDF4LHC Working Group Interim Recommendations. 2011. arXiv:1101.0538.

[132] Jonathan Pumplin, Daniel Robert Stump, Joey Huston, Hung-Liang Lai, Pavel Nadolsky, and Wu-Ki Tung. New Generation of Parton Distributions with Uncertainties from Global QCD Analysis. *Journal of High Energy Physics*, 2002(07):012, 2002. doi:10.1088/1126-6708/2002/07/012.

[133] M. R. Whalley, D. Bourilkov, and R. C. Group. The Les Houches accord PDFs (LHAPDF) and LHAGLUE. 2005. Contributed to Conference HERA and the LHC: A Workshop on the Implications of HERA and LHC Physics (Startup Meeting, CERN, 26-27 March 2004; Midterm Meeting, CERN, 11-13 October 2004), Hamburg, Germany, 21-24 Mar 2005. arXiv:hep-ph/0508110.

[134] D. Bourilkov, R. C. Group, and M. R. Whalley. LHAPDF: PDF use from the Tevatron to the LHC. 2006. Contributed to Conference TeV4LHC Workshop - 4th meeting, Batavia, Illinois, 20-22 Oct 2005. arXiv:hep-ph/0605240.

[135] LHAPDF, the Les Houches Accord PDF Interface. Accessed: 25 March 2013. URL: https://lhapdf.hepforge.org/.

[136] Pavel M. Nadolsky and Z. Sullivan. PDF uncertainties in WH production at Tevatron. *eConf*, C010630:P510, 2001. arXiv:hep-ph/0110378, doi:OSTI/788251.

[137] Zack Sullivan. Fully differential W′ production and decay at next-to-leading order in QCD. *Phys. Rev. D*, 66:075011, Oct 2002. doi:10.1103/PhysRevD.66.075011.

[138] John M. Campbell, R. Keith Ellis, and Ciaran Williams. Vector boson pair production at the LHC. *Journal of High Energy Physics*, 2011:1–36, 2011. doi:10.1007/JHEP07(2011)018.

[139] Johan Alwall, Pavel Demin, Simon de Visscher, Rikkert Frederix, Michel Herquet, Fabio Maltoni, Tilman Plehn, David L. Rainwater, and Tim Stelzer. MadGraph/MadEvent v4: the new web generation. *Journal of High Energy Physics*, 2007(09):028, 2007. doi:10.1088/1126-6708/2007/09/028.

[140] CMS Collaboration. Absolute Calibration of the Luminosity Measurement at CMS: Winter 2012 Update. CMS Physics Analysis Summary CMS-PAS-SMP-12-008, CERN, Geneva, 2012. URL: http://cds.cern.ch/record/1434360.

[141] Louis Lyons, Duncan Gibaut, and Peter Clifford. How to combine correlated estimates of a single physical quantity. *Nucl.Instrum.Meth.*, A270:110, 1988. doi:10.1016/0168-9002(88)90018-6.

[142] T. Gleisberg et al. Sherpa 1.α, a proof-of-concept version. *JHEP*, 02:056, 2004. arXiv:hep-ph/0311263, doi:10.1088/1126-6708/2004/02/056.

[143] The L3 Collaboration, P. Acciarri, et al. Measurement of energetic single-photon production at LEP. *Physics Letters B*, 346(1–2):190 – 198, 1995. URL: http://www.sciencedirect.com/science/article/pii/037026939500023E, doi:10.1016/0370-2693(95)00023-E.

[144] The DELPHI Collaboration, P Abreu, et al. Measurement of trilinear gauge couplings in e^+e^- collisions at 161 GeV and 172 GeV. *Physics Letters B*, 423(1–2):194 – 206, 1998. URL: http:

//www.sciencedirect.com/science/article/pii/S037026939800080X, doi:10.1016/S0370-2693(98)00080-X.

[145] The OPAL Collaboration, G. Abbiendi, et al. Study of Z pair production and anomalous couplings in e^+e^- collisions at $\sqrt{s}$ between 190 GeV and 209 GeV. *Eur. Phys. J. C*, 32:303, 2003.

[146] The L3 Collaboration, P. Achard, et al. Study of the $e^+e^- \to Z\gamma$ process at LEP and limits on triple neutral-gauge-boson couplings. *Phys. Lett. B*, 597:119, 2004.

[147] The LEP Electroweak Working Group, D. Abbaneo, et al. A combination of preliminary electroweak measurements and constraints on the standard model. 2004. arXiv:0412015v2.

[148] The DELPHI Collaboration, J. Abdallah, et al. Study of Triple-Gauge-Boson Couplings ZZZ, ZZgamma and Zgammagamma at LEP. *Eur. Phys. J.*, C51:525, 2007. arXiv:0706.2741, doi:10.1140/epjc/s10052-007-0345-0.

[149] The ALEPH Collaboration, S. Schael, et al. Measurement of Z-pair production in e+ e- collisions and constraints on anomalous neutral gauge couplings. *JHEP*, 04:124, 2009. doi:10.1088/1126-6708/2009/04/124.

[150] The D0 Collaboration, V. M. Abazov, et al. $Z\gamma$ production and limits on anomalous $ZZ\gamma$ and $Z\gamma\gamma$ couplings in $p\bar{p}$ collisions at $\sqrt{s} = 1.96$ TeV. *Phys. Lett. B*, 653:378, 2007.

[151] The D0 Collaboration, V. M. Abazov, et al. Measurement of the $Z\gamma \to \nu\nu\gamma$ cross section and limits on anomalous $ZZ\gamma$ and $Z\gamma\gamma$ couplings in $p\bar{p}$ collisions at $\sqrt{s} = 1.96$ TeV. *Phys. Rev. Lett.*, 102:201802, 2009.

[152] T. The CDF Collaboration, T. Aaltonen et al. Measurement of $Z\gamma$ production in pp collisions at $\sqrt{s} = 1.96$ TeV. *Phys. Rev.*, D82:031103, 2010.

[153] The CMS Collaboration, S. Chatrchyan, et al. Measurement of $W\gamma$ and $Z\gamma$ production in pp collisions at $\sqrt{s} = 7$ TeV. *Phys. Lett.*, B701:535, 2011.

[154] Measurement of $W\gamma$ and $Z\gamma$ production cross sections in pp collisions at $\sqrt{s} = 7$ TeV and limits on anomalous triple couplings with the ATLAS detector. *Phys. Lett.*, B701:535, 2012. arXiv:hep-ex/1205.2531.

[155] The CMS Collaboration, S. Chatrchyan, et al. Measurement of Wγ and Zγ production in pp collisions at $\sqrt{s} = 7$ TeV. *Physics Letters B*, 701(5):535 – 555, 2011. URL: http://www.sciencedirect.com/science/article/pii/S0370269311006551, doi:10.1016/j.physletb.2011.06.034.

[156] The ATLAS Collaboration, G. Aad, et al. Measurement of Wγ and Zγ production in proton-proton collisions at $\sqrt{s} = 7$ TeV with the ATLAS detector. *Journal of High Energy Physics*, 2011(9):1–42, 2011. doi:10.1007/JHEP09(2011)072.

[157] The ATLAS Collaboration, G. Aad, et al. Measurement of Wγ and Zγ production cross sections in pp collisions at and limits on anomalous triple gauge couplings with the ATLAS detector. *Physics Letters B*, 717(13):49 – 69, 2012. URL: http://www.sciencedirect.com/science/article/pii/S0370269312009616, doi:10.1016/j.physletb.2012.09.017.

[158] CMS Collaboration. Search for the standard model Higgs boson in the Z boson plus a photon channel in pp collisions at sqrt-s = 7 and 8 TeV. CMS Physics Analysis Summary CMS-PAS-HIG-13-006, CERN, Geneva, Mar 2013. URL: http://cdsweb.cern.ch/record/1523674.